Cluster Expansion Applied to Inelastic Scattering Experiments

Thesis by

Matthew S. Lucas

In Partial Fulfillment of the Requirements

for the Degree of

Doctor of Philosophy

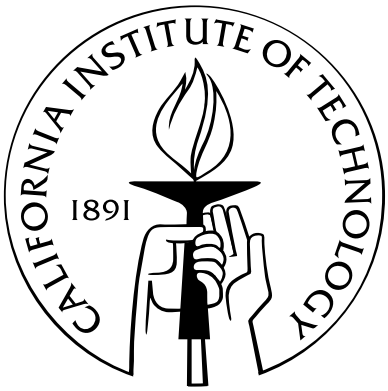

California Institute of Technology

Pasadena, California

2008

(Defended July 25, 2008)

For my mother, Sally

Abstract

The cluster expansion has found its greatest use in calculations of phase diagrams. The cluster inversion method of Connolly and Williams can be used to invert properties of ordered structures from ab initio calculations to determine the properties of disordered structures. The interaction parameters determined from the inversion quantify how each cluster type contributes to the quantity in question. In this thesis a very different approach is taken. The cluster inversion method is instead performed on measurements of properties of random solid solutions. This is possible when the number of terms required for the expansion is small. Also, the interaction parameters are extended to interaction functions, which become physically significant when only a few terms are required.

The focus of this thesis is on the phonon density of states (DOS), which is determined from the results of inelastic scattering experiments. Nuclear resonant inelastic X-ray scattering (NRIXS) is utilized to probe the phonon modes of ^{57}Fe atoms in binary body-centered cubic alloys of Fe-V, Fe-Cr, and Fe-Co. Alloying with 3d series atoms causes a softening of the ^{57}Fe phonon partial density of states (PDOS) curves with decreasing average atomic number.

For Fe-Cr, the interaction phonon partial density of states (IPDOS) functions obtained from the disordered alloys up to a combined first- and second-nearest-neighbor triangle cluster were successful in reconstructing the ^{57}Fe PDOS curves of thin-film multilayer samples of ^{57}Fe/^{56}Fe/Cr. The use of only three terms for the phonon properties of ^{57}Fe in Fe-Cr indicates a very weak dependence on the local chemical arrangement. To obtain the phonon properties of the Cr atoms, inelastic neutron scattering spectra were measured on disordered solid solutions of BCC Fe-Cr alloys. These data were reduced from time-of-flight histograms to energy spectra that resemble the DOS, but were distorted by differences in efficiencies of the atom species for phonon scattering. Cluster expansion

formalisms were developed to both correct for this neutron weighting problem, and to isolate the PDOS of Fe and Cr atoms. An asymmetry in the phonon entropy of mixing was identified, and attributed to the larger number of low-energy modes associated with like and unlike pairs in the first- and second-nearest-neighbor shells of Cr atoms, compared to Fe atoms.

The results of inelastic neutron scattering on Cu-Au are re-analyzed with the cluster expansion technique. The neutron weight correction changes both the magnitude and sign of the phonon entropy of mixing. A cluster expansion of the disordered enthalpies yields a critical temperature of the ordered Cu_3Au phase that is very similar to the experimental value, indicating the usefulness of the cluster expansion to experimental results. Although a low number of terms works very well for the low-energy modes, the optical modes are poorly treated. The failure of the cluster expansion to reproduce the optical phonon modes in the ordered Cu_3Au sample indicates a much higher dependence on the local chemical arrangement of the Cu and Au atoms.

Acknowledgements

This thesis would not have been possible without the guidance and support of my advisor, Brent Fultz, whose patience and benevolence are matched only by his genius. I hope that I can be for my students the advisor that Brent has been for me.

With the same respect must I thank Itzhak Halevy, who has served both as my mentor and friend. Itzhak and I spent many sleepless nights at the NSLS and APS. He has seen me at my worst, both sleep deprived and hungry, and I thank him for being so kind during my moments of weakness. The diamond anvil cell work that Itzhak has done with me could fill an entire thesis, and it is my failing that none of this work is presented here.

Additionally, I would like to thank my committee members—Professor William Johnson, Professor Sossina Haile, Professor Jennifer Jackson, and Dr. Wolfgang Sturhahn—for their interest in my work.

None of the experiments described in this thesis would be possible without the hard work and diligence of the scientists and staff of the Intense Pulsed Neutron Source (IPNS) and Advanced Photon Source (APS) at Argonne National Laboratory. I am indebted to Lynette Jirik and Ken Littrel for their technical support on the LRMECS instrument at IPNS. Michael Hu, Michael Lerche, Yuming Xiao, Paul Chow, Eric Rod, and Veronica O'Connor have all provided excellent support on HPCAT beamline 16ID-D at the APS. Use of the HPCAT facility was supported by DOE-BES, DOE-NNSA (CDAC), NSF, DOD TACOM, and the W.M. Keck Foundation. Use of the APS was supported by DOE-BES, under Contract No. DE-AC02-06CH11357. IPNS was funded by the U.S. Department of Energy, BES-Materials Science, under Contract W-31-109-Eng-38.

Financial support for the work in this thesis was provided by the California Institute of Technol-

ogy, the Carnegie-DOE Alliance Center, and the Department of Energy through the Basic Energy Sciences Grant DE-FG02-03ER46055.

I would like to thank the members of the Fultz group who have provided much needed help and support over the years: Tabitha Swan-Wood, Alan Yue, Ryan Monson, Olivier Delaire, Max Kresch, Rebecca Stevens, Joanna Dodd, Jiao Lin, and Chen Li. I am especially greatful for the fruitful interactions that I had with my past and present officemates: Alex Papandrew, Jorge Munõz, and Mike Winterrose. I wish the new students Lisa Mauger and Hongjin Tan best of luck, and I look forward to my continued work with Olivier at Oak Ridge National Lab. I must also thank Channing Ahn, who has always given me pertinent laboratory advice and valuable feedback concerning my progress as a graduate student.

Although often overlooked, the experimental sciences would not be possible without the work of highly skilled machinists such as Mike Vondrus. Mike has helped me with numerous projects, including the construction of furnaces for inelastic X-ray scattering and inelastic neutron scattering. I am very grateful for his friendship, and I thank his wife Masako for her wonderful cooking.

My friends at Caltech made the time spent here both tolerable and memorable. The friendships of my roommates Misha Kislitsyn and Joe Schramm have made me a better person and will always be cherished. Rafael Verduzco and Jason "Teacup" Keith were always there when I needed them most. I am also grateful for my frienships with Mary Laura Lind, Orion Crisafulli, Will "Deathwish" Ford, and all of the members of the former Caltech Ruby Football Club.

I would like to take this opportunity to thank those who have helped me along the path in the past: my former advisors and teachers Mike McHenry, Mike McElfresh, Ed Schwilm, and Joe Zinno.

An ever-present source of inspiration for me has been the love of my life, Amber. Thank you for sticking with me despite the distance these past years. It wasn't easy, but we made it. Last, and most importantly, I thank my family. None of this would have been possible without the love and support of my parents, Sally and Leonard, and my brothers Lenny and Jon. Len, thanks for always being right there behind me to show me how well I could have done, and if you allow me to give you one piece of advice: start writing now!

Preface

The objective of this thesis to present the cluster expansion as a tool that can be exploited by *experimental* materials scientists. Historically, the cluster expansion has found its greatest use in statistical mechanics. Most recently, the cluster expansion has been exploited by the theory community to calculate phase diagrams from ab initio methods. As such, most of the literature is written from the perspective of physicists and mathematicians. There is no text that presents the cluster expansion in terms that an engineer or experimentalist would readily understand. Having come from a background of both materials engineering and physics, I aimed to translate the available literature into a text that would be helpful for the engineer. The mathematics used in this thesis is at the level of an advanced undergraduate engineering student. Chapter 1 provides a brief introduction to scattering experiments with an emphasis on the differences between elastic and inelastic as well as coherent and incoherent scattering. The one dimensional example in Chapter 2 shows how to calculate a phase diagram from thermodynamic information on three ordered phases. This section could easily be converted to a homework problem for an advanced thermodynamics course. Chapter 3 presents the cluster expansion and describes how the technique can be applied to various thermodynamic values and functions. Readers with a strong background in theoretical physics may find some topics overly simplified, and should find the references more suitable for their background. However, the results provided in Chapters 4 and 5 should be of interest to both physicists and engineers.

Contents

Chapter 1

Introduction to Scattering Experiments

This introduction presents one of the main topics of this thesis: scattering. Most of the scattering experiments reported in the subsequent chapters are aimed at determination of the phonon density of states (DOS) of binary metals with varying chemical arrangements. The DOS is required to determine key thermodynamic variables such as the phonon partition function and phonon entropy. In this chapter a qualitative description of the types of scattering is presented, followed by a more detailed mathematical description of the measured intensity. Much of the content in this chapter has been taken from the texts *Experimental Inelastic Scattering* by Fultz et al. [1], and *Transmission Electron Microscopy and Diffractometry of Materials* by Fultz and Howe [2]. Some of the arguments have been revised, and new material has been provided to illustrate the key points and connections between the spatial and temporal correlation functions.

Scattering experiments are an important tool in understanding the thermodynamics of materials. From these experiments both the structure and dynamics of a system can be revealed. X-ray, electron, and neutron diffraction provide information on crystal structure and chemical order. Mössbauer spectroscopy (γ-ray scattering) provides local configurations of particular isotopes. Inelastic X-ray and neutron scattering provide the phonon density of states, a function that is key to understanding the effects of lattice dynamics on phase diagrams.

In principle these experiments are quite simple; an incident particle or wave with certain properties interacts with a scattering center and the outgoing properties are measured. When the relative

phase relationship between the incident and scattered waves is preserved, the scattering is said to be coherent. Incoherent scattering does not preserve the phase relationship between the incident and scattered waves. In addition to being either coherent or incoherent, all scattering is either elastic or inelastic, where in an elastic process there is no energy transfer to the scattering center. This leads to four possible word pairs: elastic-coherent, elastic-incoherent, inelastic-coherent, and inelastic-incoherent. Of these word pairs, most scientists and engineers are familiar with the elastic-coherent diffraction of X-rays from a polycrystalline material. The constructive interference at the Bragg reflections causes intense peaks. When the atoms are structurally disordered, as in a metallic glass for example, there is no constructive interference and the scattering is elastic-incoherent. This appears as broad peaks in intensity as a function of the scattering angle (Figure 1.1).

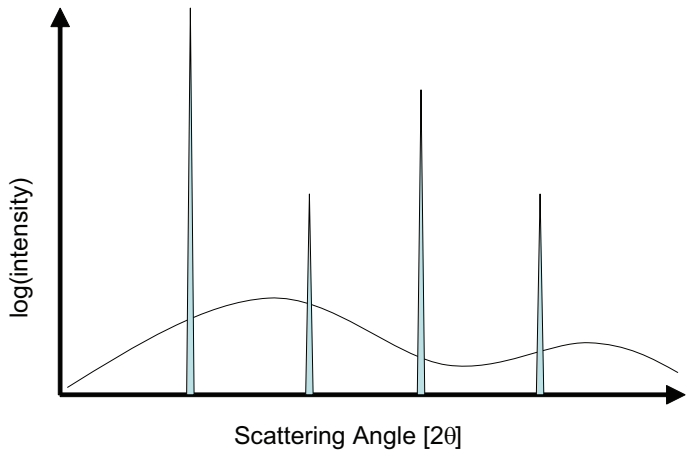

Figure 1.1: Diffraction from a polycrystalline material is given by sharp Bragg peaks, whereas the X-ray scattering from a metallic glass is given by the lower intensity diffuse pattern.

Less common are inelastic experiments. Such experiments give valuable insight into the dynamics of materials. A useful figure for explaining the inelastic-coherent and inelastic-incoherent word pairs is a plot of the scattering $S(Q, E)$ as a function of momentum transfer Q and energy transfer E from a time-of-flight chopper spectrometer. This is shown in Figure 1.2a for pure Fe at room temperature, as measured on the Low-Resolution Medium-Energy Chopper Spectrometer (LRMECS) at Argonne National Laboratory. Natural Fe is almost entirely a coherent scatterer of thermal neutrons (with $\sigma_{\mathrm{inc,Fe}} = 0.40$ and $\sigma_{\mathrm{coh,Fe}} = 11.22$ barns). Plotting the intensity as a function of momentum transfer at $E = 0$ yields a plot similar to that in Figure 1.1, where the coherent scattering is given by the

diffraction peaks and the incoherent scattering by the low intensity curve. Emanating from the diffraction peaks for $|E| > 0$ is the coherent-inelastic scattering. This scattering is closely related to the phonon dispersions for pure Fe. The calculated incoherent-inelastic scattering for pure Fe, based on the data in Figure 1.2a, is shown in Figure 1.2b. As with the incoherent-elastic scattering, the intensity does not vary as much with momentum transfer (unlike the coherent scattering). The plot in Figure 1.2c shows the results of a scattering experiment that probes only the incoherent scattering as a function of energy, and closely resembles the plot in Figure 1.2b summed over Q.[1]

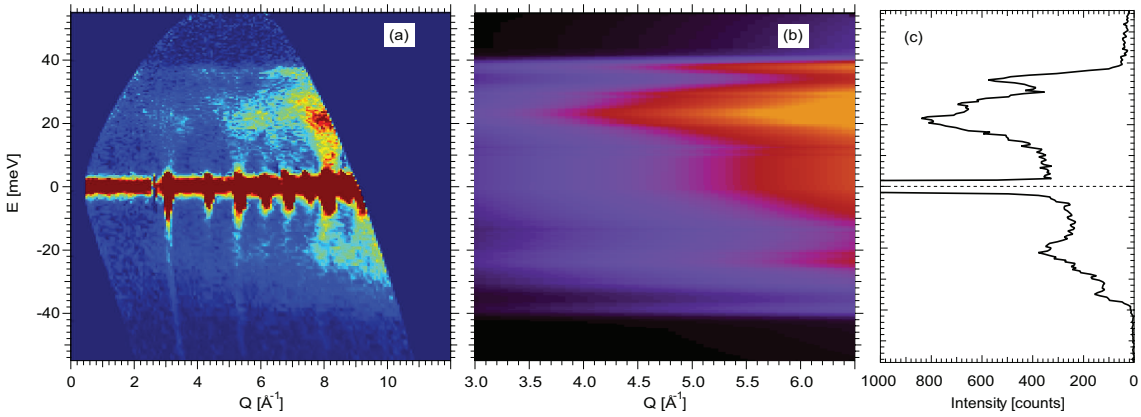

Figure 1.2: (a): Scattering as a function of energy transfer and momentum transfer from pure Fe at 293K measured on LRMECS. Intensity increases from blue to red, with the maximum intensity along $E = 0$ meV. (b): Calculated incoherent scattering from the data reduced in (a) with the elastic peak removed. (c): Scattering intensity as a function of energy for pure Fe at 293K measured using the incoherent scattering technique NRIXS (see Chapter 4).

In an elastic experiment, such as X-ray diffraction, we are interested in the atom positions $\{\boldsymbol{r}_j\}$. What we actually measure is the intensity I as a function of momentum transfer $\boldsymbol{Q}$. The scattering for the polycrystalline sample depicted in Figure 1.1 is directionally averaged so that we measure $I(Q)$ rather than $I(\boldsymbol{Q})$, where $Q = 2k\sin\theta$, k is the magnitude of the incident and scattered waves $k = |\boldsymbol{k}|$, and θ is the scattering angle. Two alternate ways of expressing the scattering geometry are given in Figure 1.3 and Figure 1.4. Here we show two different quantities: the momentum transfer to the sample $\boldsymbol{Q} \equiv \boldsymbol{k}_i - \boldsymbol{k}_f$, and the change in the scattering vector $\boldsymbol{\Delta k} \equiv \boldsymbol{k}_f - \boldsymbol{k}_i$. These vectors are opposite in direction $\boldsymbol{Q} = -\boldsymbol{\Delta k}$, but equal in magnitude $|\boldsymbol{Q}| = |\boldsymbol{\Delta k}|$. The atom positions with respect to the source and detector are given in Figure 1.5.

[1] Figure 1.2c may also be acquired by summing Figure 1.2a over Q. The large range of Q allows for proper averaging of the coherent scattering.

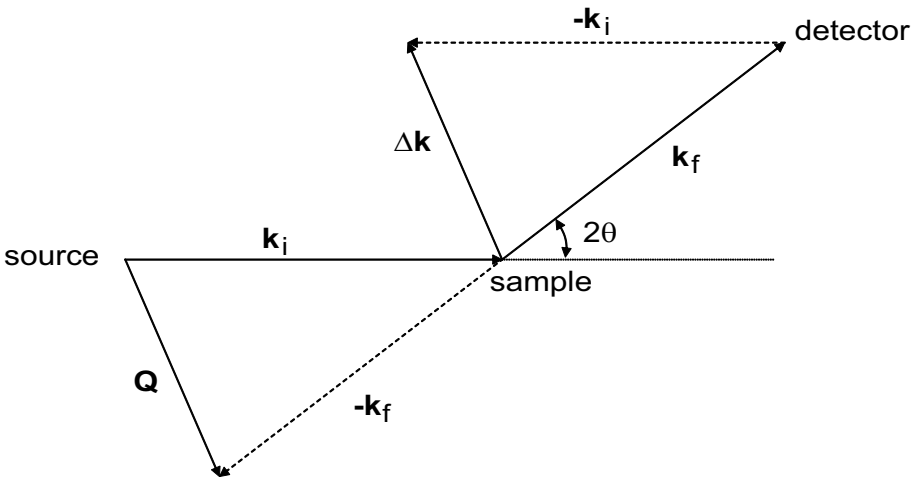

Figure 1.3: Geometry for a scattering experiment. When the source is fixed and the detector moves this is known as the $\theta - 2\theta$ geometry.

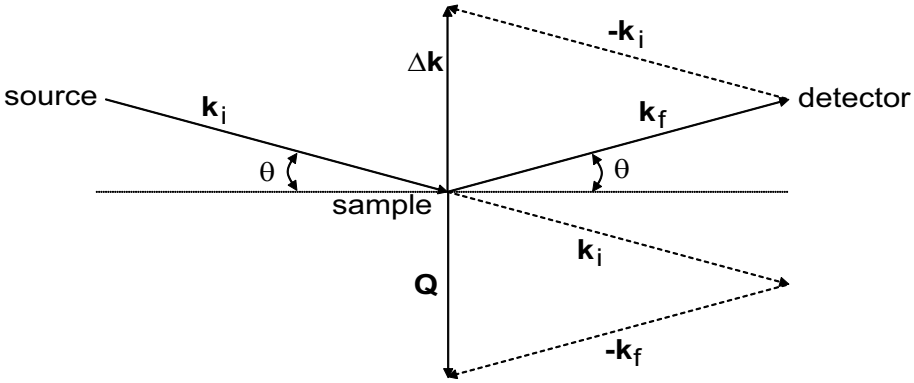

Figure 1.4: Alternate geometry for a scattering experiment. When both the source and the detector move this is known as the $\theta - \theta$ geometry.

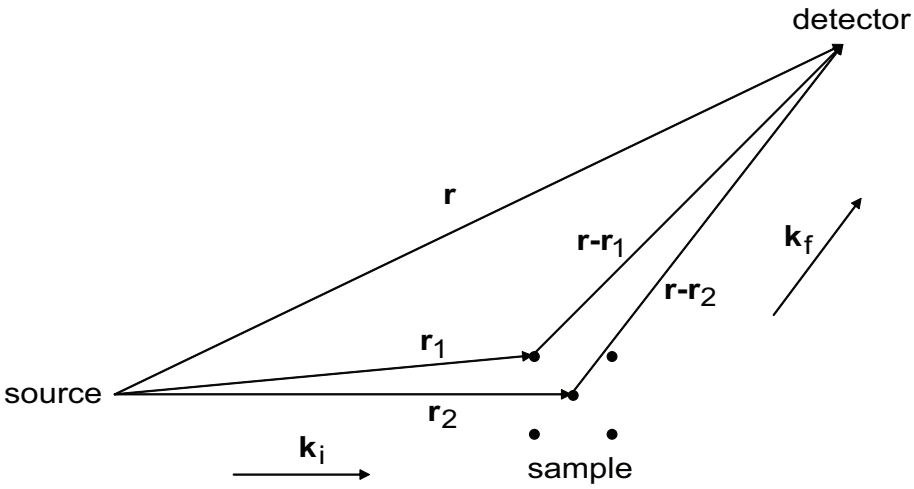

Figure 1.5: Coordinates for wave scattering, where the atoms are given by solid circles. Typically the source to sample distance is much greater than the interatomic spacing, so that the vectors $\boldsymbol{r}_1$ and $\boldsymbol{r}_2$ are parallel, as are the vectors $\boldsymbol{r} - \boldsymbol{r}_1$ and $\boldsymbol{r} - \boldsymbol{r}_2$.

One of the main themes of quantum mechanics is that particles have both a wave-like and a particle-like behavior (the wave-particle duality). At the source and detector, the photon or neutron behaves like a particle. The source emits individual particles, and the detector counts individual particles. Elsewhere the photon or neutron behaves like a wave, where constructive and destructive interference can occur. The wave-like behavior is the physical origin for the complementary nature of $\boldsymbol{Q}$ and $\boldsymbol{r}$ in quantum mechanics, $\boldsymbol{Q} \leftrightarrow \boldsymbol{r}$. Consider the scattering off of a single atom[2] depicted in Figure 1.6. The wave incident from the left is expressed as

$$\Psi_{\text{incident}} = \mathrm{e}^{\mathrm{i}(\boldsymbol{k}_i \cdot \boldsymbol{r}' - \omega t)} \tag{1.1}$$

where ω is the angular frequency. We can ignore the time dependence to emphasize the manipulations of the spatial coordinates. The time-dependence may be recovered by multiplying the results by $\mathrm{e}^{-\mathrm{i}\omega t}$. Equation 1.1 also shows the complementary nature of the energy E (given by $E = \hbar\omega$) and time t: $E \leftrightarrow t$.

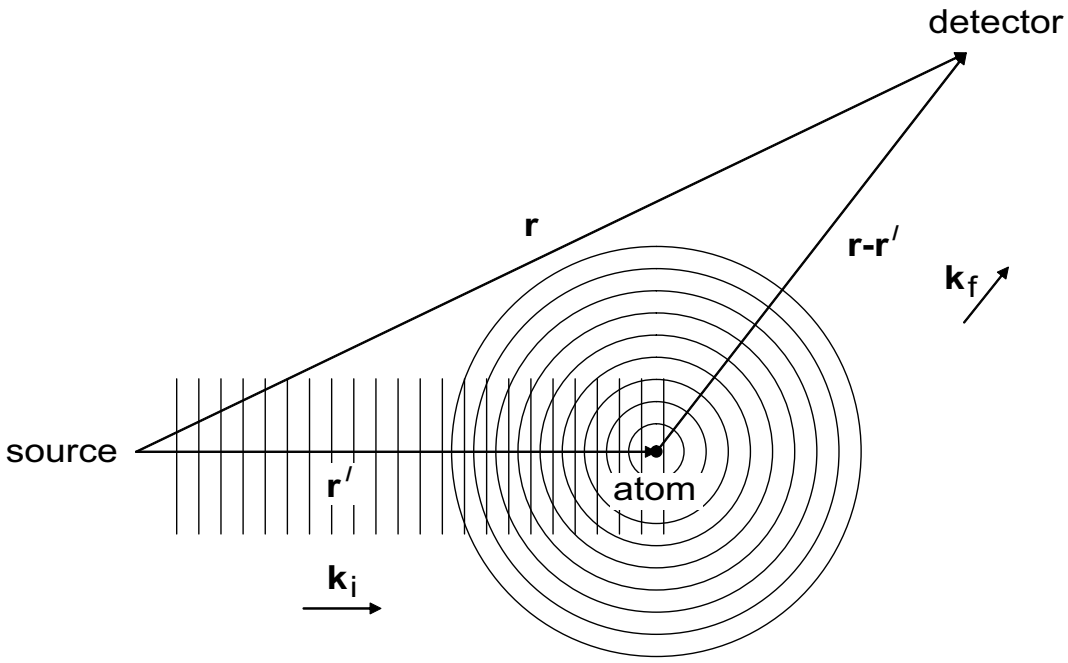

Figure 1.6: Scattering from a single atom

[2]The remaining content of this chapter has been adopted from the texts *Experimental Inelastic Scattering* by Fultz et al. [1], and *Transmission Electron Microscopy and Diffractometry of Materials* by Fultz and Howe [2].

The spherical wave traveling outwards from the center of the atom has the form

$$\Psi_{\text{scatt}} = f(\boldsymbol{k}_i, \boldsymbol{k}_f) \frac{\mathrm{e}^{\mathrm{i}k_f|\boldsymbol{r}-\boldsymbol{r}'|}}{|\boldsymbol{r}-\boldsymbol{r}'|} \tag{1.2}$$

where $f(\boldsymbol{k}_i, \boldsymbol{k}_f)$ is the scattering length and varies with the orientation of $\boldsymbol{k}_i$ and $\boldsymbol{k}_f$, and $|\boldsymbol{r}-\boldsymbol{r}'|$ is the distance from the scatterer to the detector. For X-rays, which are scattered when they cause the atomic electrons to oscillate and re-radiate, the scattering length has a strong dependence on the orientation of initial and final wavevectors. This is also the case for electrons, which are scattered by Coulomb interactions when they penetrate the positively charged atomic core. Neutrons, which are scattered by nuclei, have scattering lengths that are nearly independent of the orientation of initial and final wavevectors. The intensity of the scattered wave is given by

$$I_{\text{scatt}} = \Psi^{\star}_{\text{scatt}}\ \Psi_{\text{scatt}} = |f(\boldsymbol{k}_i, \boldsymbol{k}_f)|^2\ \frac{\mathrm{e}^{-\mathrm{i}k_f|\boldsymbol{r}-\boldsymbol{r}'|}}{|\boldsymbol{r}-\boldsymbol{r}'|}\ \frac{\mathrm{e}^{\mathrm{i}k_f|\boldsymbol{r}-\boldsymbol{r}'|}}{|\boldsymbol{r}-\boldsymbol{r}'|} = |f(\boldsymbol{k}_i, \boldsymbol{k}_f)|^2\ \frac{1}{|\boldsymbol{r}-\boldsymbol{r}'|^2} \tag{1.3}$$

where the intensity falls off as $1/r^2$.

Assuming each atom to be a point scatterer works well for showing the differences between coherent and incoherent scattering. Consider the scattering from discrete points $\{\boldsymbol{r}_j\}$ arranged on a lattice as given in Figure 1.7. Ignoring the forward beam, there is constructive interference of the scattered waves at right angles to the incident beam. Elsewhere there is destructive interference. The atoms are periodic in space so that the relative phases of the wavelets are preserved (this is the definition of coherent scattering). For coherent scattering the total scattered wave is constructed by adding the *amplitudes* of the scattered wavelets

$$\Psi_{\text{coh}} = \sum_{\boldsymbol{r}_j} \psi_{\boldsymbol{r}_j}\ . \tag{1.4}$$

Diffraction experiments measure the total coherent *intensity* I_{coh}

$$I_{\text{coh}} = \Psi^{\star}_{\text{coh}}\ \Psi_{\text{coh}} = \left| \sum_{\boldsymbol{r}_j} \psi_{\boldsymbol{r}_j} \right|^2\ . \tag{1.5}$$

This means that for constructive interference the intensity will be proportional to the square of the number of scatterers: $I_{\text{coh}} \propto N^2$.

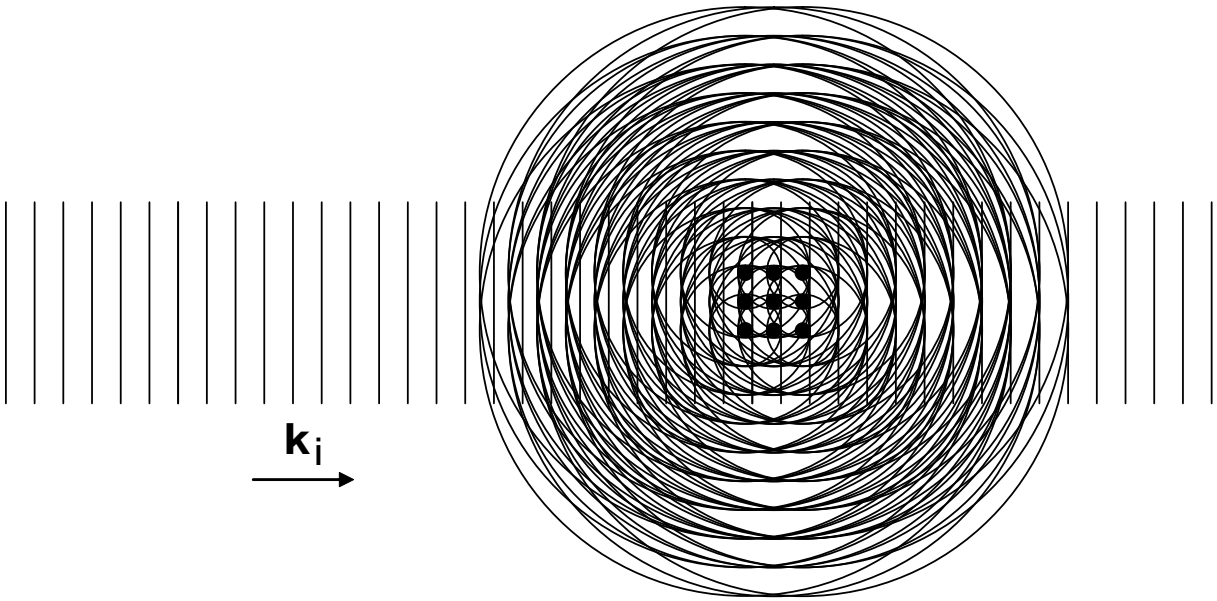

Figure 1.7: Scattering from a periodic lattice. There is constructive interference at $2\theta = 90°$.

In contrast, incoherent scattering does not preserve a phase relationship between the incident wave and scattered wavelets. For incoherent scattering it is incorrect to add the amplitudes of the scattered wavelets $\{\psi_{\boldsymbol{r}_j}\}$. Incoherently scattered wavelets do not maintain phase relationships, so they cannot interfere constructively or destructively. The total intensity of incoherent scattering, I_{inc}, is the sum of individual scattered intensities

$$I_{\text{inc}} = \sum_{\boldsymbol{r}_j} I_{\boldsymbol{r}_j} = \sum_{\boldsymbol{r}_j} \left|\psi_{\boldsymbol{r}_j}\right|^2 \ . \tag{1.6}$$

Because measurable intensities are added in incoherent scattering the intensity is proportional to the number of scatterers: $I_{\text{inc}} \propto N$.

Here we provide two examples of incoherent scattering. The phase of the wave function in Equation 1.2 may be altered if the atom positions are varied. If the atom positions are random in space then each atom has a phase that is also random. In this manner the wavelets do not maintain phase relationships. Figure 1.8 shows the scattering from a small group of randomly placed atoms.

Note the lack of constructive or destructive interference. In a metallic glass there is short range periodicity, however, which can be revealed using X-ray diffraction to acquire the radial distribution function.

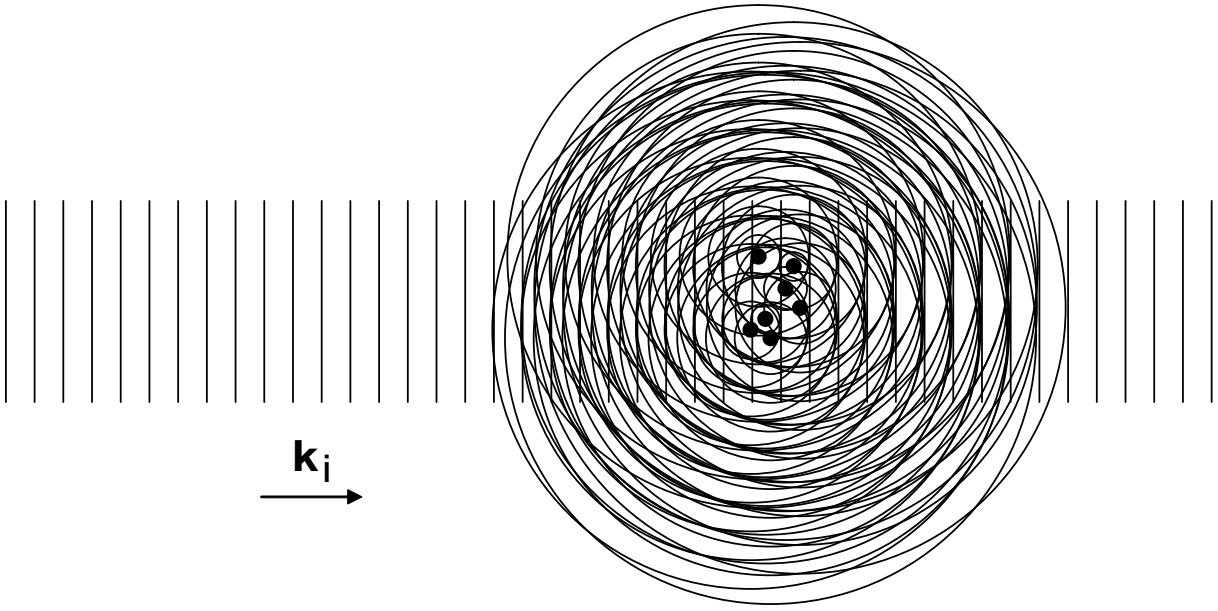

Figure 1.8: Scattering from a group of randomly placed atoms. The randomness in the positions $\{\boldsymbol{r}_j\}$ give each atom a different phase shift.

Another possibility is that the atoms are structurally ordered, such as in a crystalline material, but the atoms scatter incoherently. This means that mechanism of the scattering introduces a random phase shift ϕ_j for each atom. Equation 1.2 is then written as

$$\Psi_{\text{scatt},j} = f(\boldsymbol{k}_i, \boldsymbol{k}_f)\frac{\mathrm{e}^{\mathrm{i}(k_f|\boldsymbol{r}-\boldsymbol{r'}_j|+\phi_j)}}{|\boldsymbol{r}-\boldsymbol{r}'_j|}\ . \tag{1.7}$$

Figure 1.9 shows the same atoms in Figure 1.7 scattering incoherently. The atoms each emit with the same wavelength, but with a random phase lag. Such is the case for neutron diffraction of vanadium, which has a scattering cross-section that is almost entirely incoherent.

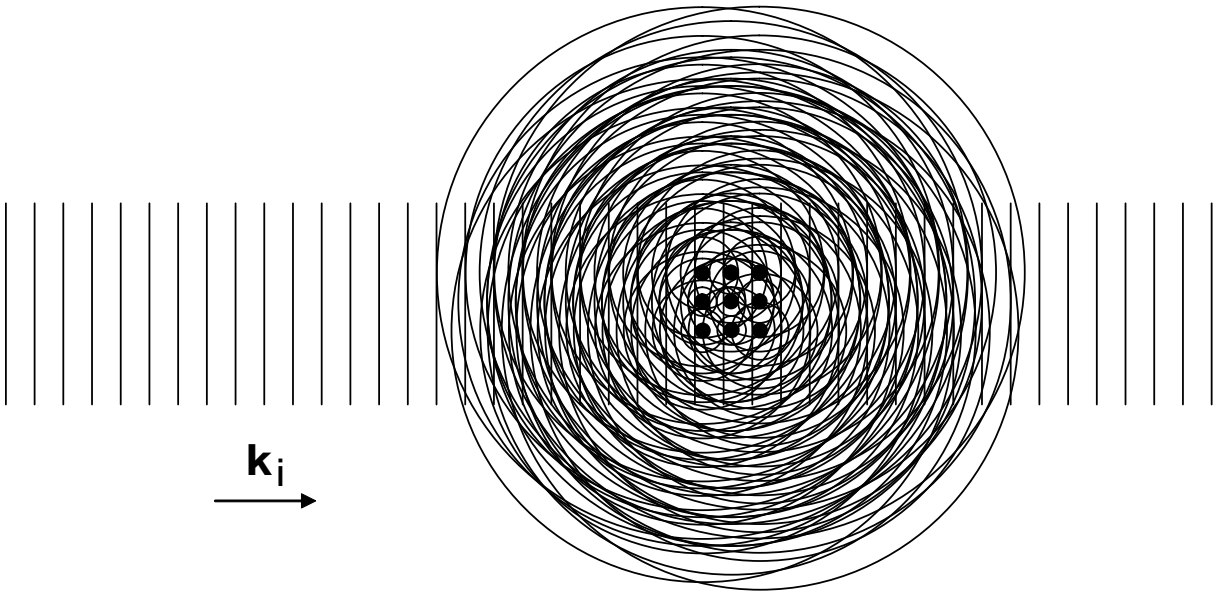

Figure 1.9: Incoherent scattering from a crystalline material. The scattering from each atom is elastic, so that ω does not change ($|\boldsymbol{k}_i| = |\boldsymbol{k}_f|$). However, a phase lag ϕ_j is randomly introduced to each atom leading to a loss of constructive and destructive interference.

Figures 1.7, 1.8, and 1.9 show the scatterers as discrete points $\{\boldsymbol{r}_j\}$. It proves convenient to consider a distribution of scatterers $f(\boldsymbol{r})$, with a continuous variable $\boldsymbol{r}$ rather than a sum over discrete points $\{\boldsymbol{r}_j\}$. We change variables as

$$\psi(\boldsymbol{Q}) = \sum_{\boldsymbol{r}_j}^{N} f_{\boldsymbol{r}_j}\ \mathrm{e}^{-\mathrm{i}\boldsymbol{Q}\cdot\boldsymbol{r}_j} = \int_{-\infty}^{\infty} f(\boldsymbol{r})\ \mathrm{e}^{-\mathrm{i}\boldsymbol{Q}\cdot\boldsymbol{r}}\ \mathrm{d}^3\boldsymbol{r}\ . \tag{1.8}$$

To equate a continuous integral to a discrete sum requires that $f(\boldsymbol{r})$ is not a smooth function of position. Over most of space $f(\boldsymbol{r})$ is zero, but at atom centers such as $\boldsymbol{r} = \boldsymbol{r}_i$, $f(\boldsymbol{r}_i)$ is a Dirac delta function times a constant $f_{\boldsymbol{r}_i}$,

$$f(\boldsymbol{r}_i) = f_{\boldsymbol{r}_i}\ \delta(\boldsymbol{r} - \boldsymbol{r}_i)\ . \tag{1.9}$$

An important property of the delta function is

$$y(x') = \int_{-\infty}^{\infty} \delta(x - x')\ y(x)\ \mathrm{d}x\ . \tag{1.10}$$

Equation 1.10 requires that $\delta(x - x')$ is zero everywhere, except at the point $x = x'$. At this point

the delta function is infinitely high, but of unit area, so the integral of Equation 1.10 picks out only the value of $y(x)$ at x'. To extend Equation 1.9 to include many atom centers, we take the sum over $\boldsymbol{r}_j$

$$f(\boldsymbol{r}) = \sum_{\boldsymbol{r}_j}^{N} f_{\boldsymbol{r}_j} \delta(\boldsymbol{r} - \boldsymbol{r}_j) \tag{1.11}$$

which satisfies the equality in Equation 1.8 between points in space $\{\boldsymbol{r}_j\}$ and a continuous function of $\boldsymbol{r}$.

The right-hand side of Equation 1.8 is an important mathematical function, namely the Fourier transform of $f(\boldsymbol{r})$

$$F_{\boldsymbol{r}} f(\boldsymbol{r}) = \int_{-\infty}^{\infty} f(\boldsymbol{r})\ \mathrm{e}^{-\mathrm{i}\boldsymbol{Q}\cdot\boldsymbol{r}}\ \mathrm{d}^3\boldsymbol{r} \tag{1.12}$$

where $F_{\boldsymbol{r}}$ operates on $f(\boldsymbol{r})$ and the subscript denotes an integral over $\boldsymbol{r}$. Thus the wavefunction is the Fourier transform of the scattering factor distribution

$$\psi(\boldsymbol{Q}) = F_{\boldsymbol{r}} f(\boldsymbol{r})\ . \tag{1.13}$$

The inverse Fourier transform $F_{\boldsymbol{Q}}^{-1}$ is given by

$$F_{\boldsymbol{Q}}^{-1} \psi(\boldsymbol{Q}) = \int_{-\infty}^{\infty} \psi(\boldsymbol{Q})\ \mathrm{e}^{\mathrm{i}\boldsymbol{Q}\cdot\boldsymbol{r}}\ \mathrm{d}^3\boldsymbol{Q} \tag{1.14}$$

so that $f(\boldsymbol{r})$ is the inverse Fourier transform[3] of the wavefunction

$$f(\boldsymbol{r}) = F_{\boldsymbol{Q}}^{-1} \psi(\boldsymbol{Q})\ . \tag{1.15}$$

We are interested in the function $f(\boldsymbol{r})$, so the inverse Fourier transform proves to be more useful. Unfortunately, we do not measure the wavefunction, we measure the intensity $I(\boldsymbol{Q})$.

[3]The integrals in Equation 1.12 and Equation 1.14 differ in form only in the sign of the exponent, so it is rather common to simply call either a Fourier transform of the other.

We define the "Patterson function," $P(\boldsymbol{r})$

$$P(\boldsymbol{r}) \equiv \int_{-\infty}^{\infty} f^*(\boldsymbol{r}')\ f(\boldsymbol{r}+\boldsymbol{r}')\mathrm{d}^3\boldsymbol{r}' \tag{1.16}$$

which is a convolution of the form

$$P(\boldsymbol{r}) = f^*(\boldsymbol{r}) * f(-\boldsymbol{r})\ . \tag{1.17}$$

This specific type of convolution is known as an "autocorrelation function." The most important feature of the Patterson function is that its Fourier transform is the diffracted intensity in kinematical theory. To show this the intensity can be written in terms of the scattered wave of Equation 1.8

$$I(\boldsymbol{Q}) = \psi^*(\boldsymbol{Q})\ \psi(\boldsymbol{Q}) = \int_{-\infty}^{\infty} f^*(\boldsymbol{r}')\ \mathrm{e}^{\mathrm{i}\boldsymbol{Q}\cdot\boldsymbol{r}'}\ \mathrm{d}^3\boldsymbol{r}' \int_{-\infty}^{\infty} f(\boldsymbol{r}'')\ \mathrm{e}^{\mathrm{i}\boldsymbol{Q}\cdot\boldsymbol{r}''}\ \mathrm{d}^3\boldsymbol{r}''\ . \tag{1.18}$$

Since $\boldsymbol{r}'$ and $\boldsymbol{r}''$ are independent variables

$$I(\boldsymbol{Q}) = \int_{-\infty}^{\infty} \left(\int_{-\infty}^{\infty} f^*(\boldsymbol{r}')\ f(\boldsymbol{r}'')\ \mathrm{e}^{-\mathrm{i}\boldsymbol{Q}\cdot(\boldsymbol{r}''-\boldsymbol{r}')}\ \mathrm{d}^3\boldsymbol{r}'' \right)\ \mathrm{d}^3\boldsymbol{r}'\ . \tag{1.19}$$

Defining $\boldsymbol{r} \equiv \boldsymbol{r}'' - \boldsymbol{r}'$ and changing variables $\boldsymbol{r}'' \rightarrow \boldsymbol{r} + \boldsymbol{r}'$ the integral can be written as

$$I(\boldsymbol{Q}) = \int_{-\infty}^{\infty} \left(\int_{-\infty}^{\infty} f^*(\boldsymbol{r}')\ f(\boldsymbol{r}+\boldsymbol{r}')\ \mathrm{e}^{-\mathrm{i}\boldsymbol{Q}\cdot\boldsymbol{r}}\ \mathrm{d}^3\boldsymbol{r} \right)\ \mathrm{d}^3\boldsymbol{r}' \tag{1.20}$$

$$I(\boldsymbol{Q}) = \int_{-\infty}^{\infty} \left(\int_{-\infty}^{\infty} f^*(\boldsymbol{r}')\ f(\boldsymbol{r}+\boldsymbol{r}')\ \mathrm{d}^3\boldsymbol{r}' \right)\ \mathrm{e}^{-\mathrm{i}\boldsymbol{Q}\cdot\boldsymbol{r}}\ \mathrm{d}^3\boldsymbol{r}\ . \tag{1.21}$$

The term in parentheses is the Patterson function defined in Equation 1.16. The intensity may now be written as

$$I(\boldsymbol{Q}) = \int_{-\infty}^{\infty} P(\boldsymbol{r})\ \mathrm{e}^{-\mathrm{i}\boldsymbol{Q}\cdot\boldsymbol{r}}\ \mathrm{d}^3\boldsymbol{r} \tag{1.22}$$

which is the Fourier transform of the Patterson function

$$I(\boldsymbol{Q}) = F_{\boldsymbol{r}} P(\boldsymbol{r}) \; . \tag{1.23}$$

Whereas the scattered wave $\psi(\boldsymbol{Q})$ is the Fourier transform of the scattering factor distribution, the scattered intensity $I(\boldsymbol{Q})$ is the Fourier transform of the Patterson function of the scattering factor distribution

$$I(\boldsymbol{Q}) = F_{\boldsymbol{r}} P(\boldsymbol{r}) = |F_{\boldsymbol{r}} f(\boldsymbol{r})|^2 \; . \tag{1.24}$$

The measured diffracted intensity provides the Patterson function, not the scattering factor distribution. This leads to "Friedel's law" that diffraction experiments cannot distinguish between an atom arrangement and the atom arrangement when it is inverted.

Thus far we have considered elastic scattering, which involves only the momentum transfers and atom positions $\{\boldsymbol{Q}, \boldsymbol{r}\}$. For inelastic scattering the same type of analysis can be performed by extension into energy and time $\{\boldsymbol{Q}, E, \boldsymbol{r}, t\}$. Again we assume the scatterers to be points. The point scatterer emits a wavelet from position $\boldsymbol{r}_j$ at time t_k, where the phase from the point emitter relative to wavelets from other point emitters is $\boldsymbol{Q} \cdot \boldsymbol{r} - \omega t_k$. The amplitude of the scattering is given by the scattering strength of the point emitter, $f(\boldsymbol{r}_j, t_k)$, which is an amplitude at a point in space and an instant in time. For the distribution in time we consider a Fourier series with different frequencies, or energies $E = \hbar\omega$.

As done in Equation 1.8, it proves convenient to consider a distribution of scatterers $f(\boldsymbol{r}, t)$ with continuous variables, $\boldsymbol{r}$ and t, rather than a sum over discrete points $\{\boldsymbol{r}_j\}$ and snapshots in time t_k. Following the analysis given by Equation 1.8, Equation 1.9, and Equation 1.11, we change variables as

$$\psi(\boldsymbol{Q}, E) = \sum_{\boldsymbol{r}_j}^{N} \sum_{t_k} f_{\boldsymbol{r}_j, t_k} \; \mathrm{e}^{-\mathrm{i}(\boldsymbol{Q} \cdot \boldsymbol{r}_j - \omega t_k)} = \int_{-\infty}^{\infty} \int_{-\infty}^{\infty} f(\boldsymbol{r}, t) \; \mathrm{e}^{-\mathrm{i}(\boldsymbol{Q} \cdot \boldsymbol{r} - \omega t)} \; \mathrm{d}^3\boldsymbol{r} \; \mathrm{d}t \tag{1.25}$$

where

$$f(\boldsymbol{r}, t) = \sum_{\boldsymbol{r}_j}^{N} \sum_{t_k} f_{\boldsymbol{r}_j, t_k} \delta(\boldsymbol{r} - \boldsymbol{r}_j) \delta(t - t_k) \; . \tag{1.26}$$

The right-hand side of Equation 1.25 is the double Fourier transform of the scattering factor distribution

$$\psi(\boldsymbol{Q}, E) = F_{\boldsymbol{r}} F_t f(\boldsymbol{r}, t) \ . \tag{1.27}$$

The inverse double Fourier transform $F_{\boldsymbol{Q}}^{-1} F_E^{-1}$ is given by

$$F_{\boldsymbol{Q}}^{-1} F_E^{-1} \psi(\boldsymbol{Q}, E) = \int_{-\infty}^{\infty} \int_{-\infty}^{\infty} \psi(\boldsymbol{Q}, E) \ \mathrm{e}^{\mathrm{i}(\boldsymbol{Q}\cdot\boldsymbol{r} - \omega t)} \ \mathrm{d}^3\boldsymbol{Q} \ \mathrm{d}\omega \tag{1.28}$$

so that $f(\boldsymbol{r}, t)$ is the inverse double Fourier transform of the wavefunction

$$f(\boldsymbol{r}, t) = F_{\boldsymbol{Q}}^{-1} F_E^{-1} \psi(\boldsymbol{Q}, E) \ . \tag{1.29}$$

In an inelastic experiment we measure $I(\boldsymbol{Q}, E)$, not the wave function $\psi(\boldsymbol{Q}, E)$.

For elastic scattering we defined the Patterson function. For inelastic scattering we define the "Van Hove function," $G(\boldsymbol{r}, t)$

$$G(\boldsymbol{r}, t) \equiv \int_{-\infty}^{\infty} \int_{-\infty}^{\infty} f^*(\boldsymbol{r}', t') \ f(\boldsymbol{r} + \boldsymbol{r}', t + t') \mathrm{d}^3\boldsymbol{r}' \ \mathrm{d}t' \tag{1.30}$$

which is a double autocorrelation function (a space-time correlation function). The Patterson function is a special case of the Van Hove function that does not consider correlations in time

$$P(\boldsymbol{r}) = \int_{-\infty}^{\infty} \int_{-\infty}^{\infty} f^*(\boldsymbol{r}', t') \ f(\boldsymbol{r} + \boldsymbol{r}', t') \mathrm{d}^3\boldsymbol{r}' \ \mathrm{d}t' \ . \tag{1.31}$$

The most important feature of the Van Hove function is that its Fourier transform is the scattered intensity in kinematical theory. Following steps similar to those used in Equations 1.18–1.21 the intensity can be written as

$$I(\boldsymbol{Q}, E) = \int_{-\infty}^{\infty} \int_{-\infty}^{\infty} G(\boldsymbol{r}, t) \ \mathrm{e}^{-\mathrm{i}(\boldsymbol{Q}\cdot\boldsymbol{r} - \omega t)} \ \mathrm{d}^3\boldsymbol{r} \ \mathrm{d}t = F_{\boldsymbol{r}} F_t \ G(\boldsymbol{r}, t) \ . \tag{1.32}$$

The Van Hove function is therefore the inverse double Fourier transform of the intensity.

$$G(\boldsymbol{r},t) = F_{\boldsymbol{Q}}^{-1} F_{E}^{-1}\ I(\boldsymbol{Q},E) \tag{1.33}$$

The coherent-inelastic scattering of phonons for pure iron is given by the higher intensity scattering emanating from the diffraction peaks for $|E| > 0$ in Figure 1.2a. As an example of this type of scattering consider an elementary excitation (for example a phonon) in a one-dimensional solid that provides a periodic modulation of the scattering factor in space and time:

$$f(x,t) = \mathrm{e}^{-\mathrm{i}(qx-\omega_0 t)}\ . \tag{1.34}$$

The Van Hove function of this scattering factor distribution can be determined using the definition of Equation 1.30 for 1-D

$$G(x,t) = \int_{-\infty}^{\infty}\int_{-\infty}^{\infty} \mathrm{e}^{\mathrm{i}(qx'-\omega_0 t')}\mathrm{e}^{-\mathrm{i}[q(x+x')-\omega_0(t+t')]}\mathrm{d}x'\ \mathrm{d}t' \tag{1.35}$$

$$G(x,t) = \int_{-\infty}^{\infty} \mathrm{e}^{\mathrm{i}qx}\ \mathrm{d}x' \int_{-\infty}^{\infty} \mathrm{e}^{-\mathrm{i}\omega_0 t}\ \mathrm{d}t' = \mathrm{e}^{\mathrm{i}qx}\int_{-\infty}^{\infty} \mathrm{d}x'\ \mathrm{e}^{-\mathrm{i}\omega_0 t}\int_{-\infty}^{\infty} \mathrm{d}t' \tag{1.36}$$

$$G(x,t) = \mathrm{e}^{\mathrm{i}(qx-\omega_0 t)} \tag{1.37}$$

where we have ignored the normalization to find that $G(x,t) = f(x,t)$ and has the form of a wave.

In 1-D the intensity is a simple form of the Van Hove function

$$I(Q,E) = \int_{-\infty}^{\infty}\int_{-\infty}^{\infty} G(x,t)\ \mathrm{e}^{-\mathrm{i}(Qx-\omega t)}\mathrm{d}x\ \mathrm{d}t\ . \tag{1.38}$$

Substituting Equation 1.37 into Equation 1.38

$$I(Q,E) = \int_{-\infty}^{\infty}\int_{-\infty}^{\infty} \mathrm{e}^{\mathrm{i}(qx-\omega_0 t)}\ \mathrm{e}^{-\mathrm{i}(Qx-\omega t)}\mathrm{d}x\ \mathrm{d}t \tag{1.39}$$

$$I(Q,E) = \int_{-\infty}^{\infty} \mathrm{e}^{\mathrm{i}(q-Q)x}\ \mathrm{d}x \int_{-\infty}^{\infty} \mathrm{e}^{\mathrm{i}(\omega-\omega_0)t}\ \mathrm{d}t\ . \tag{1.40}$$

The integrals of Equation 1.40 are in the form of a delta function [3]

$$\int_{-\infty}^{\infty} \mathrm{e}^{\mathrm{i}(a-b)\alpha}\mathrm{d}\alpha = \delta(a-b) \tag{1.41}$$

so that

$$I(Q,E) = \delta(q-Q-g)\ \delta(\omega-\omega_0) \tag{1.42}$$

where g is a reciprocal lattice vector which provides a factor of $\mathrm{e}^{\mathrm{i}gx} = 1$ in the integrand. Equation 1.42 shows that for coherent scattering the momentum transfer must match that of the wave, modulo a reciprocal lattice vector, and match the energy of the excitation, $E = \hbar\omega_0$. The scattering pictured in Figure 1.2a is from a polycrystalline sample. This gives a near continuum of scattering vectors (the incident beam and detectors are fixed so that different crystallite orientations give the variation in the direction of $\boldsymbol{Q}$).

The calculated incoherent-inelastic scattering for pure Fe is shown in Figure 1.2b. This type of scattering gives information on correlations in time, but does not consider correlations in position. The "self-correlation" function, $G_s(t)$, is defined as

$$G_s(t) \equiv \int_{-\infty}^{\infty}\int_{-\infty}^{\infty} f^*(\boldsymbol{r}',t')\ f(\boldsymbol{r}',t+t')\mathrm{d}^3\boldsymbol{r}'\ \mathrm{d}t'\ . \tag{1.43}$$

In one dimension this function is given by

$$G_s(t) = \int_{-\infty}^{\infty}\int_{-\infty}^{\infty} f^*(x',t')\ f(x',t+t')\mathrm{d}x'\ \mathrm{d}t'\ . \tag{1.44}$$

Substituting Equation 1.34 for an elementary excitation in a one-dimensional solid into $G_s(t)$ yields

$$G_s(t) = \int_{-\infty}^{\infty}\int_{-\infty}^{\infty} \mathrm{e}^{\mathrm{i}(qx'-\omega_0 t')}\mathrm{e}^{-\mathrm{i}(qx'-\omega_0 t+t')}\ \mathrm{d}x'\ \mathrm{d}t' \tag{1.45}$$

$$G_s(t) = \int_{-\infty}^{\infty} \mathrm{d}x' \int_{-\infty}^{\infty} \mathrm{e}^{-\mathrm{i}\omega_0 t}\, \mathrm{d}t' = \int_{-\infty}^{\infty} \mathrm{d}x'\, \mathrm{e}^{-\mathrm{i}\omega_0 t} \int_{-\infty}^{\infty} \mathrm{d}t' \tag{1.46}$$

$$G_s(t) = \mathrm{e}^{-\mathrm{i}\omega_0 t} \tag{1.47}$$

where we have ignored the normalization, and we find that $G_s(t)$ does not contain spatial information (as we would expect for incoherent scattering). The intensity is given by

$$I(E) = F_t\; G_s(t) = \int_{-\infty}^{\infty} G_s(t)\; \mathrm{e}^{\mathrm{i}\omega t}\; \mathrm{d}t \tag{1.48}$$

$$I(E) = \int_{-\infty}^{\infty} \mathrm{e}^{\mathrm{i}(\omega-\omega_0)t}\; \mathrm{d}t = \delta(\omega - \omega_0)\;. \tag{1.49}$$

Equation 1.49 shows that for incoherent-inelastic scattering the energy of the incident wave must match the energy of the excitation, $E = \hbar\omega_0$. Unlike the case for coherent-inelastic scattering, there is no restriction placed on $\boldsymbol{Q}$. The scattering pictured in Figure 1.2b and Figure 1.2c is from a polycrystalline sample. The lack of dependence on $\boldsymbol{Q}$ means that the incoherent scattering from a single crystal sample would be the same as that for a polycrystalline sample.

The different types of scattering are summarized in Table 1.1. Of the four possible word pairs for scattering, incoherent-elastic scattering provides the least amount of information on the scattering system. In contrast, coherent-inelastic scattering provides the most information on the scattering system. In this chapter the spatial and temporal correlation functions were introduced. In the next chapter the *chemical* correlation function of the cluster expansion is presented.

Table 1.1: Correlations for Scattering Word-Pairs

Scattering Word Pair	Correlation	Function Name	Function Symbol	Equation Number
Coherent - Inelastic	$\boldsymbol{r}, t$	Van Hove	$G(\boldsymbol{r}, t)$	1.30
Coherent - Elastic	$\boldsymbol{r}$	Patterson	$P(\boldsymbol{r})$	1.16
Incoherent - Inelastic	t	Self-Correlation	$G_s(t)$	1.43
Incoherent - Elastic	-	-	-	-

Chapter 2

1-D Phase Diagram

2.1 Statement of Problem

The purpose of this chapter is to provide an introduction to the cluster expansion method and to show its usefulness for thermodynamics.

Suppose we are interested in the properties of a 1-D infinite chain of A and B atoms on a periodic lattice. The phonon entropy and binding energy of three different samples with different configurations of A and B atoms on the lattice (Figure 2.1) have been measured (or determined via ab initio calculations) at $T = 100$K, and their values given in Table 2.1.

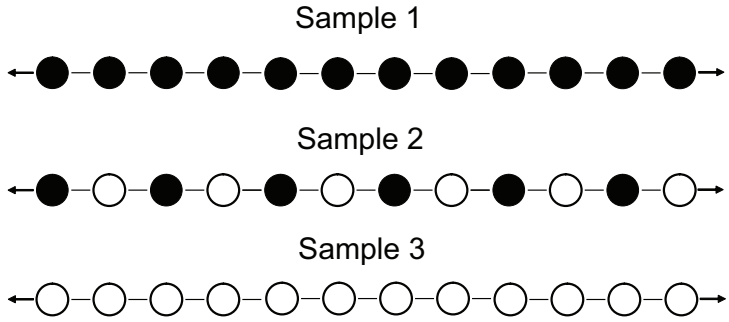

Figure 2.1: Atomic configurations on a 1-D lattice of three different samples. "A" atoms are given by the solid circles and "B" atoms by hollow circles.

Now what is the S_{ph} and E of a different configuration on the same lattice? In particular, what is the phonon entropy and binding energy of each new configuration given in Figure 2.2—ordered and disordered? Finally, what is the phase diagram of this system? To answer these questions, we first need a method of characterizing the chemical order on the lattice.

Table 2.1: Properties of 1-D Chain

m	$S_{\mathrm{ph},m}$ [k_B/atom]	E_m [eV/atom]
1	0.75	-9.68
2	0.95	-9.46
3	0.40	-9.51

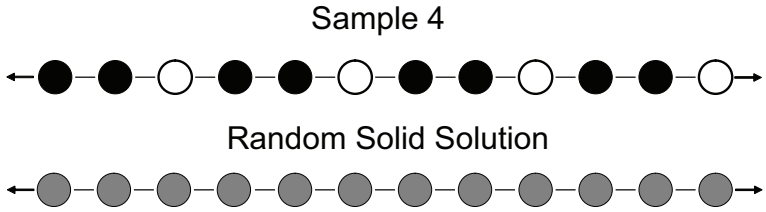

Figure 2.2: Atomic configurations on a 1-D lattice of unmeasured samples. "A" atoms are given by the solid circles and "B" atoms by hollow circles. Gray atoms represent sites that have a probability of being occupied by an "A" atom equal to the concentration of "A" atoms.

2.2 Characterizing Chemical Order

There are several ways by which chemical order can be characterized. The most obvious is to use the concentration of each species as the metric for order. The concentration of species d is given by:

$$x_d = N_d / \sum_{d'} N_{d'} \ , \tag{2.1}$$

where N_d is the number of type d atoms and the sum gives the total number of atoms. The concentration is conserved (i.e., $x_{\mathrm{A}} + x_{\mathrm{B}} = 1$ for a binary system). In general this is a poor choice, since many different decorations of the lattice can have the same concentration.

Another step towards greater detail is to count the number of pairs. We first consider the concentration of A-A, A-B, and B-B nearest neighbor pairs. The concentrations of pairs are given by:

$$x_{\mathrm{AA}} = N_{\mathrm{A-A}} / (N_{\mathrm{A-A}} + N_{\mathrm{A-B}} + N_{\mathrm{B-B}}) \tag{2.2}$$

$$x_{\mathrm{AB}} = N_{\mathrm{A-B}} / (N_{\mathrm{A-A}} + N_{\mathrm{A-B}} + N_{\mathrm{B-B}}) \tag{2.3}$$

$$x_{\mathrm{BB}} = N_{\mathrm{B-B}} / (N_{\mathrm{A-A}} + N_{\mathrm{A-B}} + N_{\mathrm{B-B}}) \tag{2.4}$$

so that the concentration of pairs is conserved ($x_{\mathrm{AA}} + x_{\mathrm{AB}} + x_{\mathrm{BB}} = 1$). Table 2.2 shows the various concentrations of the ordered samples of Figure 2.1 and Figure 2.2.

Table 2.2: Concentrations of Atoms and Pairs of Atoms in Ordered Configurations

m	x_{A}	x_{B}	x_{AA}	x_{AB}	x_{BB}
1	1	0	1	0	0
2	1/2	1/2	0	1	0
3	0	1	0	0	1
4	2/3	1/3	1/3	2/3	0

Now we introduce the cluster expansion and its metric for chemical order, the correlation function[1]. The general cluster expansion (GCE) is a method for expressing thermodynamic properties of a system in terms of its chemical arrangement, $\vec{\sigma}$. "Spin variables," σ, are used for the two species of atoms, where an A atom is assigned the factor $\sigma = +1$, and a B atom $\sigma = -1$. A cluster is a shape made by connecting a number of points n on the lattice. The correlation function ξ_n is defined as the sum over all clusters of the products of the spin variables for each atom in the cluster:

$$\xi_n = \frac{1}{N_n} \sum_{\{p_i\}} \sigma_{p_1} \sigma_{p_2} \cdots \sigma_{p_n} \ . \tag{2.5}$$

Here n also denotes the order of each term in the expansion. For example, in the GCE n={0,1,2} for the empty lattice, point, and pair terms, respectively (Figure 2.3). The number of clusters of type n is N_n. The value of the spin variable at site p is σ_p with each lattice point labeled from 1 to n [4].

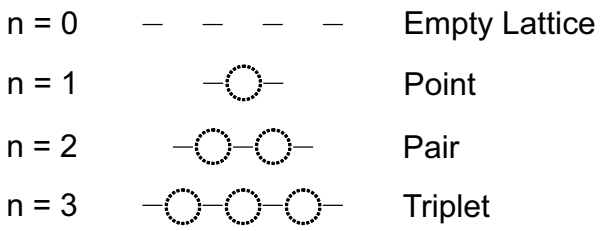

Figure 2.3: Cluster types in 1-D chain

For the 1-D case the clusters are chains containing n atoms. The value of the $n = 0$ term is

[1]This is the *chemical* correlation function. Throughout the remainder of the text the correlation function refers to that of the cluster expansion.

always 1 ($\xi_0 = 1$). The point term is a function of the composition:

$$\xi_1 = \frac{1}{N_{\rm A} + N_{\rm B}} \left[N_{\rm A}\sigma_{\rm A} + N_{\rm B}\sigma_{\rm B} \right] = \sigma_{\rm A} x_{\rm A} + \sigma_{\rm B} x_{\rm B} = x_{\rm A} - x_{\rm B} \tag{2.6}$$

$$\xi_1 = 1 - 2x_{\rm B} \quad . \tag{2.7}$$

The pair term can be written in terms of the concentrations of pairs:

$$\xi_2 = \frac{\left[N_{\rm A-A}\sigma_{\rm A}\sigma_{\rm A} + N_{\rm A-B}\sigma_{\rm A}\sigma_{\rm B} + N_{\rm B-B}\sigma_{\rm B}\sigma_{\rm B} \right]}{N_{\rm A-A} + N_{\rm A-B} + N_{\rm B-B}} \tag{2.8}$$

$$= \sigma_{\rm A}^2 x_{\rm AA} + \sigma_{\rm A}\sigma_{\rm B} x_{\rm AB} + \sigma_{\rm B}^2 x_{\rm BB} \tag{2.9}$$

$$= x_{\rm AA} - x_{\rm AB} + x_{\rm BB} \tag{2.10}$$

$$= 1 - 2x_{\rm AB} \tag{2.11}$$

where we have used the conservation of pairs $x_{\rm AA} + x_{\rm BB} = 1 - x_{\rm AB}$.

Equations 2.7 and 2.11 can readily be used in conjunction with Table 2.2 to determine the correlation functions of the different samples. The notation $\xi_{m,n}$ is introduced; where m is the label for each sample in Figure 2.1. The correlation functions for the first three samples can be written in simple terms of the order of the expansion, with $\xi_{1,n} = (+1)^n$, $\xi_{3,n} = (-1)^n$, and $\xi_{2,n}$ given by:

$$\xi_{2,n} = \begin{cases} 0 \quad , & n \text{ odd} \\ -1 \quad , & n \text{ even, } n/2 \text{ odd} \\ +1 \quad , & n \text{ even, } n/2 \text{ even} \end{cases} \quad . \tag{2.12}$$

Table 2.3: Correlation Functions of Ordered Configurations

m	$\xi_{m,0}$	$\xi_{m,1}$	$\xi_{m,2}$
1	1	1	1
2	1	0	-1
3	1	-1	1
4	1	1/3	-1/3

Graphically, the correlation functions can be determined by first selecting the smallest repeatable unit cell. Consider Sample 2, which has two possible unit cells (Figure 2.4). Unit Cell 1 contains an A atom at the center and a B atom at either edge. For the point term (concentration term) there is half of a B atom on the left, an A atom at the center, and half of a B atom on the right. An atom is counted as "half" if it is shared with a neighboring cell. The correlation function is

$$\xi_{2,1}^{\text{Cell 1}} = \frac{\frac{1}{2}(-1) + (+1) + \frac{1}{2}(-1)}{\frac{1}{2} + 1 + \frac{1}{2}} = 0 \; . \tag{2.13}$$

Two pairs are contained within the bounds of the unit cell. Each pair is fully counted (count the dash, not the atoms) and the correlation function is

$$\xi_{2,2}^{\text{Cell 1}} = \frac{(-1)(+1) + (+1)(-1)}{1 + 1} = -1 \; . \tag{2.14}$$

The triplet term consists of three figures. One figure is fully enclosed by the unit cell, while the other two figures are each shared by their neighboring cell. The $n = 3$ correlation function is then

$$\xi_{2,3}^{\text{Cell 1}} = \frac{\frac{1}{2}(+1)(-1)(+1) + (-1)(+1)(-1) + \frac{1}{2}(+1)(-1)(+1)}{\frac{1}{2} + 1 + \frac{1}{2}} = 0 \; . \tag{2.15}$$

The same analysis can be applied to Unit Cell 2. The correlation functions of both unit cells are equivalent.

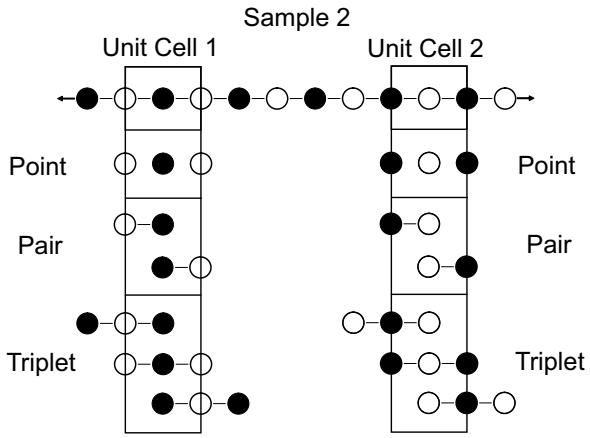

Figure 2.4: Graphical determination of correlation functions for the 1-D Sample 2.

2.3 Parameterizing Chemical Order

When parameterizing chemical order we assign a value of $S_{\rm ph}$ to each metric of the chemical order. For example, in the context of the chemical order in terms of the atomic concentration, values of s_A and s_B would be the proper parameters. The phonon entropy of any configuration, $\vec{\sigma}$, on the lattice is given by:

$$S_{\rm ph}^{\rm conc}(\vec{\sigma}) = s_{\rm A}\, x_{\rm A} + s_{\rm B}\, x_{\rm B} = s_{\rm A} + (s_{\rm B} - s_{\rm A}) x_{\rm B} = S_{\rm ph}^{\rm unmix}(x_{\rm B})\ , \tag{2.16}$$

where $s_{\rm A} = S_{\rm ph,1} = 0.75$ [$k_{\rm B}$/atom] and $s_{\rm B} = S_{\rm ph,3} = 0.40$ [$k_{\rm B}$/atom]. This is the equation of a line that connects the two end members, but which does not pass through the phonon entropy of Sample 2 ($S_{\rm ph,2}$). The label "unmix" denotes this as the phonon entropy of a system that is completely unmixed.

Using the concentration of pairs, the chemical order is parameterized with chemical exchange phonon entropies: $s_{\rm AA}$, $s_{\rm AB}$, and $s_{\rm BB}$. The phonon entropy of a given configuration on the lattice is,

$$S_{\rm ph}^{\rm pairs}(\vec{\sigma}) = s_{\rm AA}\, x_{\rm AA} + s_{\rm AB}\, x_{\rm AB} + s_{\rm BB}\, x_{\rm BB}\ , \tag{2.17}$$

where $s_{\rm AA} = S_{\rm ph,1} = 0.75$ [$k_{\rm B}$/atom], $s_{\rm AB} = S_{\rm ph,2} = 0.95$ [$k_{\rm B}$/atom], and $s_{\rm BB} = S_{\rm ph,3} = 0.40$ [$k_{\rm B}$/atom]. For the configuration of Sample 4, the value obtained using Equation 2.17 is $S_{\rm ph,4}^{\rm pairs} = 0.88\bar{3}$ [$k_{\rm B}$/atom].

The cluster expansion requires a parameter for each term in the expansion. These are referred to as *interaction parameters*, and in the case of the phonon entropy they are the *interaction phonon entropies*. For the $n = 0$ term of the expansion, the interaction phonon entropy is $s_0^{\rm ph}$, and so on for the higher terms. The phonon entropy can be written in terms of the correlation functions multiplied by their respective interaction phonon entropy (Equations 2.18–2.20).

$$S_{\rm ph,1} = s_0^{\rm ph}\, \xi_{1,0} + s_1^{\rm ph}\, \xi_{1,1} + s_2^{\rm ph}\, \xi_{1,2} \tag{2.18}$$

$$S_{\rm ph,2} = s_0^{\rm ph}\, \xi_{2,0} + s_1^{\rm ph}\, \xi_{2,1} + s_2^{\rm ph}\, \xi_{2,2} \tag{2.19}$$

$$S_{\rm ph,3} = s_0^{\rm ph}\, \xi_{3,0} + s_1^{\rm ph}\, \xi_{3,1} + s_2^{\rm ph}\, \xi_{3,2} \tag{2.20}$$

Here there are 3 equations and 3 unknowns. These equations can be written in matrix form as:

$$\left\{ \begin{array}{c} S_{\mathrm{ph},1} \\ S_{\mathrm{ph},2} \\ S_{\mathrm{ph},3} \end{array} \right\} = \left[\begin{array}{ccc} \xi_{1,0} & \xi_{1,1} & \xi_{1,2} \\ \xi_{2,0} & \xi_{2,1} & \xi_{2,2} \\ \xi_{3,0} & \xi_{3,1} & \xi_{3,2} \end{array} \right] \left\{ \begin{array}{c} s_0^{\mathrm{ph}} \\ s_1^{\mathrm{ph}} \\ s_2^{\mathrm{ph}} \end{array} \right\} , \tag{2.21}$$

or in a more compact notation as:

$$\vec{S}_{\mathrm{ph}} = [\xi_{m,n}]\, \vec{s}_{\mathrm{ph}} \ . \tag{2.22}$$

For our 1-D example the values of $\vec{S}_{\mathrm{ph}}$ and the correlation function matrix, $[\xi_{m,n}]$, are given by:

$$\vec{S}_{\mathrm{ph}} = \left\{ \begin{array}{c} 0.75 \\ 0.95 \\ 0.40 \end{array} \right\} [\mathrm{k_B/atom}] \ , \qquad [\xi_{m,n}] = \left[\begin{array}{ccc} 1 & 1 & 1 \\ 1 & 0 & -1 \\ 1 & -1 & 1 \end{array} \right] \ . \tag{2.23}$$

To get $\vec{s}_{\mathrm{ph}}$, simply invert the correlation function matrix:

$$\vec{s}_{\mathrm{ph}} = [\xi_{m,n}]^{-1}\, \vec{S}_{\mathrm{ph}} \ , \qquad [\xi_{m,n}]^{-1} = \frac{1}{4} \left[\begin{array}{ccc} 1 & 2 & 1 \\ 2 & 0 & -2 \\ 1 & -2 & 1 \end{array} \right] , \qquad \vec{s}_{\mathrm{ph}} = \left\{ \begin{array}{c} 0.7625 \\ 0.175 \\ -0.200 \end{array} \right\} [\mathrm{k_B/atom}] \ . \tag{2.24}$$

This is called the "structure inversion method," first utilized by Connolly and Williams to determine the properties of chemically disordered configurations from first-principles calculations of ordered configurations [4]. The next section treats the chemically disordered case. From the interaction phonon entropies and the correlation functions in Table 2.3, the phonon entropy of Sample 4 is determined to be $0.88\bar{3}$ [$\mathrm{k_B}$/atom]. This is the same value determined using the concentration of pairs. Both methods of characterizing the chemical order require three independent metrics. Appendix A shows the mathematical relationship between these two methods.

2.4 Random Solid Solution

For a random solid solution the probability of finding a particular atom on any site is given by the concentration of that atom species. For a binary random solid solution the probability of finding an A atom on a lattice site is $P_{\mathrm{A}} = x_{\mathrm{A}}$, and for a B atom it is $P_{\mathrm{B}} = x_{\mathrm{B}}$, so that probabilities are conserved: $P_{\mathrm{A}} + P_{\mathrm{B}} = 1$. In this section analytic expressions for the phonon entropy of a random solid solution are determined by examining the probabilities associated with a nearest neighbor pair of lattice sites (Figure 2.5).

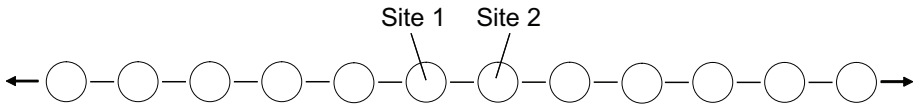

Figure 2.5: Sites used to determine the phonon entropy of a random solid solution

Table 2.4 shows how to obtain the probability of each possible pair on the two sites. Summing over the last column gives the phonon entropy of a random solid solution using the concentration of pairs method

$$S_{\mathrm{ph}}^{\mathrm{pairs}}(x_{\mathrm{B}}) = x_{\mathrm{A}}^2\, s_{\mathrm{AA}} + 2x_{\mathrm{A}}x_{\mathrm{B}}\, s_{\mathrm{AB}} + x_{\mathrm{B}}^2\, s_{\mathrm{BB}} \tag{2.25}$$

$$= (1 - x_{\mathrm{B}})^2\, s_{\mathrm{AA}} + 2(1 - x_{\mathrm{B}})x_{\mathrm{B}}\, s_{\mathrm{AB}} + x_{\mathrm{B}}^2\, s_{\mathrm{BB}} \tag{2.26}$$

where $S_{\mathrm{ph}}(x_{\mathrm{B}})$ denotes a random solid solution (as opposed to $S_{\mathrm{ph}}(\vec{\sigma})$). Comparing this to Equation 2.17 shows that for a random solid solution $x_{\mathrm{AA}} = x_{\mathrm{A}}^2$, $x_{\mathrm{AB}} = 2x_{\mathrm{A}}x_{\mathrm{B}}$, and $x_{\mathrm{BB}} = x_{\mathrm{B}}^2$.

Table 2.4: Probabilities Associated with Pair Exchange

Site 1	Site 2	P_1	P_2	$P_{1:2}$	$P_{1:2}\, s_{1:2}$
A	A	x_{A}	x_{A}	x_{A}^2	$x_{\mathrm{A}}^2\, s_{\mathrm{AA}}$
A	B	x_{A}	x_{B}	$x_{\mathrm{A}}x_{\mathrm{B}}$	$x_{\mathrm{A}}x_{\mathrm{B}}\, s_{\mathrm{AB}}$
B	A	x_{B}	x_{A}	$x_{\mathrm{B}}x_{\mathrm{A}}$	$x_{\mathrm{B}}x_{\mathrm{A}}\, s_{\mathrm{AB}}$
B	B	x_{B}	x_{B}	x_{B}^2	$x_{\mathrm{B}}^2\, s_{\mathrm{BB}}$

For a random solid solution, or any configuration, in the cluster expansion the empty lattice term is given by $\xi_0 = 1$ and the point term is given by Equation 2.7 ($\xi_1 = (1 - 2x_B)$). For the pair term the same type of analysis can be applied using the spin variables, as was done above. Table 2.5 shows a method to calculate ξ_2 for a random solid solution. Summing over the last column gives the pair correlation function for a random solid solution (Equation 2.27).

$$\xi_2 = x_A^2 - 2x_A x_B + x_B^2 = (x_A - x_B)^2 = (1 - 2x_B)^2 \tag{2.27}$$

In general it can be shown that for any lattice the correlation functions of a random solid solution are given by $\xi_n = (\sigma_A x_A + \sigma_B x_B)^n = (1 - 2x_B)^n$. The phonon entropy of a random solid solution is then:

$$S_{ph}^{CE}(x_B) = \sum_{n=0}^{\nu_g} s_n^{ph} \, (1 - 2x_B)^n \, , \tag{2.28}$$

where ν_g is the number of terms used in the cluster expansion. For the 1-D example:

$$S_{ph}^{CE}(x_B) = s_0^{ph} + s_1^{ph}(1 - 2x_B) + s_2^{ph}(1 - 2x_B)^2 \, . \tag{2.29}$$

This is plotted in Figure 2.6 along with the phonon entropy using the concentration approximation (Equation 2.16). The concentration of pairs method is equivalent to the three-term cluster expansion (see Appendix A), which is given by the solid line in Figure 2.6.

Table 2.5: Probabilities Associated with Pair Interaction

Site 1	Site 2	P_1	P_2	σ_1	σ_2	$(P_1\sigma_1)(P_2\sigma_2)$
A	A	x_A	x_A	+1	+1	x_A^2
A	B	x_A	x_B	+1	-1	$-x_A x_B$
B	A	x_A	x_A	-1	+1	$-x_B x_A$
B	B	x_B	x_B	-1	-1	x_B^2

The random solid solution provides the meaning of each of the interaction phonon entropies from the cluster expansion. The $n = 0$ term is the phonon entropy of a random solid solution of $A_{50}B_{50}$.

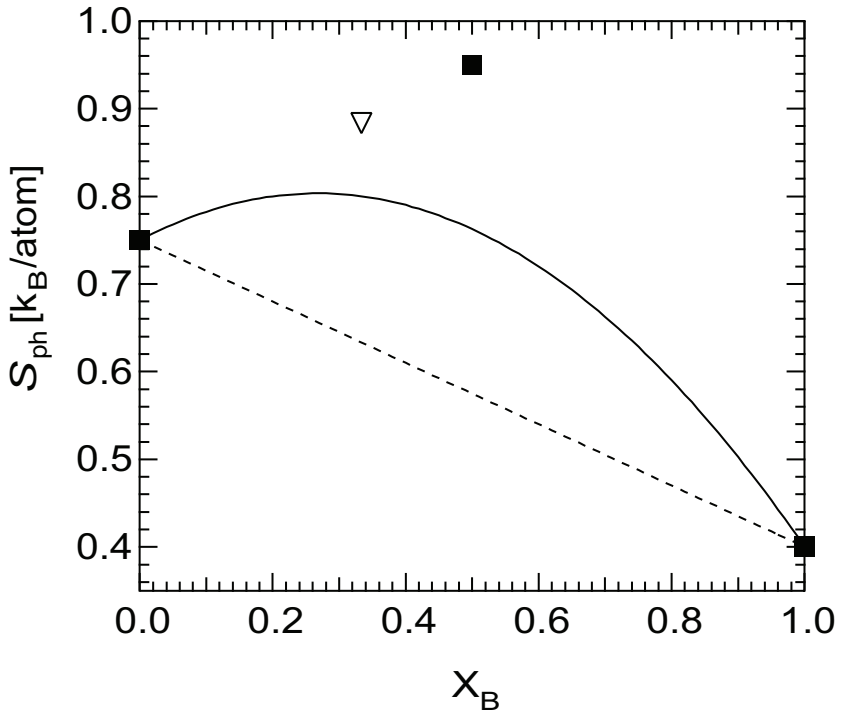

Figure 2.6: Phonon entropy of known ordered configurations (solid squares), of ordered configuration from three-term cluster expansion and concentration of pairs method (open triangle), of random solid solution using three-term cluster expansion and concentration of pairs method (solid line), and random solid solution using the concentration approximation (dashed line)

The $n = 1$ term gives the effect on the phonon entropy of changing the composition. The value $s_1^{\rm ph}$ is subtracted from $s_0^{\rm ph}$ when $x_{\rm B}$ is increased (added when $x_{\rm A}$ is increased). Since $s_1^{\rm ph} > 0$, the effect of increasing the concentration of atom B is to reduce the phonon entropy. The pair term, $n = 2$, gives the effect of like and unlike pairs of atoms on the phonon entropy. When $s_2^{\rm ph} > 0$, like pairs increase the phonon entropy. In our case $s_2^{\rm ph} < 0$, so that like pairs decrease the phonon entropy.

The phonon entropy of mixing $\Delta S_{\rm ph}(\vec{\sigma})$ is given by

$$\Delta S_{\rm ph}(\vec{\sigma}) = S_{\rm ph}(\vec{\sigma}) - \sum_d x_d \, S_{\rm ph}(x_d = 1) \tag{2.30}$$

$$= S_{\rm ph}(\vec{\sigma}) - S_{\rm ph}^{\rm unmix}(\vec{\sigma}) \, , \tag{2.31}$$

where $S_{\rm ph}(x_d = 1)$ is the phonon entropy of pure element d. Thus the phonon entropy of mixing is defined by the difference between a chemically mixed state (example: the random solid solution) and the chemically unmixed state (example: spinodally decomposed sample). For a random solid

solution this is given graphically by the vertical difference between the solid line and dashed line of Figure 2.6.

The phonon entropy of mixing in Equation 2.31 can be expressed for a binary random solid solution in terms of the interaction phonon entropies. For a three-term expansion this is:

$$\begin{aligned} \Delta S_{\rm ph}^{\rm CE}(x_{\rm B}) &= s_0^{\rm ph} + s_1^{\rm ph}(1-2x_{\rm B}) + s_2^{\rm ph}(1-2x_{\rm B})^2 \\ &\quad - \Big[(s_0^{\rm ph} + s_1^{\rm ph} + s_2^{\rm ph})(1-x_{\rm B}) + (s_0^{\rm ph} - s_1^{\rm ph} + s_2^{\rm ph})x_{\rm B}\Big] \qquad (2.32) \\ &= -4s_2^{\rm ph} x_{\rm B}(1-x_{\rm B}) \qquad . \qquad (2.33) \end{aligned}$$

The function $-4x_{\rm B}(1-x_{\rm B})$ is a parabola with a vertex at $x_{\rm B} = 1/2$. The value of $s_2^{\rm ph}$ scales this function. The phonon entropy of mixing is given in Figure 2.7

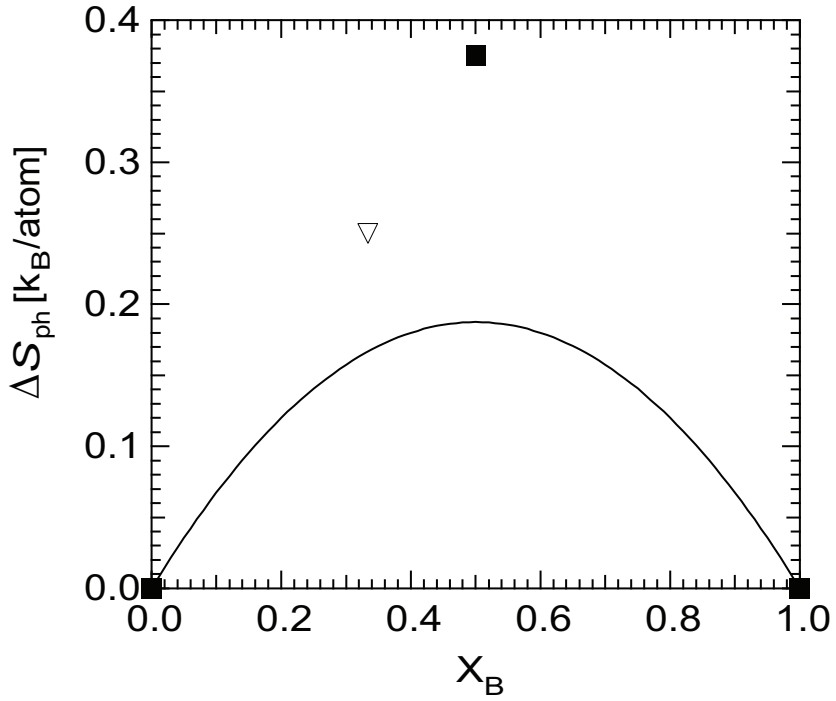

Figure 2.7: Phonon entropy of mixing of ordered samples (solid squares), ordered samples from the cluster expansion and concentration of pairs (open triangle), and disordered solid solution from cluster expansion and concentration of pairs

2.5 Phase Diagram

The essential quantity for phase stability as a function of temperature and composition at constant pressure is the Gibbs free energy, $G = H - TS$. The phase or combination of phases that minimizes G is thermodynamically most stable. Only differences in the Gibbs free energy between phases are important, not the absolute magnitude of G. The standard state is taken to be the chemically unmixed state, so that for a given phase γ we have:

$$\begin{aligned} \Delta G^{\gamma}(\vec{\sigma}, T) &= G^{\gamma}(\vec{\sigma}, T) - G^{\text{unmix}}(\vec{\sigma}, T) && (2.34) \\ &= [H^{\gamma}(\vec{\sigma}) - TS^{\gamma}(\vec{\sigma})] - \left[H^{\text{unmix}}(x_{\text{B}}) - TS^{\text{unmix}}(x_{\text{B}})\right] && (2.35) \\ &= \Delta H^{\gamma}(\vec{\sigma}) - T\Delta S^{\gamma}(\vec{\sigma}) && (2.36) \\ &= \Delta H^{\gamma}(\vec{\sigma}) - T\left[\Delta S^{\gamma}_{\text{ph}}(\vec{\sigma}) + \Delta S^{\gamma}_{\text{config}}(\vec{\sigma})\right] \quad . && (2.37) \end{aligned}$$

The 1-D example given has three different possible phases. The first is the ordered phases of samples 2 and 4. The second is the random solid solution, which is the mixed phase. The last is the unmixed phase. Both the ordered phases and the unmixed phase have no difference in configurational entropy compared to the unmixed phase: $\Delta S^{\text{unmix}}_{\text{config}}(x_{\text{B}}) = 0$ and $\Delta S^{\text{ord}}_{\text{config}}(\vec{\sigma}) = 0$. The mixed phase has a change in configurational entropy given by:

$$\Delta S^{\text{mix}}_{\text{config}}(x_{\text{B}}) = -\text{k}_{\text{B}}\left[(1 - x_{\text{B}})\ln(1 - x_{\text{B}}) + x_{\text{B}}\ln(x_{\text{B}})\right] \ . \tag{2.38}$$

The change in enthalpy between phase γ and the unmixed phase is given by:

$$\Delta H^{\gamma}(\vec{\sigma}) = \Delta E^{\gamma}(\vec{\sigma}) - P\Delta V^{\gamma}(\vec{\sigma}) \ . \tag{2.39}$$

In our example $\Delta V^{\gamma}(\vec{\sigma}) = 0$ so that $\Delta H^{\gamma}(\vec{\sigma}) = \Delta E^{\gamma}(\vec{\sigma})$. Following the procedure used for the phonon entropy:

$$\vec{\mathcal{L}} = [\xi_{m,n}]^{-1}\,\vec{E} \ , \tag{2.40}$$

where $\mathcal{L}_n$ are the *interaction binding energies*,

$$\vec{\mathcal{L}} = \left\{ \begin{array}{c} -9.5275 \\ -0.0850 \\ -0.0675 \end{array} \right\} \text{[eV/atom]} \; . \tag{2.41}$$

The binding energies are plotted in Figure 2.8. As with the phonon entropy, the enthalpy of mixing can be written as a simple function of the $n = 2$ term of the expansion:

$$\Delta H^{\text{mix}}(x_{\text{B}}) = -4\mathcal{L}_2 x_{\text{B}}(1 - x_{\text{B}}) \; . \tag{2.42}$$

The change in enthalpy for the chemically ordered samples is plotted in Figure 2.9 along with the enthalpy of mixing. At this point, the ordered phases can be eliminated as the thermodynamically stable phases by noting that $\Delta H^{\text{ord}} > \Delta H^{\text{mix}}$ and $\Delta S^{\text{ord}}_{\text{ph}} < \Delta S^{\text{mix}}_{\text{config}}$ so that $\Delta G^{\text{ord}} > \Delta G^{\text{mix}}$. This means that Samples 2 and 4 are metastable phases, which perhaps could be created by non-equilibrium techniques.

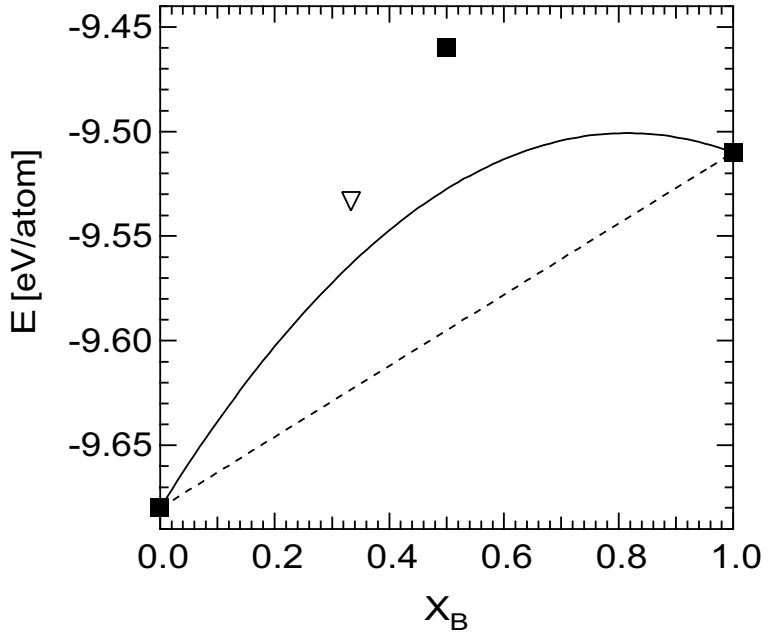

Figure 2.8: Binding energies of known ordered configurations (solid squares), of ordered configuration from three-term cluster expansion (open triangle), of random solid solution (solid line), and of unmixed phase (dashed line)

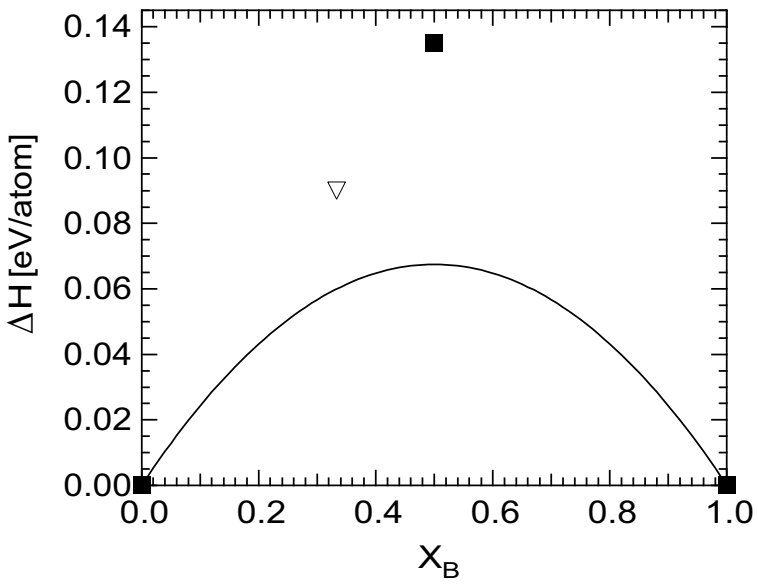

Figure 2.9: Difference in enthalpy between various phases and unmixed phase. The various phases are the ordered samples (solid squares), ordered sample from the cluster expansion (open triangle), and disordered solid solution (line).

With the ordered phases eliminated as being thermodynamically unstable, there are only two possible phases in this example: chemically unmixed and chemically mixed. Since $\Delta G^{\rm unmix} = 0$ the only function of interest is $\Delta G^{\rm mix}(x_{\rm B})$:

$$\begin{aligned} \Delta G^{\rm mix}(x_{\rm B}, T) &= \Delta H^{\rm mix}(x_{\rm B}) - T\left[\Delta S^{\rm mix}_{\rm ph}(x_{\rm B}) + \Delta S^{\rm mix}_{\rm config}(x_{\rm B})\right] \qquad (2.43) \\ &= 4\left[T s_2^{\rm ph} - \mathcal{L}_2\right] x_{\rm B}(1-x_{\rm B}) + {\rm k_B}T\left[(1-x_{\rm B})\ln(1-x_{\rm B}) + x_{\rm B}\ln(x_{\rm B})\right] \ . \qquad (2.44) \end{aligned}$$

The Gibbs free energy of mixing is plotted in Figure 2.10 for a number of different temperatures. For a certain range of temperatures the Gibbs free energy of mixing can be lowered by deviating from a random solid solution and separating into a mixture of two phases of different compositions. Figure 2.11 shows that a random solid solution with $x_{\rm B} = 0.50$ at $T = 800$K can lower its Gibbs free energy of mixing substantially by decomposing into two phases: an A-atom-rich phase with $x_{\rm B} \simeq 0.08$ and a B-atom-rich phase with $x_{\rm B} \simeq 0.92$. This is a simple model of spinodal decomposition, which requires "up-hill" diffusion, since the atoms tend to unmix. The phase boundary is known as the miscibility gap.

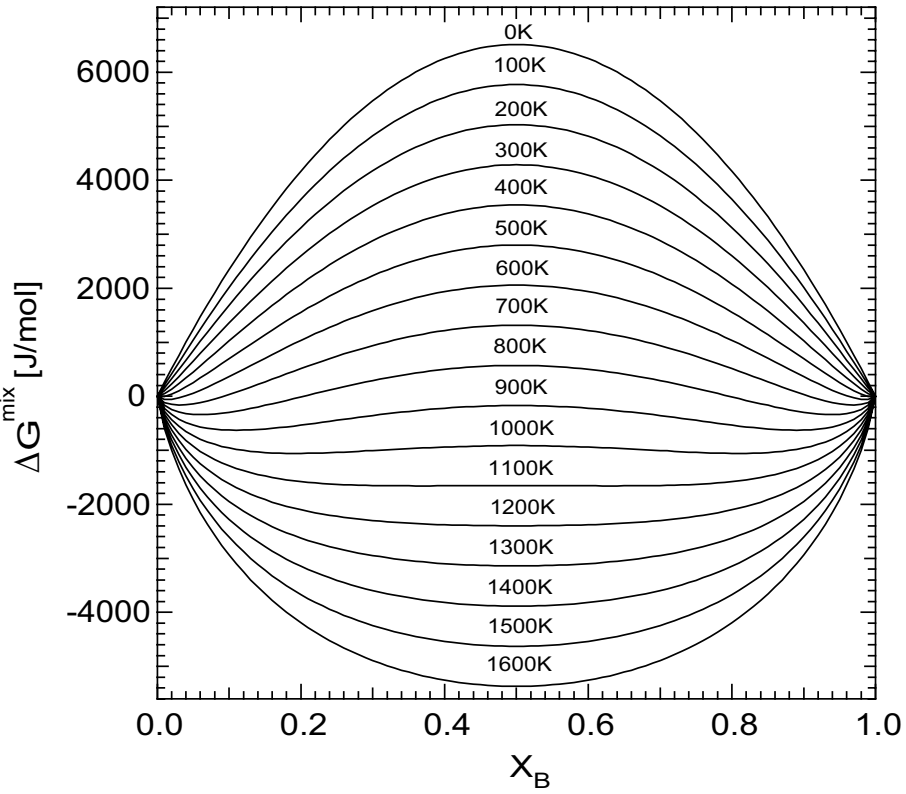

Figure 2.10: Gibbs free energy of mixing for 1-D example

The phase diagram is constructed by finding the phase or combination of phases that gives the lowest Gibbs free energy. When the combination of phases has a lower Gibbs free energy than the individual phases, the equilibrium between them is determined by the lowest points at which the chemical potentials of the phases are equal. Diagrammatically, this can be determined by drawing a line that connects the curves at points where both the intercept and slope are equal in all phases. This is the common tangent construction. For a binary system with only two phases this is mathematically equivalent to solving the two equations for $x_{\mathrm{B}}^{\mathrm{crit},1}$ and $x_{\mathrm{B}}^{\mathrm{crit},2}$:

$$\left.\frac{\mathrm{d}}{\mathrm{d}x_{\mathrm{B}}}\Delta G^{\alpha'}(x_{\mathrm{B}},T)\right|_{x_{\mathrm{B}}=x_{\mathrm{B}}^{\mathrm{crit},1}} = \left.\frac{\mathrm{d}}{\mathrm{d}x_{\mathrm{B}}}\Delta G^{\alpha''}(x_{\mathrm{B}},T)\right|_{x_{\mathrm{B}}=x_{\mathrm{B}}^{\mathrm{crit},2}} \tag{2.45}$$

$$\Delta G^{\alpha'}(x_{\mathrm{B}}^{\mathrm{crit},1},T) - x_{\mathrm{B}}^{\mathrm{crit},1}\left.\frac{\mathrm{d}}{\mathrm{d}x_{\mathrm{B}}}\Delta G^{\alpha'}(x_{\mathrm{B}},T)\right|_{x_{\mathrm{B}}=x_{\mathrm{B}}^{\mathrm{crit},1}} = \Delta G^{\alpha''}(x_{\mathrm{B}}^{\mathrm{crit},2},T) - x_{\mathrm{B}}^{\mathrm{crit},2}\left.\frac{\mathrm{d}}{\mathrm{d}x_{\mathrm{B}}}\Delta G^{\alpha''}(x_{\mathrm{B}},T)\right|_{x_{\mathrm{B}}=x_{\mathrm{B}}^{\mathrm{crit},2}} . \tag{2.46}$$

The phase diagram for this system is shown in Figure 2.12. The critical temperature of chemical

unmixing can be shown to be

$$T^{\text{crit}} = \frac{-\mathcal{L}_2}{\frac{R}{2} - s_2^{\text{ph}}} \tag{2.47}$$

where careful attention must be paid to the units[2]. The critical temperature in this example is 1118.98 K. If the vibration entropy of mixing were zero ($s_2^{\text{ph}} = 0$), then the critical temperature would be 1566.7 K. This shows that the positive phonon entropy of mixing plays the role of destabilizing the miscibility gap by reducing the critical temperature.

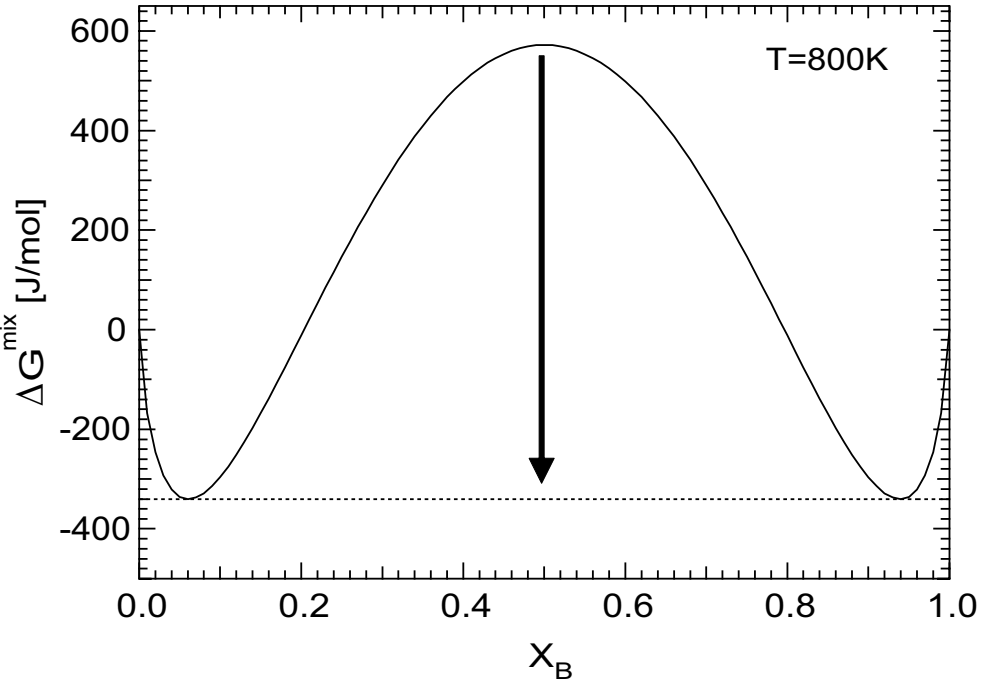

Figure 2.11: Gibbs free energy of mixing for 1-D example at $T = 800$K. The dashed line is a common tangent of the A-atom-rich and B-atom-rich phases. The arrow shows the decrease in Gibbs free energy from the unmixing.

[2]The reader interested in the origin of this equation should refer to the section titled *Criteria for Phase Stability in Regular Solutions* in [5]. The choice of R or k_B in Equation 2.47 depends on the units of $\mathcal{L}_2$ and s_2^{ph}.

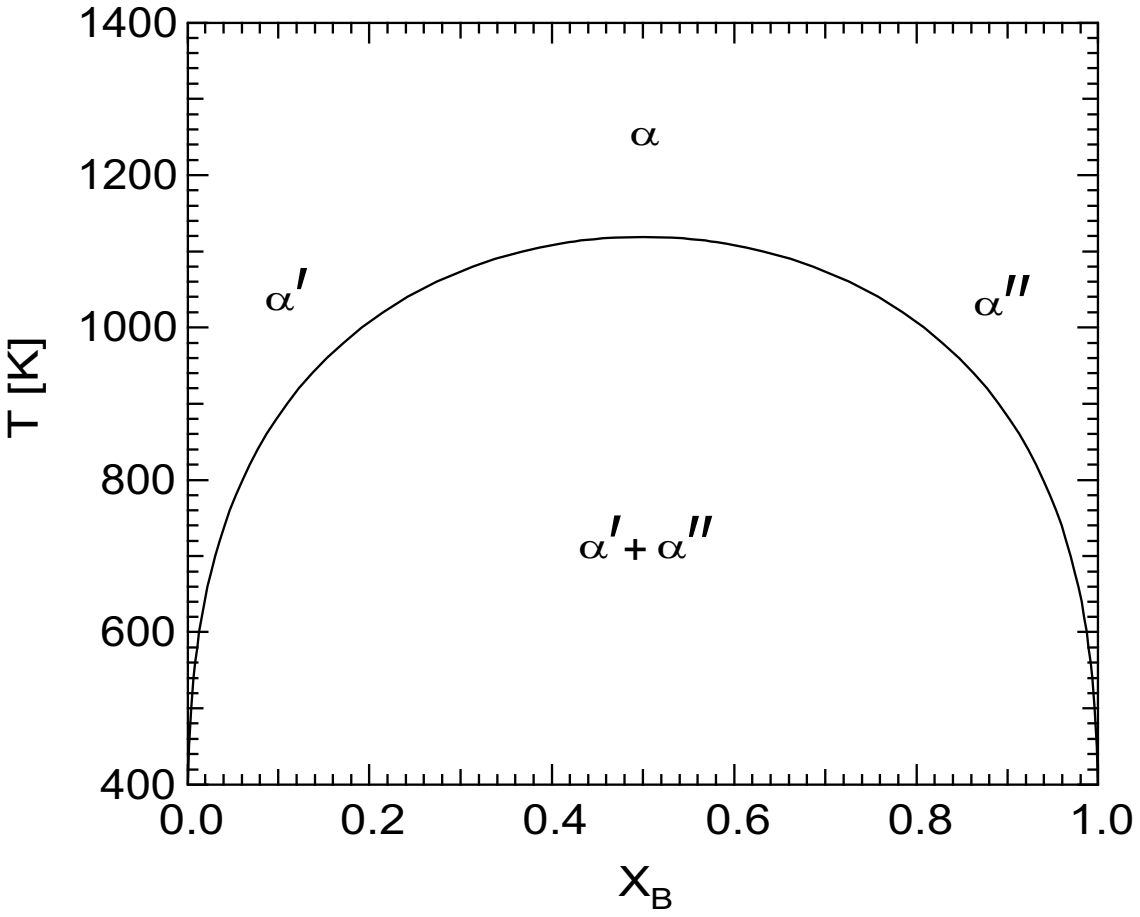

Figure 2.12: Phase diagram for 1-D example. The α phase is a random solid solution of A and B atoms. The α' phase is an A-atom-rich random solid solution, and the α'' phase is a B-atom-rich random solid solution.

Chapter 3

Cluster Expansion

3.1 General and Local Properties

As described in Chapter 2, the general cluster expansion (GCE) is a method of expressing thermodynamic properties of an alloy in terms of its chemical arrangement, $\vec{\sigma}$. The GCE is utilized for overall thermodynamic properties, such as the total enthalpy of formation or total phonon entropy (as opposed to the phonon *partial* entropy). In this framework, spin variables σ are used for the two species of atoms, where an A atom is assigned the factor $\sigma = +1$, and a B atom $\sigma = -1$. A cluster is a shape made by connecting a number of points n on the lattice. The correlation function ξ_n is given by Equation 2.5. For a random solid solution of A and B atoms the correlation function is given by

$$\xi_n = (1 - 2x_{\mathrm{B}})^n \ . \tag{3.1}$$

For a given thermodynamic quantity J, with a set of values $J_m(\vec{\sigma})$ of known configurations $\vec{\sigma}$ corresponding to the label m, interaction parameters $\mathcal{J}_n$ can be determined by inverting the correlation function matrix $[\xi_{m,n}]$,

$$\mathcal{J}_n = \sum_{m=0}^{\nu_g - 1} J_m(\vec{\sigma}) \ [\xi_{m,n}]^{-1} \ . \tag{3.2}$$

Here ν_g is the number of terms used in the GCE, and $[\xi_{m,n}]^{-1}$ is the inverted correlation function matrix. Knowledge of $\mathcal{J}_n$ can then be used to construct the thermodynamic quantity for any set of

configurations, $J_j(\vec{\sigma})$, using:

$$J_j(\vec{\sigma}) = \sum_{n=0}^{\nu_g - 1} \mathcal{J}_n \ [\xi_{j,n}] \ . \tag{3.3}$$

A partial thermodynamic quantity is defined as the projection onto a particular atom type of the thermodynamic quantity. For example, the phonon partial entropy of atom B is the phonon entropy contribution from the B atoms only. Partial quantities provide more detail about thermodynamic contributions and therefore require a more complex cluster expansion technique. The local order cluster expansion (LOCE) is a method for expressing thermodynamic properties of a particular type of atom in terms of its local chemical arrangement, $\vec{\sigma_l}$. In the LOCE, the clusters must contain the local point of interest, l (e.g., an A atom) [6]. A cluster is a shape made by connecting a number of points $n+1$ on the lattice, where the $+1$ arises from the inclusion of the local point in all clusters. In the LOCE, $n = 0$ is the point term because every point cluster is the atom of interest, d, with $\sigma^d_{l=d} = +1$. The pair and triangle terms correspond to $n = 1$ and $n = 2$, respectively. For a binary system of A and B atoms two different correlation functions must be used. The correlation functions for a random solid solution of A and B atoms around a local point containing an A atom are:

$$\xi_n(\mathrm{A}) = (1 - 2x_\mathrm{B})^n \ . \tag{3.4}$$

For a local point containing a B atom the correlation functions are:

$$\xi_n(\mathrm{B}) = (1 - 2x_\mathrm{A})^n = (-1)^n \xi_n(\mathrm{A}) \ . \tag{3.5}$$

The machinery of Equation 3.2 and Equation 3.3 remains valid for quantities in the LOCE by replacing $\mathcal{J}_n$ with $\mathcal{J}_n(d)$, $J(\vec{\sigma})$ with $J(\vec{\sigma}_l, d)$, and ν_g with ν_l. Here the dependence on d denotes a LOCE with a d atom as the atom at the local point of interest, and ν_l is the number of terms.

An example using the 1-D Sample 4 of Figure 2.2 is given below to show how the correlation functions are determined using the LOCE. As suggested in Chapter 2, it is first useful to determine the unit cell, which is boxed in Figure 3.1. First consider the "A" atom LOCE. Only clusters that

contain an A atom are counted, and the spin variables have the values $\sigma^{\rm A}_{l=\rm A} = +1$ and $\sigma^{\rm B}_{l=\rm A} = -1$. The correlation functions are determined by summing over the clusters,

$$\xi_{4,1}(\mathrm{A}) = \frac{(-1)(+1) + (+1)(+1) + (+1)(-1)}{3} = -\frac{1}{3}\ , \tag{3.6}$$

$$\xi_{4,2}(\mathrm{A}) = \frac{\frac{1}{2}(+1)(-1)(+1) + (-1)(+1)(+1) + (+1)(+1)(-1) + \frac{1}{2}(+1)(-1)(+1)}{3} = -1\ , \tag{3.7}$$

where the factor of 1/2 is used when a cluster is shared by a neighboring cell. Note that for the A atom LOCE all of the clusters used in the GCE are used, as all of the clusters contain A atoms. Now consider the "B" atom LOCE. Only clusters that contain a B atom are counted, and the spin variables have the values $\sigma^{\rm A}_{l=\rm B} = -1$ and $\sigma^{\rm B}_{l=\rm B} = +1$. The correlation functions are determined by summing over the clusters,

$$\xi_{4,1}(\mathrm{B}) = \frac{(+1)(-1) + (-1)(+1)}{2} = -1\ , \tag{3.8}$$

$$\xi_{4,2}(\mathrm{B}) = \frac{\frac{1}{2}(-1)(+1)(-1) + (+1)(-1)(-1) + (-1)(-1)(+1) + \frac{1}{2}(-1)(+1)(-1)}{3} = +1\ . \tag{3.9}$$

Note that as the cluster size increases there are less clusters excluded. Also note that for the B

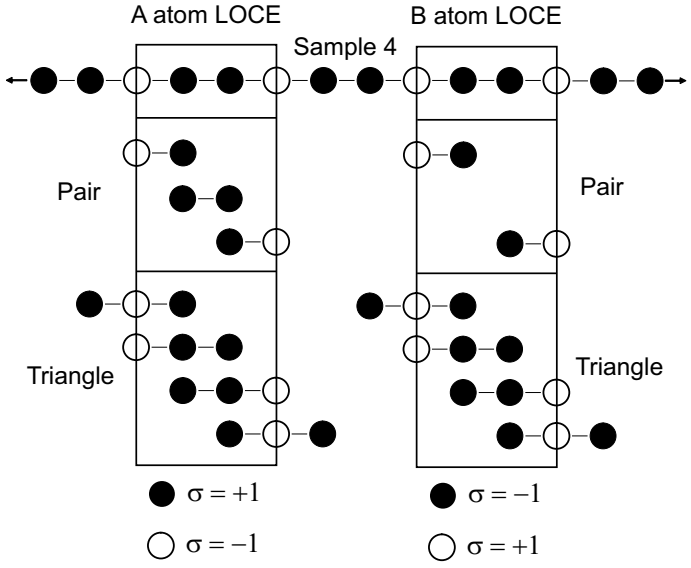

Figure 3.1: Graphical display of clusters used in local order cluster expansions with both A and B atoms as the atom of interest. "A" atoms are solid circles and "B" atoms hollow circles.

atom LOCE the correlation functions up to the pair term are the same as for Sample 2 of Figure 2.1.

When the LOCE and GCE are both used to describe the same quantity, the number of terms used for each cluster expansion are related by $\nu_g = \nu_l + 1$. For instance, a three-term LOCE uses clusters up to the triangle term. The equivalent GCE must use four terms in the expansion to include the triangle term. As an example consider the phonon entropy, which is a linear combination of the phonon partial entropies

$$S_{\rm ph}(\vec{\sigma}) = \sum_d x_d \, S_{\rm ph}(\vec{\sigma}_l, d) \; . \tag{3.10}$$

Here x_d is the concentration of atom species d and $S_{\rm ph}(\vec{\sigma}_l, d)$ is the phonon partial entropy of atom species d with local chemical arrangement $\vec{\sigma}_l$. Both sides of this equation can be expanded with the cluster formalism

$$\sum_{n=0}^{\nu_g - 1} s_n^{\rm ph} \; \xi_n = \sum_d x_d \; \sum_{n=0}^{\nu_l - 1} s_n^{\rm ph}(d) \; \xi_n(d) \; , \tag{3.11}$$

where $s_n^{\rm ph}$ is the interaction phonon entropy for the n-th term of the general cluster expansion. Similarly, $s_n^{\rm ph}(d)$ is the interaction phonon *partial* entropy for the n-th term of the *local* cluster expansion. If we limit our analysis to a random solid solution of A and B atoms, the equation can be written in terms of the concentration

$$\sum_{n=0}^{\nu_g - 1} s_n^{\rm ph} \; (1 - 2x_{\rm B})^n = (1 - x_{\rm B}) \; \sum_{n=0}^{\nu_l - 1} s_n^{\rm ph}({\rm A}) \; (1 - 2x_{\rm B})^n + x_{\rm B} \sum_{n=0}^{\nu_l - 1} s_n^{\rm ph}({\rm B})(-1)^n (1 - 2x_{\rm B})^n \; . \tag{3.12}$$

For this equation to be valid (i.e., having the powers of the concentration match on the LHS and RHS), the number of terms of the expansions must be related by $\nu_g = \nu_l + 1$.

Expressing the interaction parameters in terms of the random solid solution gives a simple method for relating the GCE and LOCE. A relationship between $s_n^{\rm ph}$ and $s_n^{\rm ph}(d)$ is found by expanding the RHS of Equation 3.12 in powers of $x_{\rm B}$ and matching terms. For a binary system the GCE and LOCE are related by the equations

$$s_0^{\rm ph} = \frac{1}{2}[s_0^{\rm ph}({\rm A}) + s_0^{\rm ph}({\rm B})] \tag{3.13}$$

$$s_n^{\rm ph}(E) = \frac{1}{2}[(s_{n-1}^{\rm ph}({\rm A}) + s_n^{\rm ph}({\rm A})) + (-1)^n(s_{n-1}^{\rm ph}({\rm B}) + s_n^{\rm ph}({\rm B}))], \;\; 1 \leq n < \nu_g - 1 \tag{3.14}$$

$$s_{\nu_g-1}^{\rm ph}(E) = \frac{1}{2}[s_{\nu_l-1}^{\rm ph}({\rm A}) + (-1)^n s_{\nu_l-1}^{\rm ph}({\rm B})] \qquad . \tag{3.15}$$

For $\nu_g = 4$ this can be written in matrix form as

$$\left\{ \begin{array}{c} s_0^{\rm ph} \\ s_1^{\rm ph} \\ s_2^{\rm ph} \\ s_3^{\rm ph} \end{array} \right\} = 1/2 \left[\begin{array}{ccc|ccc} 1 & 0 & 0 & 1 & 0 & 0 \\ 1 & 1 & 0 & -1 & -1 & 0 \\ 0 & 1 & 1 & 0 & 1 & 1 \\ 0 & 0 & 1 & 0 & 0 & -1 \end{array} \right] \left\{ \begin{array}{c} s_0^{\rm ph}({\rm A}) \\ s_1^{\rm ph}({\rm A}) \\ s_2^{\rm ph}({\rm A}) \\ s_0^{\rm ph}({\rm B}) \\ s_1^{\rm ph}({\rm B}) \\ s_2^{\rm ph}({\rm B}) \end{array} \right\} , \tag{3.16}$$

where the left half of the separation denotes the A atom type and the right half the B atom type. In more compact notation

$$\vec{s}_{\rm ph} = [R]\ \vec{s}_{\rm ph}(d)\ , \tag{3.17}$$

where the matrix $[R]$ relates the interaction phonon entropies of the GCE with the interaction phonon partial entropies of the LOCE.

3.1.1 Entropy of Mixing

This section is given for the specific case of the phonon entropy, though it is easily extended to other thermodynamic quantities such as the enthalpy. In Section 2.4 the phonon entropy of mixing is defined (Equation 2.31). In a similar manner the phonon partial entropy of mixing is defined as

$$\Delta S_{\rm ph}(\vec{\sigma}, d) = S_{\rm ph}(\vec{\sigma}, d) - \sum_{d'} x_{d'}\ S_{\rm ph}(x_{d'} = 1, d)\ , \tag{3.18}$$

where $S_{\rm ph}(x_{d'} = 1, d)$ is the phonon entropy of pure element d when $d' = d$ and is the phonon entropy of impurity amounts of d in d' when $d' \neq d$. For a random solid solution using a three-term LOCE, the only contribution to the phonon partial entropy of mixing $\Delta S_{\rm ph}(x_d, d)$ comes from the $n = 2$ term and is,

$$\Delta S_{\rm ph}(x_d, d) = -4x_d(1 - x_d)s_2^{\rm ph}(d) \; . \tag{3.19}$$

The total phonon entropy of mixing of Equation 2.31 is, in terms of the interaction phonon partial entropies,

$$\Delta S_{\rm ph}(x_{\rm B}) = -4x_{\rm B}(1 - x_{\rm B}) \left\{ \frac{[s_1^{\rm ph}({\rm B}) + s_1^{\rm ph}({\rm A})]}{2} + \; x_{\rm B} \; s_2^{\rm ph}({\rm B}) + (1 - x_{\rm B}) \; s_2^{\rm ph}({\rm A}) \right\} \; . \tag{3.20}$$

The function $-4x_{\rm B}(1 - x_{\rm B})$ is a parabola with a vertex at $x_{\rm B} = 1/2$. The first term in brackets scales this function. If both $s_1^{\rm ph}(d)$ are negative, this term introduces a positive entropy of mixing. The remaining terms, associated with $s_2^{\rm ph}(d)$, are the equation of a line. This function introduces an asymmetry to the phonon entropy of mixing when $s_2^{\rm ph}({\rm A}) \neq s_2^{\rm ph}({\rm B})$.

3.2 Application to Thermodynamic Functions

Quantities such as the phonon entropy provide very little information on what is occuring in the material. A much higher level of detail is found in the functions from which these quantities are derived, namely the density of states curves. The density of states gives the number of states that particles (or quasi-particles) can occupy per unit volume of crystal per unit energy. In the case of phonons, the phonon density of states (DOS) provides the number of phonons in a given energy range per atom. This function is derived from the phonon partition function, from which all of the phonon thermodynamic information is obtained. The DOS is of interest in its own right because it gives insight into interatomic forces, and the DOS curves have considerable structure that is lost when the phonon entropy is obtained by averaging over all modes of vibration. In the case of electrons,

the electronic density of states (EDOS) is necessary for calculating the electronic partition function and also provides information on the electronic structure.

The cluster expansion is easily applied to functions by simply allowing the interaction parameters to have an energy dependence. The machinery of Equation 3.2 and Equation 3.3 remains valid for functions using the GCE by replacing $\mathcal{J}_n$ with $\mathcal{J}_n(E)$ and $J(\vec{\sigma})$ with $J(E,\vec{\sigma})$. Similarly, in the LOCE Equation 3.2 and Equation 3.3 remains valid for functions by replacing $\mathcal{J}_n(d)$ with $\mathcal{J}_n(E,d)$ and $J(\vec{\sigma}_l,d)$ with $J(E,\vec{\sigma}_l,d)$.

3.2.1 Phonon Density of States

The phonon density of states (DOS), $g(E,\vec{\sigma})$, and phonon partial density of states (PDOS), $g(E,\vec{\sigma}_l,d)$, are normalized to one in energy and have non-negative values,

$$\int_0^{E^c(\vec{\sigma})} g(E,\vec{\sigma})\ \mathrm{d}E \ = \ 1 \ ; \ g(E,\vec{\sigma}) \geq 0 \ \text{ for } \ E \leq E^c(\vec{\sigma}) \ , \tag{3.21}$$

$$\int_0^{E^c(\vec{\sigma})} g(E,\vec{\sigma}_l,d)\ \mathrm{d}E \ = \ 1 \ ; \ g(E,\vec{\sigma}_l,d) \geq 0 \ \text{ for } \ E \leq E^c(\vec{\sigma}) \ . \tag{3.22}$$

Here $E^c(\vec{\sigma})$ is the phonon cutoff energy, which is a function of the chemical arrangement and is defined as

$$g(E,\vec{\sigma}) = 0 \ , \ E > E^c(\vec{\sigma}) \ . \tag{3.23}$$

As an example, the DOS of pure copper, a random solid solution of $Cu_{50}Au_{50}$, and pure gold are shown in Figure 3.2. All three of the samples are face-centered cubic (FCC). The cutoff energy of the three curves is roughly linear with concentration.

There are two methods for arriving at the interaction functions, both of which are mathematically rigorous for the phonon entropy, but only one method accurately describes the phonon density of states. The first derivation provides interaction functions that show the contributions to the phonon entropy from the number of modes at each energy E. The second derivation uses an energy rescaled by the phonon cutoff. This rescaled energy is denoted by the symbol $\mathcal{E}$. The interaction functions

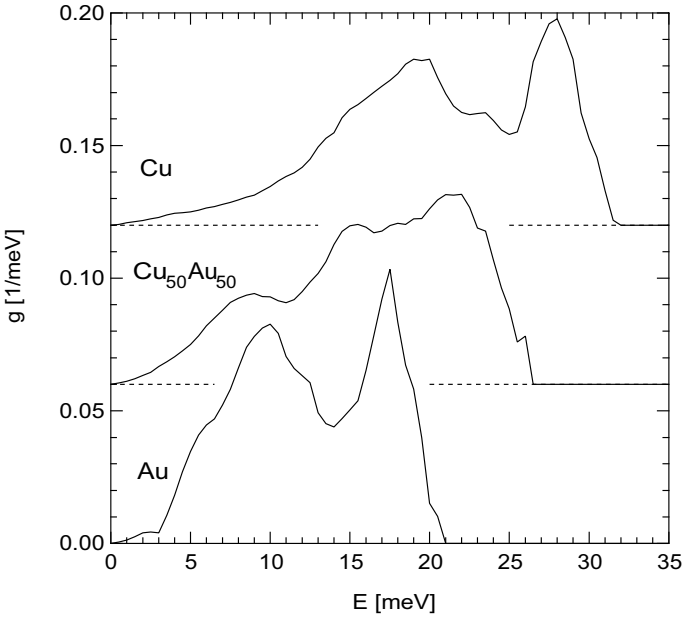

Figure 3.2: Phonon density of states curves for pure Cu, $Cu_{50}Au_{50}$ random solid solution (neutron-weighted), and pure Au. The curves are adapted from Bogdanoff et al. [7] and are offset by integer multiples of 0.06 meV^{-1}. Dashed lines indicate the zero for offset curves.

from both methods are termed "interaction phonon density of states" (IDOS) and are differentiated by the use of either E or $\mathcal{E}$.

3.2.1.1 Interaction Phonon Density of States: $\mathcal{G}_n(E)$

The phonon entropy $S_{\text{ph}}(\vec{\sigma})$ for a specific chemical arrangement $\vec{\sigma}$ corresponding to the label m is, in the quasiharmonic approximation [8],

$$S_{\text{ph}}^{m}(\vec{\sigma}) = 3\text{k}_\text{B} \int_0^\infty f^\star(E)\ g_m(E,\vec{\sigma})\ \text{d}E\ , \tag{3.24}$$

with

$$f^\star(E) \equiv (f(E)+1)\ \ln(f(E)+1)\ -\ f(E)\ \ln(f(E))\ , \tag{3.25}$$

where $f(E)$ is the Planck distribution. Both $f(E)$ and $g(E,\vec{\sigma})$ are obtained at the same temperature. The function $f^\star(E)$ is plotted in Figure 3.3 for various temperatures. Although not typically done,

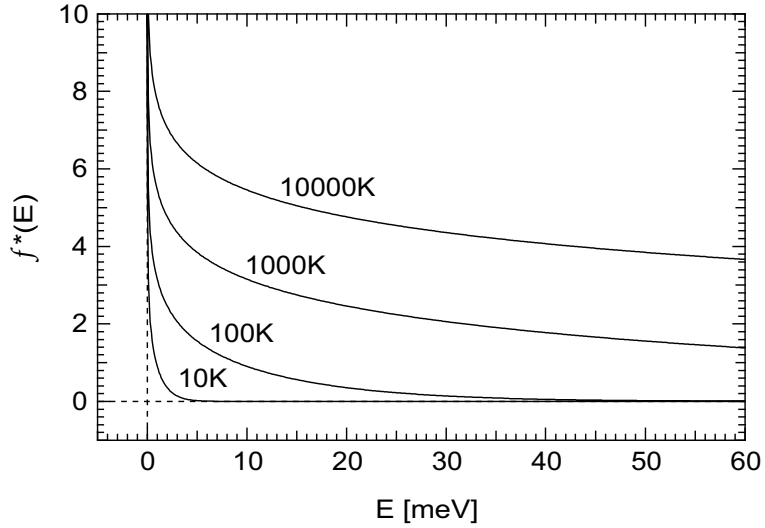

Figure 3.3: Values of the function $f^\star(E)$ for various temperatures. Note the higher weighting of the low-energy phonons. Dashed lines indicate the zero.

the phonon entropy can be written as a function of the energy

$$S^m_{\rm ph}(E,\vec{\sigma}) = 3{\rm k_B}\int_0^E f^\star(E')\ g_m(E',\vec{\sigma})\ {\rm d}E'\ . \tag{3.26}$$

The left-hand side of this equation can be expressed with the cluster expansion

$$\sum_{n=0}^{\nu_g-1} s^{\rm ph}_n(E)\ [\xi_{m,n}] = 3{\rm k_B}\int_0^E f^\star(E')\ g_m(E',\vec{\sigma})\ {\rm d}E'\ . \tag{3.27}$$

With independent phonons, consistent with harmonic or quasiharmonic theory, it is possible to evaluate a partial contribution to $s^{\rm ph}_n(E)$ from individual phonons, or from phonons within a small range of energy. Differentiating with respect to E gives the contribution from phonons within the energy range from E to $E+{\rm d}E$

$$g_m(E,\vec{\sigma}) = \frac{1}{3k_{\rm B}f^\star(E)}\sum_{n=0}^{\nu_g-1}\left(\frac{\rm d}{{\rm d}E}s^{\rm ph}_n(E)\right)[\xi_{m,n}]\ . \tag{3.28}$$

Comparing Equation 3.28 to Equation 3.3 gives the expression for the interaction phonon density of states (IDOS)

$$\mathcal{G}_n(E) = \frac{1}{3k_{\mathrm{B}}f^{\star}(E)}\frac{\mathrm{d}}{\mathrm{d}E}s_n^{\mathrm{ph}}(E)\ . \tag{3.29}$$

The IDOS functions $\mathcal{G}_n(E)$ can be used to construct density of states curves for any configuration of atoms

$$g_j(E,\vec{\sigma}) = \sum_{n=0}^{\nu_g-1}\mathcal{G}_n(E)\left[\xi_{m,n}\right]\ . \tag{3.30}$$

However, the curves $g_j(E,\vec{\sigma})$ do not obey Equation 3.21 if the cutoff energy varies with chemical arrangement (the DOS created from the IDOS functions $\mathcal{G}_n(E)$ may have negative energies).

The Cu-Au DOS curves in Figure 3.2 provide a simple example. The Cu atoms are assigned $\sigma = +1$ and the Au atoms $\sigma = -1$. The samples are labeled $m = 1$ for Cu, $m = 2$ for $Cu_{50}Au_{50}$, and $m = 3$ for Au. The correlation function matrix and its inverse are given by

$$\left[\xi_{m,n}\right] = \begin{bmatrix} 1 & 1 & 1 \\ 1 & 0 & 0 \\ 1 & -1 & 1 \end{bmatrix}\ ,\ \left[\xi_{m,n}\right]^{-1} = \frac{1}{2}\begin{bmatrix} 0 & 2 & 0 \\ 1 & 0 & -1 \\ 1 & -2 & 1 \end{bmatrix}\ . \tag{3.31}$$

The IDOS functions constructed following the equation

$$\mathcal{G}_n(E) = \sum_{m=0}^{\nu_g-1} g_m(E,\vec{\sigma})\left[\xi_{m,n}\right]^{-1}\ , \tag{3.32}$$

are given in Figure 3.4. Note that the $n = 0$ term is the $Cu_{50}Au_{50}$ random solid solution, which is normalized to one. The integral of the IDOS for the $n > 0$ terms is zero when the limit of integration is taken to infinity.

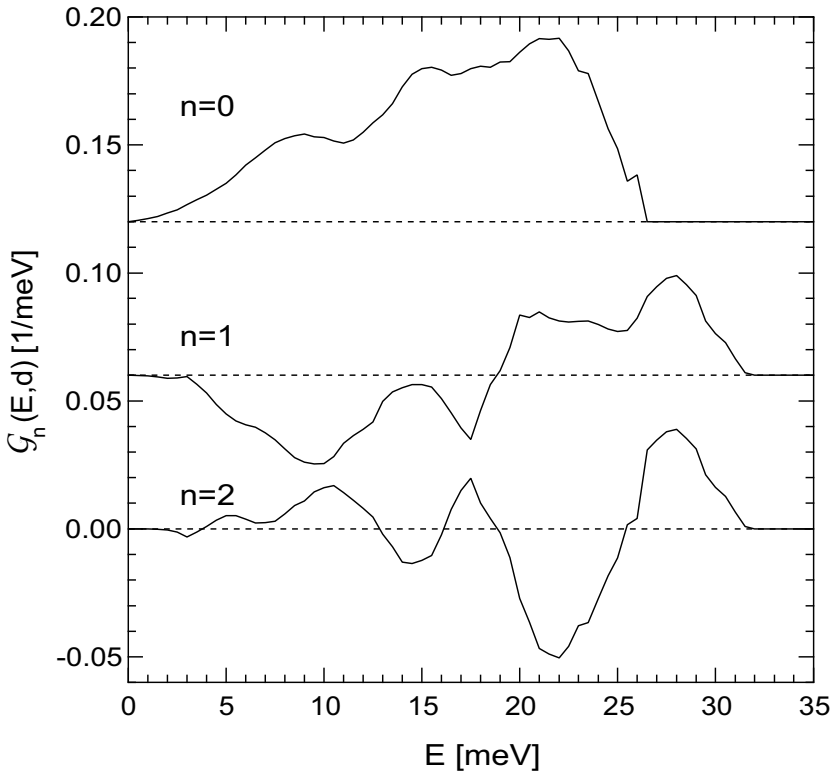

Figure 3.4: Interaction phonon density of states curves for Cu-Au. The curves are offset by integer multiples of 0.06 meV^{-1}. Dashed lines indicate the zero.

These IDOS curves can be used to produce any DOS curves for a given chemical arrangement on the FCC lattice. The correlation functions for various FCC ordered structures (Figure 3.5) are presented in the article by Connolly and Williams [4], which are reproduced in Table 3.1. Here $n = 1$ is the point cluster, $n = 2$ is the nearest-neighbor (NN) pair, $n = 3$ is the NN triangle, and $n = 4$ is the NN tetrahedron (Figure 3.6). These correlation functions are used to construct the ordered DOS in Figure 3.7. This plot shows that the cutoff energy is not properly accounted for using a cluster expansion as a function of the energy E. These DOS are all normalized to one so long as the integral is taken to infinity (as opposed to the value where the DOS becomes negative).

Table 3.1: Values of ξ_n for FCC Ordered Structures

Formula	Structure	ξ_0	ξ_1	ξ_2	ξ_3	ξ_4
Cu	FCC	1	1	1	1	1
Cu_3Au	$L1_2$	1	$\frac{1}{2}$	0	$-\frac{1}{2}$	-1
CuAu	$L1_0$	1	0	$-\frac{1}{3}$	0	1
$CuAu_3$	$L1_2$	1	$-\frac{1}{2}$	0	$\frac{1}{2}$	-1
Au	FCC	1	-1	1	-1	1

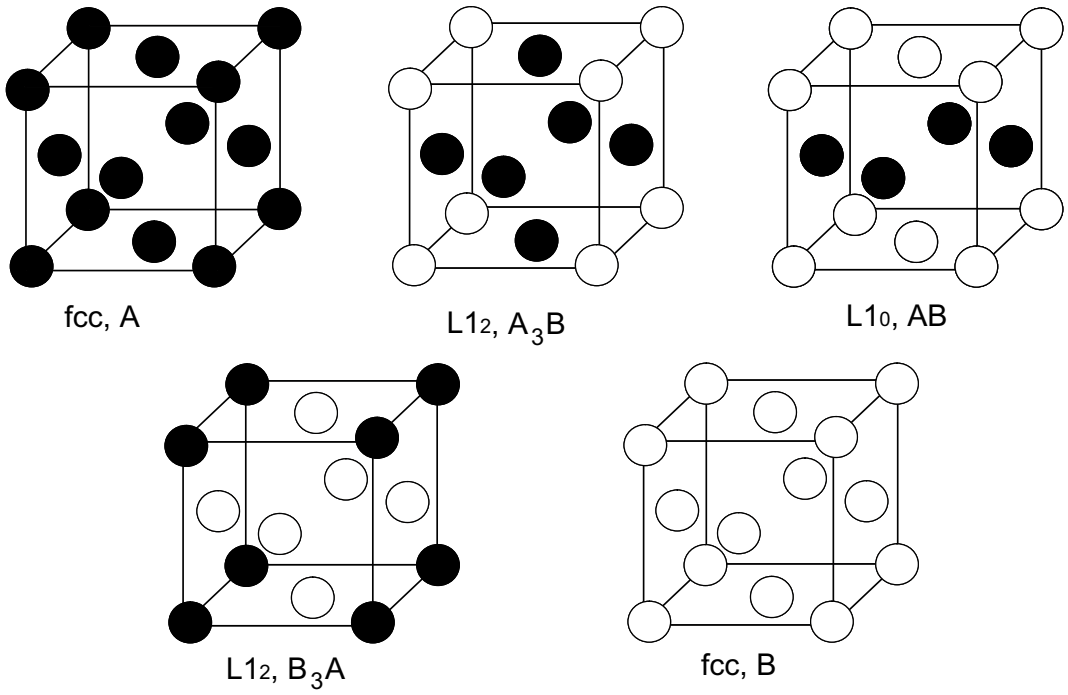

Figure 3.5: FCC ordered structures

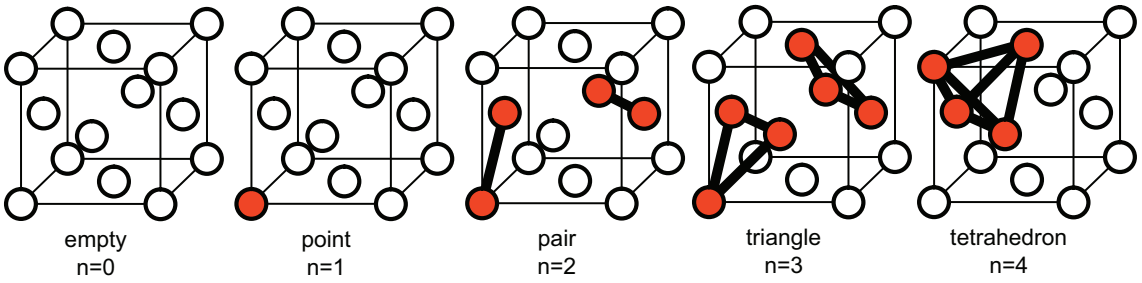

Figure 3.6: Clusters for the FCC structure

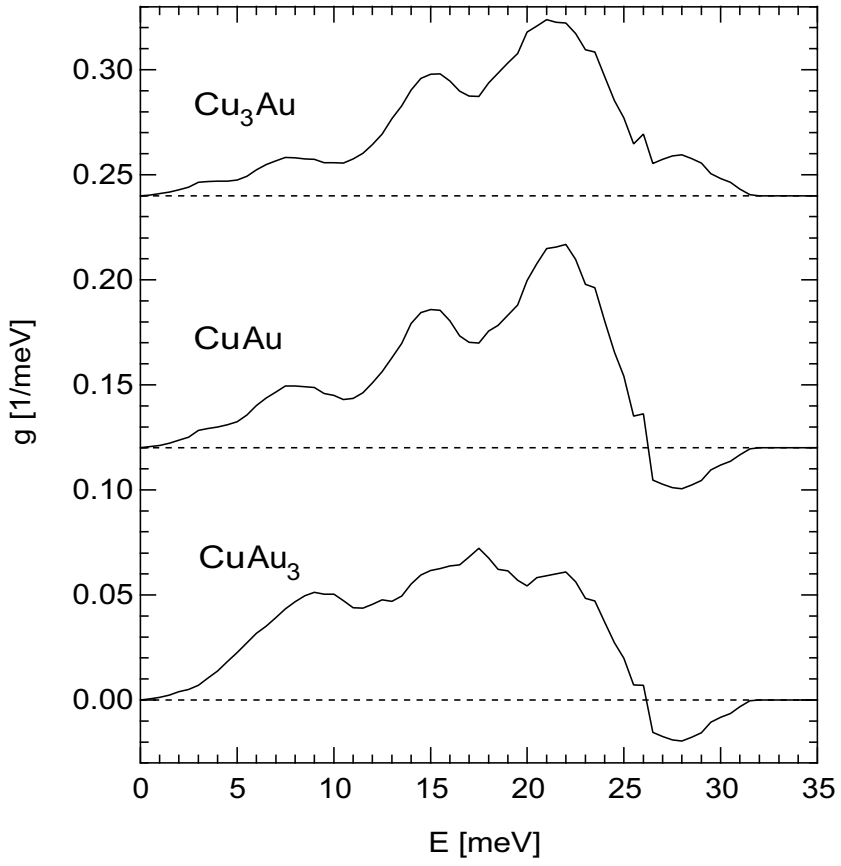

Figure 3.7: DOS of ordered structures constructed using IDOS in Figure 3.4 and correlation functions in Table 3.1. The curves are offset by integer multiples of 0.12 meV^{-1}. Dashed lines indicate the zero.

The IDOS curves as a function of E, although not producing useful DOS, remain useful in showing which phonon modes contribute to the phonon interaction entropy

$$s_n^{\mathrm{ph}}(E) = 3k_{\mathrm{B}} \int_0^E f^\star(E')\mathcal{G}_n(E')\mathrm{d}E' \ . \tag{3.33}$$

The $n = 2$ term is of particular interest as it scales the phonon entropy of mixing (Equation 2.33). For Cu-Au at room temperature this is shown in Figure 3.8. The final value of the phonon interaction entropy is $s_2^{\mathrm{ph}} = 0.05$ [$\mathrm{k_B}$/atom], so that the phonon entropy of mixing is negative with a minimum value of -0.05 [$\mathrm{k_B}$/atom]. The value of s_2^{ph} is positive primarily due to the modes in the energy range of 4 to 11 meV. In general, the low-energy modes contribute most to the phonon entropy and the phonon entropy of mixing due to the weighting factor $f^\star(E)$.

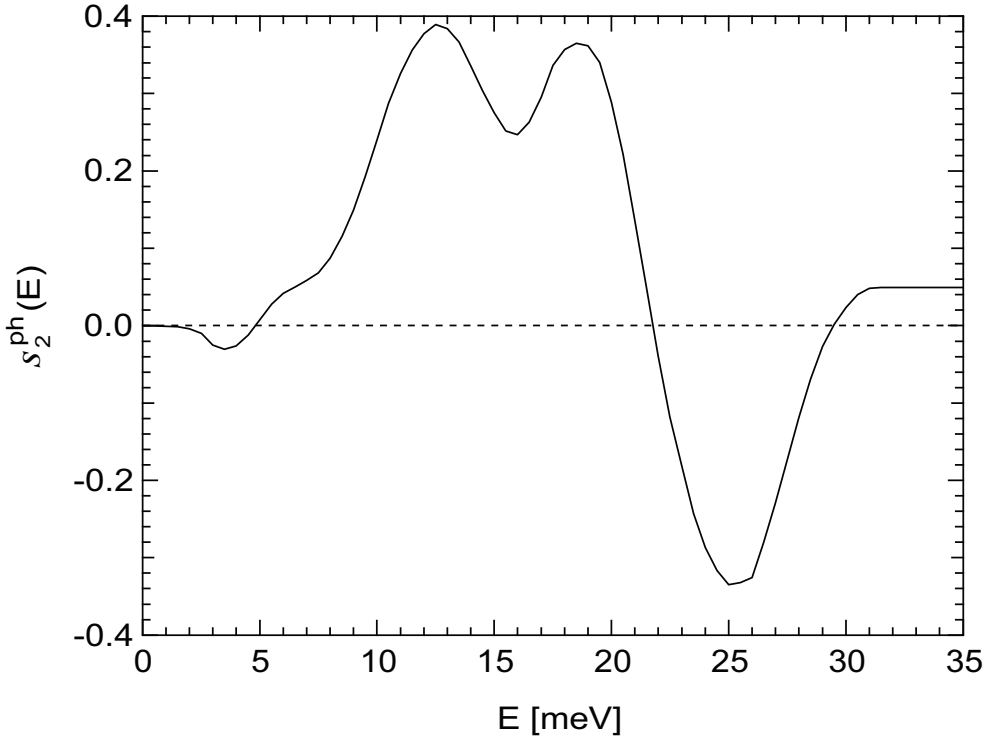

Figure 3.8: Interaction phonon entropy at room temperature (293K) as a function of energy for the $n = 2$ term of a GCE for the Cu-Au alloys presented in Figure 3.2

3.2.1.2 Interaction Phonon Density of States: $\mathcal{G}_n(\mathcal{E})$

The problems associated with a cluster expansion of the phonon density of states in the previous section can be avoided by properly accounting for the phonon cutoff energy. Here we begin with the phonon entropy, where the limit of integration is taken as the phonon cutoff energy

$$S^m_{\rm ph}(\vec{\sigma}) = 3{\rm k_B} \int_0^{E^c(\vec{\sigma})} f^\star(E)\ g_m(E,\vec{\sigma})\ {\rm d}E\ . \tag{3.34}$$

The rescaled energy $\mathcal{E}$ is

$$\mathcal{E} = \mathcal{E}(\vec{\sigma}) = \frac{E}{E^c(\vec{\sigma})}\ , \tag{3.35}$$

which can be used to perform a change of variables

$$S^m_{\rm ph}(\vec{\sigma}) = \frac{3{\rm k_B}}{E^c(\vec{\sigma})} \int_0^1 f^\star(\mathcal{E})\ g_m(\mathcal{E},\vec{\sigma})\ {\rm d}\mathcal{E}\ . \tag{3.36}$$

As done in the previous section, the phonon entropy can be written as a function

$$S^m_{\rm ph}(\mathcal{E},\vec{\sigma}) = \frac{3{\rm k_B}}{E^c(\vec{\sigma})} \int_0^{\mathcal{E}} f^\star(\mathcal{E}')\ g_m(\mathcal{E}',\vec{\sigma})\ {\rm d}\mathcal{E}'\ ,\ 0 \le \mathcal{E} \le 1 \tag{3.37}$$

which can be written in terms of the cluster expansion on the LHS

$$\sum_{n=0}^{\nu_g-1} s^{\rm ph}_n(\mathcal{E})\ [\xi_{m,n}] = \frac{3{\rm k_B}}{E^c(\vec{\sigma})} \int_0^{\mathcal{E}} f^\star(\mathcal{E}')\ g_m(\mathcal{E}',\vec{\sigma})\ {\rm d}\mathcal{E}'\ . \tag{3.38}$$

Differentiating with respect to $\mathcal{E}$ gives

$$g_m(\mathcal{E},\vec{\sigma}) = \frac{E^c(\vec{\sigma})}{3k_{\rm B}f^\star(\mathcal{E})} \sum_{n=0}^{\nu_g-1} \left(\frac{\rm d}{{\rm d}\mathcal{E}} s^{\rm ph}_n(\mathcal{E})\right) [\xi_{m,n}]\ , \tag{3.39}$$

so that the IDOS are

$$\mathcal{G}_n(\mathcal{E}) = \frac{E^c(\vec{\sigma})}{3k_{\rm B}f^\star(\mathcal{E})} \frac{\rm d}{{\rm d}\mathcal{E}} s^{\rm ph}_n(\mathcal{E})\ . \tag{3.40}$$

It seems redundant that the IDOS should also be a function of the chemical arrangement. However, the cluster expansion is designed to be used on a lattice with a constant lattice parameter. In the Cu-Au system, and most real systems, the lattice parameter varies with composition. Rescaling the energy by the cutoff helps to separate the effects of changes in bond length and bond stiffness from the effects of atom arrangement for which the cluster expansion is designed. The cutoff energy itself can also be expressed with the cluster expansion as

$$E_m^c(\vec{\sigma}) = \sum_{n=0}^{\nu_g - 1} \epsilon_n^c \ [\xi_{m,n}] \ , \tag{3.41}$$

where ϵ_n^c are the interaction cutoff energies.

For Cu-Au the DOS as a function of $\mathcal{E}$ is given in Figure 3.9. The cutoff interaction parameters are $\epsilon_0^c = 26.5$ meV, $\epsilon_1^c = 5.5$ meV, and $\epsilon_2^c = 0$ meV. These interaction parameters correspond to a linear relationship between the cutoff energy and the composition. The DOS are normalized by the cutoff energy

$$\int_0^1 g_m(\mathcal{E}, \vec{\sigma}) \, d\mathcal{E} \ = 1/E^c(\vec{\sigma}) \ , \tag{3.42}$$

so that the Au DOS in Figure 3.9 has the largest area under the curve.

A cluster expansion in $\mathcal{E}$ is done using the same mathematics as presented in Equations 3.30 and 3.32. The IDOS in $\mathcal{E}$ for Cu-Au is shown in Figure 3.10. Up to $n = 2$, the IDOS and IPDOS have normalizations that can be expressed in terms of simple linear functions of the cutoff energies of random solid solutions.

$$\left.\begin{array}{c} \int_0^1 \mathcal{G}_n(\mathcal{E}) \, d\mathcal{E} \\ \int_0^1 \mathcal{G}_n(\mathcal{E}, d) \, d\mathcal{E} \end{array}\right\} = \begin{cases} \left[E^c(x_{\mathrm{B}} = \frac{1}{2})\right]^{-1} & , \quad n = 0 \\ \frac{1}{2}\left[[E^c(x_{\mathrm{B}} = 0)]^{-1} - [E^c(x_{\mathrm{B}} = 1)]^{-1}\right] & , \quad n = 1 \\ \frac{1}{2}\left[[E^c(x_{\mathrm{B}} = 0)]^{-1} - [E^c(x_{\mathrm{B}} = 1)]^{-1}\right] - \left[E^c(x_{\mathrm{B}} = \frac{1}{2})\right]^{-1} & , \quad n = 2 \end{cases} \ . \tag{3.43}$$

The IDOS are then used, along with the interaction cutoff energies, to produce the DOS of the ordered structures listed in Table 3.1. The result is shown in Figure 3.11. Comparison of this

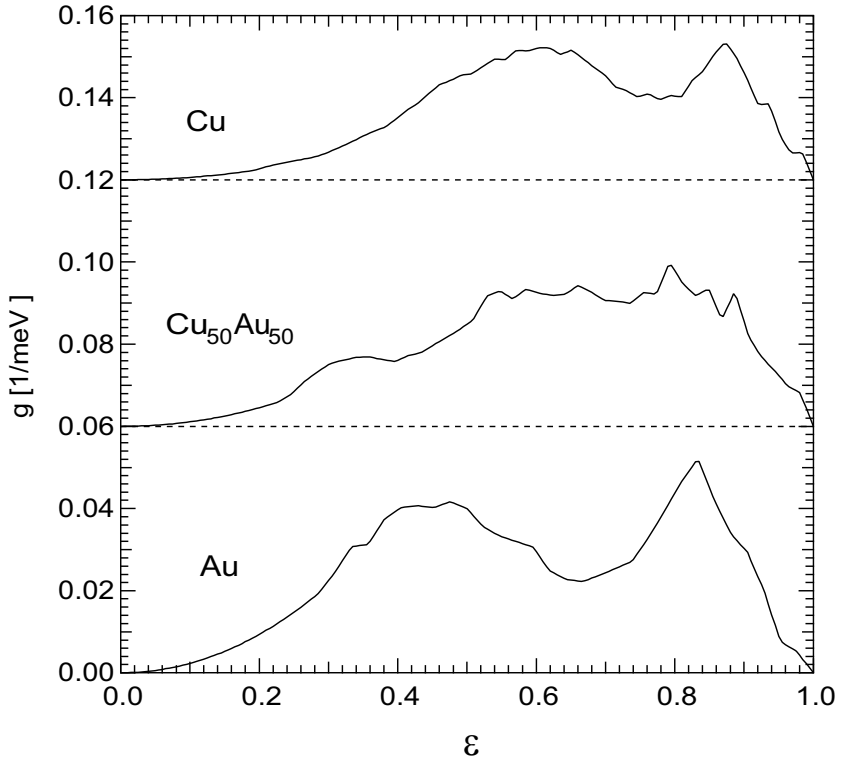

Figure 3.9: Phonon density of states curves for pure Cu, $Cu_{50}Au_{50}$ random solid solution (neutron-weighted), and pure Au as a function of the rescaled energy $\mathcal{E}$. The curves are offset by integer multiples of 0.06 meV^{-1}. Dashed lines indicate the zero for offset curves.

figure to Figure 3.7 shows the differences between the DOS constructed with $\mathcal{G}_n(E)$ and the DOS constructed with $\mathcal{G}_n(\mathcal{E})$.

A cluster expansion in $\mathcal{E}$ is the correct method when dealing with the phonon density of states curves. The IDOS $\mathcal{G}_n(\mathcal{E})$ are a function of the chemical arrangement. As such, they cannot be simply related to the phonon entropy and phonon entropy of mixing. A cluster expansion in E is ideal when dealing with the phonon entropy. Though the expansions in $\mathcal{E}$ and E give the same results for the phonon entropy, the latter can be used to point out the contribution to the phonon entropy from phonons at each energy E.

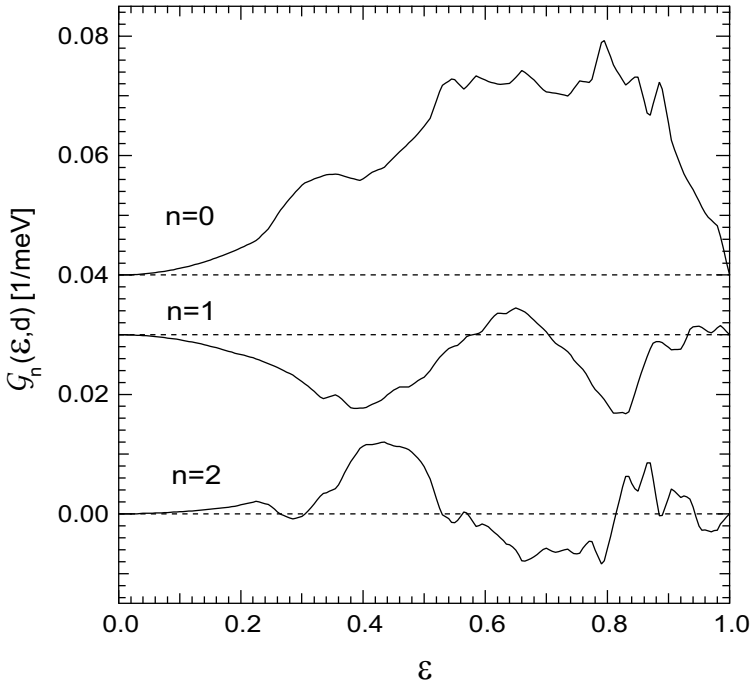

Figure 3.10: Interaction phonon density of states curves for Cu-Au. The $n = 1$ and $n = 2$ curves are offset by 0.03 meV^{-1} and 0.04 meV^{-1}, respectively. Dashed lines indicate the zero.

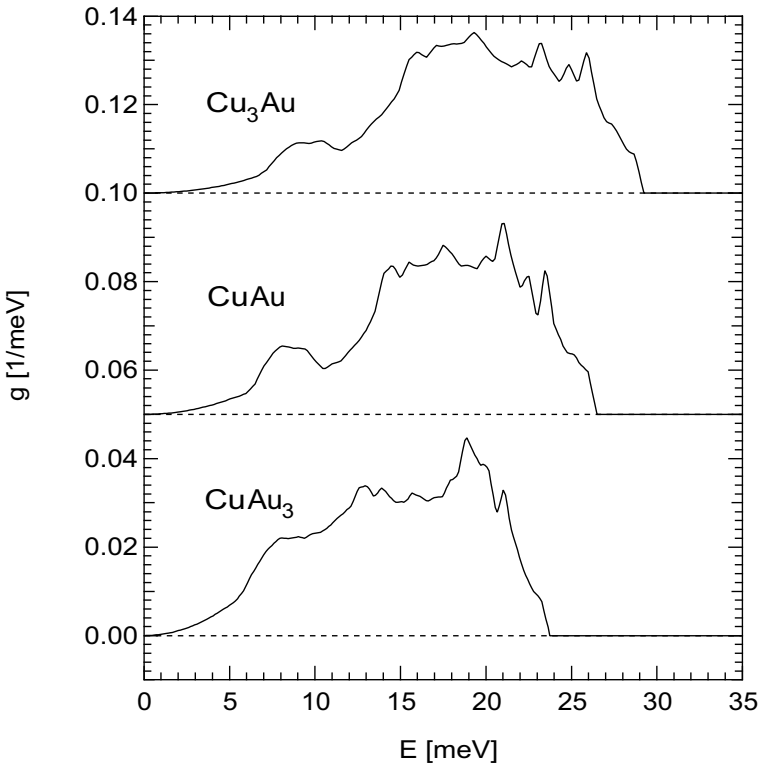

Figure 3.11: DOS of ordered structures constructed using IDOS in Figure 3.10 and correlation functions in Table 3.1. The curves are offset by integer multiples of 0.05 meV^{-1}. Dashed lines indicate the zero.

3.2.2 Electronic Density of States

The electronic entropy is given by

$$S_{\rm el}(\vec{\sigma}) = {\rm k_B} \int_{-\infty}^{\infty} F^{\star}(E)\ n(E,\vec{\sigma})\ {\rm d}E\ , \tag{3.44}$$

where $F^{\star}(E)$ is

$$F^{\star}(E) = -\left\{[1-F(E)]\ln[1-F(E)] + F(E)\ln F(E)\right\}\ , \tag{3.45}$$

$F(E)$ is the Fermi distribution, and $n(E,\vec{\sigma})$ is the electronic density of states (EDOS) at energy E. The energy is taken with respect to the Fermi energy E_F, which is set as the zero of energy. The Fermi distribution and the weighting factor $F^{\star}(E)$ are plotted in Figure 3.12.

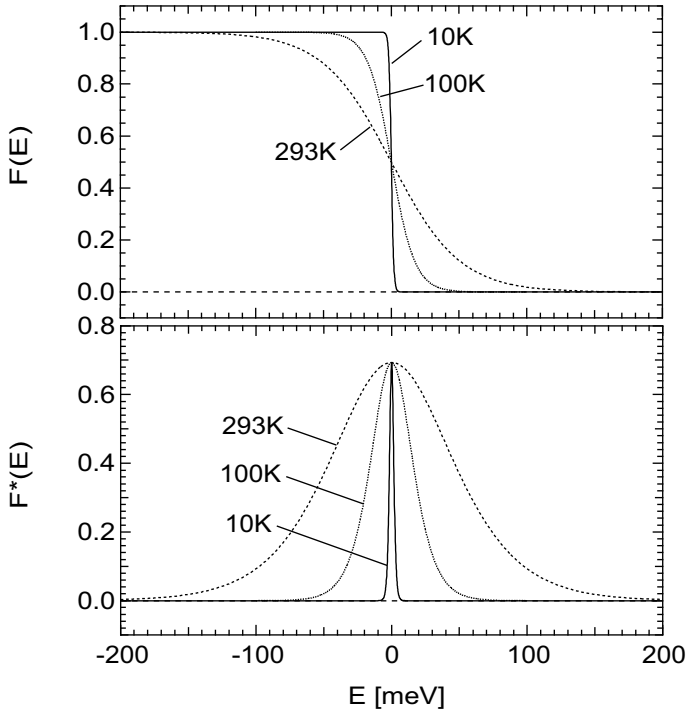

Figure 3.12: Weighting functions for the electronic entropy. Dashed lines indicate the zero.

In some ways a cluster expansion of the electronic density of states is easier to perform than a cluster expansion of the phonon density of states. Unlike phonons, which are bosons and can occupy the same state, electrons are fermions and obey Fermi-Dirac statistics. Electronic energies are on the order of eV, as opposed to the meV range for phonon energies, which means that only a small

portion of the EDOS contributes to the electronic entropy (see the function $F^{\star}(E)$ in Figure 3.12). This also means that the problem associated with the cutoff energy for phonons does not exist for electrons.

As with the phonon entropy, we begin by writing the electron entropy as a function of energy

$$S_{\mathrm{el}}^{m}(E,\vec{\sigma}) = \mathrm{k_B} \int_{-\infty}^{E} F^{\star}(E')\ n_m(E',\vec{\sigma})\ \mathrm{d}E' \ , \tag{3.46}$$

and then express the LHS with the cluster expansion,

$$\sum_{n=0}^{\nu_g-1} s_n^{\mathrm{el}}(E)\ [\xi_{m,n}] = \mathrm{k_B} \int_{-\infty}^{E} F^{\star}(E')\ n_m(E',\vec{\sigma})\ \mathrm{d}E' \ , \tag{3.47}$$

where $s_n^{\mathrm{el}}(E)$ is the interaction electronic entropy. Differentiating with respect to E gives

$$n_m(E,\vec{\sigma}) = \frac{1}{k_{\mathrm{B}} F^{\star}(E)} \sum_{n=0}^{\nu_g-1} \left(\frac{\mathrm{d}}{\mathrm{d}E} s_n^{\mathrm{el}}(E) \right) [\xi_{m,n}] \ . \tag{3.48}$$

Comparing Equation 3.48 to Equation 3.3 gives the expression for the interaction electronic density of states (IEDOS)

$$\mathcal{N}_n(E) = \frac{1}{k_{\mathrm{B}} F^{\star}(E)} \frac{\mathrm{d}}{\mathrm{d}E} s_n^{\mathrm{el}}(E) \ . \tag{3.49}$$

The IEDOS functions $\mathcal{N}_n(E)$ can be used to construct the electronic density of states curves for any configuration of atoms

$$n_j(E,\vec{\sigma}) = \sum_{n=0}^{\nu_g-1} \mathcal{N}_n(E)\ [\xi_{m,n}] \ . \tag{3.50}$$

A cluster expansion of the EDOS was first performed by Geng et al. [9] on the Ni-Al system. The calculations done in this article were non-spin polarized. In the case that one is examining systems with magnetic effects, for example Fe-Cr, the spin must be taken into account. To account for the two different polarizations (spin up $\uparrow$, spin down $\downarrow$) the IEDOS can simply be given a spin dependence. The spin up IEDOS is then $\mathcal{N}_n^{\uparrow}(E)$ and the spin down IEDOS is $\mathcal{N}_n^{\downarrow}(E)$.

3.3 Application to Thermodynamic Values

There are a number of thermodynamic properties that depend on the phonon and electron density of states curves. Most physical quantities of interest, such as the free energy, internal energy, or entropy, are integrations over the DOS or EDOS. If cluster expansions of the DOS and EDOS work well, it is expected that cluster expansions of these physical quantities will work at least as well, if not better. For example, the binding energy (or cohesive energy) is an integral over the EDOS [10]

$$E(\vec{\sigma}) = \int E' \; F(E') \; n(E', \vec{\sigma}) \; \mathrm{d}E' \; . \tag{3.51}$$

The electronic heat capacity of the solid is the temperature derivative of this quantity

$$C_{\mathrm{el}}(\vec{\sigma}) = \frac{\partial}{\partial T} E(\vec{\sigma}) = \frac{\partial}{\partial T} \int E' \; F(E') \; n(E', \vec{\sigma}) \; \mathrm{d}E' \; . \tag{3.52}$$

The phonon heat capacity is

$$C_{\mathrm{ph}}(\vec{\sigma}) = \frac{\partial}{\partial T} \int E' \; f(E') \; g(E', \vec{\sigma}) \; \mathrm{d}E' \; . \tag{3.53}$$

The total heat capacity in simple non-magnetic alloys is almost entirely attributed to phonons, and to a much lesser extent the electrons. This is due to the relatively small variation of the Fermi-Dirac distribution with temperature (compare Figure 3.3 and Figure 3.12).

3.3.1 Bulk Modulus

Other properties can be determined from equations of state (EOS). For example, the Murnaghan EOS relates the binding energy as a function of volume to the zero pressure bulk modulus B_0, volume V_0, pressure derivative of the bulk modulus B_0', and energy E_0

$$E(V) = E_0 + \frac{B_0 \; V}{B_0'} \left\{ \frac{(V_0/V)^{B_0'}}{B_0' - 1} + 1 \right\} - \frac{B_0 V_0}{B_0' - 1} \; . \tag{3.54}$$

The bulk modulus B is a measure of a material's resistance to uniform compression

$$B = -V\frac{\mathrm{d}P}{\mathrm{d}V} = \frac{1}{K}\,, \tag{3.55}$$

where P is the pressure, V is the volume, and the minus sign accounts for a decrease in the volume with increasing pressure. Often the compressibility K of a material is quoted, which is simply the inverse of the bulk modulus. Typically the zero pressure bulk modulus is given

$$B_0 = -V_0\left.\frac{\mathrm{d}P}{\mathrm{d}V}\right|_{V=V_0} = \frac{1}{K_0}\,. \tag{3.56}$$

Theoretically, the bulk modulus may be determined by calculating $E(V)$ and fitting to an EOS such as that in Equation 3.54. Ab initio calculations are best suited for calculations of ordered structures, so that the cluster inversion method is used for the disordered properties. The results of preliminary calculations on the Fe-Pt system are given here as an example [11]. The $E(V)$ curves in Figure 3.13 were determined using the Vienna Ab initio Simulation Package (VASP) for the ordered structures in Figure 3.5.

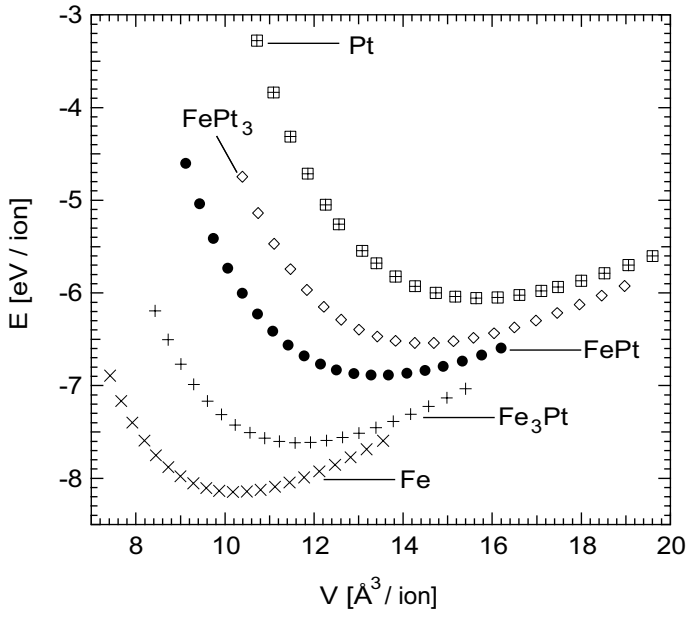

Figure 3.13: E(V) for FCC ordered structures from VASP calculations

VASP can be used to relax the structure and determine the equilibrium volume and energy. As with the DOS, the first step in performing the cluster expansion is to rescale. In this case the volume is rescaled by V_0 to get the reduced volume v and the energy reduced by E_0 to get the reduced energy e so that Equation 3.54 becomes

$$e(v) = -\frac{E(v)}{E_0} = -1 - \frac{B_0\ V_0}{B_0'\ E_0}\ v\left\{\frac{v^{-B_0'}}{B_0' - 1} + 1\right\} + \frac{B_0 V_0}{(B_0' - 1)\, E_0}\ , \tag{3.57}$$

where $v = V/V_0$ and the minus sign ensures that $e(v = 1)$ is the minimum. This allows a cluster expansion to be performed for systems that have a large variation in the equilibrium volume with composition, as is the case for Fe-Pt. The equilibrium bulk modulus is best fit over a few percent change in the equilibrium volume. The $e(v)$ curves are given in Figure 3.14, with the fit parameters given in Table 3.2.

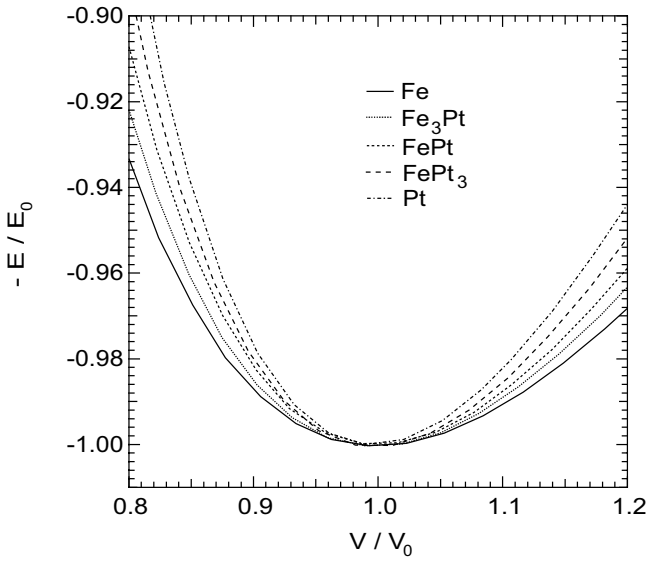

Figure 3.14: Reduced energy versus reduced volume for FCC ordered structures from VASP calculations

From the ordered structures the disordered properties can be determined through the cluster expansion. Here our discussion is focused on disordered $FePt_3$ ($Fe_{25}Pt_{75}$). There are two paths forward for determining the disordered properties. The first is a cluster expansion of $e(v)$ utilizing a cluster expansion for the parameters E_0 and V_0. From the interaction parameters $\mathcal{E}_n^0$ and $\mathcal{V}_n^0$ and

Table 3.2: Fit Parameters of $E(V)$ for FCC Ordered Structures

Formula	Structure	x_{Pt}	V_0 [Å^3/ion]	E_0 [eV/ion]	B_0 [GPa]	B_0'
Fe	FCC	0	10.267	-8.146	272.6	4.47
Fe_3Pt	$L1_2$	0.25	11.695	-7.614	260.2	4.60
FePt	$L1_0$	0.5	13.458	-6.888	237.1	4.37
$FePt_3$	$L1_2$	0.75	14.521	-6.538	239.5	4.91
Pt	FCC	1	15.795	-6.056	241.5	4.78

interaction functions $\varepsilon_n(v)$ (Figure 3.15), the disordered $e(v)$ can be determined and fit to B_0 and B_0'. The second possibility is to simply perform a cluster expansion for all of the parameters. The interaction parameters are presented in Table 3.3. The first method yields values of $B_0 = 239.4$ GPa and $B_0' = 4.15$ and the second method $B_0 = 240.7$ GPa and $B_0' = 4.74$ for $Fe_{25}Pt_{75}$. The values are similar and, considering the difficulty in experimentally determining B_0', it appears that a cluster expansion of only B_0 is valid and can be done with only a few terms.

Table 3.3: Interaction Parameters for Fe-Pt

n	$\mathcal{V}_n^0$ [Å^3/ion]	$\mathcal{E}_n^0$ [eV/ion]	$\mathcal{B}_0$ [GPa]	$\mathcal{B}_0'$
0	13.229	-7.009	245.98	4.59
1	1.399	0.530	-9.05	0.12
2	-0.081	-0.040	3.74	0.05
3	-0.004	-0.002	0.31	-0.01
4	0.008	0.004	-0.24	-0.01

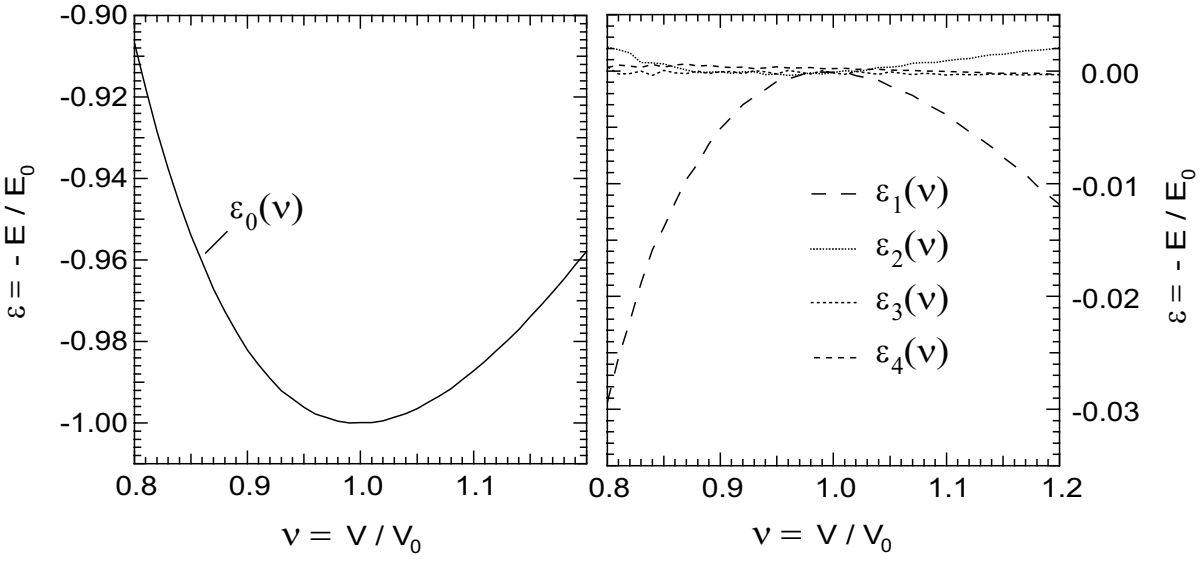

Figure 3.15: Interaction functions $\varepsilon_n(v)$ for reduced energy versus reduced volume for FCC ordered structures of Fe-Pt from VASP calculations. Note the smaller scale for $n > 0$.

3.3.2 Electron-Phonon coupling parameter

Here we provide the specific example of the electron-phonon coupling parameter $\lambda_{\rm ep}$. The strength of the interaction between electrons and phonons, as quantified by the parameter $\lambda_{\rm ep}$, is related to the EDOS at the Fermi level and the average phonon energy. In the McMillan theory of strong-coupled superconductors [12], the electron-phonon coupling constant is

$$\lambda_{\rm ep} = \frac{N(E_F)\ \langle I^2 \rangle}{M \langle \omega^2 \rangle} \tag{3.58}$$

where $N(E_F)$ is the value of the EDOS at the Fermi level E_F, $\langle I^2 \rangle$ is the average over the Fermi surface of the square of the electron-phonon interaction matrix element, M is the nuclear mass, and the average of the square of the phonon frequency $\langle \omega^2 \rangle$ is

$$\langle \omega^2 \rangle = \frac{\int d\omega\ \omega\ \alpha^2(\omega)\ g(\omega)}{\int d\omega\ \alpha^2(\omega)\ g(\omega)/\omega} \tag{3.59}$$

with $\alpha^2(\omega)\ g(\omega)$ the direction-averaged Èliashberg coupling function. Often $\alpha^2(\omega)\ g(\omega)$ is very similar to the DOS $g(\omega)$, so that one can use the experimental $g(\omega)$ to estimate $\langle \omega^2 \rangle$ [13, 14]. It is expected that $\lambda_{\rm ep}$ can be expressed with the cluster expansion using as many terms as necessary for both the DOS and EDOS.

One system that may be of interest is Nb-Mo. Both molybdenum and niobium are BCC and fully miscible as a random solid solution. Furthermore, these elements are superconductors, with critical temperatures of $T_c^{\rm Mo} = 0.915$K and $T_c^{\rm Nb} = 9.25$K. The critical temperature of superconductivity can be estimated from $\lambda_{\rm ep}$ in the McMillan theory by

$$T_c = \frac{\theta_{\rm D}}{1.45} \exp\left[\frac{-1.04(1+\lambda_{ep})}{\lambda_{ep} - \mu^\star(1+0.62\lambda_{ep})}\right] , \tag{3.60}$$

where $\mu^\star$ is the effective Coulomb repulsion potential for the electrons and $\theta_{\rm D}$ is the Debye temperature and represents the average phonon temperature. The Debye temperature for Mo is $\theta_{\rm D}^{\rm Mo} = 380$K and for Nb is $\theta_{\rm D}^{\rm Nb} = 275$K. An empirical approach was taken by McMillan [12] to determine λ_{ep}

in the Nb-Mo system (solid circles in Figure 3.16). These results indicate that a three-term GCE is adequate for characterizing the electron-phonon coupling, where the interaction parameters are $\Lambda_0^{ep} = 0.8588$, $\Lambda_1^{ep} = -1.5863$, and $\Lambda_2^{ep} = 1.1379$. However, the phonon properties were linear interpolations of the two end members. Calculations performed by Sacchetti [15] indicate that a six-term LOCE (seven-term GCE) may be necessary for this system. Interestingly, these calculations indicate that λ_{ep}(Mo) is enhanced in the presence of Nb.

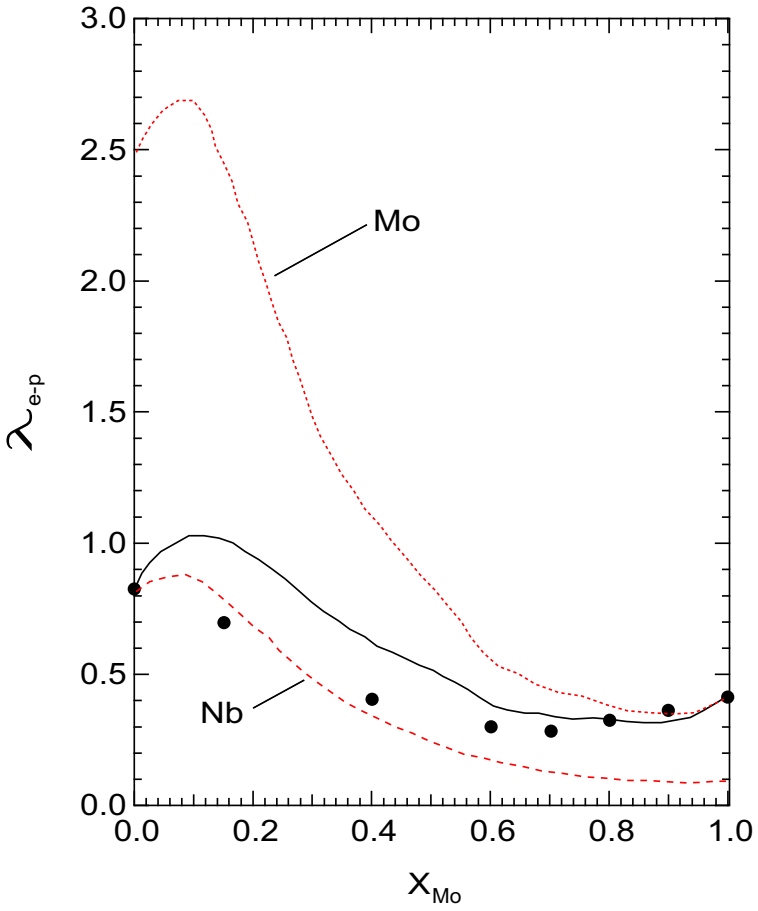

Figure 3.16: Electron-phonon coupling parameter as a function of Mo concentration for Nb-Mo alloys. The solid circles are from an empirical analysis by McMillan. The solid curve is the total λ_{ep} from calculations by Sacchetti. The dashed curves are the partial e-p coupling parameters from these calculations. Figure adapted from Sacchetti [15].

3.4 Random Solid Solution Correlation Function Matrices

A cluster expansion that uses only random solid solution properties to determine the interaction parameters/functions is limited in the number of terms due to the decaying correlation functions of Equation 3.1,

$$\lim_{n\to\infty} \xi_n = \lim_{n\to\infty} (1 - 2x_{\mathrm{B}})^n = 0 \; . \tag{3.61}$$

If a useful cluster expansion can be performed with only a few terms, it is possible to overcome some difficulties associated with using correlation functions from disordered alloys. An even more significant issue is the lack of unique information obtained from cluster functions with larger n—the correlation function basis becomes ill-conditioned with an increasing number of terms. In practice, this means that although the fit to the thermodynamic functions may improve with n, the higher-order interaction parameters may not be determined reliably with experimental data on random solid solutions.

3.4.1 Matrix Condition Number

The condition of the $[\xi_{m,n}]$ matrix can be described in part by the absolute value of the determinant, which is the volume of the figure bounded by the vectors of the matrix. If a matrix is degenerate, e.g., if two of its vectors lie in the same direction, the volume of this figure will be zero, as is its determinant. The other extreme is a matrix whose vectors span the space maximally. Here the volume of this figure and the determinant are maximized.

An upper bound on the determinant of a $\nu \times \nu$ matrix with complex elements restricted to modulus M is known from the Hadamard Maximum Determinant Problem [16]

$$|\mathrm{Det}A| \leq M^{\nu} \nu^{\nu/2} \; . \tag{3.62}$$

Our $\nu \times \nu$ matrix of correlation functions $[\xi_{m,n}]$ has all elements of modulus 1 or less (Equation 3.1). A $(-1, 1)$ matrix—a matrix whose elements lie on the unit sphere—can be constructed for $[\xi_{m,n}]$

only up to $\nu = 2$, however. For $\nu > 2$ the maximum value of the determinant is

$$|\mathrm{Det}A| = M^{\nu} 2^{-\nu} (\nu + 1)^{(\nu+1)/2} \,, \tag{3.63}$$

where M is the largest modulus of the basis vectors. A matrix of correlation functions that satisfies Equation 3.63 spans the space maximally. Our matrix composed of only correlation functions given by Equation 3.1 is a Vandermonde matrix [17]. Its determinant is

$$|\mathrm{Det}V| = \prod_{1 \le i < j \le \nu} (\xi_{1,j} - \xi_{1,i}) \,, \tag{3.64}$$

which was maximized to find the set of alloys that provide an $[\xi_{m,n}]$ matrix that spans the space maximally. The results of this are given in Table 3.4.

Table 3.4: Determination of Disordered Alloys That Maximize the Determinant of $[\xi_{m,n}]$

ν	$\{\xi$ Basis$\}$	$\{x_{\mathrm{A}}\}$
2	$\{-1, 1\}$	$\{1, 0\}$
3	$\{-1, 0, 1\}$	$\{1, 1/2, 0\}$
4	$\{-1, -1/\sqrt{5}, 1/\sqrt{5}, 1\}$	$\{1, 0.72, 0.28, 0\}$
5	$\{-1, -\sqrt{3/7}, 0, \sqrt{3/7}, 1\}$	$\{1, 0.83, 1/2, 0.17, 0\}$
6	$\{-1, -0.77, -0.29, 0.29, 0.77, 1\}$	$\{1, 0.88, 0.64, 0.36, 0.12, 0\}$
7	$\{-1, -0.83, -0.47, 0, 0.47, 0.83, 1\}$	$\{1, 0.92, 0.73, 1/2, 0.27, 0.08, 0\}$

ν	$\lvert\mathrm{Det}V\rvert$	$2^{-\nu}(\nu+1)^{(\nu+1)/2}$	$\nu^{\nu/2}$
2	2	-	2
3	2	2	5.196
4	1.1449	3.494	16
5	0.3665	6.75	55.90
6	0.0643	14.118	216
7	0.0061	32	907.49

Using the determinant as a measure of the condition of the $[\xi_{m,n}]$ matrix simplifies the task of finding the best set of compositions for the disordered alloys. A better measure, however, is the matrix condition number, κ,

$$\kappa(V) = \|V\|_2 \|V^{-1}\|_2 \,. \tag{3.65}$$

Here the double brackets denote the matrix norm and the subscript denotes the use of the 2-norm.

The condition number is a measure of the sensitivity of a matrix to numerical operations. A matrix with a condition number of 1 is perfectly conditioned, whereas an infinite condition number occurs when V is singular [18]. In our linear system we take the matrix entries to have machine precision, which is the maximum possible relative error in representing a number as floating point. The IDOS functions do have an associated error, where error propagation from Equation 3.32 yields

$$\delta\mathcal{G}_n(E) = \left[\sum_{m=0}^{\nu-1} \left(\delta g_m(E)\ [\xi_{m,n}]^{-1}\right)^2\right]^{1/2} . \tag{3.66}$$

The value of κ/ν multiplied by the error bars on the measured disordered alloy DOS provides the upper limit on the error bars for the IDOS functions. Table 3.5 shows κ and the ratio κ/ν corresponding to $[\xi_{m,n}]$ for the disordered alloy compositions presented in Table 3.4.

Table 3.5: Properties of Disordered Alloy Basis Matrix of Table 3.4

ν	κ	κ/ν
2	1	0.5
3	3.22504	$1.075013\bar{3}$
4	6.7837	1.695925
5	17.1128	3.42256
6	38.3611	$6.39351\bar{6}$
7	95.389	13.627

3.4.2 Least-Squares Inversion

The correlation function matrix composed entirely of correlation functions of random solid solutions is a Vandermonde matrix [17], as stated in the previous section. Along with having a simple determinant, this matrix is also used in performing least-squares fittings to polynomials. The correlation functions of random solid solutions are polynomials and are therefore amenable to a least-squares inversion (LSI). The main benefit of performing a LSI is that more data points can be utilized than terms used in the cluster expansion. This is not the case for a direct inversion using the Connolly-Williams technique, which produces a term for each input configuration. This fitting can be performed for ab initio calculations, which provide values of thermodynamic functions without error bars. Unfortunately, disordered structures are difficult to model with computational methods.

This inversion scheme is better suited for measurements, which have error bars associated with each data point.

For k known configurations, the thermodynamic values can be expanded with ν interaction parameters

$$\begin{aligned} J_1 &= \mathcal{J}_0 + \mathcal{J}_1 (1-2x_1) + \mathcal{J}_2 (1-2x_1)^2 + \ldots + \mathcal{J}_{\nu-1} (1-2x_1)^{\nu-1} \\ J_2 &= \mathcal{J}_0 + \mathcal{J}_1 (1-2x_2) + \mathcal{J}_2 (1-2x_2)^2 + \ldots + \mathcal{J}_{\nu-1} (1-2x_2)^{\nu-1} \\ \vdots &= \qquad\qquad\qquad\qquad \vdots \\ J_k &= \mathcal{J}_0 + \mathcal{J}_1 (1-2x_k) + \mathcal{J}_2 (1-2x_k)^2 + \ldots + \mathcal{J}_{\nu-1} (1-2x_k)^{\nu-1} \quad . \end{aligned} \tag{3.67}$$

This can be written in matrix form as

$$\vec{J} = [\xi_{m,n}] \vec{\mathcal{J}} \tag{3.68}$$

where

$$\vec{J} = \left\{ \begin{array}{c} J_1 \\ J_2 \\ \vdots \\ J_k \end{array} \right\} \; , \; [\xi_{m,n}] = \left[\begin{array}{ccccc} 1 & (1-2x_1) & (1-2x_1)^2 & \ldots & (1-2x_1)^{\nu-1} \\ 1 & (1-2x_2) & (1-2x_2)^2 & \ldots & (1-2x_2)^{\nu-1} \\ \vdots & & & \ldots & \vdots \\ 1 & (1-2x_k) & (1-2x_k)^2 & \ldots & (1-2x_k)^{\nu-1} \end{array} \right] \; , \; \vec{\mathcal{J}} = \left\{ \begin{array}{c} \mathcal{J}_0 \\ \mathcal{J}_1 \\ \vdots \\ \mathcal{J}_{\nu-1} \end{array} \right\} \tag{3.69}$$

When $k = \nu - 1$, a direct inversion is performed. However, when $k > \nu - 1$ a least-squares inversion is performed:

$$\vec{\mathcal{J}} = \left([\xi_{m,n}]^{\mathrm{T}} [\xi_{m,n}] \right)^{-1} [\xi_{m,n}]^{\mathrm{T}} \; \vec{J} \, . \tag{3.70}$$

Each data point has an associated error δ. The error-weighting matrix Ω is given by diagonal elements that are inversely proportional to the error bars,

$$\Omega_{mm} = \frac{1}{\delta_m} \, . \tag{3.71}$$

This matrix places more weight on those measurements with better statistics (smaller error bars). The weighted LSI is then

$$\vec{\mathcal{J}} = \left([\xi_{m,n}]^{\mathrm{T}} \ \Omega \ [\xi_{m,n}] \right)^{-1} [\xi_{m,n}]^{\mathrm{T}} \ \Omega \ \vec{J} \, . \tag{3.72}$$

This method also allows for the determination of the number of terms needed to successfully describe a data set. The metric for the goodness of a fit is the reduced χ^2, which is also known as the $\chi^2/\mathrm{N_d}$. Here $\mathrm{N_d} = k - p$ is the number of degrees of freedom, k is the number of data points (in this case the number of alloys measured), and p is the number of parameters in the fitting (in this case the number of terms ν used in the cluster expansion). The expected value of χ^2 is the number of degrees of freedom, so that a good fit should have a reduced χ^2 of approximately 1 ($\chi^2/\mathrm{N_d} \sim 1$). The value of χ^2 is determined from

$$\chi^2 = \sum_{i=1}^{k} \frac{\left[y_i - f(x_i) \right]^2}{\delta_i^2} \, , \tag{3.73}$$

where y_i are the measured values, $f(x_i)$ are the fit values, and δ_i is again the error on the measurements. In the case of the phonon density of states, the fit is performed at each energy (E or $\mathcal{E}$). In this case an average value of χ^2, where the average is performed over E or $\mathcal{E}$, is needed for the fit to the entire DOS

$$\langle \chi^2(E) \rangle = \frac{\sum_{i=1}^{\mathcal{N}} \chi^2(E_i) \ \Delta E}{\sum_{i=1}^{\mathcal{N}} \Delta E} = \frac{1}{E_c^{\max}} \sum_{i=1}^{\mathcal{N}} \chi^2(E_i) \ \Delta E = \frac{1}{\mathcal{N}} \sum_{i=1}^{\mathcal{N}} \chi^2(E_i) \, , \tag{3.74}$$

where ΔE is the experimental step size of the measured DOS (assumed to be constant for the entire data set), $E_c^{\max}$ is the largest value of the cutoff energy for the entire set of DOS curves, and $\mathcal{N}$ is the number of points in the DOS curves ($\mathcal{N} = E_c^{\max}/\Delta E$). Typically we process our data into DOS curves with $\Delta E = 0.5$ meV. In the case of the energy relative to the cutoff

$$\langle \chi^2(\mathcal{E}) \rangle = \frac{\sum_{i=1}^{\mathcal{N}} \chi^2(\mathcal{E}_i) \ \Delta \mathcal{E}}{\sum_{i=1}^{\mathcal{N}} \Delta \mathcal{E}} = \sum_{i=1}^{\mathcal{N}} \chi^2(\mathcal{E}_i) \ \Delta \mathcal{E} \, . \tag{3.75}$$

Here $\mathcal{N} = 1/\Delta\mathcal{E}$ so that the denominator is equal to one.

Chapter 4

Nuclear Resonant Inelastic X-Ray Scattering

4.1 Introduction

This section provides a very short and basic overview of the Nuclear Resonant Inelastic X-ray Scattering (NRIXS) technique. This technique is not simple to understand and a full explanation is beyond the scope of this chapter. There are a number of excellent monographs, papers, and thesis chapters in the literature for this technique and those related to it (Mössbauer spectroscopy and Nuclear Forward Scattering (NFS)). *An Introduction to Mössbauer Spectroscopy* [19] is an excellent starting point for the beginner. *Nuclear Condensed Matter Physics Using Synchrotron Radiation* [20] describes the details of the NFS and NRIXS techniques, including both experimental and theoretical aspects. There are a number of articles describing the experimental details [21, 22], theoretical aspects [23, 24], data analysis techniques [25, 26], and general aspects [27, 28, 29, 30, 31, 32, 33, 34] of NRIXS and related techniques.

4.1.1 NRIXS

Modern synchrotrons, such as the Advanced Photon Source, offer high spectral brilliance radiation and a time structure. These two features give rise to the possibility of NRIXS and NFS, which are Mössbauer experiments performed in the time-domain. NRIXS is incoherent inelastic γ-ray

scattering and NFS is coherent elastic Mössbauer spectroscopy[1]. In its most basic terms NRIXS is similar to a Mössbauer experiment where the radioactive source is replaced by synchrotron radiation, the energy is scanned over meV rather than neV, the detector must discriminate in the time-domain (rather than energy), and the recoil energy is what is under investigation[2]. The aim of the following paragraphs is to elucidate the above statements.

Figure 4.1 shows the decay processes of the excited state of a ^{57}Fe atom. The incident γ-ray must have exactly the right amount of energy to excite the nucleus. A deviation on the order of neV will not allow the gamma ray to be absorbed. If a ^{57}Fe nucleus in a crystal were momentarily bombarded with a large spectrum of γ-ray energies, the nucleus would be excited regardless of its vibrational state. If the pulse were short, on the order of a few nanoseconds (ns), then the decay product could be measured (the half-life of the excited state is 97.8 ns). This is because the nuclear excited state is long-lived compared to any electronic state that may have been excited during the initial pulse (Figure 4.2). The most efficient detection method for the delayed scattering is with an avalanche photodiode (APD). The APD has a very good time resolution (on the order of 1 ns for a 10×10 mm^2 area silicon APD [30]).

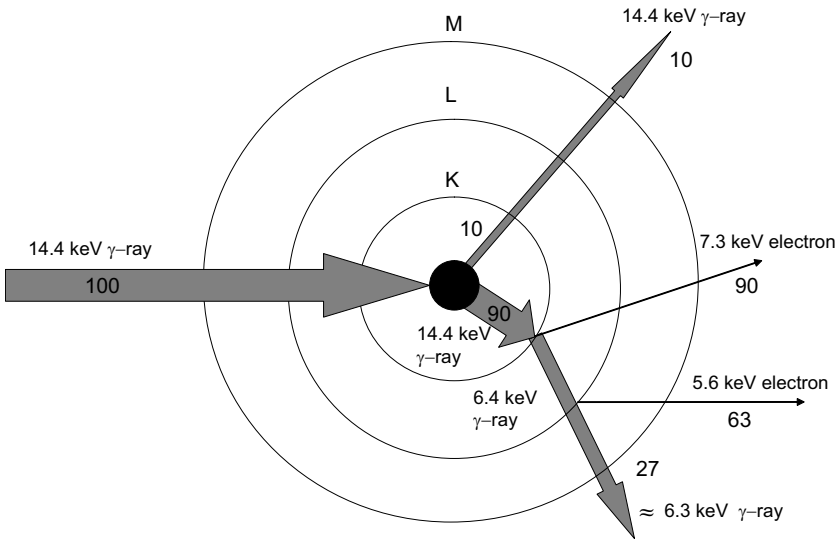

Figure 4.1: Decay processes of ^{57}Fe nuclear excited state. Most of the 14.4 keV γ-rays are converted to high energy electrons in the K and L electronic shell. Figure adapted from [35].

[1]NFS is interesting because it involves a nuclear exciton. The existence of coherent scattering requires that the γ-ray interact with the entire ensemble of ^{57}Fe nuclei. However, this topic is beyond the scope of the current thesis.

[2]Mössbauer spectroscopy is recoilless whereas the recoil energy is measured with NRIXS.

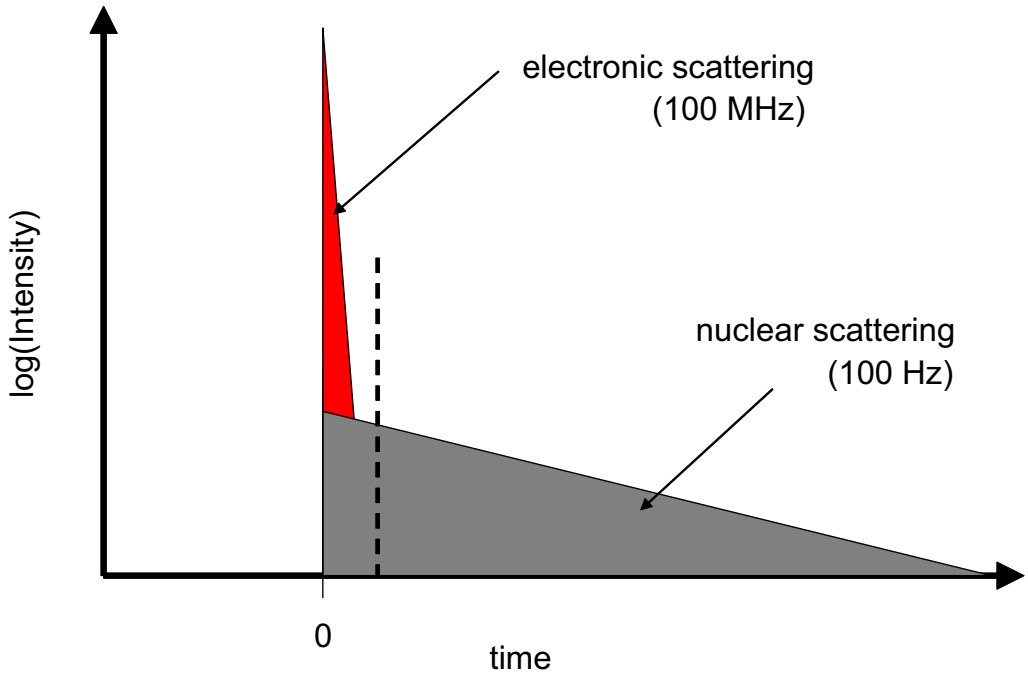

Figure 4.2: Scattered intensity versus time. The zero indicates the initial synchrotron pulse. Above the dashed line all of the counts are from decay of the nuclear excited state. Figure adopted from W. Sturhahn [30].

Next consider the case where a large number of ^{57}Fe nuclei are momentarily bombarded by γ-rays with a bandwidth of 1 meV and an energy 20 meV greater than the resonance energy. In order for a nucleus to absorb a γ-ray, the extra 20 meV of energy must also be absorbed by the nucleus. Quantum mechanically, this is possible if the nucleus creates a phonon or phonons that match this energy. Similarly, if the energy of the γ-rays is 20 meV lower than the resonance energy, a phonon (or phonons) must be annihilated for a ^{57}Fe nucleus to absorb the photon. At low temperatures there is more phonon creation than annihilation, so we would expect more delayed counts for $E_{\rm trans} = E_\gamma - E_{\rm res} = +20$ meV than $E_{\rm trans} = -20$ meV. Performing a scan in energy gives the intensity as a function of the energy transfered to the sample $E_{\rm trans}$. For pure Fe at various temperatures this is shown in Figure 4.3. The 21 K data most closely resembles the DOS for pure Fe. Note the increasing phonon annihilation with temperature. BCC Fe has a cutoff of $\sim$ 40 meV, so that the counts greater than this correspond to multiple phonons interacting with the γ-ray. This data was recently taken at beamline 16ID-D at the Advanced Photon Source (APS) at the Argonne National Laboratory (ANL) using a furnace custom built by the author.

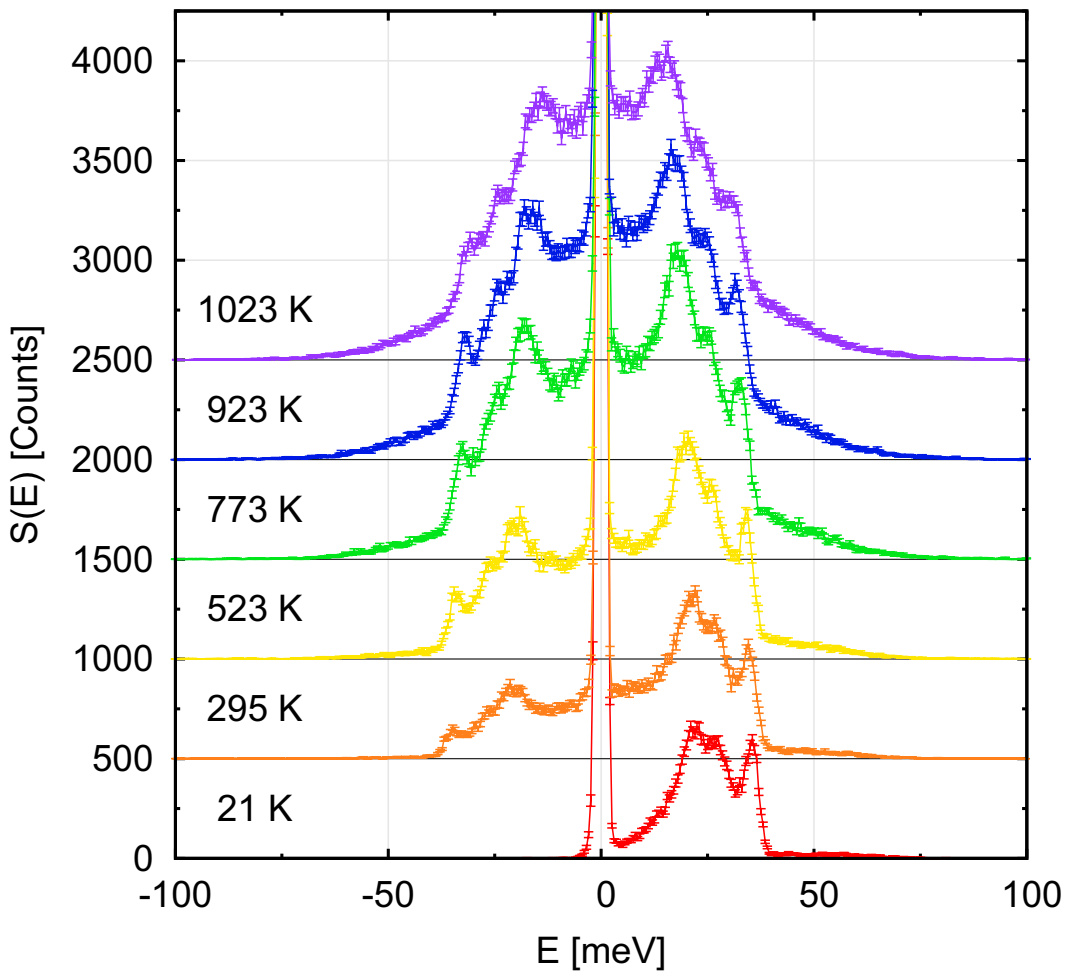

Figure 4.3: Scattering as a function of energy transferred to the sample for pure ^{57}Fe as a function of temperature. Phonon annihilation corresponds to $E < 0$ and phonon creation $E > 0$. The intense elastic peak ($E = 0$) is cut short. Curves are offset by integer multiples of 500 counts.

It is necessary to note that the results presented in Figure 4.3 are for the DOS of pure ^{57}Fe. If the ^{57}Fe were alloyed with another element, the measurement would yield the projection of the DOS onto the motions of ^{57}Fe atoms, otherwise known as the phonon partial density of states (PDOS). In the following sections we present results of compositional effects on the ^{57}Fe PDOS. These effects are analyzed within the formalism of the cluster expansion.

4.2 Fe-Cr

4.2.1 Introduction

The Fe-Cr system was selected for experimental study in part due to previous inelastic neutron scattering studies of phonons in Fe-Cr alloys [36, 37, 38, 8], and more importantly they were planned to complement previous measurements of the ^{57}Fe phonon partial density of states (PDOS) curves by Ruckert et al. on monolayers of ^{57}Fe in epitaxial FeCr multilayers [39]. The present experiment investigates the projection of the phonon density of states onto the motions of ^{57}Fe atoms in disordered BCC solid solutions of Fe-Cr. The Fe-Cr disordered solid solutions and thin films have similar lattice parameters (BCC Fe and Cr have lattice parameters of 2.87 and 2.88 Å, respectively). This helps reduce volume effects, simplifying the interpretations of changes in the PDOS in terms of the local chemical order.

After explaining experimental details of the BCC ^{57}Fe-Cr samples and the results of the NRIXS measurements, we extract the interaction functions for the PDOS curves. These IPDOS functions, obtained from the present NRIXS data and measurements on BCC ^{57}Fe-Cr alloys by Ruckert et al., are then used to reconstruct the PDOS functions from multilayered thin films [39]. The PDOS functions of the multilayered samples are reproduced surprisingly well using clusters up to the triangle, and up to second-nearest-neighbor distances from ^{57}Fe atoms.

4.2.2 Experimental Methods

Alloys of $Fe_{1-x}Cr_x$ for $x_{Cr} = \{0.70,0.47,0.30\}$ were prepared by arc-melting under an argon atmosphere using 99.99% Fe and 99.995% Cr. The alloys of composition $x_{Cr} = \{0.47,0.30\}$ were enriched to contain approximately 13 at.% of the ^{57}Fe isotope. The alloy of composition $Fe_{30}Cr_{70}$ was not enriched and therefore contained approximately 0.6 at.% of the ^{57}Fe isotope. There was negligible mass loss and minimal surface oxidation after melting, so the compositions are expected to be accurate to 0.1 at.%. The samples with $x_{Cr} = \{0.47,0.30\}$ were cold-rolled to final thickness, sealed in a quartz tube under an argon atmosphere, then annealed at 1100°C for 72 h. The brittle ingot

of $Fe_{30}Cr_{70}$ was sealed in a quartz tube under an argon atmosphere, annealed at 1100°C for several hours, sectioned with a diamond saw, sanded to a thickness of 70 microns, and stress-relieved at 400°C. X-ray diffraction patterns were measured on all samples both before and after the heat treatments. The patterns showed diffraction peaks from only the BCC phase. There was no evidence of sigma phase or oxide.

Transmission Mössbauer spectrometry was performed on all samples at room temperature with a conventional constant acceleration spectrometer, using a source of 75 mCi of ^{57}Co in Rh. Mössbauer spectrometry has been used extensively to characterize BCC Fe-Cr alloys and the sigma phase compound [8, 40, 41, 42, 43, 44]. The ^{57}Fe atom serves as a probe of its local environment, detecting the presence of Cr atoms in its first and second coordination spheres. The Mössbauer spectra of Figure 4.4 are typical of those of disordered solid solutions [41, 42, 43, 44]. The broadened magnetic sextets are expected for the high Cr concentrations in these alloys. No paramagnetic peak is detected in the center of the spectra from $Fe_{30}Cr_{70}$ or $Fe_{53}Cr_{47}$ that could indicate the presence of Fe atoms in Cr-rich regions caused by spinodal decomposition [8]. The high ^{57}Fe content in the two enriched samples contributes an unfortunate saturation distortion to the spectrum, however.

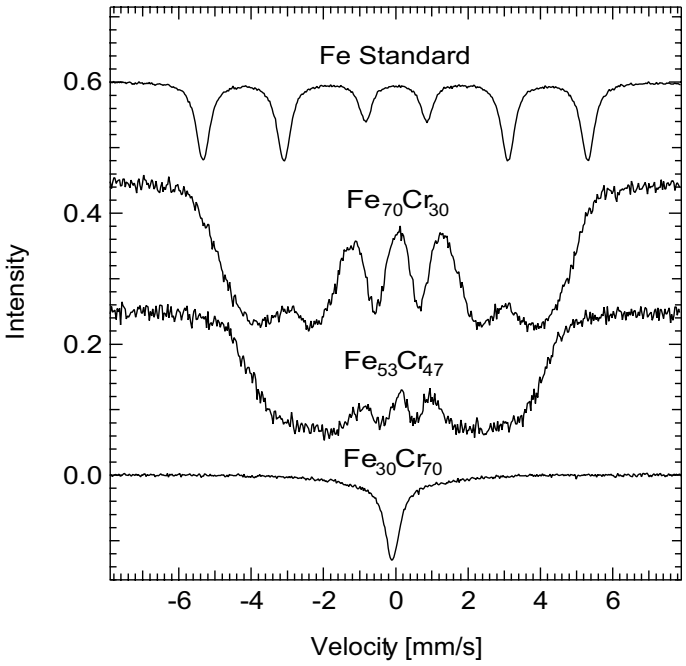

Figure 4.4: Conventional room temperature Mössbauer spectra of the BCC Fe-Cr alloys

Nuclear resonant inelastic X-ray scattering (NRIXS)[45, 46, 28] was performed on all of the alloys at hutch 16-IDD at the Advanced Photon Source (APS) at the Argonne National Laboratory (ANL). Each sample was placed at a grazing angle to the incident photon beam. The incident photon energy was tuned to 14.413 keV, the nuclear resonance energy of ^{57}Fe. The delayed signal was measured from a single avalanche photodiode positioned 90° from the direction of the beam. Data were collected in scans of incident photon energy from –80 to +80 meV from the resonant energy, with a monochromator resolution of 2.2 meV. The $Fe_{30}Cr_{70}$, $Fe_{53}Cr_{47}$, and $Fe_{70}Cr_{30}$ samples were measured for 12 hours, 5 hours, and 17 hours, respectively.

4.2.3 Experimental Results

The NRIXS spectra are shown in Figure 4.5. The error bars are consistent with differences in ^{57}Fe enrichment and measuring times. The intense elastic peak at $E = 0$ extends well off the figure. Nuclear scattering with phonon creation contributes to the intensity to the right of the elastic peak; phonon annihilation processes contribute to the intensity at left. The raw scattering data were summed and analyzed using the program PHOENIX [26], which performs all of the calculations necessary to determine the ^{57}Fe partial phonon DOS, including removal of the elastic peak and multiphonon corrections. The ^{57}Fe PDOS curves for the three alloys measured in this experiment and those from Ruckert et al. [39] are shown in Figure 4.6.

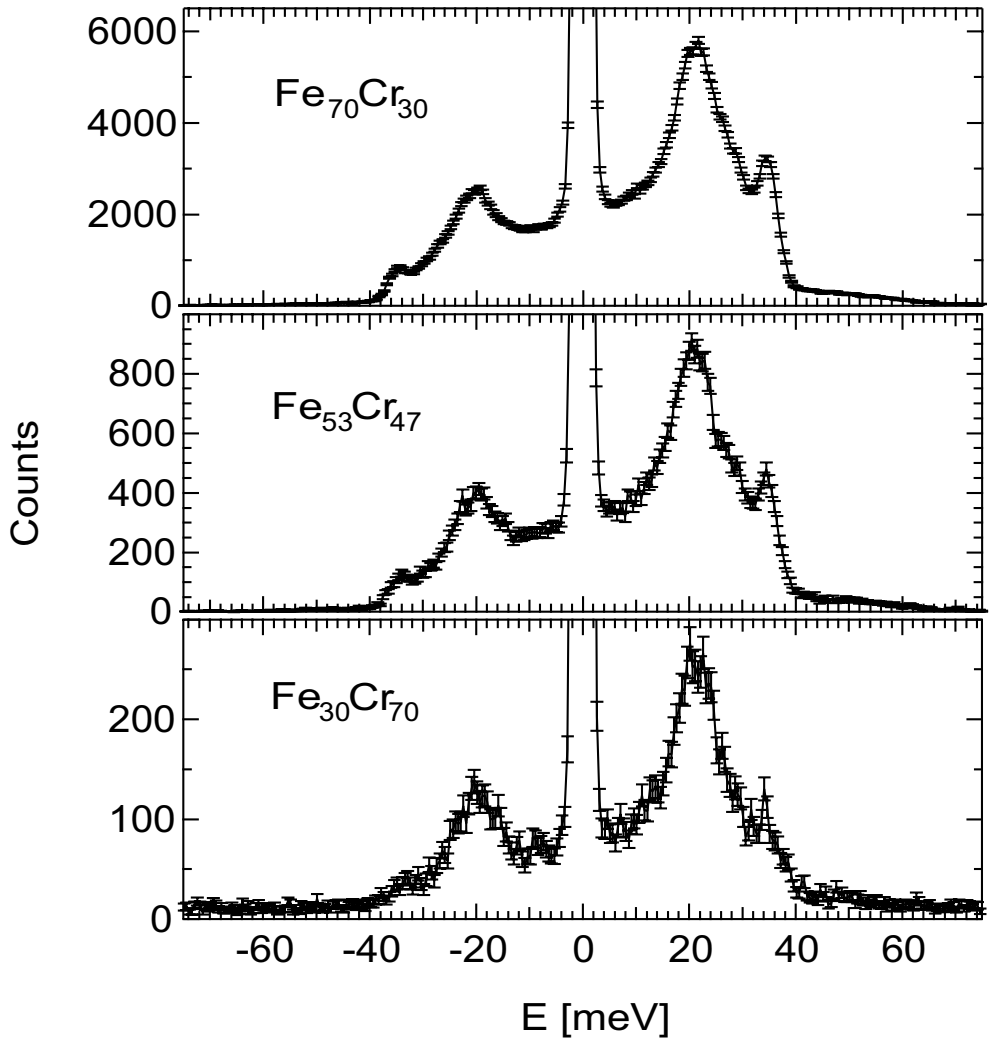

Figure 4.5: Measured NRIXS spectra acquired from the three BCC Fe-Cr samples at room temperature

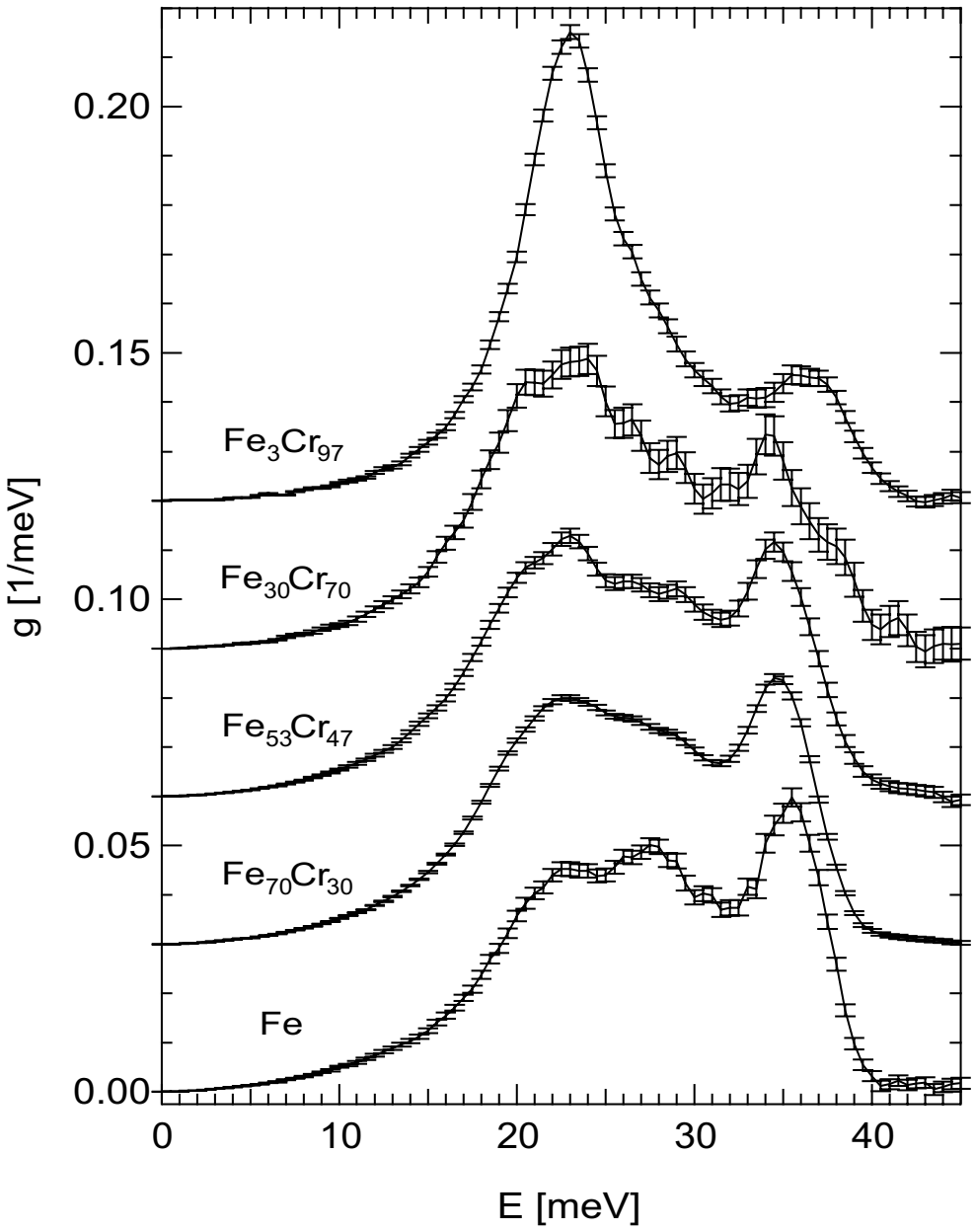

Figure 4.6: ^{57}Fe PDOS curves for the BCC Fe-Cr alloys measured with NRIXS. The alloy Fe_3Cr_{97} and pure Fe come from the results of Ruckert et al. [39].

4.2.4 IPDOS: Direct Inversion

The value of κ/ν_l (where κ is the condition number, Equation 3.65, of the correlation function matrix $\xi_{m,n}$ and ν_l is the number of terms used in the local order cluster expansion) multiplied by the error bars on the measured alloy PDOS provides the upper limit on the error bars for the IPDOS functions determined from a direct inversion. Table 4.1 shows the alloy compositions that were used in this experiment, along with the determinant and the ratio κ/ν_l of the corresponding $\xi_{m,n}$ matrix. The PDOS of all the Fe-Cr alloys is shown in Figure 4.6

Table 4.1: Properties of Fe-Cr Alloy Basis Matrix

ν_l	$\{x_{\mathrm{Cr}}\}$	$\lvert \mathrm{Det}V \rvert$	κ/ν_l
2	$\{0.97, 0\}$	1.94	0.505
3	$\{0.97, 0.47, 0\}$	1.82	1.10
4	$\{0.97, 0.70, 0.30, 0\}$	0.94	1.87
5	$\{0.97, 0.70, 0.47, 0.30, 0\}$	0.14	6.97

The interaction phonon partial density of states (IPDOS) functions $\mathcal{G}_n(E, \mathrm{Fe})$ up to the triangle term, determined using the alloy sets in Table 4.1, are shown in Figure 4.7 with increasing number of terms, ν_l. These were calculated from a direct inversion using Equation 3.32. The functions through the triangle interaction, $\mathcal{G}_2(E, \mathrm{Fe})$, keep a consistent shape with increasing ν_l, although the triangle function has some change in shape for $\nu_l = 5$. The error bars increase in size as ν increases in a manner that is consistent with the ratio κ/ν_l given in Table 4.1.

4.2.5 Local Order Effects in Fe-Cr

The contribution to the ^{57}Fe PDOS for each of the terms in the cluster expansion for $\nu_l = 3$ using the alloys $x_{Cr} = \{0, 0.47, 0.97\}$ is shown explicitly in Figure 4.7. Each of the IPDOS functions can interpreted as follows. The $n = 0$ term is the ^{57}Fe PDOS of a random solid solution of $Fe_{50}Cr_{50}$. The $n = 1$ term shows the effect on the PDOS of having different numbers of Fe and Cr atoms in the 1NN and 2NN shells of the ^{57}Fe atom. The triangle term, $n = 2$, shows the effect of having like and unlike pairs of atoms within the 1NN and 2NN shells of the ^{57}Fe atom. The function $\mathcal{G}_1(E, \mathrm{Fe})$ is added to the PDOS when the atom in the 1NN and 2NN shell of the ^{57}Fe atom is Fe,

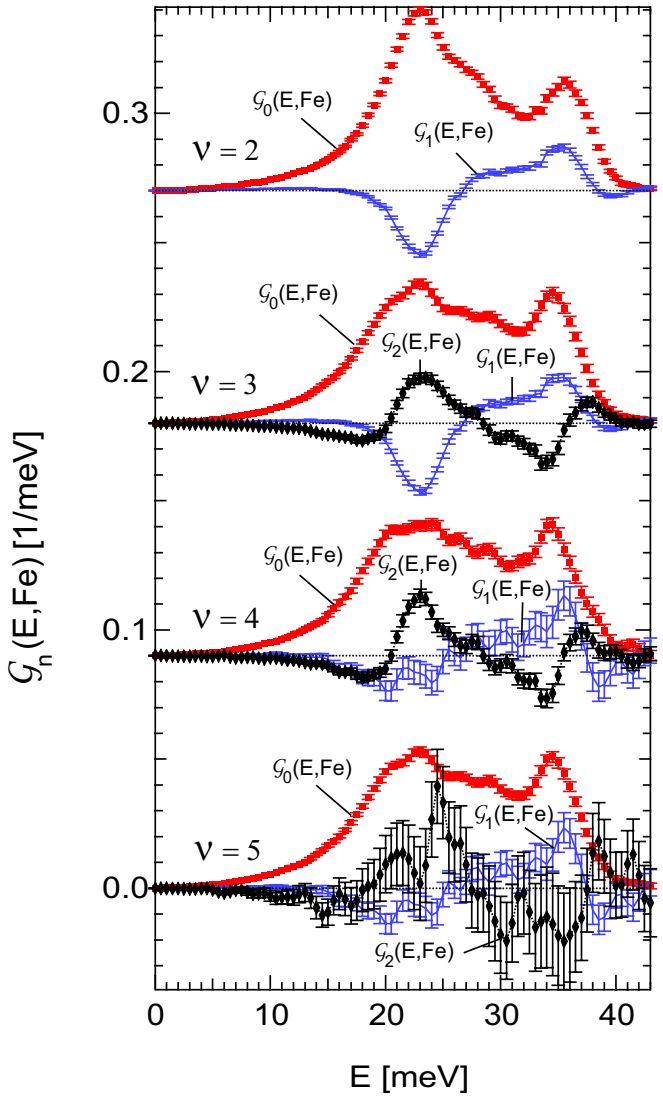

Figure 4.7: Interaction phonon partial density of states functions from direct inversions of the disordered alloys, showing changes with the number of terms

and subtracted when it is Cr. The effect of Fe atoms in the 1NN and 2NN shell of the ^{57}Fe atom is therefore to decrease the number of low-energy modes and increase the number of high-energy modes, whereas Cr does the opposite. The function $\mathcal{G}_2(E, \mathrm{Fe})$ is added when a pair in the 1NN or 2NN shell of the ^{57}Fe atom is composed of two of the same atoms. Like pairs increase the number of low-energy modes while decreasing the number of high-energy modes, whereas unlike pairs do the opposite. These statements about the effects of local atomic order on the PDOS were made possible by the cluster expansion analysis. For Fe-Cr, these are the largest effects of local atomic order on the partial phonon DOS.

4.2.6 IPDOS: Least-Squares Inversion

The least squares inversion of the PDOS curves provides a method for determining the number of terms needed to accurately describe the phonon properties in Fe-Cr. Unlike the direct inversion, which uses the information from specific alloys to construct the IPDOS functions, the LSI uses all of the PDOS curves in the analysis. The IPDOS functions from the LSI in E are given in Figure 4.8a and in $\mathcal{E}$ in Figure 4.8b, with the results of the fitting in Table 4.2. The $\chi^2(E)/\mathrm{N_d}$ is plotted in Figure 4.9. The fit in E is poor for the lowest energy modes and the modes in the energy range 20 to 26 meV. The two fits (in E and $\mathcal{E}$) are very similar due to the weak dependence of the cutoff energy with chemical arrangement. For the Fe-Cr system a three- or four-term local order cluster expansion is suitable for the phonon properties of the Fe atoms.

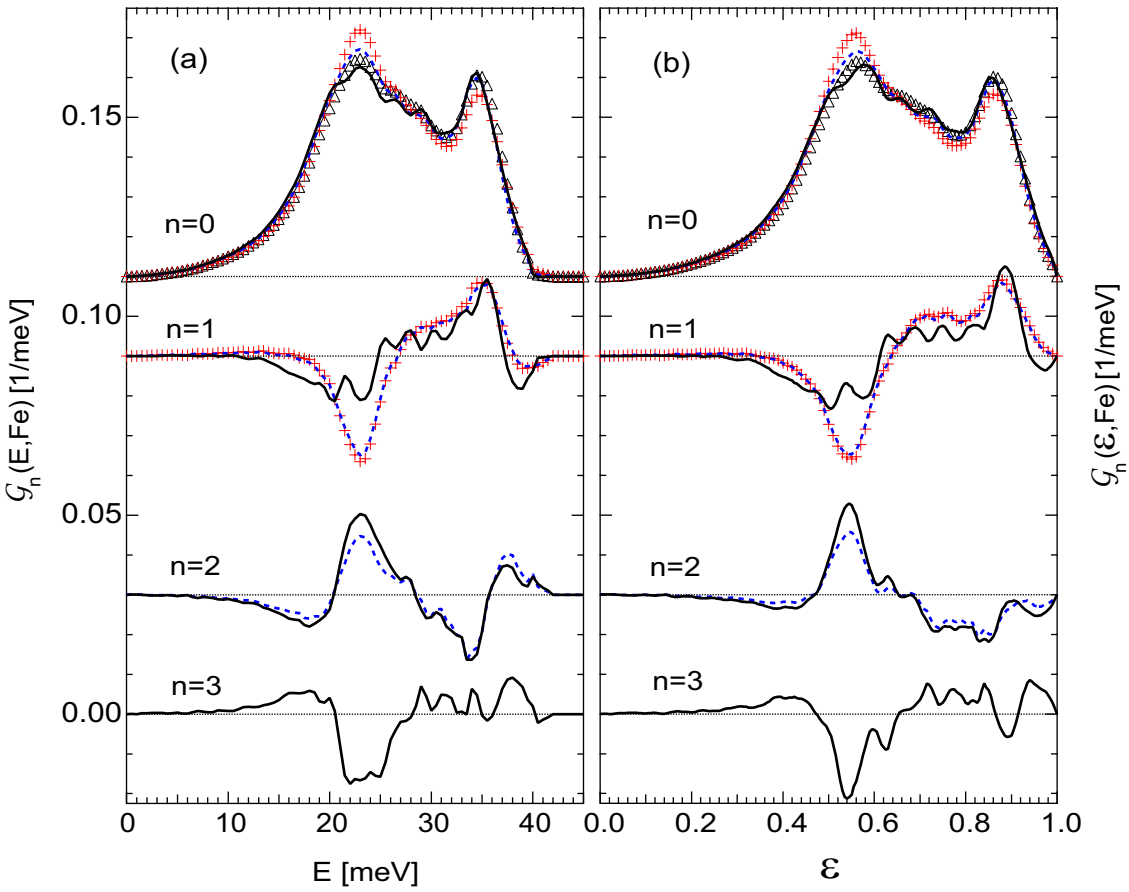

Figure 4.8: Interaction phonon partial density of states functions from cluster expansions of the disordered alloys using least-squares analysis. The number of terms used in the expansion are $\nu_l = 1$ (open triangles), $\nu_l = 2$ (crosses), $\nu_l = 3$ (dashed lines), and $\nu_l = 4$ (solid lines).

Table 4.2: $\langle\chi^2\rangle/\mathrm{N_d}$ for Fits

ν_l	$\langle\chi^2(E)\rangle/\mathrm{N_d}$	$\langle\chi^2(\mathcal{E})\rangle/\mathrm{N_d}$
1	39.10	42.31
2	13.52	12.53
3	2.83	2.79
4	0.68	0.74

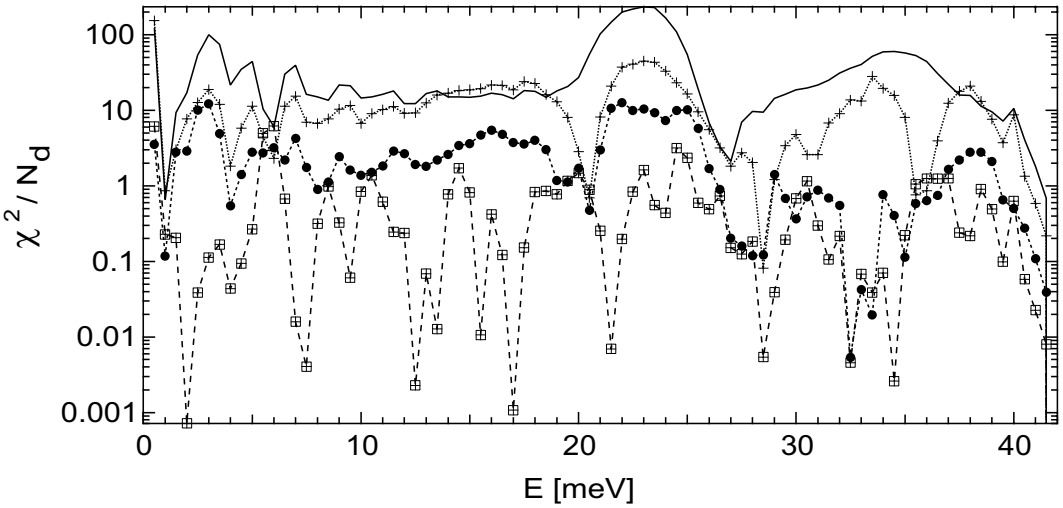

Figure 4.9: $\chi^2/\mathrm{N_d}$ as a function of energy for the fits where the number of terms used in the expansion are $\nu_l = 1$ (solid line), $\nu_l = 2$ (crosses), $\nu_l = 3$ (filled circles), and $\nu_l = 4$ (squares with crosses). The fit in $\mathcal{E}$ is similar.

4.2.7 Application of Local Cluster Expansion to Thin Films

Ruckert et al., prepared thin-film multilayer samples by molecular-beam epitaxy, using layers of ^{56}Fe, ^{57}Fe, and Cr in different orders on the (001) plane, as shown in Figure 4.10 [39]. Spectra from these samples give a unique opportunity for testing: 1) if the cluster parameters obtained from disordered alloys are transferable to a very different type of chemical structure, and 2) the range of effective cluster interactions that are needed for describing the phonon DOS in Fe-Cr. Only the PDOS of the ^{57}Fe atoms at the interface of the Fe and/or Cr layers were measured in the NRIXS experiments of Ruckert et al. For example, the thin-film sample FeCr1 depicted in Figure 4.10 has the active layer of ^{57}Fe separated from the Cr layers by 4 layers of ^{56}Fe. The FeCr1 ^{57}Fe partial phonon DOS is almost identical to that of pure BCC Fe, showing that the local atomic environment information needed to describe its phonon properties is of shorter range than the distance to the Cr layer.

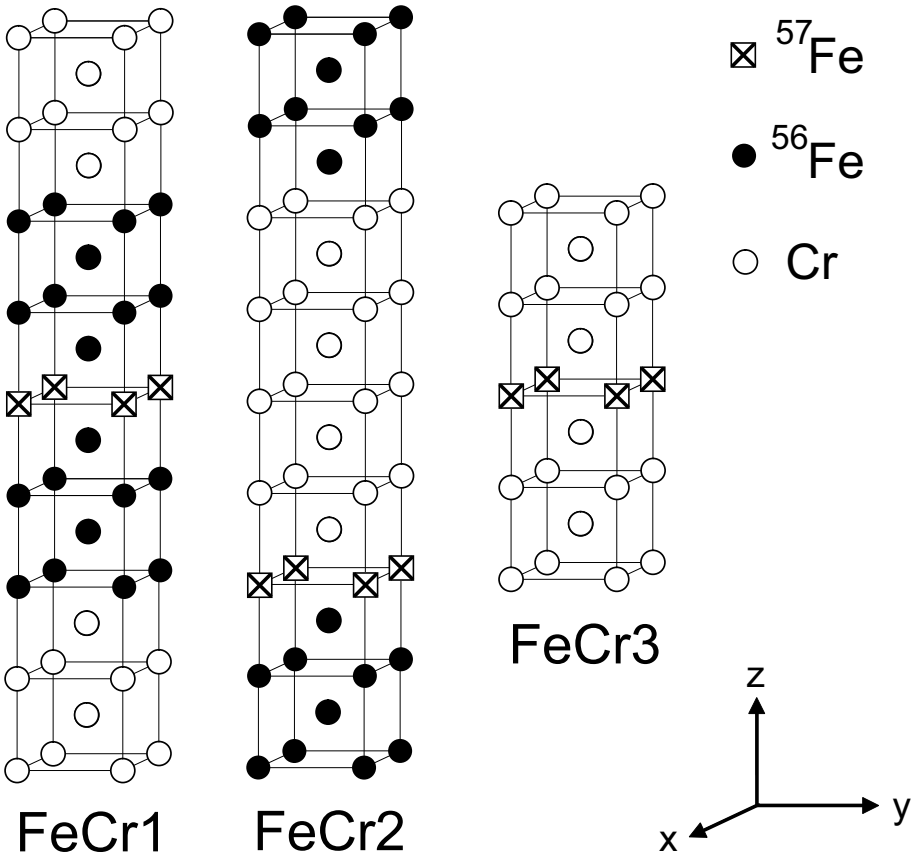

Figure 4.10: Superstructure of thin-film samples of Ruckert et al. [39]. From left to right: FeCr1, FeCr2, FeCr3. Empty circles are Cr, filled circles ^{56}Fe, and squares with an "x" inside are ^{57}Fe.

The correlation functions of the multilayers were determined using the ^{57}Fe local structure shown in Figure 4.10. The 1NN and 2NN distances are similar in the BCC structure and therefore the 1NN and 2NN atoms were both used when determining the correlation functions of the pair and triangle terms. When determining the triangle term, only clusters containing at least one 1NN pair from the ^{57}Fe atom were included, because a triangle cluster consisting of two 2NN pairs extending from the ^{57}Fe atom would include a 3NN pair as the hypotenuse. The specific pair and triangle clusters used are shown in Figure 4.11 along with the tetrahedron cluster.

Figure 4.12 shows the ^{57}Fe PDOS curves of the thin-film multilayers obtained using the IPDOS functions from a three-term direct inversion of the disordered alloys (see Figure 4.7) and the correlation functions given in Table 4.3. The correlation functions of the alloys measured in this experiment are also provided for comparison. The experimental ^{57}Fe PDOS curves vary significantly for the

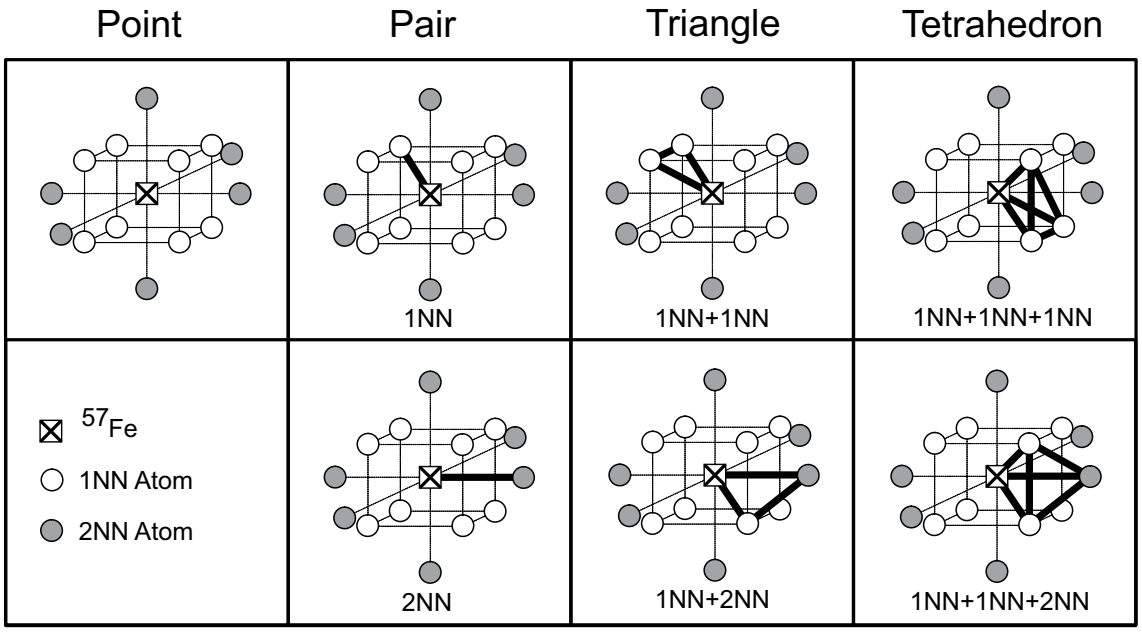

Figure 4.11: Clusters used to describe the phonon partial density of states curves of the ^{57}Fe atoms at the interface of the thin-film multilayer samples. The 1NN and 2NN pair and triangle clusters are shown, and are taken to be equivalent in the analysis.

Table 4.3: Correlation Functions of Thin Films and Alloys

Sample	ξ_0	ξ_1	ξ_2	ξ_3
FeCr2	1	2/7	1/3	0
FeCr3	1	-3/7	1/9	-1/3
$Fe_{70}Cr_{30}$	1	0.4	0.16	0.064
$Fe_{53}Cr_{47}$	1	0.06	0.0036	0.000216
$Fe_{30}Cr_{70}$	1	-0.4	0.16	-0.064

different Fe-Cr alloys and structures (Figures 4.6 and 4.12), and the atomic structures of the disordered solid solutions and the multilayer thin films are substantially different. We therefore consider the calculated curves in Figure 4.12 to be remarkably successful.

It is evident from Table 4.3 that the local order ^{57}Fe correlation functions of the FeCr3 multilayer and the $Fe_{30}Cr_{70}$ disordered solid solution are almost equal. Also, the correlation functions of the FeCr2 multilayer are both slightly greater than those of the $Fe_{53}Cr_{47}$ disordered solid solution. This provides an opportunity to test the cluster expansion without having to perform a matrix inversion. Figure 4.13 shows that the ^{57}Fe partial phonon DOS are very similar for samples with similar correlation functions. This provides strong evidence that the DOS are functions of the local chemical environment, as the thin-film multilayers and disordered alloys have quite dissimilar

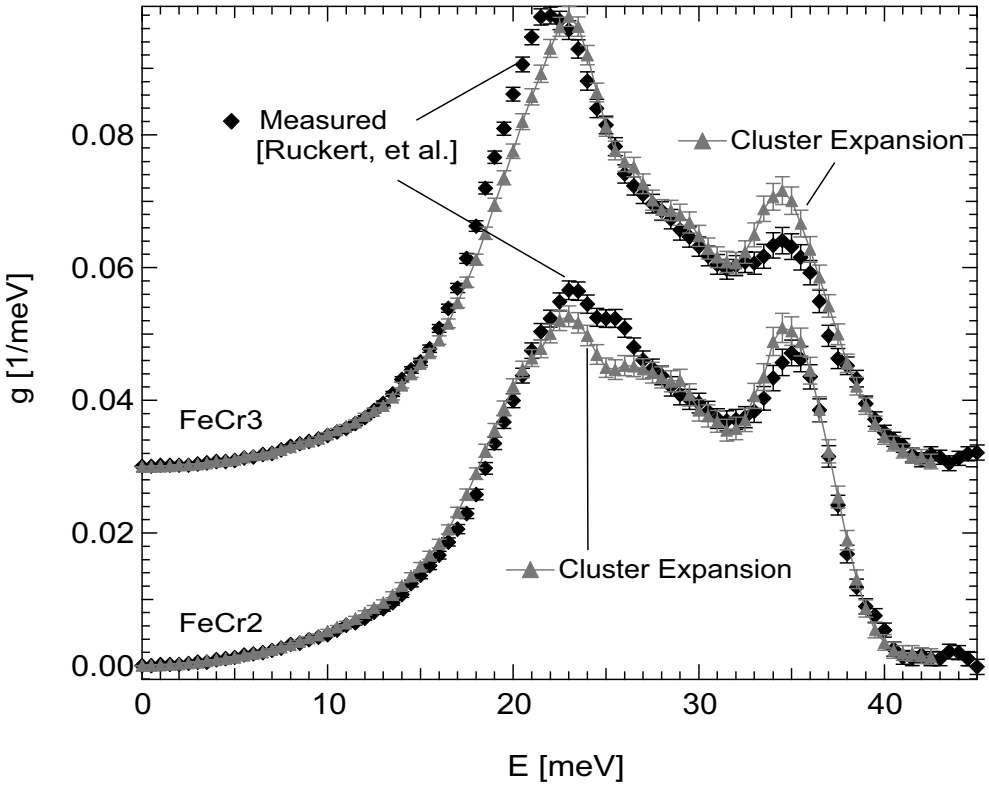

Figure 4.12: Phonon partial density of states curves of the thin-film multilayers, and functions calculated from correlation functions from disordered alloys using a three-term expansion.

long-range order.

The Fe-Cr system was well suited for identifying effects of local chemical order on phonons. We expect this method to work as well or better for fully ordered samples that are BCC and maintain the same lattice parameter for the different phases. In systems that are fully miscible in the BCC phase, such as CrV, perhaps only the DOS curves of the end members and the equiatomic alloy are needed to account for the main trends of the vibrational properties for all of the alloy concentrations.

4.2.8 Conclusion

Phonon partial density of states (PDOS) curves for ^{57}Fe atoms were measured by nuclear resonant inelastic X-ray scattering for disordered BCC Fe-Cr alloys. The IPDOS functions up to the triangle cluster in the local order cluster expansion were used to successfully reconstruct the ^{57}Fe partial phonon DOS functions measured by Ruckert et al., on Fe/Cr multilayers prepared by molecular

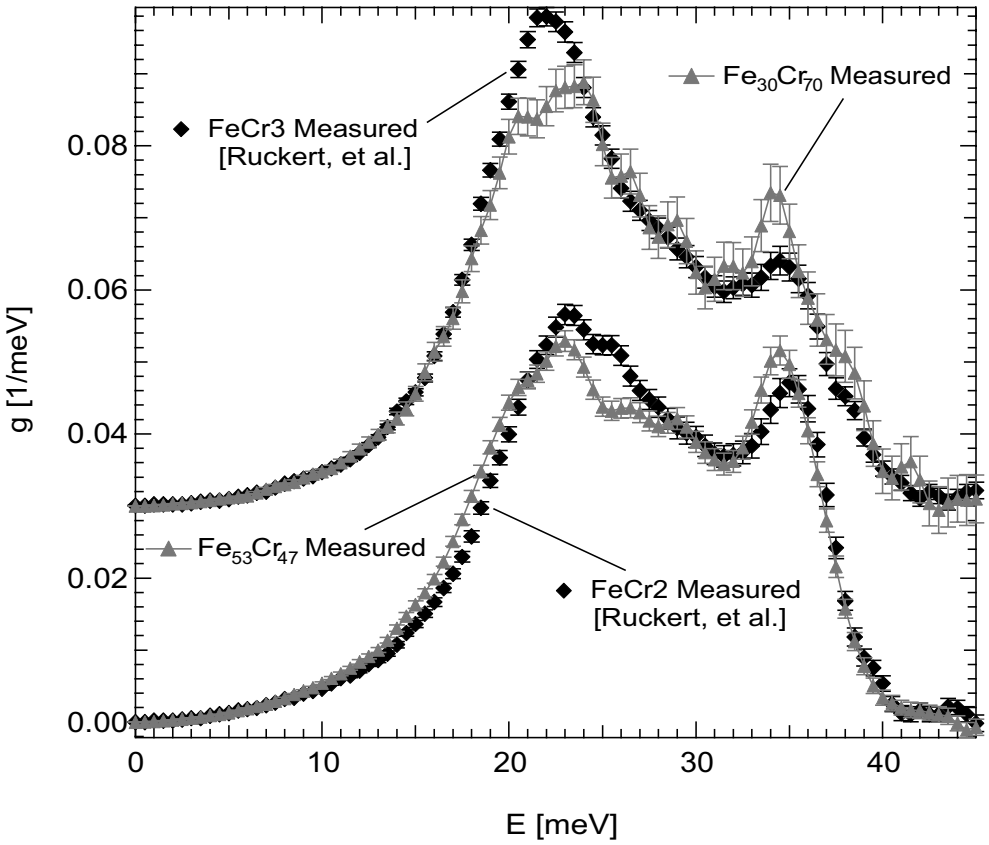

Figure 4.13: Partial phonon DOS curves of the thin-film multilayers compared to the disordered solid solution with the most similar local order ^{57}Fe correlation functions.

beam epitaxy. This success indicates that the interaction functions are transferable to different chemical arrangements of Fe and Cr on the BCC lattice, and the main trends in phonon entropy of the Fe-Cr system can be accounted for with relatively small clusters.

4.3 3d Series ^{57}Fe PDOS

The usefulness of the cluster expansion for Fe-Cr alloys prompts the question of whether or not the same analysis can be done on other systems. The Fultz group was awarded a week of time on beamline 16ID-D at the APS, which was utilized to perform measurements on ^{57}Fe alloyed with various elements. Several systems in the 3d series were chosen as candidates due to relatively large phase fields of BCC or FCC stability. Fe-V was the first system chosen due to the similarity of its phase diagram to that of Fe-Cr. Also measured was the Fe-Co system. The Fe-Co phase diagram has ~ 70 at.% stability of the BCC random solid solution.

21 $^2D_{3/2}$	22 $^3F_2$	23 $^4F_{3/2}$	24 $^7S_3$	25 $^6S_{5/2}$	26 $^5D_4$	27 $^4F_{9/2}$	28 $^3F_4$	29 $^2S_{1/2}$	30 $^1S_0$
Sc	**Ti**	**V**	**Cr**	**Mn**	**Fe**	**Co**	**Ni**	**Cu**	**Zn**
Scandium	Titanium	Vanadium	Chromium	Manganese	Iron	Cobalt	Nickel	Copper	Zinc
44.955910	47.867	50.9415	51.9961	54.938049	55.845	58.933200	58.6934	63.546	65.409
$[Ar]3d4s^2$	$[Ar]3d^24s^2$	$[Ar]3d^34s^2$	$[Ar]3d^54s$	$[Ar]3d^54s^2$	$[Ar]3d^64s^2$	$[Ar]3d^74s^2$	$[Ar]3d^84s^2$	$[Ar]3d^{10}4s$	$[Ar]3d^{10}4s^2$
6.5615	6.8281	6.7462	6.7665	7.4340	7.9024	7.8810	7.6398	7.7264	9.3942

Figure 4.14: Section of periodic table showing the 3d elements

The Fe-Co system also has the benefit of a stable ordered phase. This provides a further test of application of the cluster expansion to the ^{57}Fe PDOS. There are other systems outside of the 3d BCC series that would prove interesting to study. The Fe-Pt and Fe-Pd systems have stable ordered phases similar to those found in Cu-Au. Fe-Ni and Fe-Au offer a large range of FCC stability. Fe-Ru and Fe-Os have a large range of HCP phase stability. Unfortunately, elements with higher Z tend to absorb the 14.4 and 6.4 keV γ-rays. The attenuation length τ of various elements are given in Table 4.4.

Table 4.4: Attenuation Length of Elements

Element	τ(14.4 keV) [μm]	τ(6.4 keV) [μm]
Ti	55.21	6.346
V	36.52	4.322
Cr	28.04	3.402
Co	16.59	16.48
Ni	14.24	13.72
Pd	21.20	2.485
Os	2.801	1.509
Pt	2.742	1.447
Au	2.941	1.503
Fe	20.12	18.62

4.3.1 Fe-V

Vanadium is to the left of Cr on the periodic table of the elements (Figure 4.14). Just as in the Fe-Cr system there are three solid phases in the phase diagram of Fe-V: BCC (α), FCC (γ), and Sigma (σ). Fe-V does not exhibit spinodal decomposition and the sigma phase is stable to much higher temperatures. The Fe-V phase diagram is presented in Figure 4.15.

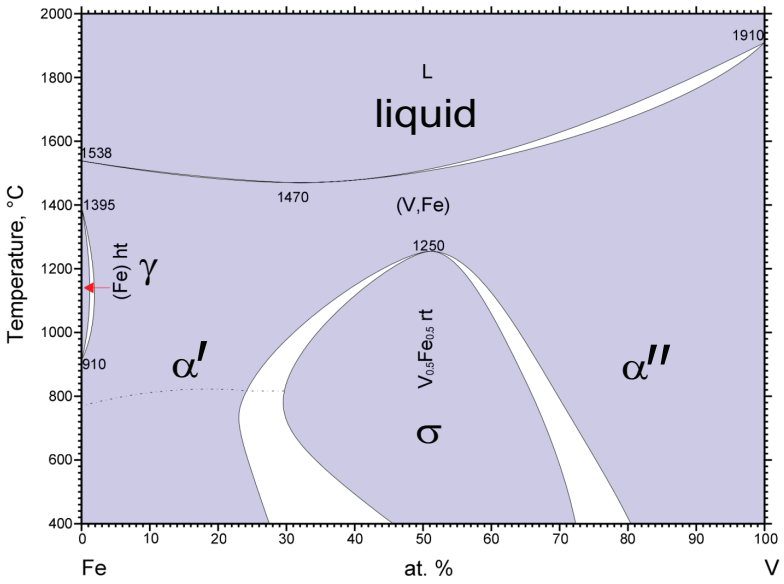

Figure 4.15: Fe-V phase diagram adopted from ASM International Alloy Phase Diagrams Center [47, 48, 49, 50, 51, 52].

Alloys of stoichiometric $Fe_{1-x_V}V_{x_V}$ for $x_V = \{0.99, 0.95, 0.90, 0.80, 0.70, 0.50, 0.25, 0\}$ were prepared from shots of 99.99% natural Fe, 96.06% enriched ^{57}Fe, and 99.8% V by arc-melting under an argon atmosphere. There was negligible mass loss and little visible surface oxidation after melting, so the compositions are expected to be accurate to 0.1 at. %. Samples with $x_V \leq 0.50$ were prepared with enriched ^{57}Fe only. The $Fe_{75}V_{25}$ sample was 10% enriched and the pure Fe sample was 50% enriched. After the melt the samples were cold rolled to thicknesses of 20 to 50 μm with the exception of the more brittle $Fe_{50}V_{50}$ which was rolled to $\sim$ 200 μm. X-ray diffraction performed after rolling indicated that all of the samples were in the BCC phase with prefered orientation along the <100> direction (Figure 4.16). The lattice parameter increases linearly with increasing vanadium concentration. A piece from each of the samples was sealed in a quartz tube under vacuum, then

annealed at 1100°C for one hour followed by a quench into iced brine. The anneal was performed to reduce the prefered orientation and remove any strain induced by the rolling. The $Fe_{50}V_{50}$ transformed into the sigma phase from the heat treatment, as is evident in Figure 4.16. For this alloy the as-rolled sample was used for the BCC measurement, whereas the as-quenched sample was used for all of the other BCC alloys.

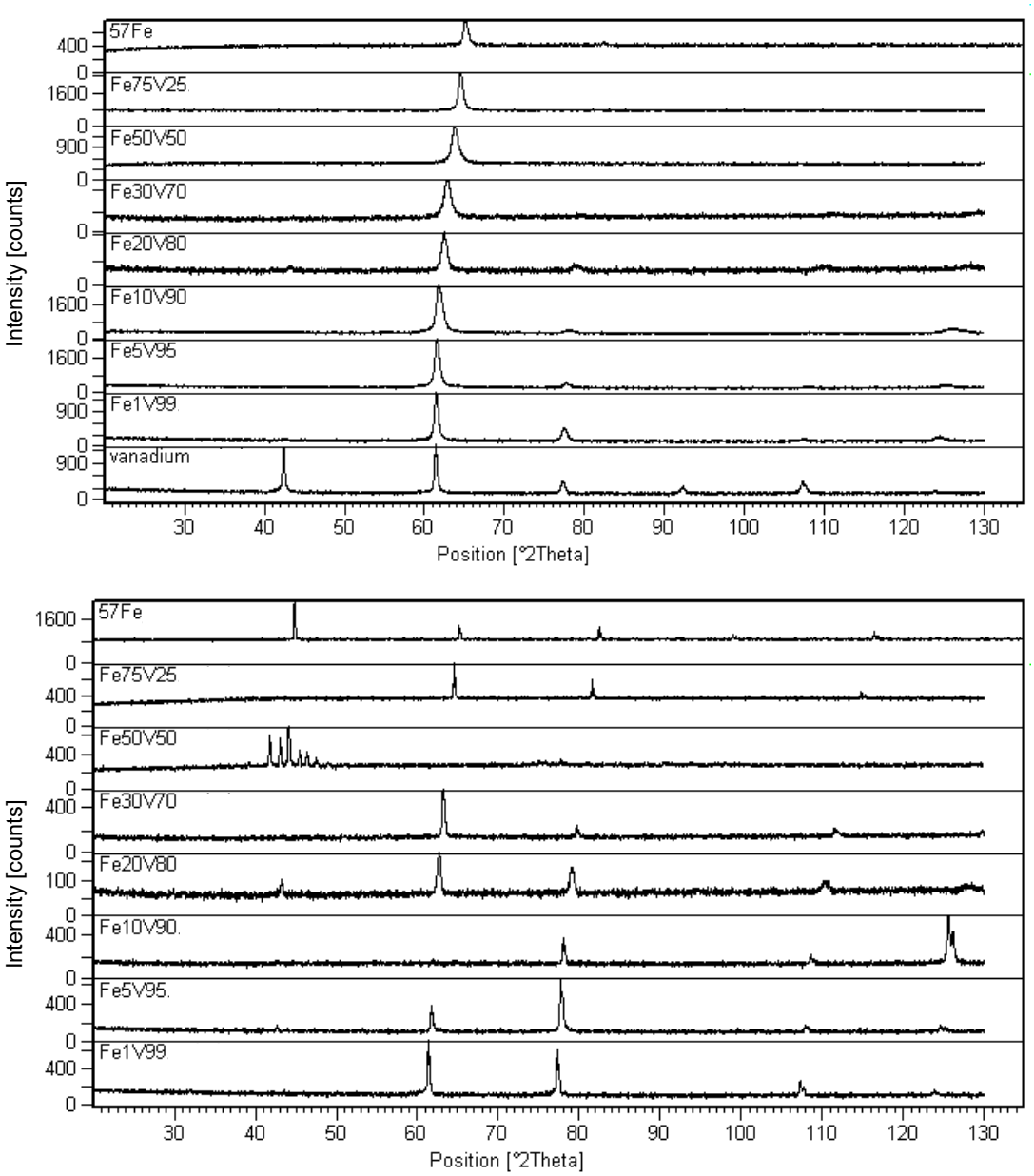

Figure 4.16: Top: X-ray diffraction of Fe-V alloys after rolling. Bottom: X-ray diffraction of Fe-V alloys after rolling and quench from 1100 C into iced brine

Nuclear resonant inelastic X-ray scattering (NRIXS)[45, 46, 28] was performed on all of the alloys at hutch 16-IDD at the Advanced Photon Source (APS) at the Argonne National Laboratory (ANL). Each sample was placed at a grazing angle to the incident photon beam. The incident photon energy was tuned to 14.413 keV, the nuclear resonance energy of ^{57}Fe. The delayed signal was measured from two avalanche photodiodes positioned 90° from the direction of the beam with a gap between the Be windows of $\sim$ 2 mm. Data were collected in scans of incident photon energy from –70 to +70 meV from the resonant energy, in steps of 0.5 meV counting for 10 seconds per step, with a monochromator resolution of 2.2 meV. Table 4.5 lists the number of scans performed for each alloy.

The raw scattering data were summed and analyzed using the program PHOENIX [26], which performs all of the calculations necessary to determine the ^{57}Fe partial phonon DOS, including removal of the elastic peak and multiphonon corrections. The ^{57}Fe partial phonon DOS curves for the Fe-V BCC alloys are shown in Figure 4.17. As with the Fe-Cr series, the Fe impurity PDOS in V is shifted to the low-energy modes. The cutoff energy varies more with V concentration than for Cr. The Fe-V PDOS rescaled by the cutoff energy is shown in Figure 4.18 with the cutoff energies given in Table 4.5.

Table 4.5: Number of Scans and Cutoff Energies for BCC Fe-V Alloys

Alloy	Scans	E^c [meV]
Fe_1V_{99}	6	35.0
Fe_5V_{95}	2	35.5
$Fe_{10}V_{90}$	1	36.5
$Fe_{20}V_{80}$	1	38.0
$Fe_{30}V_{70}$	1	38.5
$Fe_{50}V_{50}$	1	38.5
$Fe_{75}V_{25}$	1	39.5
Fe	1	40

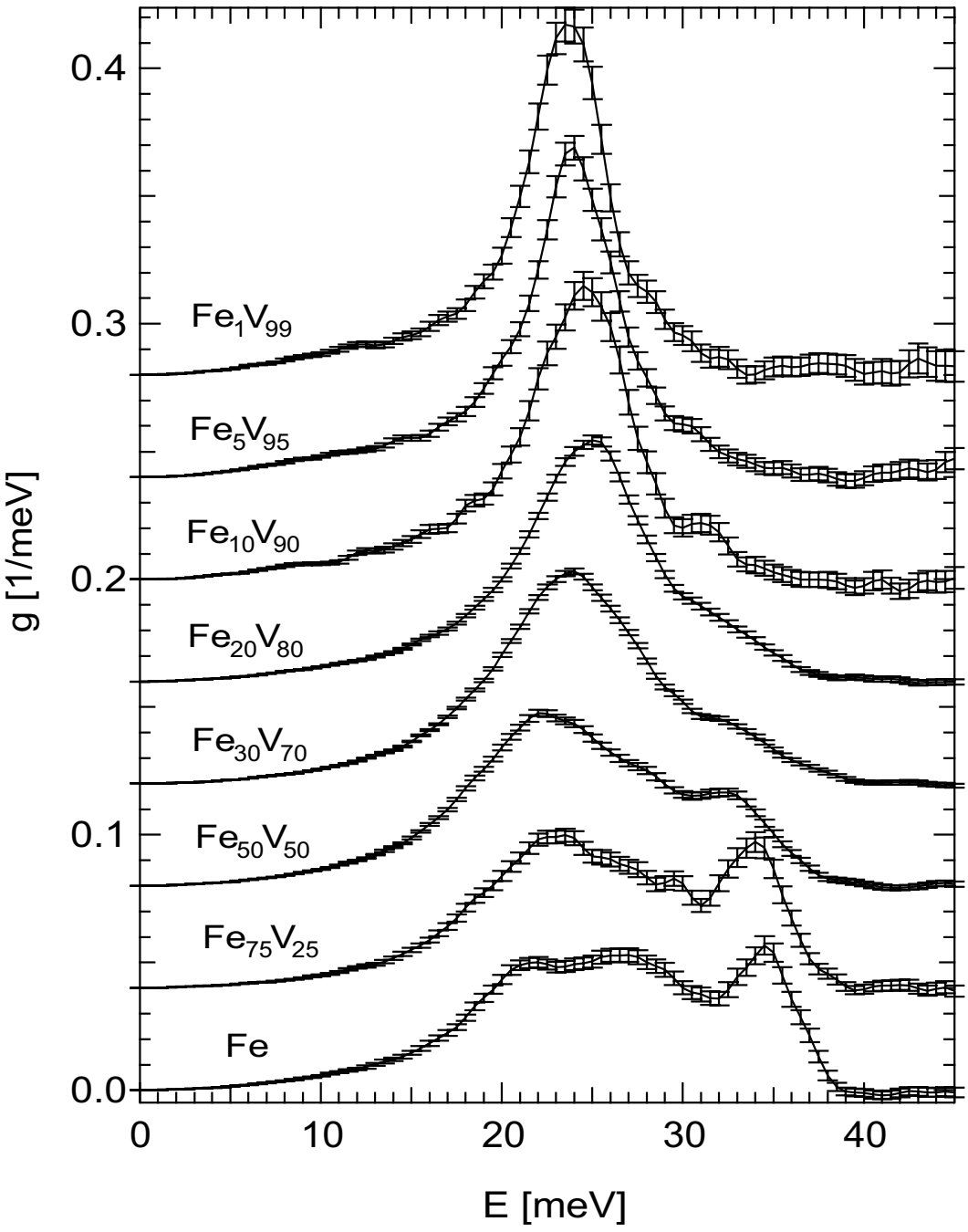

Figure 4.17: Phonon partial density of states of ^{57}Fe in BCC Fe-V alloys

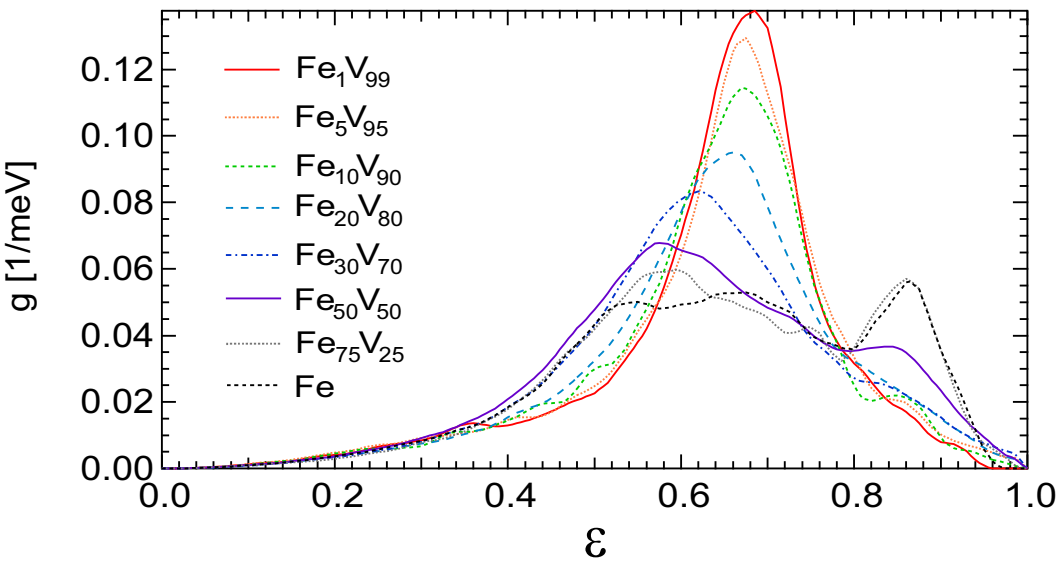

Figure 4.18: Phonon partial density of states of ^{57}Fe in BCC Fe-V alloys rescaled to the cutoff energy

The cutoff energy can be fit using the least-squares inversion. The values of the interaction cutoff energies for $\nu_g = 3$ are $\epsilon_0^c = 39.1432$ meV, $\epsilon_1^c = 2.21272$ meV, and $\epsilon_2^c = -1.63187$ meV. Similarly, a least-squares inversion can be performed for the PDOS as a function of both E and $\mathcal{E}$. The fits to the PDOS indicate that a six-term cluster expansion is necessary for the Fe-V system. This may be due to error bars that poorly reflect the error associated with each point in the PDOS. Alternatively, this could point out that the ^{57}Fe PDOS is more sensitive to local chemical arrangements when alloyed with V rather than Cr. For the remainder of the analysis in this thesis we limit the expansion of the ^{57}Fe PDOS in Fe-V to three terms in order to compare the results to those for Fe-Cr. The IPDOS functions are given in Figure 4.19 in E and Figure 4.20 in $\mathcal{E}$.

Table 4.6: $\langle\chi^2\rangle/\mathrm{N_d}$ for Fits to Fe-V PDOS

ν_l	$\langle\chi^2(E)\rangle/\mathrm{N_d}$	$\langle\chi^2(\mathcal{E})\rangle/\mathrm{N_d}$
3	6.54	5.27
4	5.99	3.95
5	2.75	2.34
6	1.43	1.23
7	0.72	0.75

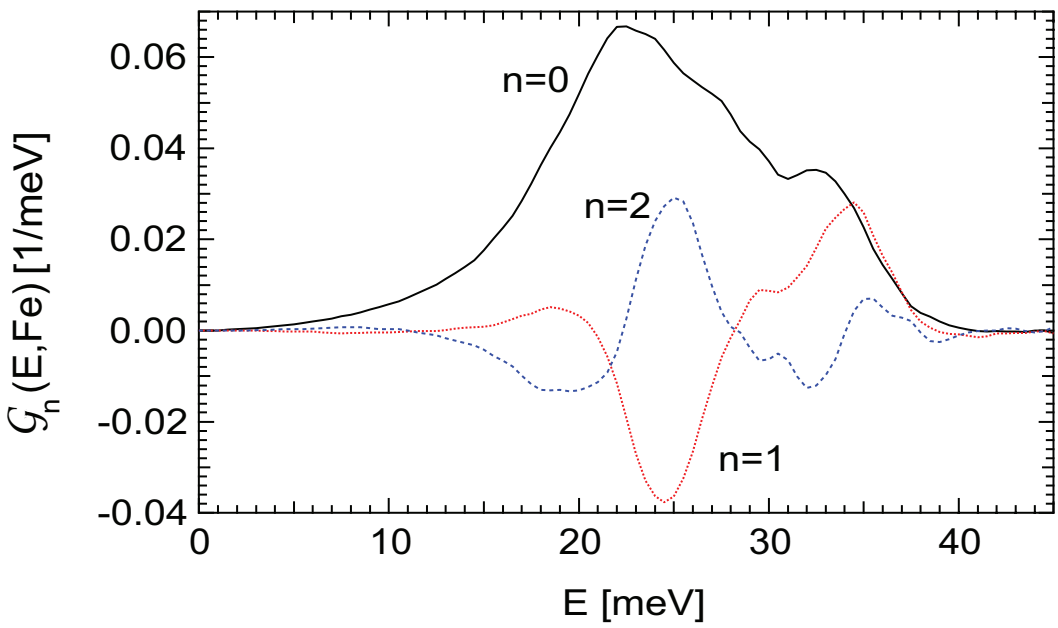

Figure 4.19: Interaction phonon partial density of states of ^{57}Fe in Fe-V as a function of E using a three-term local order cluster expansion

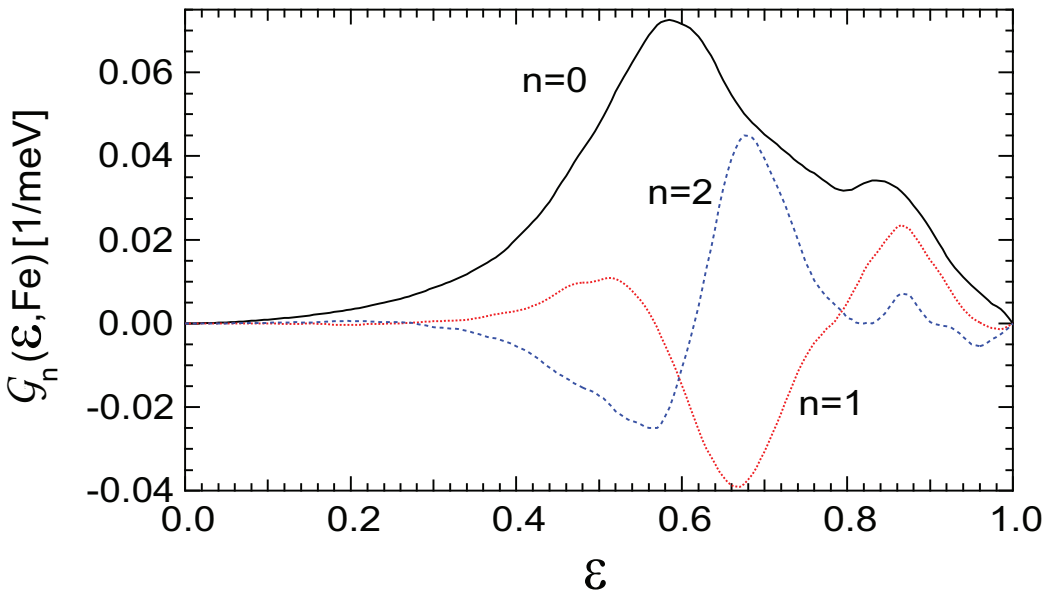

Figure 4.20: Interaction phonon partial density of states of ^{57}Fe in Fe-V as a function of the energy rescaled to the cutoff energy using a three-term local order cluster expansion

4.3.2 Fe-Co

At ambient temperature and pressure Co has the HCP structure. When alloyed with Fe the BCC phase is stable over a large concentration range. There is a range of B2 stability, though the kinetics of the ordered phase are slow. The Fe-Co phase diagram is presented in Figure 4.21. Alloys of stoichiometric $Fe_{1-x_{Co}}Co_{x_{Co}}$ for $x_{Co} = \{0.70, 0.60, 0.50, 0.40, 0.30, 0.20, 0.10, 0\}$ were prepared from shots of 99.99% natural Fe, 96.06% enriched ^{57}Fe, and 99.9+% Co by arc-melting under an argon atmosphere. There was negligible mass loss and little visible surface oxidation after melting, so the compositions are expected to be accurate to 0.1 at. %. All of the samples contained between 30 and 40 at. % ^{57}Fe. After the melt the samples were cold rolled to a thickness of 20 to 50 μm. X-ray diffraction performed after rolling indicated that all of the samples were in the BCC phase with prefered orientation along the <100> direction (Figure 4.22). The lattice parameter increases approximately linearly with increasing cobalt concentration.

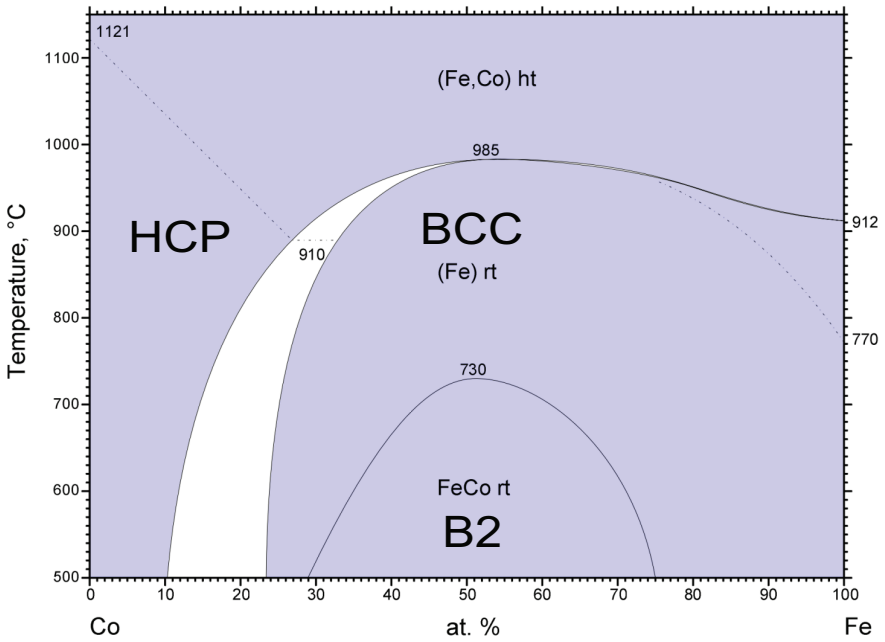

Figure 4.21: Fe-Co phase diagram adopted from ASM International Alloy Phase Diagrams Center [53, 54, 55]

To reduce the prefered orientation and remove any strain induced by the rolling the samples were sealed in quartz tubes and given the following heat treatments: $Fe_{90}Co_{10}$ was annealed at 1000°C

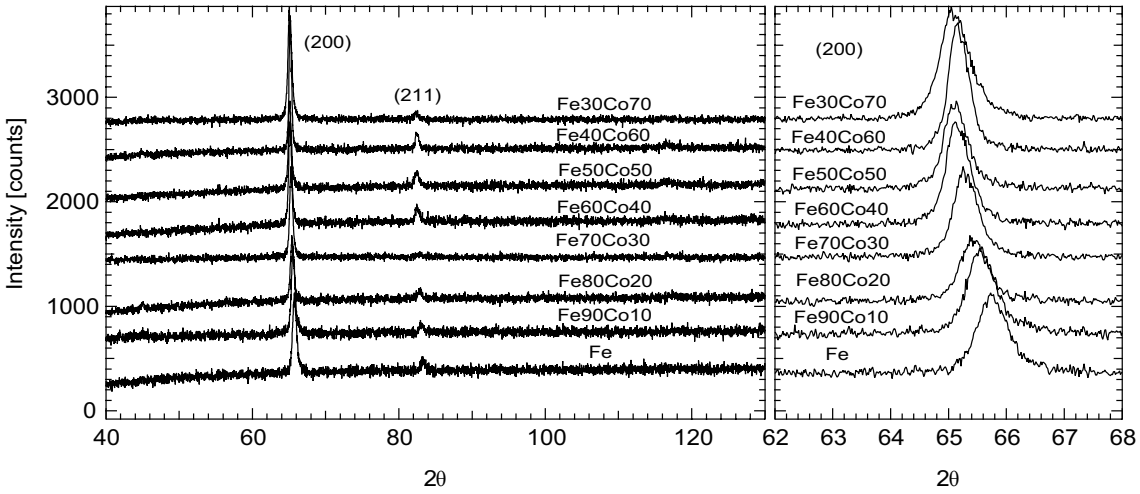

Figure 4.22: X-ray diffraction of Fe-Co alloys after rolling

for 1.5 hours and quenched; $Fe_{80}Co_{20}$ was annealed at 900°C for 14 hours and quenched; $Fe_{70}Co_{30}$ was annealed at 900°C for 14 hours and quenched; $Fe_{60}Co_{40}$ was annealed at 1000°C for 2 hours, 900°C for 1 hour, 800°C for 4 hours and quenched; $Fe_{50}Co_{50}$ was annealed at 1000°C for 2 hours and quenched; $Fe_{40}Co_{60}$ was annealed at 1000°C for 2 hours, 900°C for 1 hour, 800°C for 4 hours and quenched; and $Fe_{30}Co_{70}$ was annealed at 920°C for 2 hours, 800°C for 11 hours, and allowed to air cool. The X-ray diffraction patterns for the random solid solutions after the heat treatments are shown in Figure 4.23.

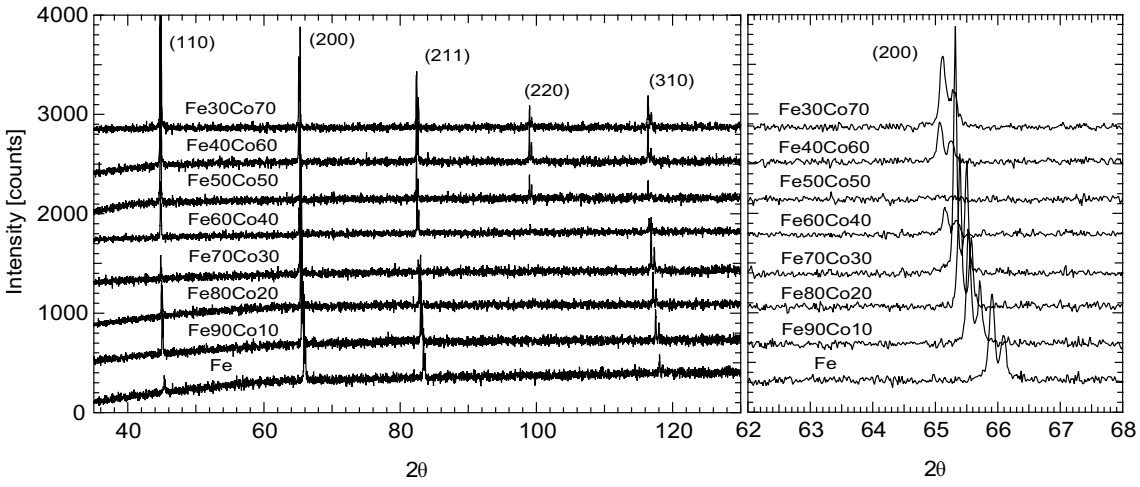

Figure 4.23: X-ray diffraction of Fe-Co alloys after their respective heat treatments. Note that the broadening of the peaks has decreased enough so that the Cu Kα_1 and Kα_2 are visible.

To create B2 order, the as-rolled $Fe_{50}Co_{50}$ alloy was sealed in a quartz tube and annealed at 1000°C for 1 hour, 950°C for 1 hour, 900°C for 1 hour, 850°C for 1 hour, 800°C for 2 hours, 750°C for 2 hours, 700°C for 6 hours, 650°C for 12 hours, and 600°C for 4 days, followed by air cooling. The electronic scattering of X-rays from Fe and Co are very similar, which explains the lack of superlattice peaks in the X-ray diffraction patterns. The differences of the intensities of the peaks is due to texture.

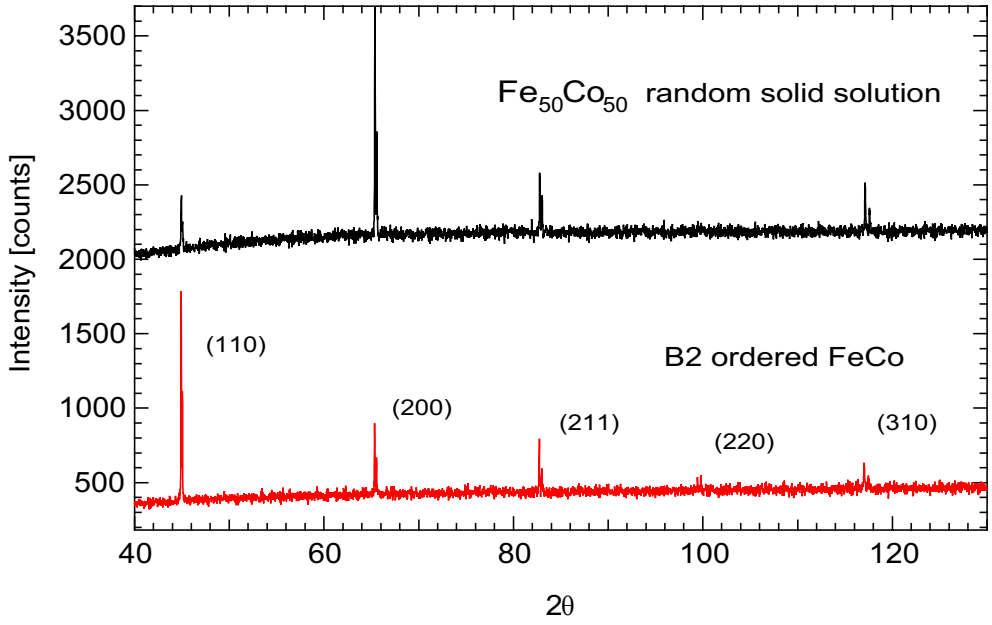

Figure 4.24: X-ray diffraction of ordered (bottom) and disordered (top) 50-50 FeCo alloys

NRIXS was performed following the procedure given in Section 4.3.1. The samples all contain approximately the same enrichment of ^{57}Fe, which was high enough for a single scan to be performed for each alloy. The data analysis procedure was the same as used in Section 4.3.1. The ^{57}Fe PDOS for the random solid solutions is presented in Figure 4.25 and the B2 ordered sample in Figure 4.26. The cutoff energy varies very little with Co concentration (Table 4.7). There is an increase in the high-energy modes, a decrease in the medium-energy modes, and an increase in the low-energy modes upon alloying with Co. The effect of ordering on the 50-50 alloy is to increase the number of modes in the energy range 20 to 25 meV, while lowering the number of high-energy and low-energy modes. The PDOS as a function of the energy rescaled to the cutoff are presented in Figure 4.27.

Table 4.7: Cutoff Energies for BCC Fe-Co Alloys

Alloy	E^c [meV]
$Fe_{30}Co_{70}$	38.0
$Fe_{40}Co_{60}$	38.0
$Fe_{50}Co_{50}$	38.5
$Fe_{60}Co_{40}$	38.5
$Fe_{70}Co_{30}$	39.0
$Fe_{80}Co_{20}$	39.0
$Fe_{90}Co_{10}$	39.0
Fe	39.0

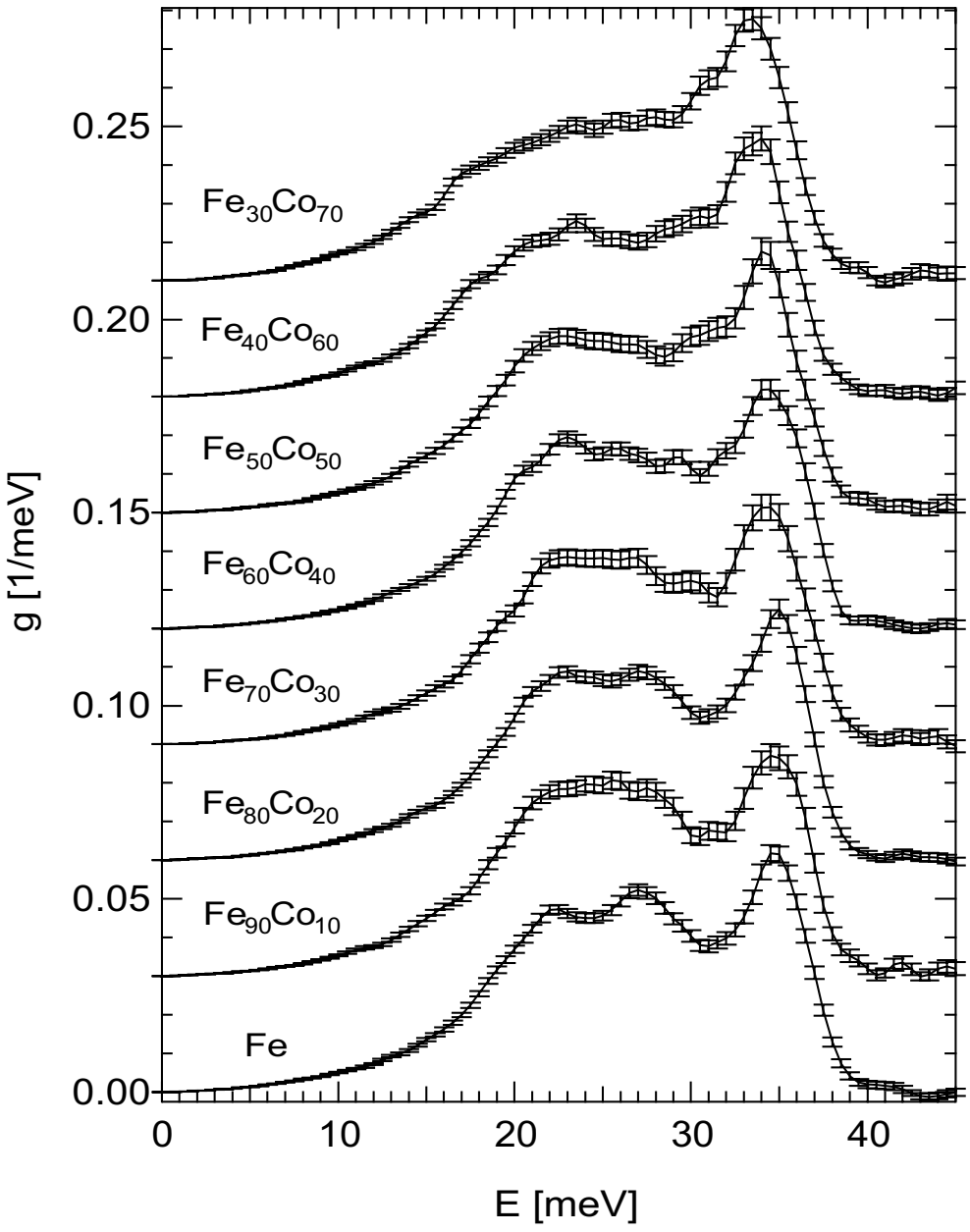

Figure 4.25: Phonon partial density of states of ^{57}Fe in BCC Fe-Co alloys

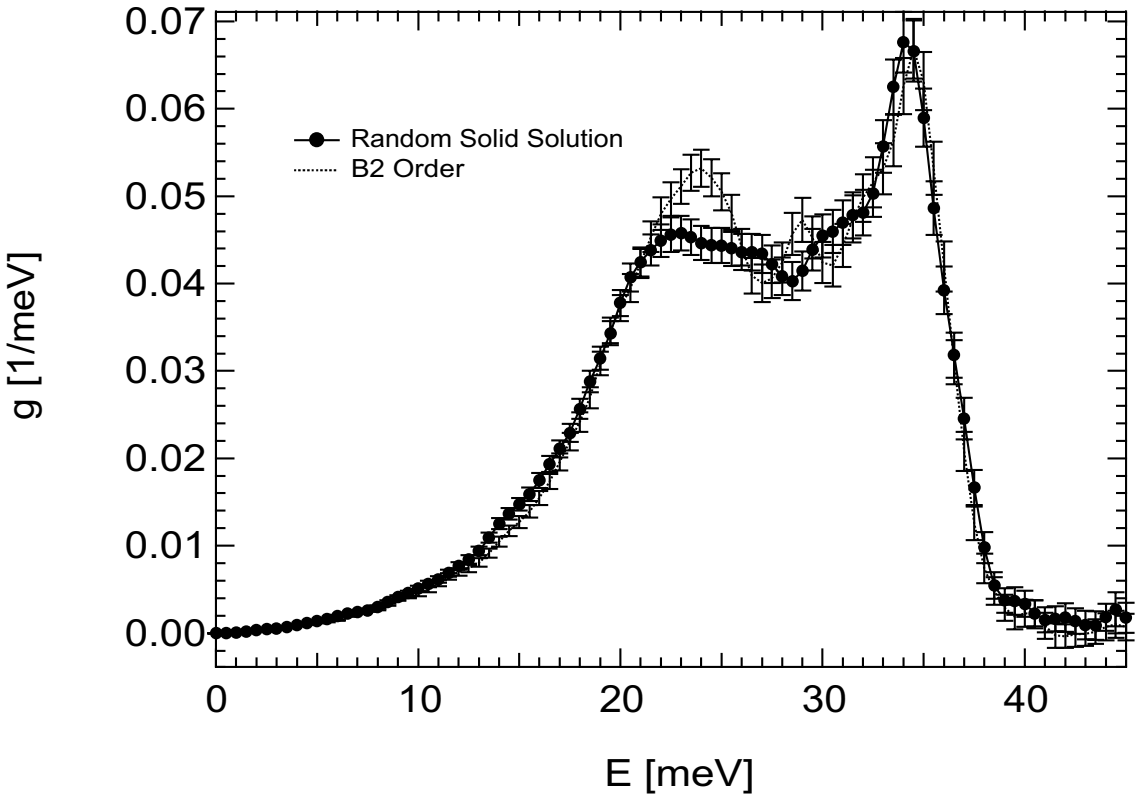

Figure 4.26: Phonon partial density of states of ^{57}Fe in disordered BCC $Fe_{50}Co_{50}$ and ordered B2 FeCo. Both samples came from the same ingot and were only given different heat treatments according to the phase diagram.

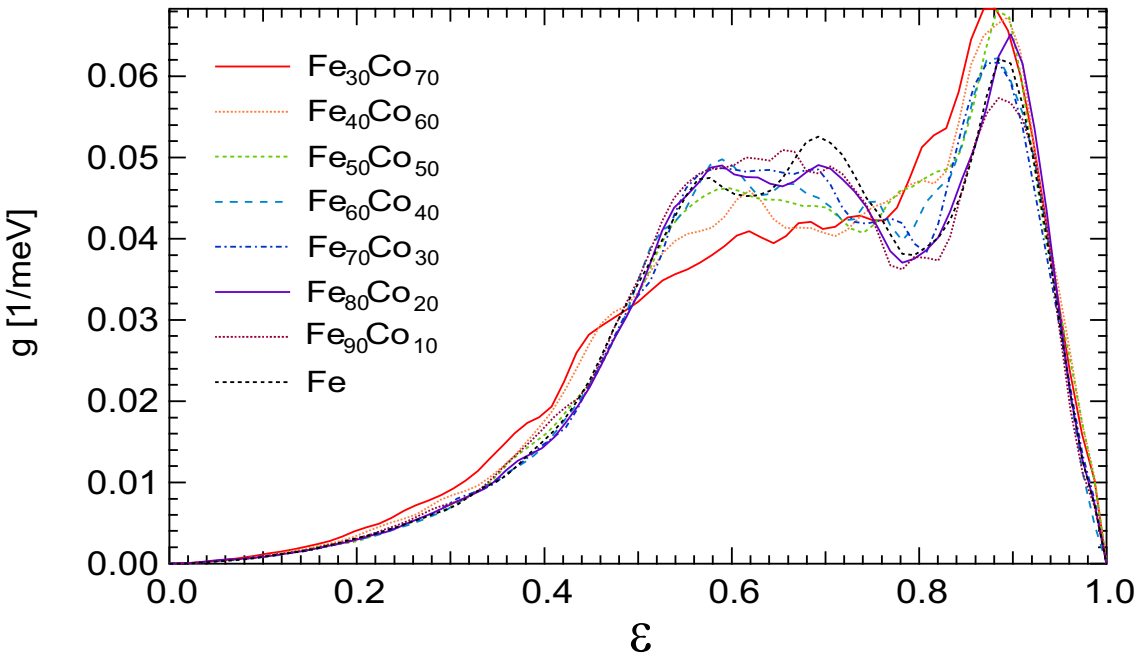

Figure 4.27: ^{57}Fe phonon partial density of states curves as a function of the energy rescaled by the cutoff

With little change in the PDOS as a function of composition it would appear that the Fe-Co system is ideally suited for a cluster expansion analysis. The cutoff energies decrease only slightly with composition, and with such large error bars a least-squares fit indicates that only a single term in the expansion is necessary. The fits to the cutoff energies for $\nu_g = 2$ and $\nu_g = 3$ are shown in Figure 4.28. The three-term fit indicates a cutoff energy for BCC Co of 36.5 meV. A least-squares inversion of the ^{57}Fe PDOS in Fe-Co reveals that a three-term LOCE is suitable. The values of $\langle\chi^2\rangle/\mathrm{N_d}$ are given in Table 4.8 and the IPDOS in Figure 4.29. These values indicate that the expansion performed in $\mathcal{E}$ is slightly better than an expansion performed in E. The IPDOS for $\nu_l = 3$ are plotted in Figure 4.29. Note that there is less modulation in $\mathcal{G}_n(\mathcal{E}, \mathrm{Fe})$ than $\mathcal{G}_n(E, \mathrm{Fe})$, especially at high energies.

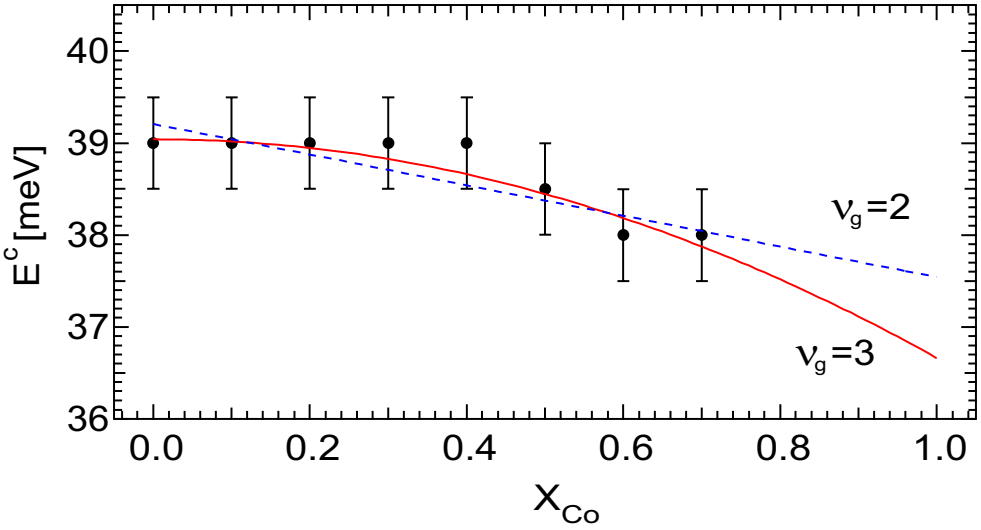

Figure 4.28: Cutoff energies for BCC Fe-Co from the measurements (points with error bars), from a fit using a two-term GCE (dashed line), and from a fit using a three-term GCE (solid line)

Table 4.8: $\langle\chi^2\rangle/\mathrm{N_d}$ for Fits to Fe-Co PDOS

ν_l	$\langle\chi^2(E)\rangle/\mathrm{N_d}$	$\langle\chi^2(\mathcal{E})\rangle/\mathrm{N_d}$
3	1.45	1.27
4	0.93	0.76
5	0.77	0.73
6	0.87	0.80
7	0.90	0.73

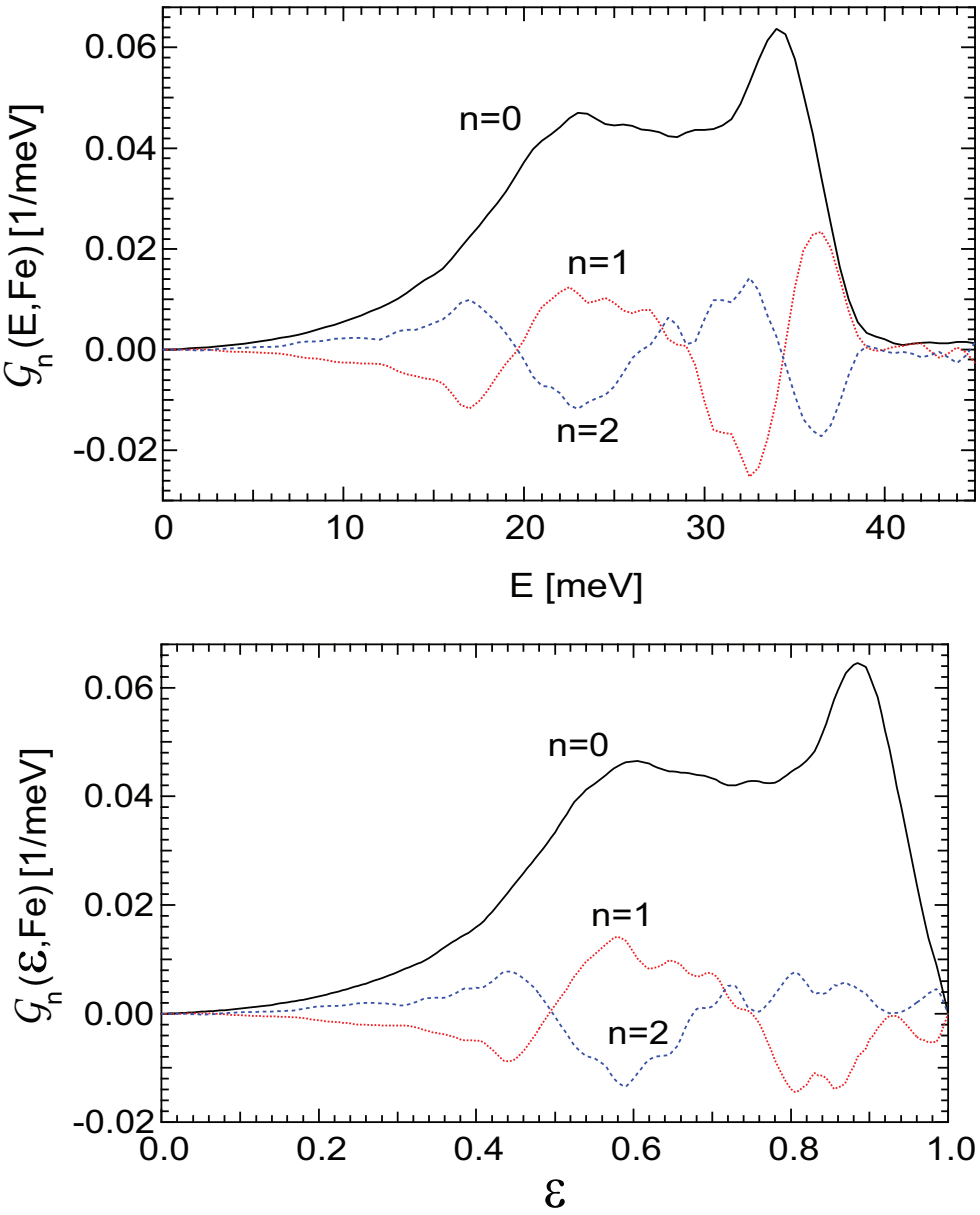

Figure 4.29: Top: Interaction phonon partial density of states of ^{57}Fe in Fe-Co as a function of E using a three-term local order cluster expansion. Bottom: Same as top except as a function of $\mathcal{E}$

The IPDOS in Figure 4.29 can be used to fit to the PDOS of the B2 ordered sample. It is unlikely that there is perfect order in the sample, so a fit can be used to infer order. The fitting parameters and goodness of the fits are given in Table 4.9. Based on these values a 4-term LOCE in $\mathcal{E}$ suitably recreates the B2 ordered PDOS (Figure 4.30).

Table 4.9: Results of Fit to B2 Ordered Sample

Expansion	ν_l	ξ_0	ξ_1	ξ_2	ξ_3	ξ_4	$\chi^2/\mathrm{N_d}$
E	3	1	-0.165	-0.417	-	-	1.94
E	4	1	-0.057	-0.268	-0.270	-	1.91
E	5	1	-0.014	-0.284	-0.262	-0.324	1.83
$\mathcal{E}$	3	1	-0.001	-0.435	-	-	1.03
$\mathcal{E}$	4	1	-0.076	-0.471	-0.506	-	0.94
$\mathcal{E}$	5	1	0.216	-0.072	-0.034	-0.081	1.05

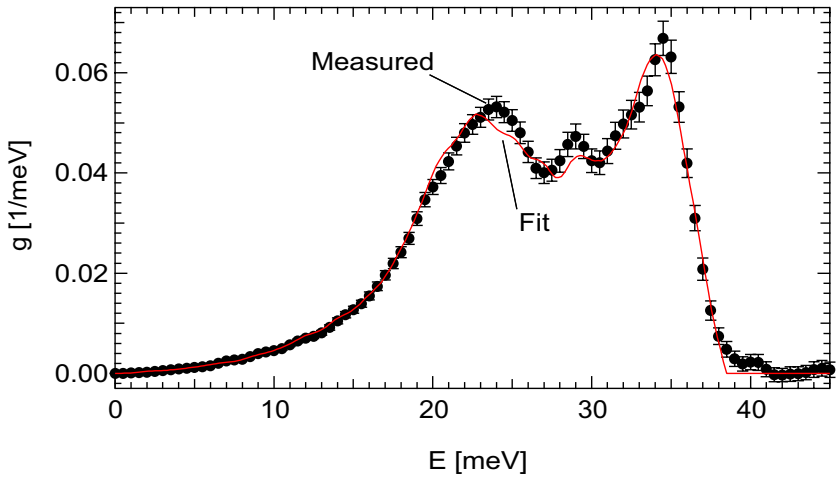

Figure 4.30: Fit to measured B2 ordered FeCo alloy using four-term LOCE with energy rescaled to the cutoff

The correlation functions from the fit to the B2 ordered sample indicate that the sample does not have perfect B2 order, and neither is it a perfect random solid solution. The correlation functions for perfect B2 order using the clusters in Figure 4.11 are $\xi_0 = 1$, $\xi_1 = -1/7$, $\xi_2 = -1/3$, $\xi_3 = 0$, whereas for a random solid solution they are $\xi_0 = 1$, $\xi_1 = 0$, $\xi_2 = 0$, $\xi_3 = 0$. The fit indicates correlation functions between B2 order and randomness. The ordered phase nucleates and grows inwards from grain boundaries [56], so the correlation functions may indicate a mix of ordered and disordered zones. However, this fitting method cannot be used to accurately determine the chemical order of the measured sample due to the relatively small changes in the PDOS with composition.

The fact that the IPDOS are capable of fitting a sample with a different chemical arrangement is further evidence that the phonon properties can be successfully expressed with low numbers of terms in the cluster expansion.

One interesting use of the cluster expansion is to extrapolate the properties of alloy phases that are unstable from those that are stable. For instance, it is not possible to measure the impurity amount of Fe in BCC Co at ambient temperature and pressure. The IPDOS in Figure 4.29 have been used to construct the impurity PDOS of Fe in BCC Co shown in Figure 4.31.

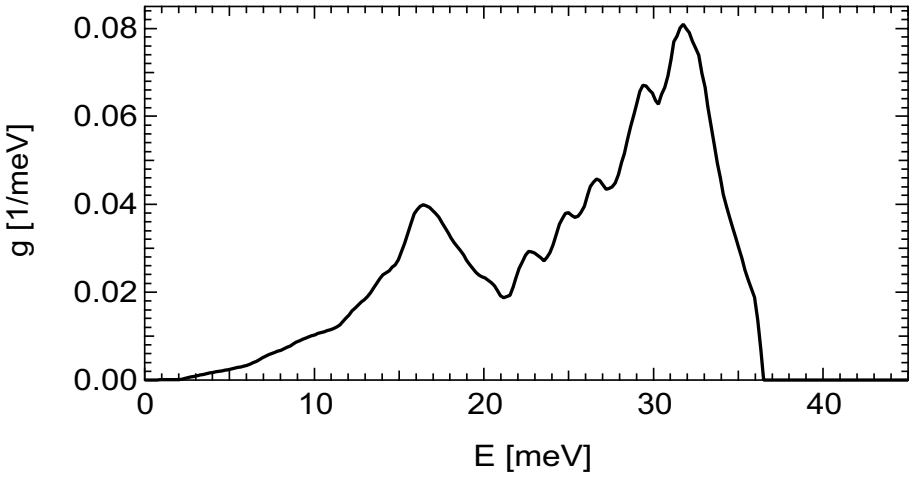

Figure 4.31: ^{57}Fe PDOS of Fe impurity in BCC Co determined from a three-term cluster expansion of the measured alloy properties

4.3.3 BCC Trends

4.3.3.1 IPDOS Functions

The effects of alloying for the measurements made in this thesis can be summed up in a single plot using the IPDOS from each alloying element. This is shown in Figure 4.32 using a three-term LOCE in E. The $n = 0$ term shows that the 50-50 alloys stiffen with increasing number on the periodic table. This stiffening is less a shift of the cutoff energy and more of a shift of the low-energy modes to high energies. The $n = 1$ term also shows this effect. The modes in the energy range 18 to 28 meV increase with V atoms in the 1NN and 2NN shell of the ^{57}Fe. This effect is diminished with Cr and opposite for Co.

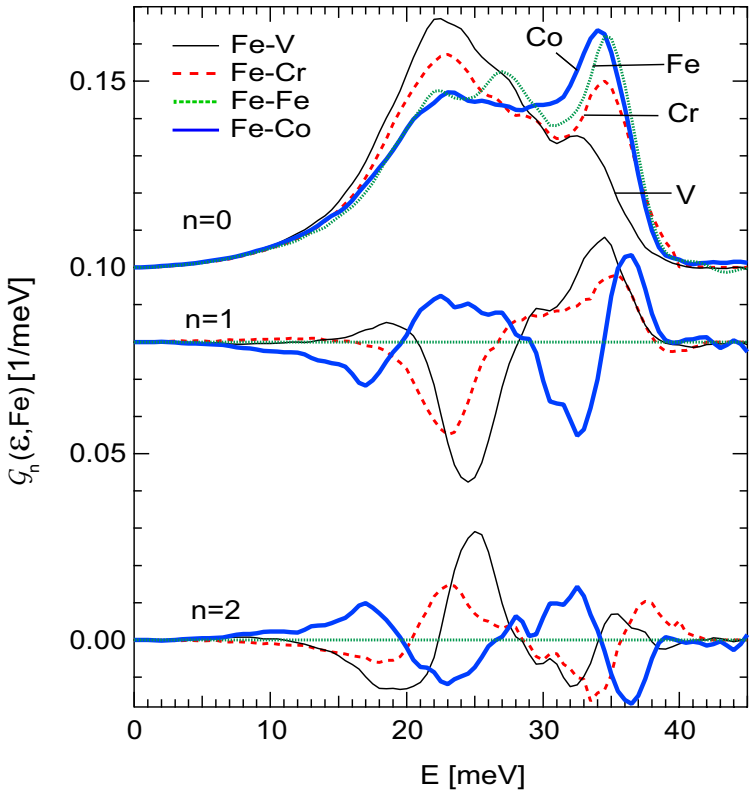

Figure 4.32: Interaction partial phonon density of states of Fe in BCC V, Cr, Fe, and Co. There are obvious trends with increasing number of d-electrons and mass of the alloying species.

4.3.3.2 Force and Mass Effects

The effect of alloying on the ^{57}Fe PDOS in the 3d series is a shift of the modes from a central peak to higher and lower energy modes as the average atomic number Z increases. This is best shown in a plot where the ^{57}Fe PDOS curves are offset by an amount proportional to ΔZ where

$$\Delta Z = Z_{\mathrm{Fe}} - \langle Z \rangle = x_{\mathrm{B}}(Z_{\mathrm{B}} - Z_{\mathrm{Fe}}) = (1 - x_{\mathrm{Fe}})(Z_{\mathrm{B}} - Z_{\mathrm{Fe}}) \tag{4.1}$$

and $\langle Z \rangle$ is the average atomic number of the alloy

$$\langle Z \rangle = x_{\mathrm{Fe}} Z_{\mathrm{Fe}} + x_{\mathrm{B}} Z_{\mathrm{B}} \ . \tag{4.2}$$

Figure 4.33 shows measured ^{57}Fe PDOS curves that are offset by an amount proportional to $-\Delta Z$.

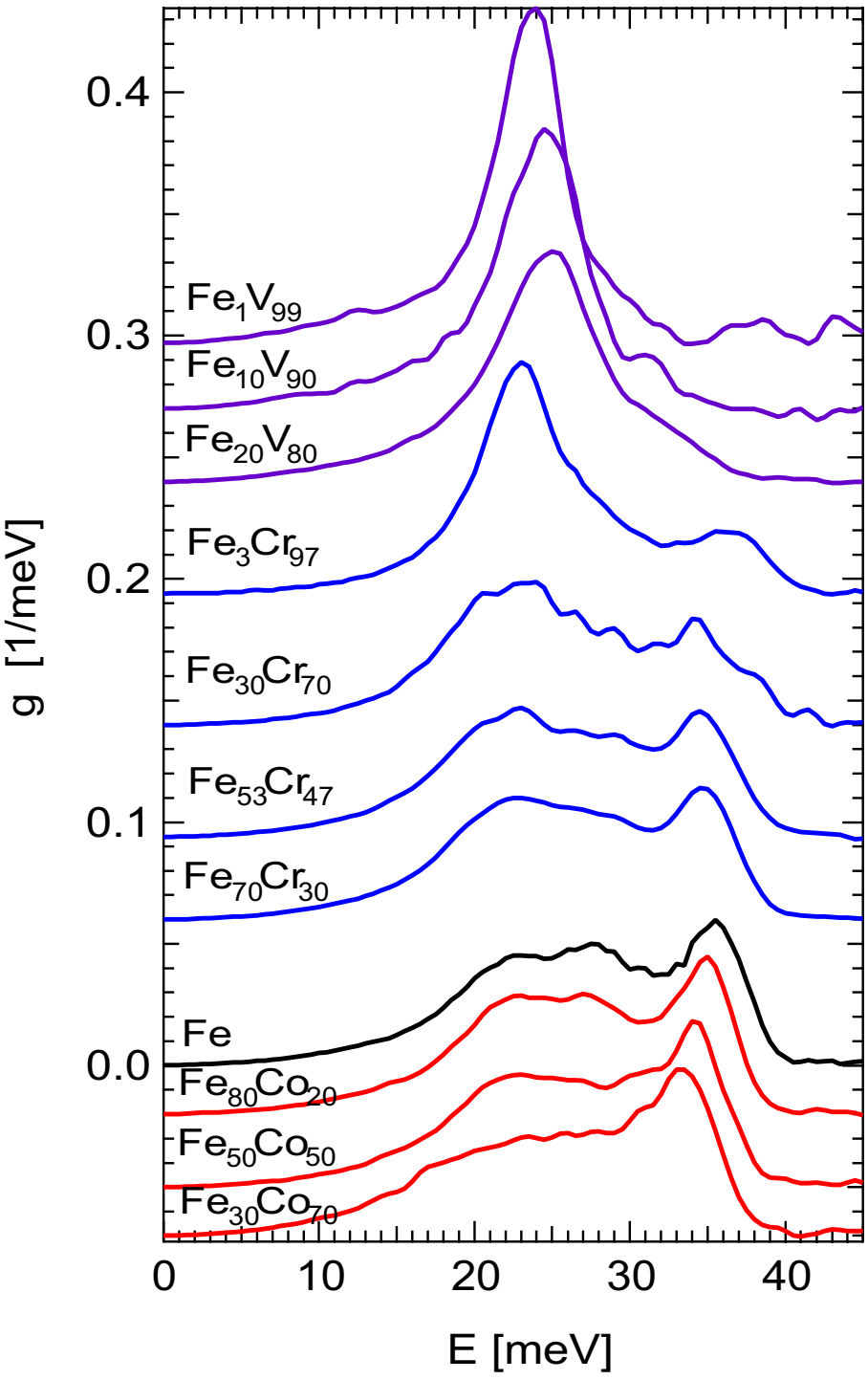

Figure 4.33: PDOS of ^{57}Fe measured in various alloys. The curves are offset by an amount equal to $-\Delta Z/10$.

The masses of the alloying elements shown in this plot are all within 8 atomic mass units and represent only a ±10% mass difference from pure natural Fe. This suggests that the effects are related more to the forces present on the ^{57}Fe atoms than the mass differences between the ^{57}Fe atoms and the alloying element. There is a relatively simple method for testing this hypothesis.

The lattice dynamics of crystals with dilute impurities was developed by Mannheim [57, 46] with Green's function techniques for interatomic force-constants described by a single longitudinal stiffness (Appendix C). The assumption is made that the introduction of the impurity perturbs only the first-nearest-neighbor (1NN) bonds to the impurity atom. The only information required for this theory are the DOS of the pure host, the mass ratio of the host to impurity atoms $m_{\mathrm{h}}/m_{\mathrm{d}}$, and the ratio of the host-host force constant to the impurity-host force constant $K_{\mathrm{h-h}}/K_{\mathrm{d-h}}$. The pure DOS of Fe, V, and Cr are approximately similar (Figure 4.34) and the Green's function method washes out most of the details in the DOS. Therefore we use the Fe DOS as the host DOS for all of the host elements. Although the Fe PDOS changes considerably with Cr concentration the total DOS varies much less [38], so assuming the Fe DOS as the host DOS for all alloys is not unreasonable[3]. This gives only two fitting parameters: the ratios of the masses and forces.

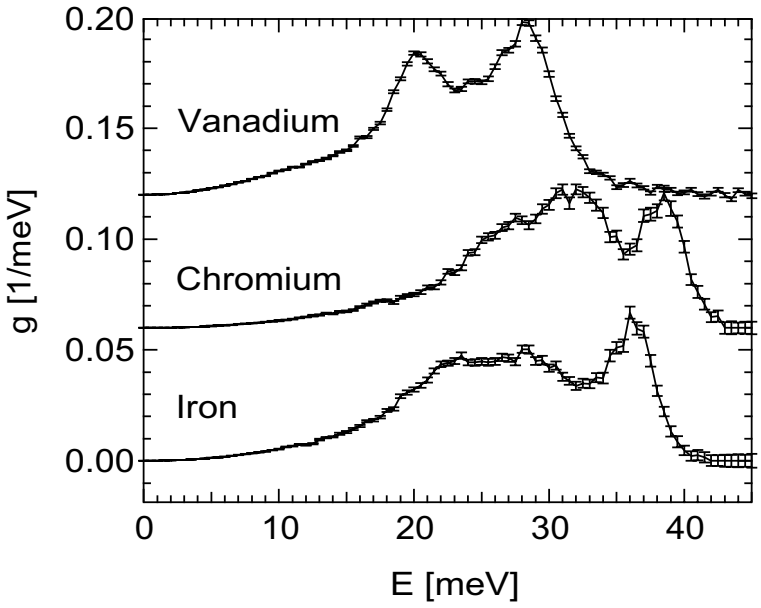

Figure 4.34: Phonon density of state curves measured for Fe, Cr, and V at 293K [58, 59]

[3]For vanadium this is an unreasonable approximation, though this assumption does not change the results of the following arguments.

Assuming the forces do not change, we can look at the mass effects. The PDOS of impurity amounts of ^{57}Fe in V, Cr, natural Fe, and Co from the Mannheim model are given in Figure 4.35. It is apparent that mass differences do not play a very large role in the differences in the PDOS of ^{57}Fe.

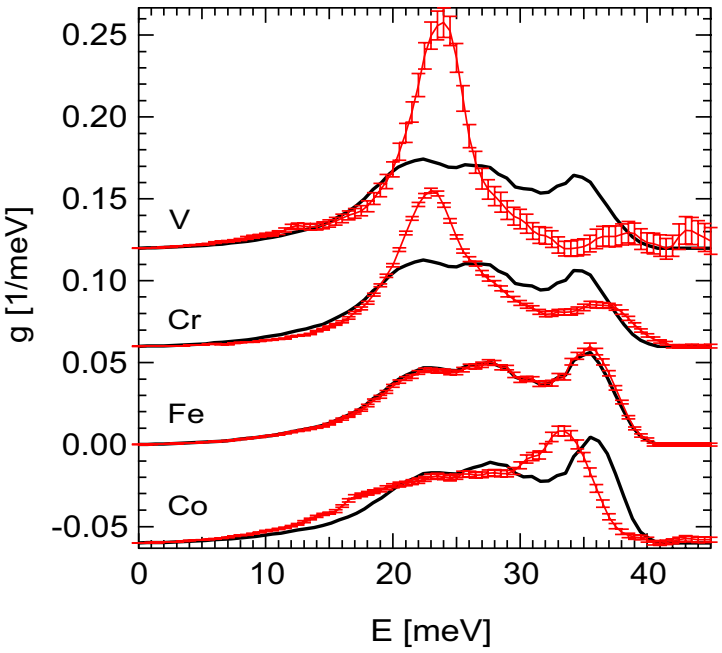

Figure 4.35: PDOS of impurity amounts of ^{57}Fe measured in V, Cr, natural Fe, and Co (lines with error bars). For Co, the alloy $Fe_{30}Co_{70}$ is shown. The measurements are compared to PDOS calculated with the Mannheim model using only the differences in the mass between ^{57}Fe and the host element (solid lines). For ^{57}Fe in natural Fe the change in the PDOS is not beyond the error bars in the measurement.

The effects of mass are small within the Mannheim model for the alloys measured, so we take the ratio of the masses to be constant and equal to 1 for all alloys. With the host DOS assumed to be pure Fe for all elements, the only fitting parameter is the ratio of the force constants $K_{\mathrm{h-h}}/K_{\mathrm{d-h}}$. We have assumed the host to have the same DOS, so that $K_{\mathrm{d-h}}$ is the actual fitting parameter. We define a parameter α such that

$$K_{\mathrm{Fe-h}} = \alpha \; K_{\mathrm{h-h}} \; . \tag{4.3}$$

The PDOS for various values of α are plotted in Figure 4.36. This plot is qualitatively similar to Figure 4.35, proving that the effects on the ^{57}Fe have a much greater dependence on the forces than the mass.

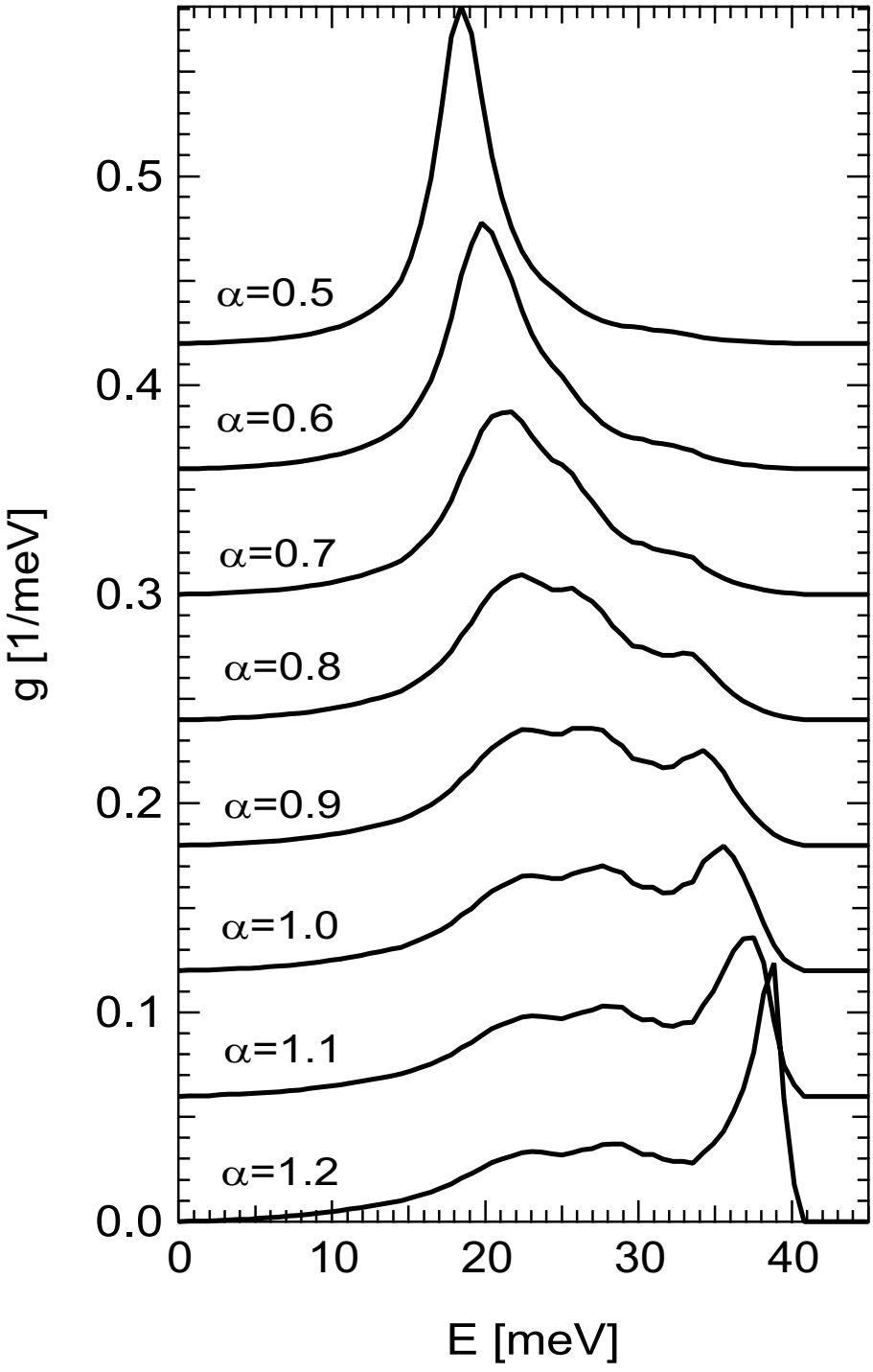

Figure 4.36: Phonon partial density of states curves calculated using Mannheim model with pure Fe as the host DOS and varying values of the force constant ratio α. Increasing values of α correspond to increasing local forces. The similarity in this plot with Figure 4.33 indicates that the effect of alloying is primarily due to changes in the local forces rather than mass effects.

Figure 4.36 qualitatively shows that changes in the local forces are responsible for the changes in the ^{57}Fe PDOS in Fe-V, Fe-Cr, and Fe-Co. However, there is a distinct quantitative difference that should be pointed out. The height of the peak for $\alpha = 0.55$ (interpolate between $\alpha = 0.5$ and $\alpha = 0.6$) is the same as for Fe_1V_{99} but the energy is 5 meV less than the measured value. This discrepancy is made worse when the DOS of pure vanadium is used as the host DOS. This is likely due to the assumptions made in the Mannheim model of a single longitudinal stiffness and that the introduction of the impurity perturbs only the first-nearest-neighbor (1NN) bonds to the impurity atom. With all of these assumptions, the success of the Mannheim approach is likely to be somewhat fortuitous. Nonetheless, the calculations in Figure 4.36 directly show that softening of the local bonds is responsible for the observed phonon softening.

4.3.3.3 Origin of Force Differences

Having shown that changes in the forces on the ^{57}Fe atom are responsible for the observed changes in the Fe PDOS, the aim is now to pinpoint the origin of these force changes.

There is significant evidence in the literature from Mössbauer experiments of an increase in the $4s$ occupation of the ^{57}Fe atom with decreasing ΔZ [60, 61, 62, 63, 64, 65, 66]. Figure 4.37 shows a plot from Akai et al. [62] that relates the isomer shift with the change of the Fe s-charge. There is an increase in the s-charge on the ^{57}Fe atom when an element such as chromium or vanadium is in its nearest-neighbor shell. With more electrons the ^{57}Fe atoms are screened from the local forces causing a softening of the ^{57}Fe PDOS upon alloying with V and Cr. For Co, charge is transfered from the Fe atom to the Co atom, resulting in a decrease of the charge on the ^{57}Fe atom. Therefore there are less electrons for screening, resulting in a stiffening of the ^{57}Fe PDOS upon alloying with Co.

This argument given above is weak since other electrons also participate in the screening, and the angular momentum gets a bit messy in transition metals. Identifying the s-electron contributions is important for Mössbauer hyperfine interactions, which is the reason for Akai's work, but does not work well for identifying the origins of forces on the ^{57}Fe atoms.

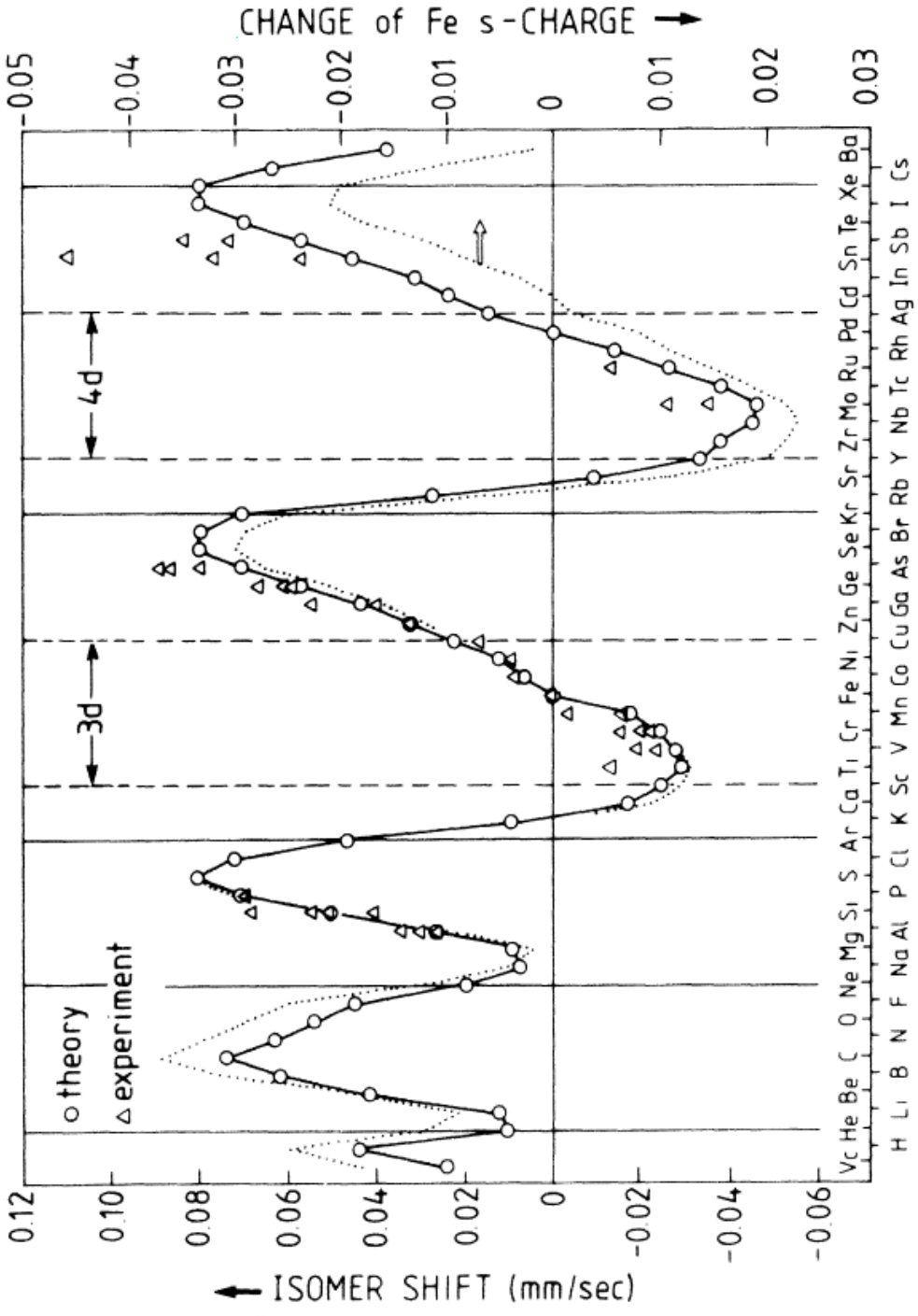

Figure 4.37: Figure and caption from Akai et al. [62]: Calculated isomer shift of a nearest-neighbor Fe atom as a function of the nuclear charge Z of the impurity (left-hand scale). The triangles are experimental values for dilute Fe alloys. The dotted line gives the change Δn_s of the number of Fe s electrons and refers to the right-hand inverted scale.

The rigid-band model provides a simple method for interpreting the effects of alloying on the electronic density of states of 3d transition metals. This model assumes that the s and d bands are rigid in shape as atomic number changes. The only difference between atoms is the location of the Fermi energy E_F [67]. An example of the rigid-band model for an Fe-Ni alloy is presented in Figure 4.38. This is a very simple model and fails for all but perturbations in the composition between two very similar atoms. For example, the spin-up and spin-down d bands are shifted with respect to each other because Fe is ferromagnetic. Alloying of Fe with a paramagnetic species such as vanadium cannot be treated with this model. Another failing of this model is that it assumes that the electronic density of states is the same for both atoms in the alloy. Nonetheless, there is some insight that can be achieved with this model.

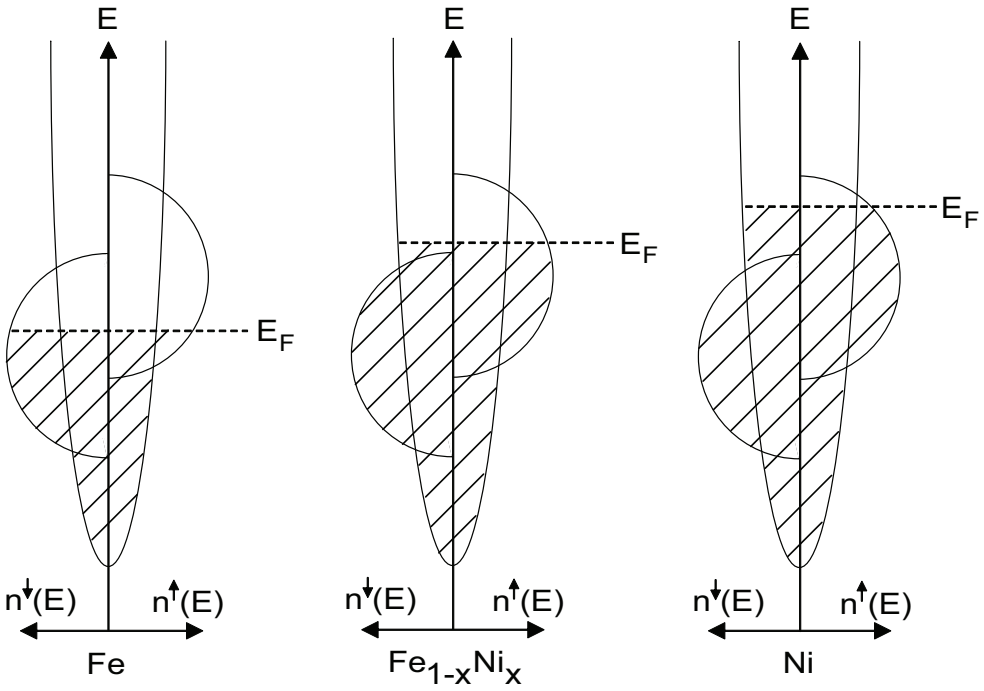

Figure 4.38: Example of the rigid-band model for Fe-Ni alloys. The s band is given by the parabola and the d band by the half circles. The bands remain rigid and only the Fermi energy shifts between the elements and the alloy. Figure adopted from [67].

Consider an alloy of Fe and V, where Fe is taken to be paramagnetic so that the rigid-band model can be applied. Based on Figure 4.38, we would expect that the Fe atoms lose charge and the V atoms gain charge when alloyed (i.e., $E_F^{\mathrm{V}} < E_F^{\mathrm{Fe}}$). The Fe atoms will experience stiffer forces, as

there are less electrons available for screening. This is not what is determined from experiment. For this model to give the correct result we must assume that, although the total electronic density of states may be given by the rigid-band model, the partial electronic density of states of the two atoms species can differ. A simple example is given for the $Fe_{50}V_{50}$ alloy in Figure 4.39. The electronic partial density of states curve of Fe is larger than for V, especially at the Fermi energy. With more electrons than the V atoms the local forces on the Fe atoms are lower than those for V atoms, leading to the observed softening.

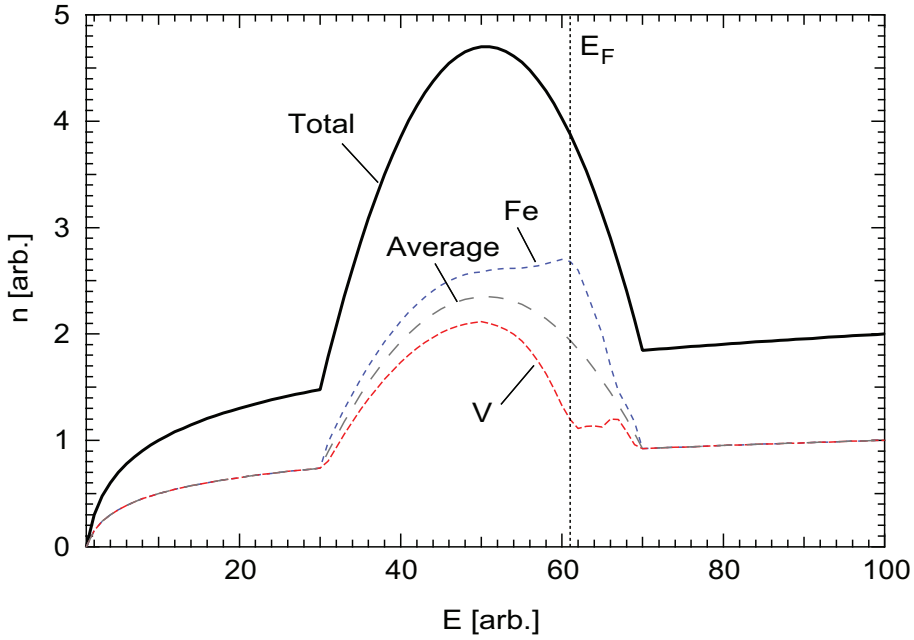

Figure 4.39: Example of the rigid-band model for an $Fe_{50}V_{50}$ alloy. These curves are for illustrative purposes only, and do not represent actual data. The total electronic density of states for the paramagnetic state is given by the solid line. The Fe and V electronic partial density of states curves differ from each other, but sum to the total electronic density of states. The curve labeled "Average" shows 1/2 of the total and the average of the Fe and V electronic partial density of states curves.

The argument above is very simple and there remains much work to be done to complete the Fe-V and Fe-Co data sets. Inelastic neutron scattering should be performed to determine the total DOS and PDOS of the V and Co atoms. Ab initio calculations would also help to determine the origin of the changes in the local forces and relate them more accurately to the changes in the ^{57}Fe PDOS. Analyzing the results of ab initio calculations on the local electronic properties of the Fe atoms should provide a relationship between the electronic structure and the ^{57}Fe PDOS curves.

Chapter 5

Inelastic Neutron Scattering

5.1 Technique

This chapter presents and analyzes results from the low-resolution medium-energy chopper spectrometer (LRMECS). LRMECS is a time-of-flight chopper spectrometer located at the intense pulsed neutron source (IPNS, recently shut down) at Argonne National Laboratory. A layout of the instrument is shown in Figure 5.1.

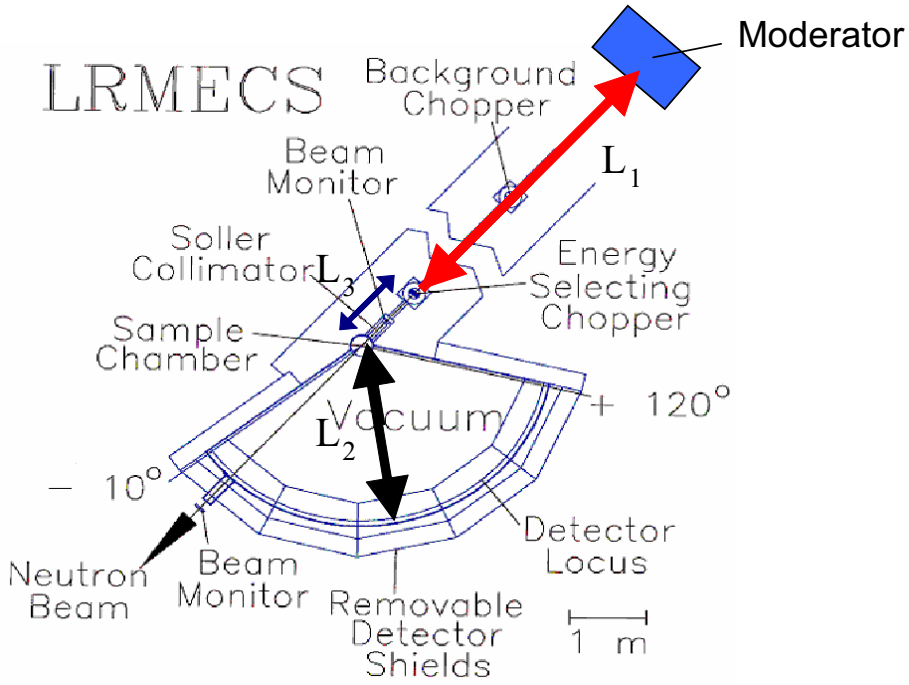

Figure 5.1: Equipment layout for the LRMECS instrument

Neutrons are created by bombarding heavy nuclei with protons in a process known as spallation.

These neutrons are then thermalized (slowed down to kinetic energies corresponding to approximately room temperature) in the moderator, which is a tank filled with solid methane at a set temperature. When the neutrons exit the moderator the velocity distribution has the character of solid methane, plus a high energy tail from "epithermal" neutrons that are not fully moderated. As these neutrons travel down the primary flight path (given by $L_1 + L_3$ in Figure 5.1) the difference in velocities causes the neutron pulse to spread in distance. The energy of the neutrons incident on the sample is chosen by chopping the moderated pulse (the energy selecting chopper is often referred to as the Fermi chopper). A chopper is a cylindrical can filled with a neutron absorbing material with a curved slit that allows neutrons to pass through only when it rotates. The frequency of the rotation and phase difference with the neutron pulse determines the energy of neutrons that pass through. Another chopper, placed earlier in the flight path and known as the t_0 chopper, acts to block the initial flash of particles created during the spallation. The t_0 chopper also prevents fortuitously timed slow-moving neutrons from a previous pulse from passing through the E_0 chopper during a second pulse (see Figure 5.2).

To first order, the energy resolution depends on the length of the primary flight path. The longer the path for the neutrons to travel, the more spread in distance the neutrons of different energy become. This allows for a finer chopping of the pulse and a smaller variation in the incident energy. The cost of this finer energy selection is a loss of counts. LRMECS offered a high-count-rate, low-resolution option for experimenters. In contrast, HRMECS (the high-resolution alternative) provided the low-count-rate, high-resolution option. The formula for the energy resolution of a time-of-flight chopper spectrometer is

$$\frac{\Delta\hbar\omega}{E_i} = \left\{ \left[\frac{2\Delta t_c}{t_c} \left(1 + \frac{L_1 + L_3}{L_2} \left(1 - \frac{\hbar\omega}{E_i} \right)^{\frac{3}{2}} \right) \right]^2 + \left[\frac{2\Delta t_m}{t_c} \left(1 + \frac{L_3}{L_2} \left(1 - \frac{\hbar\omega}{E_i} \right)^{\frac{3}{2}} \right) \right]^2 \right\}^{\frac{1}{2}}, \quad (5.1)$$

where $\hbar\omega$ is the energy of the excitation, E_i is the incident energy, Δt_c is the chopper burst time width (how long the chopper allows neutrons to pass through), t_c is the time of flight at the chopper, and Δt_m is the moderator pulse width [68]. The flight paths of LRMECS and other similar instruments

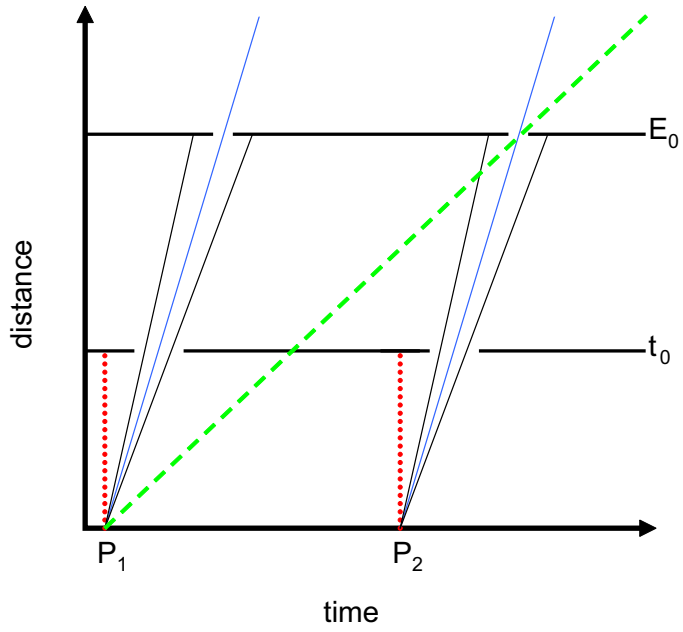

Figure 5.2: Illustration of the purpose of the choppers. The dotted line with nearly infinite velocity is the incident flash from the spallation event. The solid lines correspond to thermal neutrons, the energy of which are chosen by the E_0 chopper. The dashed line corresponds to a slow moving neutron that would pass through the E_0 chopper unless otherwise blocked by the t_0 chopper.

are given in Table 5.1.

Table 5.1: Characteristics of TOF Chopper Spectrometers

Instrument	$L_1 + L_3$	L_2
PHAROS	18 + 2	4
LRMECS	7	2.5
HRMECS	13.8	4
ARCS	11.6 + 2	3

As a side note, one of the biggest problems with performing measurements at a spallation source has historically been the low counts. Some technological advances, including neutron guides, have helped to boost the count rate at these sources. However, the largest technological leap is currently underway at Oak Ridge National Lab with the introduction of the Spallation Neutron Source (SNS). This facility is increasing the flux at the source by using a flowing liquid mercury (Hg) target. The flowing Hg gives higher cooling rates and allows for more incident protons. This is similar to a rotating anode X-ray source, where the rotation allows the target to cool, thus raising the maximum allowable current. A photo of the target at the SNS is shown in Figure 5.3. The wide-angular range

chopper spectrometer (ARCS) at the SNS will provide similar resolution to the HRMECS instrument (and lower resolution than PHAROS at the Lujan Center at Los Alamos National Laboratory) with a flux on the order of 1000 times greater than that provided at IPNS. This flux, unheard of in the pulsed-source neutron-scattering community, will allow new and interesting experiments on the dynamics of materials.

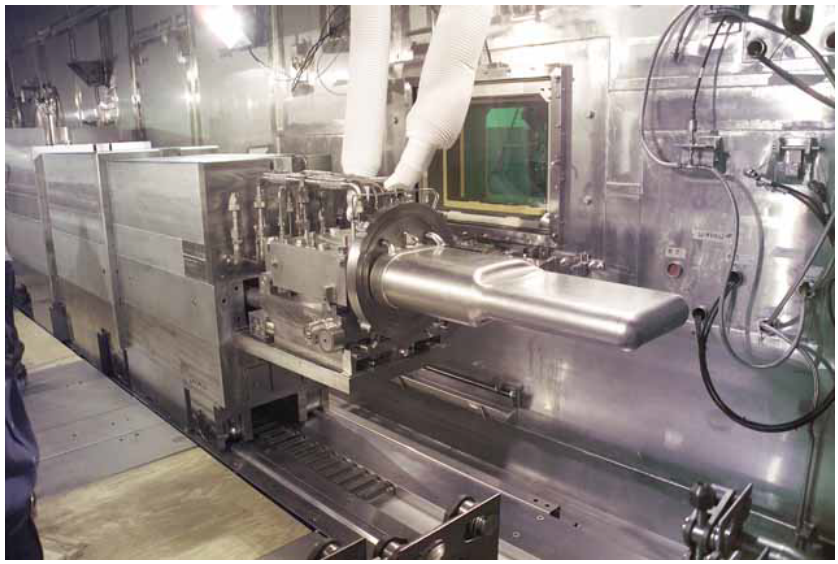

Figure 5.3: Flowing liquid mercury target at the Spallation Neutron Source. The entire assembly is fitted onto a track. All work done to the target is performed by robots in the sealed target room.

The raw data from LRMECS is intensity as a function of detector number and time of flight. For pure Fe measured on LRMECS at room temperature this is shown in Figure 5.4. The main feature in these data is the high-intensity elastic peak located at approximately 750 microseconds (μs). The timing begins when the pulse exits the moderator, so the neutrons require ~ 750 μs to travel down the primary flight path to scatter elastically off of the sample and travel through the detector chamber. The neutrons that arrive earlier than 750 μs have gained energy from the sample, thus increasing their speed and arriving earlier at the detectors. Neutrons that arrive later than 750 μs have lost energy to the sample, thus lowering their speed. Figure 5.4 also shows a few "dead" detectors and detectors giving spurious counts. These detectors can be masked or interpolated in the data analysis, and the efficiencies of the working detectors can be calibrated with data from a white beam run on vanadium. The data in intensity as a function of detector number and time of

flight is processed into intensity as a function of energy transfer E and momentum transfer Q, which is denoted by $S(Q, E)$. This is shown in Figure 5.5. This is the key figure for the data, as $S(Q, E)$ is directly related to the double-differential cross section

$$\left(\frac{d\sigma}{d\Omega dE'}\right) = \frac{\sigma}{4\pi\hbar}\frac{k'}{k} N\, S(\mathbf{Q}, E) \tag{5.2}$$

where k' is the magnitude of the scattered wave vector, k is the magnitude of the incident wave vector, and N is the number of scatterers in the system. The raw data was plotted using the program ISAW [69] and $S(Q, E)$ determined using the reduction code described in reference [70].

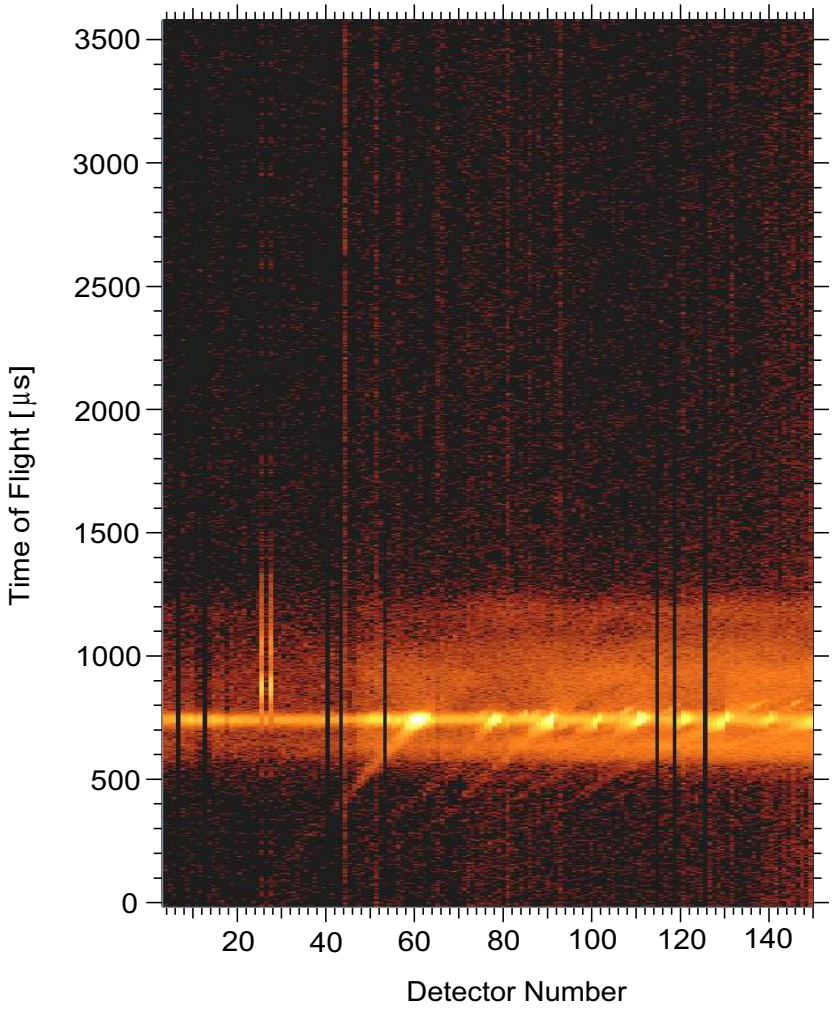

Figure 5.4: Scattering from pure Fe at 293K measured on LRMECS. Bright areas correspond to higher intensity.

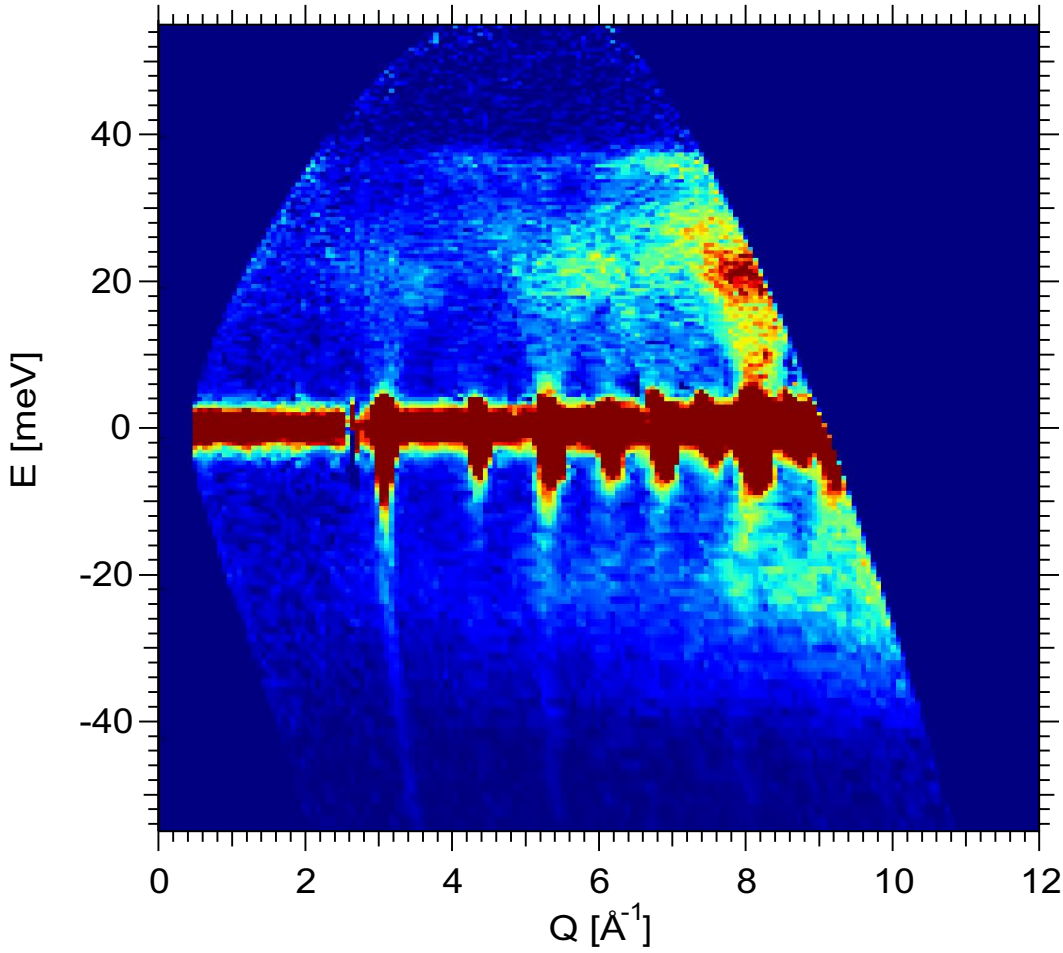

Figure 5.5: Scattering as a function of energy transfer and momentum transfer from pure Fe at 293K measured on LRMECS. Intensity increases from blue to red, with the maximum intensity along $E = 0$ meV.

5.2 Fe-Cr

5.2.1 Introduction

The Fe PDOS curves in Figure 4.6 are only half of the story for the lattice dynamics and phonon entropy of Fe-Cr alloys. Ideally Cr would also have a Mössbauer isotope and the PDOS curves of Cr would also be measured. Unfortunately nature is not so kind. Another method for determination of the lattice dynamics is with inelastic neutron scattering. One of the most desirable and problematic attributes of neutron scattering is the large variation of the scattering cross section for the elements and their isotopes. In the following sections we describe an experiment and analysis technique aimed

at overcoming this "neutron-weighting" problem as it pertains to the Fe-Cr system.

5.2.2 Experiment

Alloys of stoichiometric $Fe_{1-x_{Cr}}Cr_{x_{Cr}}$ for $x_{Cr} = \{1, 0.99, 0.97, 0.90, 0.80, 0.70, 0.47, 0.30, 0\}$ were prepared from shots of 99.99% Fe and 99.995% Cr by arc-melting under an argon atmosphere. There was negligible mass loss and little visible surface oxidation after melting, so the compositions are expected to be accurate to 0.1 at. %. The samples of composition $x_{Cr} \geq 0.70$ were then crushed to a thickness corresponding to a neutron scattering probability of 10%. The samples were sealed in quartz tubes under an argon atmosphere and annealed at 1100°C for several hours, followed by a quench into iced brine to ensure that the samples were random solid solutions. Samples with higher Fe concentration were ductile enough to be cold rolled to thicknesses corresponding to a neutron scattering probability of 10%. These samples were sealed in quartz tubes under an argon atmosphere and annealed for several days at 1100°C. The longer anneal time for the rolled samples reduced crystallographic orientation induced by the rolling.

X-ray diffraction patterns were acquired for all samples both before and after the anneal. The patterns indicated that all samples had the BCC structure. There was no measurable evidence of the sigma phase or of oxidation. Mössbauer spectroscopy was performed on all of the samples after the anneal. The spectra showed no indication of chemical unmixing.

Time-of-flight inelastic neutron scattering data were acquired using the Low-Resolution Medium-Energy Chopper Spectrometer (LRMECS) instrument at the Intense Pulsed Neutron Source at Argonne National Laboratory. Samples were mounted in thin-wall aluminum cans of dimensions 7 cm × 10 cm. The incident beam of monochromatic neutrons had an energy of approximately 60 meV. The flat sample packages were tilted at a 45 degree angle off the direction of the incident beam to minimize self shielding. All spectra were measured at room temperature. Background data were acquired from the empty aluminum cans under the same conditions.

5.2.3 Data Analysis and Results

Our data include both coherent and incoherent scattering from samples that are both polyatomic and polycrystalline. The total scattering cross section is given by the sum of the coherent and incoherent scattering. The incoherent neutron scattering cross section for nuclear scattering by a single crystal monatomic system is

$$\left(\frac{d\sigma}{d\Omega dE'}\right)^{\text{inc}} = \frac{k'}{k}\frac{N\,\sigma_{\text{inc}}}{2\pi\hbar}e^{-2W}\int e^{\langle UV\rangle}e^{(-i\omega t)}dt\,, \tag{5.3}$$

where $U = -i\mathbf{Q}\cdot\mathbf{u}(0)$, $V = i\mathbf{Q}\cdot\mathbf{u}(t)$. The variables σ_{inc}, $\mathbf{u}(t)$, W, N, $\mathbf{k}$, $\mathbf{k}'$, $\mathbf{Q}$, and $E = \hbar\omega$ are, respectively, the incoherent cross section, instantaneous atomic position, Debye-Waller factor, number of atoms in the system, initial and final neutron wavevectors, phonon wavevector (wavevector transfer), and phonon energy. Our first approximation is that all the measured scattering is incoherent. Despite the fact that both Fe and Cr are strong coherent scatterers (with $\sigma_{\text{inc,Fe}} = 0.40$, $\sigma_{\text{coh,Fe}} = 11.22$, $\sigma_{\text{inc,Cr}} = 1.66$, and $\sigma_{\text{inc,Cr}} = 1.83$ barns), the incoherent approximation (IA) is acceptable when the inelastic scattering is measured over a broad range of $\mathbf{Q}$ and E [71], and the structure in $\mathbf{Q}$ is averaged and neglected.

The incoherent scattering cross section contains both elastic and inelastic contributions. The elastic scattering can be removed from the raw data, so we concern ourselves with only the inelastic scattering. The inelastic scattering is a sum of the single and multiphonon scattering

$$\left(\frac{d\sigma}{d\Omega dE'}\right)^{\text{inc}}_{\text{inelastic}} = \sum_{n=1}^{\infty}\left(\frac{d\sigma}{d\Omega dE'}\right)^{\text{inc}}_{n-\text{phonon}}\,, \tag{5.4}$$

where n denotes the number of phonons created or annihilated in the scattering event,

$$\left(\frac{d\sigma}{d\Omega dE'}\right)^{\text{inc}}_{n-\text{phonon}} = \frac{k'}{k}\frac{N\,\sigma_{\text{inc}}}{4\pi\hbar}\frac{e^{-2W}}{n!}\left(\frac{3\hbar}{2m}\right)^{n}[P(\omega)]^{n-\text{convolution}} \tag{5.5}$$

m is the mass of the scatterer, and

$$P(\omega) = \frac{\langle (\boldsymbol{Q}\cdot\boldsymbol{e}_s)^2\rangle_\omega}{\omega} g(\hbar\omega)\langle n_\omega + 1\rangle + \frac{\langle (\boldsymbol{Q}\cdot\boldsymbol{e}_s)^2\rangle_{-\omega}}{-\omega} g(-\hbar\omega)\langle n_{-\omega}\rangle \ . \tag{5.6}$$

The index s specifies a single vibrational mode and the notation $[f]^{n-\text{convolution}}$ specifies the sequential convolution of n instances of the function f. For example,

$$[P(\omega)]^{1-\text{convolution}} \equiv P(\omega) \tag{5.7}$$

and

$$[P(\omega)]^{2-\text{convolution}} = \int_{-\infty}^{\infty} P(x)P(\omega - x)\mathrm{d}x \ . \tag{5.8}$$

The quantity $\langle (\boldsymbol{Q}\cdot\boldsymbol{e}_s)^2\rangle_\omega$ is the value of $(\boldsymbol{Q}\cdot\boldsymbol{e}_s)^2$ averaged over all modes of frequency ω. The incoherent one-phonon scattering for a monatomic polycrystalline sample is then:

$$\left(\frac{d\sigma}{d\Omega dE'}\right)^{\text{inc}}_{1-\text{phonon}} = \frac{k'}{k}\frac{\sigma_{\text{inc}}}{4\pi}\frac{N}{4m}\, Q^2\, e^{-2W}\frac{g(\hbar\omega)}{\omega}\left[\coth\left(\frac{1}{2}\hbar\omega\beta\right) \pm 1\right] \tag{5.9}$$

where $\beta = 1/(k_B T)$. The + denotes phonon creation and the − phonon annihilation.

For a polyatomic sample we invoke a virtual crystal approximation which assumes a single mass and scattering factor for an average atom:

$$g^{\text{nw}}(E,\vec{\sigma})\, e^{(-2\langle W\rangle_d)}\left\langle\frac{\sigma_{\text{sc}}}{m}\right\rangle_d = \sum_d g(E,\vec{\sigma}_l,d)\, e^{-2W_d}\frac{\sigma^d_{\text{sc}}}{m_d} \ . \tag{5.10}$$

Here $g^{\text{nw}}(E,\vec{\sigma})$ is the DOS that results from the virtual crystal approximation and is termed the neutron-weighted DOS (NWDOS), which is a function of the configuration of atoms on the lattice $\vec{\sigma}$. The phonon partial density of states (PDOS) of atom d for a given local chemical arrangement $\vec{\sigma}_l$ is given by $g(E,\vec{\sigma}_l,d)$. The $\langle ...\rangle_d$ denotes an average over all atoms. The $g^{\text{nw}}(E,\vec{\sigma})$ are obtained from the raw data by the following procedure:

The raw data, in intensity as a function of detector number and time of flight, were first corrected

for the efficiency of the detectors, using a white beam measurement of pure vanadium (a fully incoherent scatterer). The data were then normalized using the integrated intensity in the beam monitor. An average of the counts at the longest times of flight was taken as an estimate of the time-of-flight independent background and removed. The data were rebinned into intensity, I, as a function of angle, ϕ, from 5° to 145° by 0.6°, and energy, E, from -65.0 to 65.0 meV by 0.5 meV. The data were again rebinned to give intensity $I(Q, E)$, where Q is the wavevector-transfer which ranged from 0.0 to 13.5 Å^{-1} by 0.0675 Å^{-1}. The spectrum from the empty container, scaled by 0.9 to account for the self-shielding of the sample, was subtracted from the data. An example of such a corrected $I(Q, E)$ is shown in Figure 5.6. The data were cropped below $Q \approx 2.8\,\text{Å}^{-1}$ to minimize contributions from magnetic scattering, which dominates at small Q. After removal of an elastic peak centered about 0 meV, the data below approximately 10 meV were replaced by the function $\mathcal{A}E/(1 - \exp(-\beta E))$ with $\mathcal{A}$ a normalization constant determined from the data. The instrument resolution for positive neutron energy transfer is much better than for negative (see Figure 5.6), so only the data for $E > 0$ were used for determining $g^{\text{nw}}(E, \vec{\sigma})$.

Finally, under the assumptions of the virtual crystal approximation and the incoherent approximation, we recover the one phonon DOS using the iterative procedure described by Sears et al. [72] as modified by Kresch et al. [70]. This procedure corrects for thermal occupancy, Debye-Waller factor, multiphonon (2- through 5-phonon) and multiple scattering as a function of Q, and then the (neutron-weighted) phonon DOS is the sum over all Q of the corrected data. These neutron-weighted phonon DOS (NWDOS) curves are normalized to one in energy and presented in Figure 5.7.

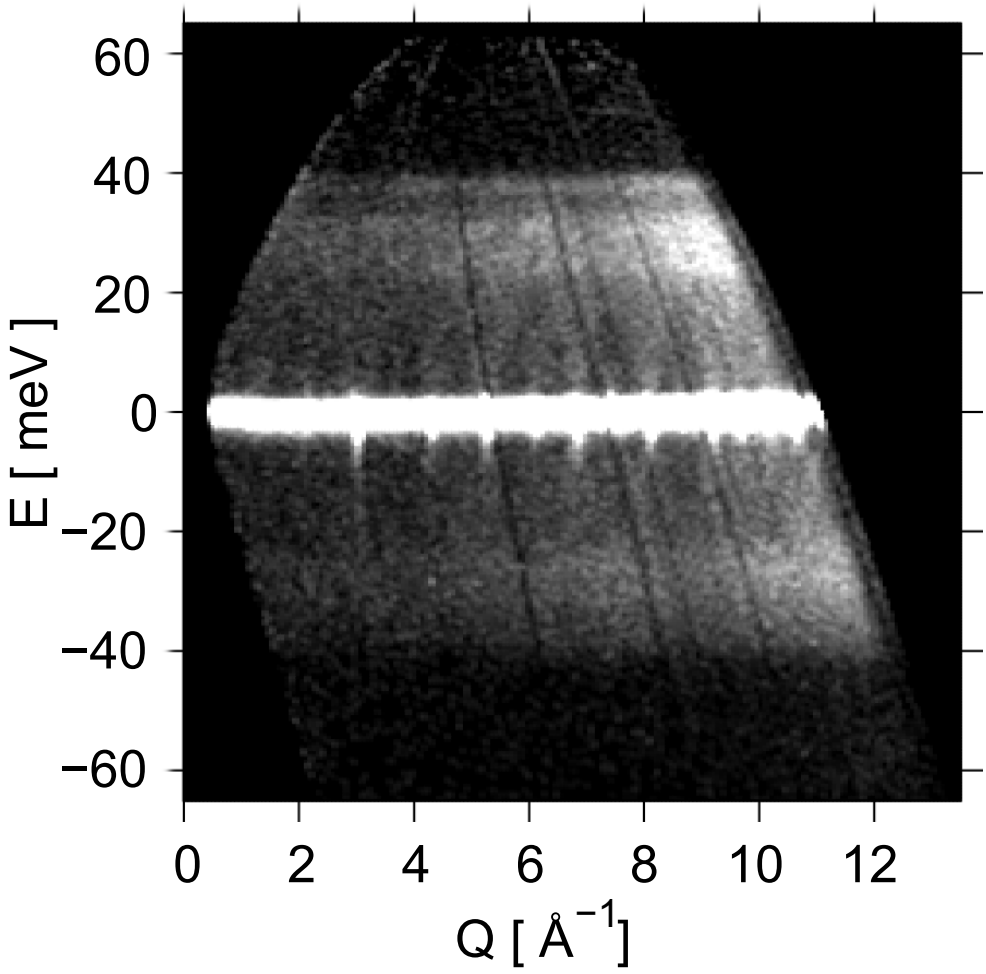

Figure 5.6: Measured $I(Q, E)$ for pure Cr, where E is the neutron energy transfer to the sample. White indicates areas of higher intensity, with the large elastic peak evident at 0 meV. Coherent scattering can be seen to emanate from the Bragg peaks.

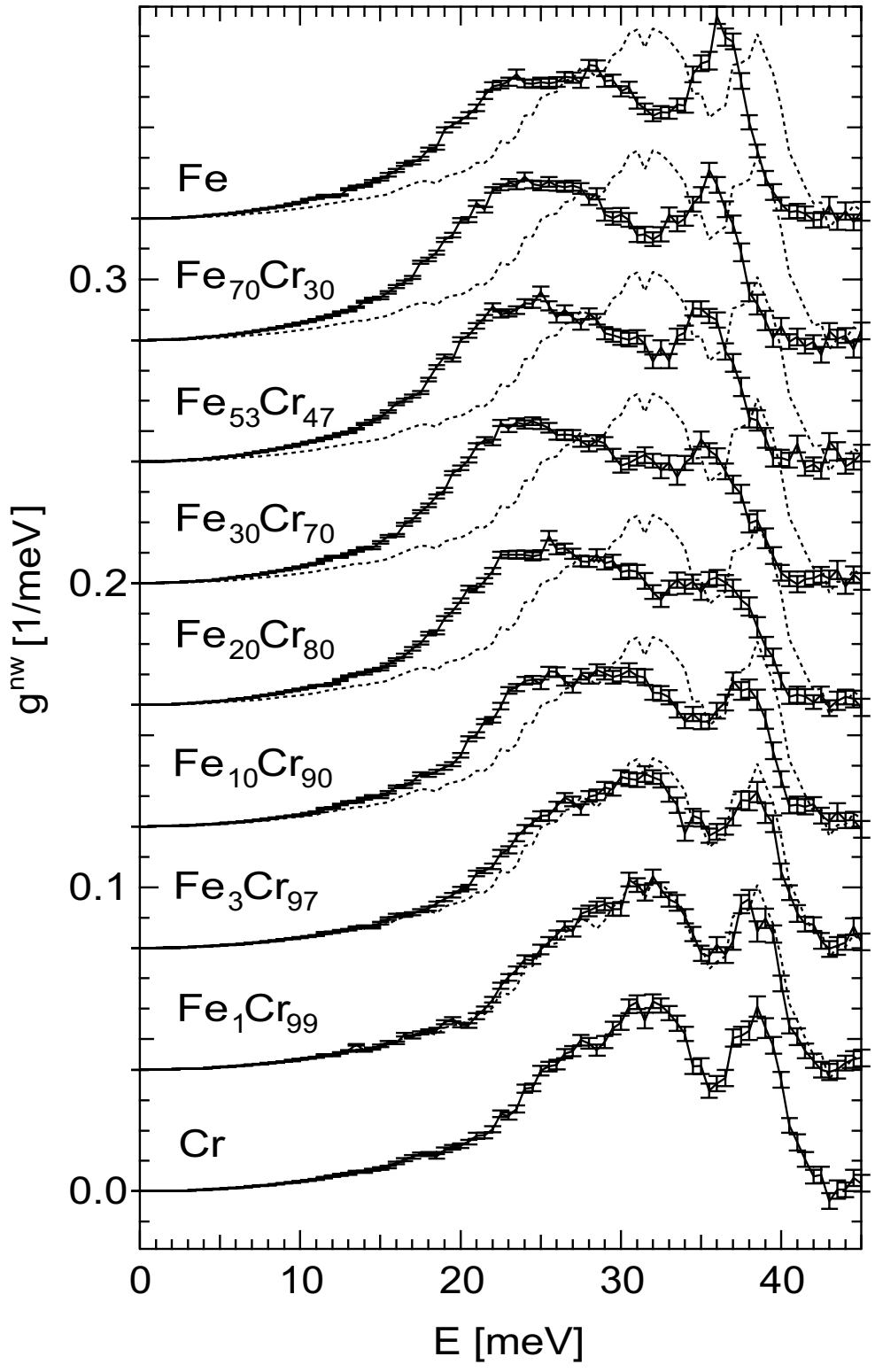

Figure 5.7: Measured neutron-weighted phonon density of states curves for alloys $g^{\mathrm{nw}}(E)$, and $g(E)$ for elements. The dashed lines are the measured Cr DOS for comparison. Curves are offset by integer multiples of 0.04 meV^{-1}.

5.2.4 Phonon Partial DOS

The NWDOS is a linear combination of the PDOS, distorted by differences in the efficiencies of phonon scattering of the different atoms. To calculate thermodynamic quantities, such as the vibrational entropy or phonon contribution to the heat capacity, the undistorted total phonon DOS is required:

$$g(E,\vec{\sigma}) = \sum_d g(E,\vec{\sigma}_l,d)x_d \ , \tag{5.11}$$

where $g(E,\vec{\sigma}_l,d)$ is the PDOS and x_d is the concentration of atom species d ($0 \leq x_d \leq 1$). We assume $\exp[-2(\langle W\rangle_d - W_d)] \simeq 1$, which is most reliable at low temperatures, so that Equation 5.10 becomes:

$$g^{\mathrm{nw}}(E,\vec{\sigma}) = \left\langle \frac{\sigma_{\mathrm{sc}}}{m} \right\rangle_d^{-1} \sum_d g(E,\vec{\sigma}_l,d)\frac{\sigma_{\mathrm{sc}}^d}{m_d}x_d \ , \tag{5.12}$$

where the normalization factor is given by:

$$\left\langle \frac{\sigma_{\mathrm{sc}}}{m} \right\rangle_d = \left(\sum_d \frac{\sigma_{\mathrm{sc}}^d}{m_d}x_d \right). \tag{5.13}$$

In our case, phonon scattering from natural Fe is approximately three times stronger than from natural Cr, or $\sigma_{\mathrm{sc}}^{\mathrm{Fe}}/m_{\mathrm{Fe}} \simeq 3\sigma_{\mathrm{sc}}^{\mathrm{Cr}}/m_{\mathrm{Cr}}$. The data reduction technique described in Section 5.2.3 produces a NWDOS, where the Fe PDOS is over-weighted by a factor of 3. This distorts the NWDOS from the true DOS if the Fe PDOS differs from the Cr PDOS, with a larger distortion if the PDOS curves differ significantly.

The available Fe PDOS curves from NRIXS [73] can be used directly in a neutron-weight correction for the alloys $Fe_{30}Cr_{70}$, $Fe_{53}Cr_{47}$, and $Fe_{70}Cr_{30}$. The Cr PDOS curves can then be determined using Equation 5.12, with the results shown in Figure 5.8. Especially at low Fe concentrations, knowledge of the Fe PDOS from NRIXS is useful for determining the Cr PDOS. At higher Fe concentrations, the scattering from the Cr atoms is overwhelmed by that of Fe atoms, and a larger Fe PDOS must be removed from the measured NWDOS to determine the Cr PDOS. The result is an inherently poor signal-to-noise for the Cr PDOS, as is evident in Figure 5.8 for the alloy $Fe_{70}Cr_{30}$.

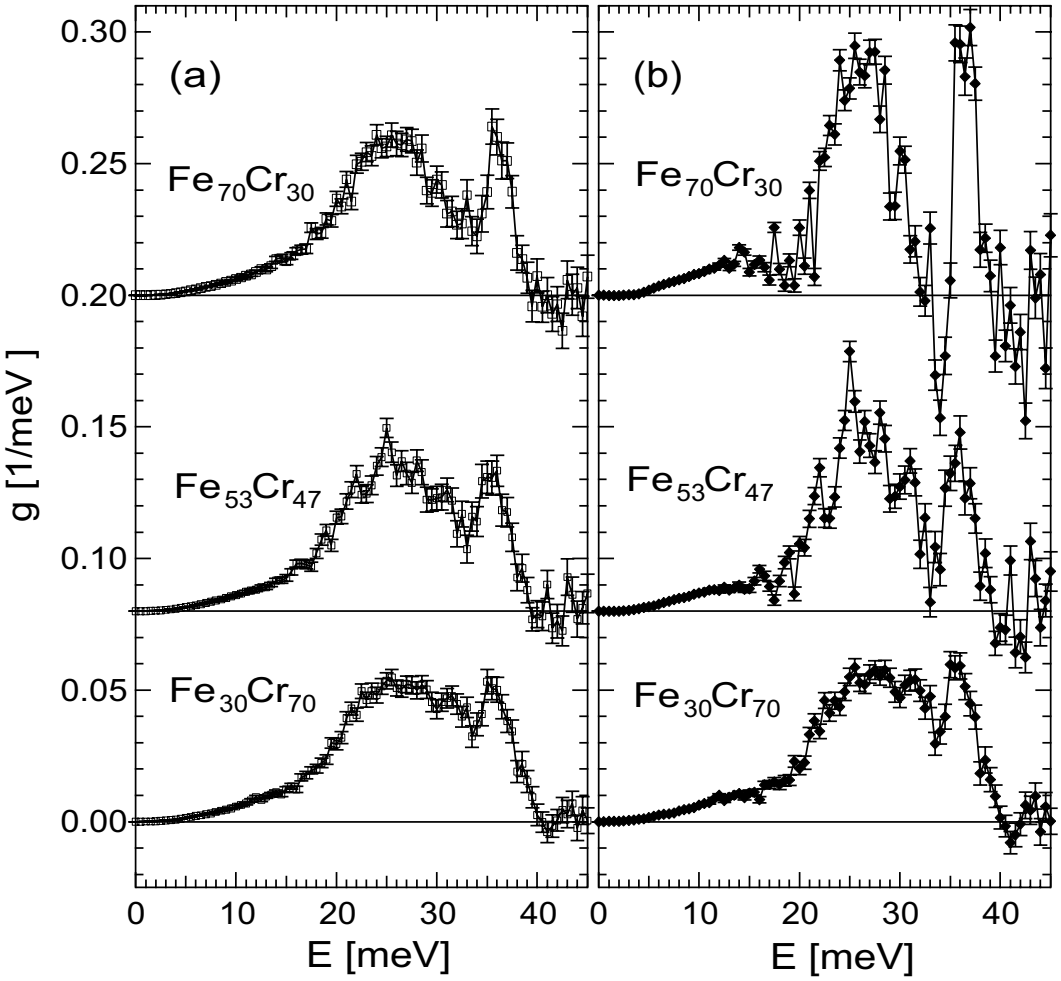

Figure 5.8: (a) Neutron-weight corrected DOS for $Fe_{30}Cr_{70}$, $Fe_{53}Cr_{47}$, and $Fe_{70}Cr_{30}$ using Fe PDOS curves from NRIXS [73]. (b) Cr PDOS curves determined from measured NWDOS and Fe PDOS curves from NRIXS. The curves for $Fe_{53}Cr_{47}$ and $Fe_{70}Cr_{30}$ are offset by 0.08 and 0.20 meV^{-1}, respectively.

The following sections describe a different method for determining the Cr and Fe PDOS curves. This method utilizes a cluster expansion technique to extract chemical trends from the NWDOS curves. For inputs, this method requires two PDOS curves from dilute Fe-Cr and Cr-Fe alloys. Section 5.2.4.1 shows how these two "impurity" PDOS curves can be derived from the data set in Figure 5.7 with two different methods. Only the results of neutron scattering experiments are used in the subsequent analysis. The available results from NRIXS [73, 39] provide a verification of the method.

5.2.4.1 PDOS in the Dilute Limit

This section presents two methods for obtaining the PDOS of an impurity atom in an otherwise pure host. The first method uses only the measured NWDOS curves of Figure 5.7, but the statistical quality of the present data requires the use of the second method. Both methods rely on the assumption that the PDOS of the host atoms is unaltered by the impurity atoms. For V with impurities of Cr this assumption has been shown to be good, owing to the similarities of the Fermi surface of V and V-Cr [74, 59], and for the same reason we expect this to be valid for Fe-Cr. The PDOS measured by NRIXS of Fe_3Cr_{97} provides a check of this assumption for Fe-Cr.

Comparing the measured DOS of the pure element to the measured NWDOS of a sample with small amounts of impurity atoms can provide the PDOS of the impurity atom. Following Equation 5.12 the PDOS of impurity atom i in pure element host h, $g(E, x_\mathrm{i}, \mathrm{i})$, is given by:

$$g(E, x_\mathrm{i}, \mathrm{i}) = \left[\frac{\sigma_\mathrm{sc}^\mathrm{h}}{M_\mathrm{h}} \frac{M_\mathrm{i}}{\sigma_\mathrm{sc}^\mathrm{i}} \frac{(1-x_\mathrm{i})}{x_\mathrm{i}} + 1\right] g^\mathrm{nw}(E, x_\mathrm{i}) - \left[\frac{\sigma_\mathrm{sc}^\mathrm{h}}{M_\mathrm{h}} \frac{M_\mathrm{i}}{\sigma_\mathrm{sc}^\mathrm{i}} \frac{(1-x_\mathrm{i})}{x_\mathrm{i}}\right] g(E, x_\mathrm{h} = 1) \; . \tag{5.14}$$

Here $g(E, x_\mathrm{h} = 1)$ denotes the measured DOS of the pure host element, $g^\mathrm{nw}(E, x_\mathrm{i})$ denotes the measured NWDOS of the pure host with impurities of atom i, and x_i is the atomic fraction of the solute atoms. Figure 5.9a shows the impurity PDOS of 3 at% Fe in Cr determined with this method by weighted subtraction of the lower curves of Figure 5.7. Although the error bars are quite large, it is apparent that the agreement with the result of NRIXS [39] is reasonable. Within the quality of our experimental results, a decomposition into host plus impurity PDOS curves is successful for Fe-Cr dilute alloys. Determination of the Cr PDOS curves from this method suffers from much larger error bars due to the lower scattering efficiency of Cr atoms. Another method for acquiring the PDOS of impurity Cr atoms is required.

The lattice dynamics of crystals with dilute impurities was developed by Mannheim [57, 46] with Green's function techniques for interatomic force-constants described by a single longitudinal stiffness (Appendix C). The assumption is made that the introduction of the impurity perturbs only the first-nearest-neighbor (1NN) bonds to the impurity atom. The only information required for

this theory is the DOS of the pure host, the mass ratio of the host to impurity atoms $m_{\rm h}/m_{\rm d}$, and the ratio of the host-host force constant to the impurity-host force constant $K_{\rm h-h}/K_{\rm d-h}$. The force constants of Fe-Cr alloys have been determined previously by inelastic neutron scattering [38]. The ratio $K_{\rm h-h}/K_{\rm d-h}$ can be approximated by the ratio of the 1NN longitudinal force constants of the pure host with the 50-50 alloy

$$\frac{K_{\rm h}}{K_{\rm i-h}} \simeq \frac{C^{\rm h}_{111xx}}{C^{\rm i_{50}h_{50}}_{111xx}} \ . \tag{5.15}$$

For Fe in Cr, this ratio is 1.26, which is similar to the value of 1.25 reported previously [75]. The value obtained for Cr in Fe is 1.01, which has been used in determining the impurity Cr PDOS in Fe. The impurity PDOS of Fe determined from the Mannheim method using the pure Cr DOS measured with LRMECS is shown in Figure 5.9c. The results of the Mannheim method for the PDOS curves of both Fe and Cr in the dilute limit are used in the analysis that follows below.

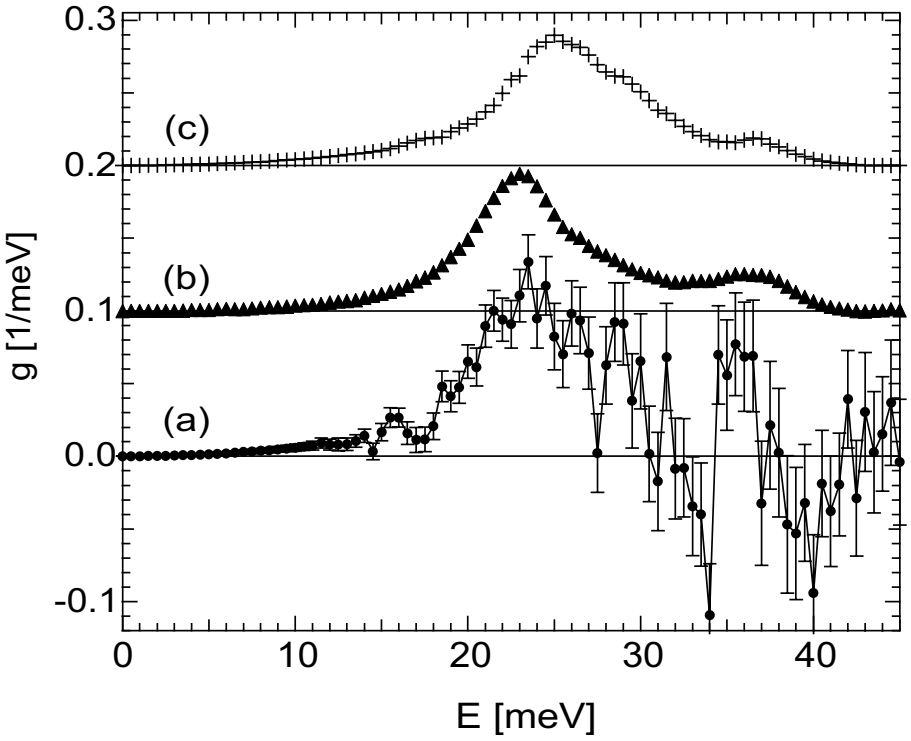

Figure 5.9: PDOS of Fe in Fe_3Cr_{97} determined from (a) the results in the present article following the subtraction method given in the text, (b) the results of NRIXS from the literature [39] (offset by 0.1 meV^{-1}), (c) the Mannheim Method with $K_{\tt Cr-Cr}/K_{\tt Fe-Cr} = 1.26$ using pure Cr measured at LRMECS (offset by 0.2 meV^{-1}).

The first step in performing a cluster expansion is to rescale the NWDOS curves by the phonon

cutoff energy, $E^c(\vec{\sigma})$. The GCE used for Fe-Cr is fourth order, whereas the data set on Fe-Cr contains nine values of the cutoff energy. To include all of the measured information into ϵ_n^c a weighted least-squares fitting is performed with the $E_m^c(\vec{\sigma})$ measured for the random solid solutions. The weighted sum of the squares for error are:

$$\chi^2 = \sum_{m=1}^{N} \frac{(E_m^c(x_m) - E_{\text{Fit}}^c(x_m))^2}{(\delta E_m^c(x_m))^2} \ . \tag{5.16}$$

The summation index m denotes the N measured alloys and $E_{\text{Fit}}^c(x_m)$ denotes the cutoff energy created from ϵ_n^c for the alloy with concentration x_m. The ϵ_n^c can then be written as:

$$\begin{Bmatrix} \epsilon_0^c \\ \epsilon_1^c \\ \epsilon_2^c \\ \epsilon_3^c \end{Bmatrix} = \left[[\xi_{m,n}]^{\mathrm{T}} [\Omega] [\xi_{m,n}] \right]^{-1} [\xi_{m,n}]^{\mathrm{T}} [\Omega] \ \vec{E}^c(x_m) \tag{5.17}$$

where $[\Omega]$ is the error-weighting matrix given by diagonal elements $1/\delta E_m^c(x_m)$ and the terms of $\vec{E}^c(x_m)$ are given by $E_m^c(x_m)$. For Fe-Cr the fit to the cutoff energies are given in Figure 5.10 and the ϵ_n^c determined from the fit are given in Table 5.2. The measured NWDOS as a function of $\mathcal{E}$ are shown in Figure 5.11.

Table 5.2: Values of Interaction Cutoff Energy Parameters

n	ϵ_n^c [meV]
0	40.089
1	-0.888
2	1.797
3	-0.007

The next step is to determine the neutron-weighted interaction phonon density of states (NWI-DOS) functions, $\mathcal{G}_n^{\text{nw}}(\mathcal{E})$. The limitations of using random solid solutions for determination of interaction functions were assessed using the condition number of the correlation function matrix in Section 3.4.1. Here we simply note that only a small number of terms can be used when extracting chemical trends from measurements of random solid solutions, owing to the lack of both

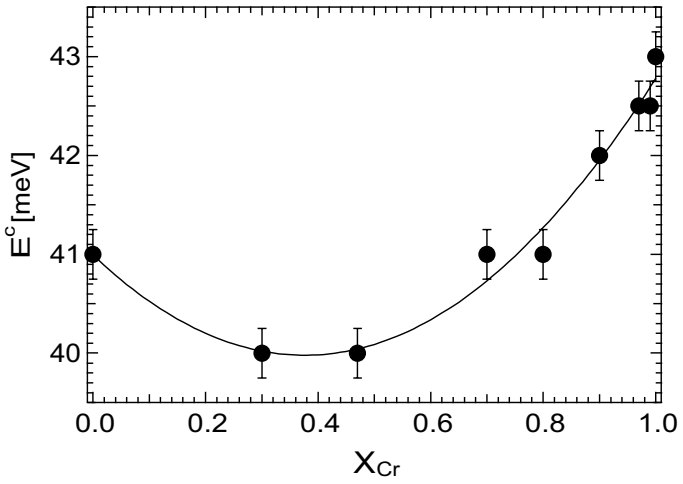

Figure 5.10: Cutoff energy as a function of concentration. The solid line indicates the fit curve using the cluster expansion.

long-range and short-range order. For this reason a GCE using four terms, up to the triangle cluster, is utilized for the NWDOS. The relation between the NWDOS curves of a random solid solution of concentration x_{Cr}, $g^{\mathrm{nw}}(\mathcal{E}, x_{\mathrm{Cr}})$, and the NWIDOS functions is (following Equation B.6),

$$g^{\mathrm{nw}}(\mathcal{E}, x_{\mathrm{Cr}}) \left\langle \frac{\sigma_{\mathrm{sc}}}{m} \right\rangle_d^{-1} = \sum_{n=0}^{3} \mathcal{G}_n^{\mathrm{nw}}(\mathcal{E})(1 - 2x_{\mathrm{Cr}})^n \ . \tag{5.18}$$

Since there are more measurements than terms used in the expansion, the problem is over-specified and a weighted least-squares fitting must be performed to include all of the measured information into the NWIDOS functions. The NWIDOS functions and impurity PDOS curves can be used to determine the IPDOS functions, $\mathcal{G}_n(\mathcal{E}, d)$, following the method described in Appendix B.

5.2.4.2 Interaction Phonon Partial Density of States functions of Fe-Cr

The IPDOS functions of Fe and Cr in Fe-Cr determined from fits to the neutron scattering data and the impurity PDOS curves determined from the Mannheim method (Section 5.2.4.1) are shown in Figure 5.12. For comparison, the PDOS curves of Fe in Fe-Cr alloys determined from NRIXS [39, 73] were also used to construct the IPDOS functions of Fe, and both sets of $\mathcal{G}_n(\mathcal{E}, \mathrm{Fe})$ are compared in Figure 5.13. The curves match well, especially in their compositional trends, and agreement is best for the higher Fe concentrations where the neutron scattering analysis is most reliable.

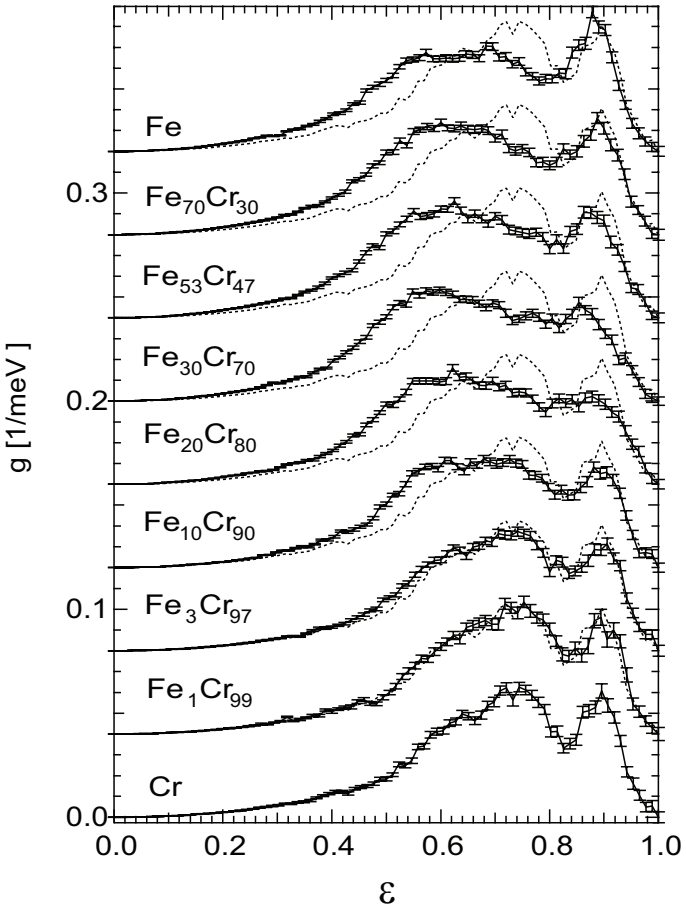

Figure 5.11: Neutron-weighted phonon density of states measured at LRMECS using the energy relative to the cutoff. The dashed curve is pure Cr for reference. Curves are offset by integer multiples of 0.4 meV^{-1}.

The effects of local order on the PDOS curves of Fe in Fe-Cr were explained in Section 4.2.5 in terms of the $\mathcal{G}_n(\mathcal{E}, \mathrm{Fe})$, and the same interpretation is successful for the effects of local order on the PDOS curves of Cr in Fe-Cr. The $n = 0$ term is the Cr PDOS of a random solid solution of $Fe_{50}Cr_{50}$. The $n = 1$ term gives the effect on the PDOS of having different numbers of Fe and Cr atoms in the 1NN and 2NN shells of the Cr atom. The triangle term, $n = 2$, gives the effect of like or unlike pairs of atoms within the 1NN and 2NN shells of the Cr atom. The function $\mathcal{G}_1(\mathcal{E}, \mathrm{Cr})$ is added to $\mathcal{G}_0(\mathcal{E}, \mathrm{Cr})$ when the atom in the 1NN and 2NN shell of the Cr atom is Cr, and subtracted when it is Fe. Figure 5.12 shows that the effect of Cr atoms in the 1NN and 2NN shell of the Cr atom is to decrease the number of modes in the ranges of $0 \leq \mathcal{E} \leq 0.59$ and $0.83 \leq \mathcal{E} \leq 1$, while increasing the number of modes in the range $0.59 < \mathcal{E} < 0.83$. The function $\mathcal{G}_2(\mathcal{E}, \mathrm{Cr})$ adds to both

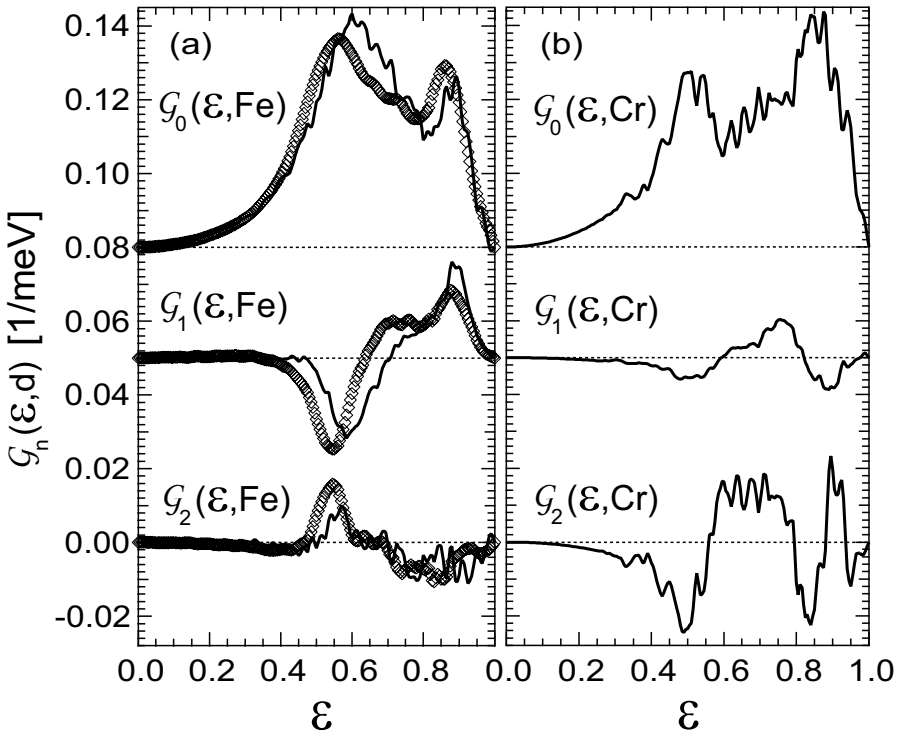

Figure 5.12: IPDOS functions of Fe (a) and Cr (b) in Fe-Cr determined from neutron scattering (solid lines) and NRIXS (thick curve). The $n = 0$ and $n = 1$ terms are offset by 0.08 and 0.05 meV^{-1}, respectively.

$\mathcal{G}_0(\mathcal{E},\mathrm{Cr})$ and $\mathcal{G}_1(\mathcal{E},\mathrm{Cr})$ when a pair in the 1NN and 2NN shell of the Cr atom is composed of two of the same atoms. Pairs of like atoms decrease the number of modes in the ranges $0 \leq \mathcal{E} \leq 0.56$, $0.80 \leq \mathcal{E} \leq 0.88$, and $0.94 \leq \mathcal{E} \leq 1$, while increasing the number of modes in the remaining ranges, whereas unlike pairs do the opposite.

Comparing the Fe and Cr IPDOS functions in Figure 5.12 provides further information on how local order alters the phonons in Fe-Cr. To show the effects of Cr concentration on both the Fe and Cr PDOS curves, the function $\mathcal{G}_1(\mathcal{E},\mathrm{Fe})$ must be multiplied by -1, as shown in Figure 5.14. With increasing Cr concentration, each of these functions is added to its respective PDOS. In both cases, increasing the Cr concentration decreases the number of low-energy modes in the range $0 \leq \mathcal{E} \leq 0.37$. In the range $0.37 < \mathcal{E} \leq 0.67$ the effects of Cr on the PDOS curves is opposite in sign, with the magnitude of the increase in the Fe modes being much larger than the decrease for Cr. For $\mathcal{E} > 0.82$, the longitudinal modes of both Fe and Cr are reduced (shifted to lower $\mathcal{E}$) by increasing the concentration of Cr. The functions $\mathcal{G}_2(\mathcal{E},\mathrm{Fe})$ and $\mathcal{G}_2(\mathcal{E},\mathrm{Cr})$ have similar features in the range

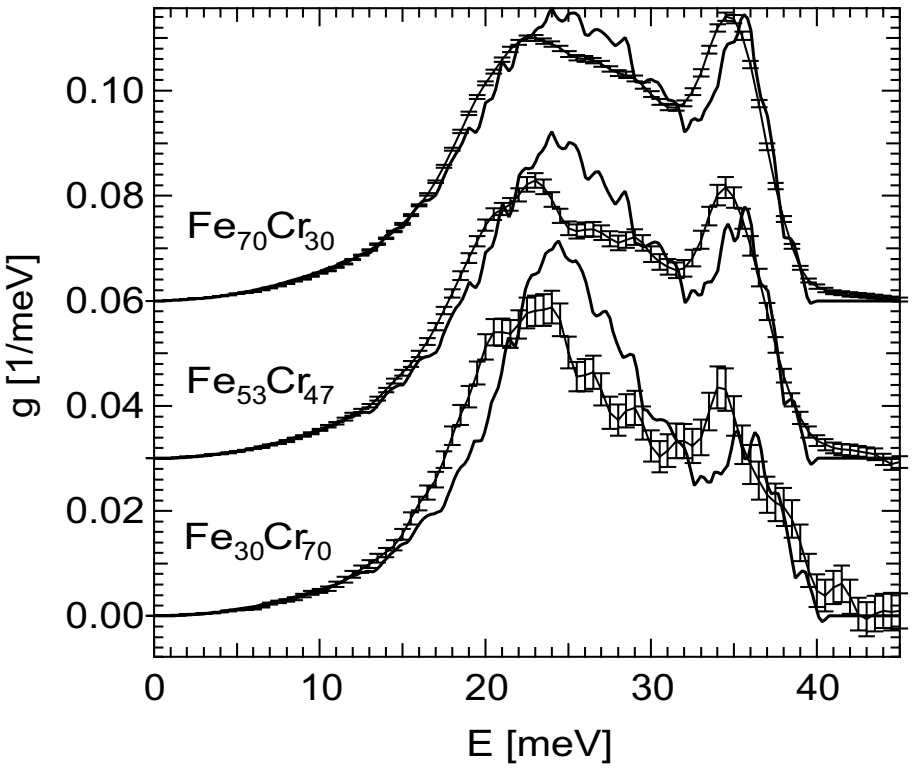

Figure 5.13: PDOS curves of Fe determined from neutron scattering (lines) and NRIXS (lines with error bars). Curves are offset by integer multiples 0.03 meV^{-1}.

$0 \leq \mathcal{E} \leq 0.70$, indicating similar effects of the pair interaction on the longitudinal modes of both the Fe and Cr PDOS.

The IPDOS functions can be used to construct the PDOS curves of Fe and Cr atoms for our alloys (Figure 5.15). These PDOS curves can then be used to construct the neutron-weight-corrected DOS curves following Equation 5.11. The results are shown in Figure 5.16. It is evident that the neutron weight correction stiffens all of the DOS curves. This is expected, as the Fe PDOS curves have more low-energy modes than the Cr PDOS curves, especially below $\mathcal{E} = 0.7$, but Fe atoms are more efficient scatterers.

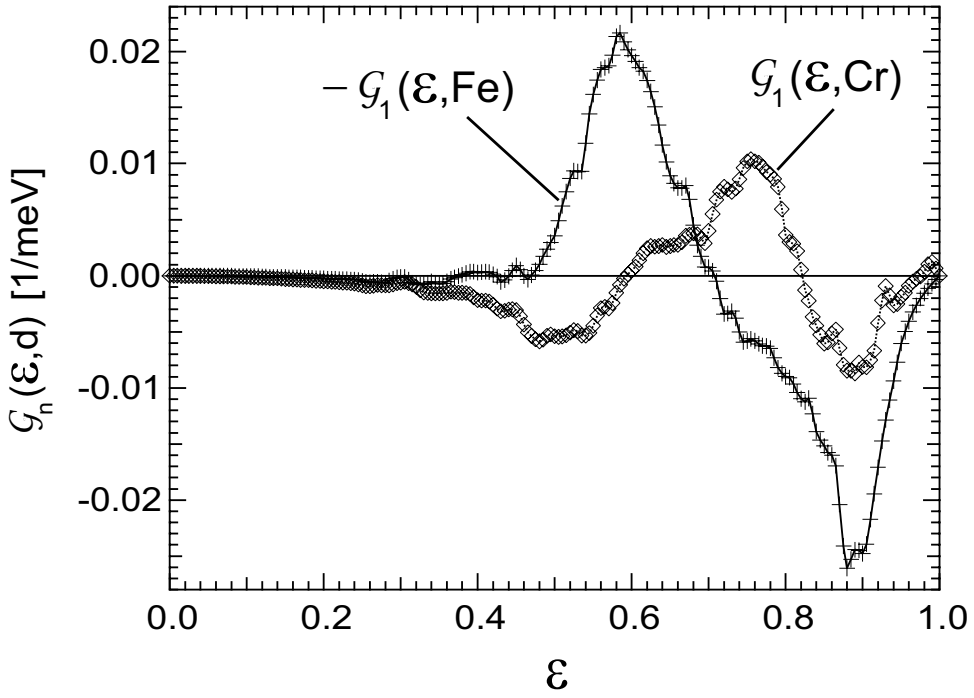

Figure 5.14: The dependence on Cr concentration of the Fe and Cr PDOS curves. The minus sign for Fe accounts for the $(-1)^n$ in Equation 3.5.

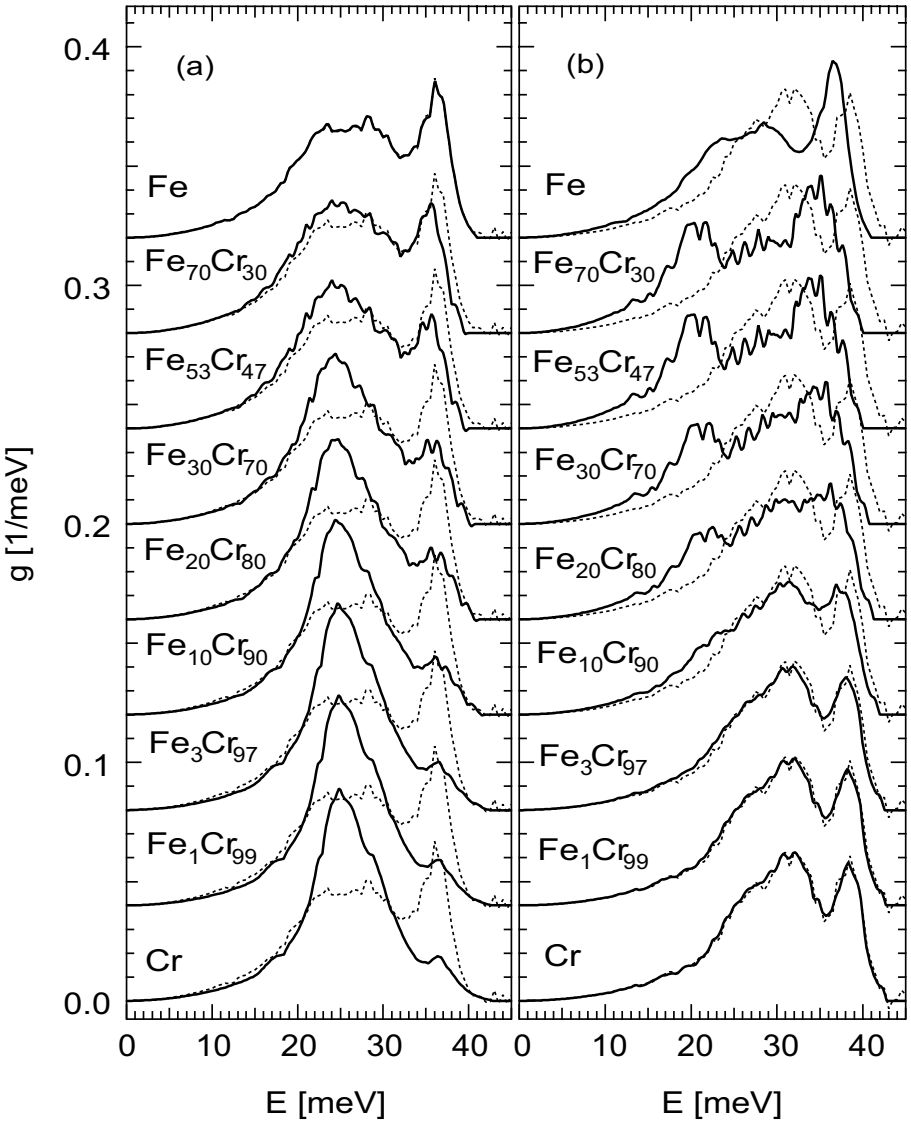

Figure 5.15: PDOS curves from the cluster expansion fitting method for the concentrations of the alloys measured: (a) Fe PDOS curves (solid lines) and measured pure Fe DOS (dashed line), and (b) Cr PDOS curves (solid lines) and measured pure Cr DOS (dashed line). Curves are offset by integer multiples 0.04 meV^{-1}.

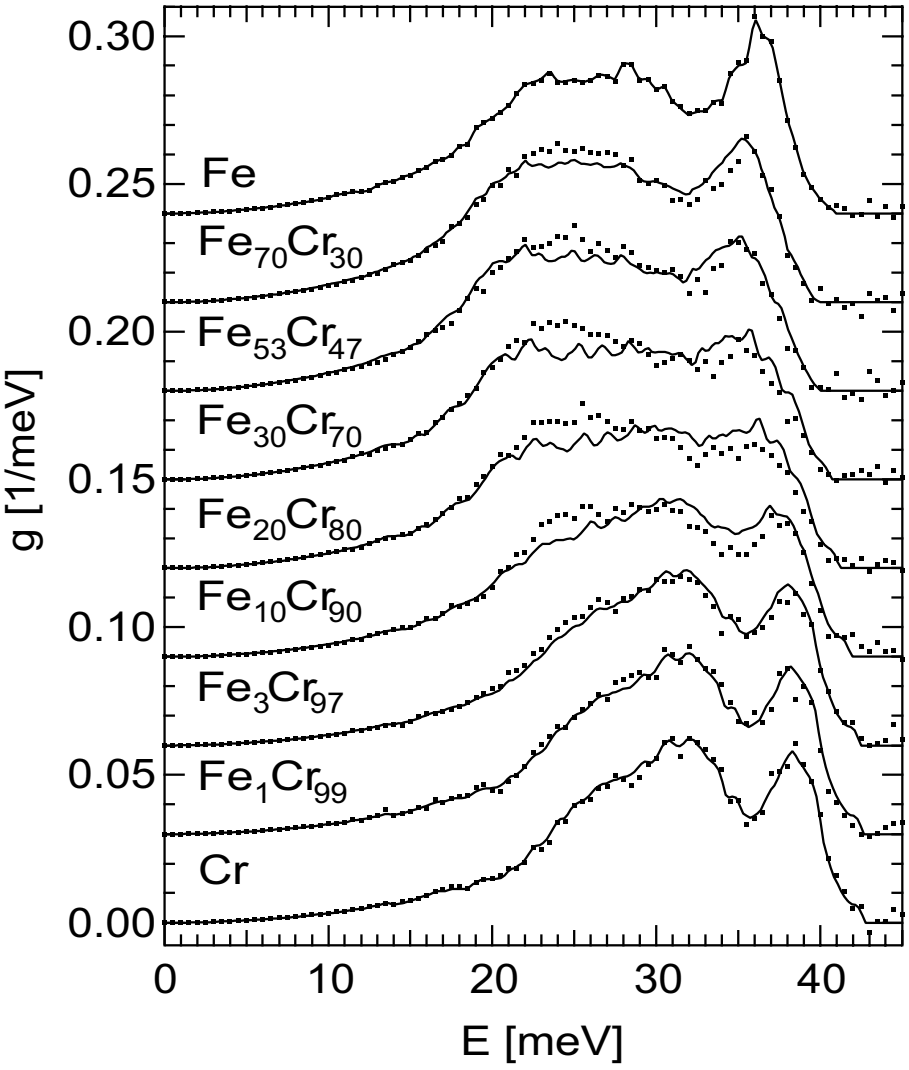

Figure 5.16: Neutron-weight-corrected DOS curves from cluster expansion method (solid line) and measured neutron-weighted DOS curves (dots). Curves are offset by integer multiples 0.03 meV^{-1}.

5.2.5 Phonon Entropy

The phonon entropies of mixing from the neutron-weighted and weight-corrected DOS curves evaluated at 293K are shown in Fig 5.17. The entropy of mixing of the corrected DOS curves is lower than for the measured NWDOS curves due to the higher scattering efficiency of the low-energy Fe modes.

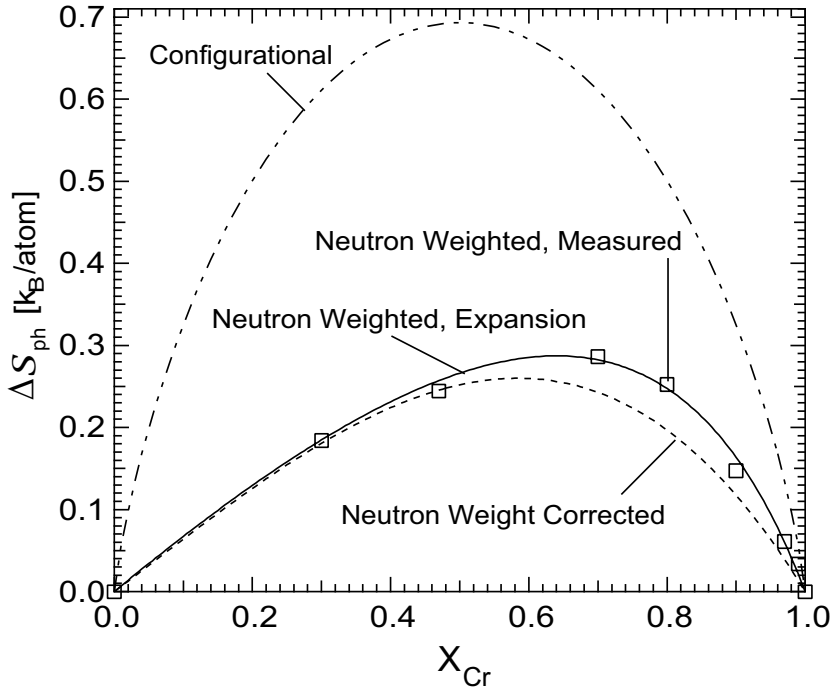

Figure 5.17: Phonon entropy of mixing determined at 293K for measured NWDOS curves (open squares), cluster expansion of measured NWDOS curves (solid line), and neutron-weight-corrected DOS curves (dashed line). The configurational entropy of a fully random solid solution is included to show the relative magnitude of the phonon entropy.

The phonon partial entropy $S_{\rm ph}(\vec{\sigma}_l, d)$ for the specific local chemical arrangement of atom d in a binary system A-B is, in the quasiharmonic approximation,

$$S_{\rm ph}(\vec{\sigma}_l, d) = 3{\rm k_B} \int_0^\infty f^\star(E)\; g(E, \vec{\sigma}_l, d)\; {\rm d}E\;. \tag{5.19}$$

A LOCE in E must be used to show the effects of each term in the cluster expansion for each atom (see Section 3.2.1.1). For a random solid solution using a three-term LOCE, the only contribution to the phonon partial entropy of mixing $\Delta S_{\rm ph}(x_d, d)$ of Equation 3.19 comes from the $n = 2$ term.

The interaction phonon partial entropies $s_n^{\rm ph}(d)$ are listed in Table 5.3 for room temperature and 2000K. Only the $n = 0$ term has a strong dependence on $f^\star(E)$, so Equation 3.19 is approximately independent of temperature. The magnitude of the phonon partial entropy of mixing of Cr is much larger than that of Fe. The function $f^\star(E)$ is largest at low energies, so the differences between $s_2^{\rm ph}$(Fe) and $s_2^{\rm ph}$(Cr) can be primarily attributed to the low-energy modes from 0 to $\sim$ 25 meV.

Table 5.3: Values of Interaction Phonon Entropies

	$s_n^{\rm ph}$(Fe) [k_B/atom]		$s_n^{\rm ph}$(Cr) [k_B/atom]		$s_n^{\rm ph}$ [k_B/atom]	
n \ $T[K]$	293	2000	293	2000	293	2000
0	3.20	8.83	3.14	8.76	3.17	8.795
1	-0.05	-0.05	-0.10	-0.11	0.055	0.13
2	-0.08	-0.11	-0.27	-0.29	-0.25	-0.28
3	-	-	-	-	0.095	0.09

The total phonon entropy of mixing as a function of the interaction partial phonon entropies is given by Equation 3.20 in Section 3.1.1. The function $-4x_{\rm Cr}(1-x_{\rm Cr})$ is a parabola with a maximum at $x_{\rm Cr} = 1/2$. The first term in brackets scales this function. In this case, since both $s_1^{\rm ph}(d)$ are negative, this term introduces a positive entropy of mixing. The remaining terms, associated with $s_2^{\rm ph}(d)$, are the equation of a line. This function introduces an asymmetry to the phonon entropy of mixing when $s_2^{\rm ph}(\text{Fe}) \neq s_2^{\rm ph}(\text{Cr})$. The phonon entropy of mixing is shifted towards pure Cr because $\mathcal{G}_2(E, \text{Cr}) < \mathcal{G}_2(E, \text{Fe})$ in the energy range 0 to $\sim$ 25 meV.

The critical temperature and composition of the miscibility gap in Fe-Cr are 905K and $x_{\rm Cr} = 0.51$, respectively [76]. Assuming no change in the DOS curves as a function of temperature (i.e., anharmonic effects), the values of $s_{\rm ph}^n(d)$ for $n > 0$ do not change appreciably over the temperature range of BCC stability. Equation 3.20 can be used to determine the effect of the phonon entropy on the miscibility gap for spinodal decomposition. When the phonon entropy of mixing in the BCC phase is removed, the miscibility gap shifts up in temperature and towards pure Cr, with a critical temperature and composition of 1268K and $x_{\rm Cr} = 0.61$, respectively (the unmixed BCC phase becomes more stable compared to the mixed BCC phase, so the critical temperature increases). It is known that the enthalpy of mixing is also shifted towards pure Cr [77, 78, 79, 80], so the phonon

entropy counteracts the asymmetry of the enthalpy of mixing (especially at higher temperatures). Thus the role of the phonon entropy of mixing is to lower the critical temperature of the miscibility gap and shift it towards the equiatomic composition.

The cluster expansion analysis delivers a higher level of detail about how the phonon entropy of mixing depends on local arrangements of atoms [73]. At low concentrations of Fe in a Cr host, there is a substantial distortion of the Fe PDOS curves compared to pure Fe, and there is a smaller distortion of the PDOS curves of Cr in Fe (Figure 5.14 and Figure 5.15). A comparison of $\mathcal{G}_1(\mathcal{E}, \mathrm{Fe})$ and $\mathcal{G}_1(\mathcal{E}, \mathrm{Cr})$ (Figure 5.14) shows that the concentration dependence of the PDOS curves is opposite for the transverse modes, but similar for the longitudinal modes. For Fe-Cr alloys, the PDOS curves of both Fe and Cr atoms undergo an average softening upon alloying. This leads to a net positive phonon entropy of mixing, but the net softening of the Cr PDOS curves is greater. At low concentrations of Fe in Cr, the large softening of the Cr PDOS curves (compared to the Fe PDOS of dilute Cr in Fe) causes the phonon entropy of mixing to rise rapidly with Fe concentration, giving a skewness to the concentration dependence of the phonon entropy of mixing versus composition (Figure 5.17). Changes in the shape of the PDOS of the majority species are relatively small, yet most of the phonon thermodynamics of mixing can be attributed to changes in low-energy vibrations of the solvent species, especially Cr. It is expected that other alloy systems will have different entropic weights of their atom species, and these can be quantified by examining the IPDOS functions $\mathcal{G}_n(E, d)$.

5.2.6 Fe-Cr Phase Diagram

In the previous section we discussed the implications of the phonon entropy of mixing on the miscibility gap of Fe-Cr. If one could imagine a device that could turn off the phonon entropy of mixing in the BCC phase, the miscibility gap would shift up in temperature and towards pure Cr. This would be equivalent to artificially setting s_2^{ph} and s_3^{ph} equal to zero in Table 5.3. The question then arises, what if we were to set $s_2^{\mathrm{ph}} = s_3^{\mathrm{ph}} = 0$ with all of the other phases in the Fe-Cr system present? Phrased differently, what happens to the phase diagram of Fe-Cr if we were to turn off the phonon

entropy of mixing in the BCC phase only? Since the stability of the BCC random solid solution is decreased, we expect that all of the other phases will become more stable in comparison.

The Gibbs free energy curves have been determined previously for the Fe-Cr system using the CALPHAD method [76]. The phase diagram calculated from these Gibbs free energy curves is given by dashed lines in Figure 5.18. The phase diagram includes three solid phases: BCC (α), FCC (γ), and Sigma (σ). The BCC phase exhibits spinodal decomposition at lower temperatures. The Fe-rich phase is denoted by α' and the Cr-rich phase by α''. When the phonon entropy of mixing in the BCC phase is removed, the phase diagram is drastically altered (solid lines in Figure 5.18).

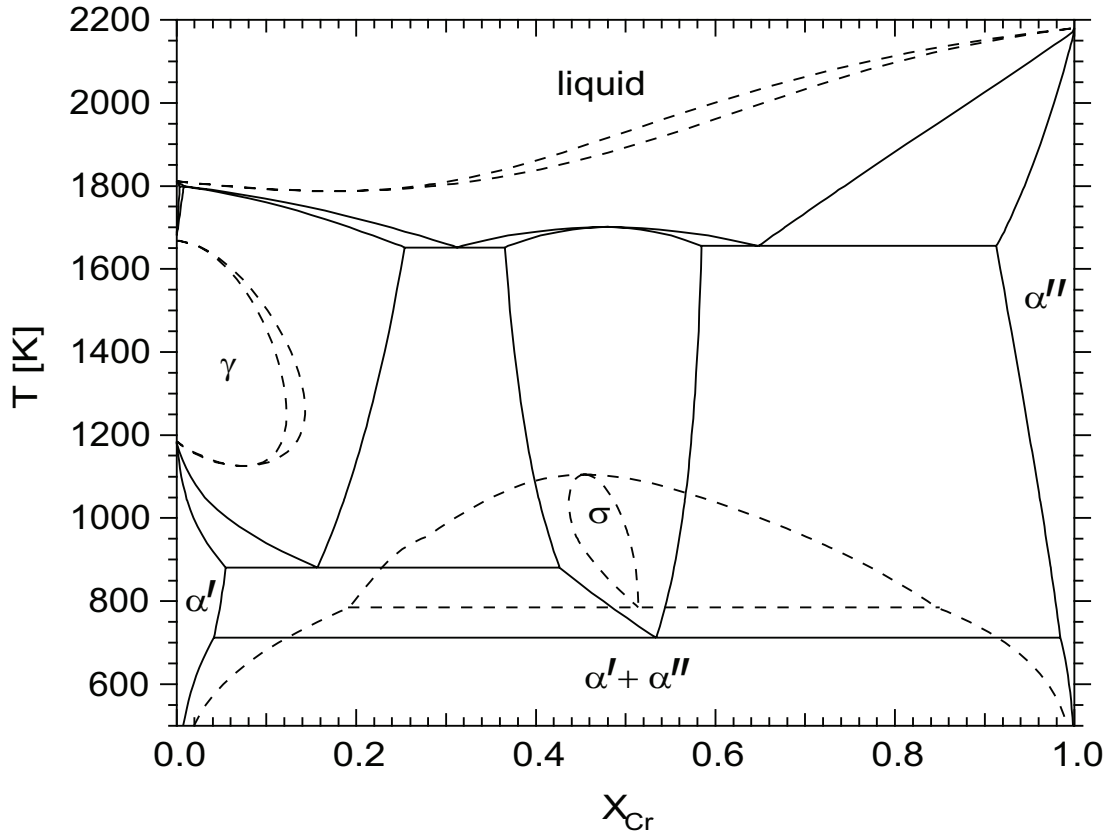

Figure 5.18: Phase diagram of Fe-Cr with the phonon entropy of mixing in the BCC phase set to zero. The dashed lines indicate that actual phase diagram.

Removal of the phonon entropy of mixing in only the BCC phase has the effect of increasing the stability of the FCC and Sigma phases considerably. The liquidus temperature is significantly lowered in the range $x_{\mathrm{Cr}} = 0.2$ to pure Cr. A congruent melting point for the sigma phase occurs at a critical temperature of 1701K and critical composition of $x_{\mathrm{Cr}} = 0.48$. Eutectic phase transitions

occur at critical temperatures of 1652K and 1655K for the $\gamma + \sigma$ and $\sigma + \alpha'$, respectively. Eutectoid transitions occur at critical temperatures of 712K and 881K for $\alpha' + \alpha''$ and $\alpha' + \sigma$, respectively. A peritectic transition occurs at 1799K. It must be noted that a full analysis should also consider the removal of the phonon entropy of mixing for all of the phases present in the phase diagram. However, the present analysis does show that the effect of the phonon entropy on the Fe-Cr phase diagram is probably considerable.

5.2.7 Conclusion

Neutron-weighted phonon density of states (NWDOS) curves were measured by inelastic neutron scattering for Fe-Cr random solid solutions of various compositions. Within the formalism of the cluster expansion, methods for extracting the interaction phonon density of states (IPDOS) functions from the NWDOS curves are described for random solid solutions (Appendix B). From the cluster expansion analysis, phonon partial DOS (PDOS) curves were found for Fe and Cr in the different random solid solutions of Fe-Cr. The Fe PDOS curves are similar to those determined previously by NRIXS, as are the Fe IPDOS functions.

Using Fe and Cr PDOS curves, it is straightforward to correct the inelastic neutron scattering from Fe-Cr alloys for the neutron weighting caused by differences in phonon scattering efficiencies of the two elements. The corrected DOS curves are stiffer than their neutron-weighted counterparts, owing to the higher scattering efficiency of the lower-energy Fe modes, and this lowers the phonon entropy of mixing that would otherwise be deduced from NWDOS curves obtained from a direct reduction of inelastic scattering data under the virtual crystal assumption.

The phonon entropy is dominated by changes in the Cr PDOS curves, which undergo an average softening when Cr atoms are placed in an Fe-Cr host. The softening of the Cr PDOS curves is also responsible for the compositional asymmetry of the phonon entropy of mixing. The dominant effect on the phonon entropy is from changes in the low-energy modes of the Cr PDOS curves caused by 1NN and 2NN Fe neighbors. The phonon entropy both shifts the miscibility gap in composition towards the equiatomic, and lowers the critical temperature by $\sim$ 350K.

5.3 CuAu

5.3.1 Introduction

The Cu-Au system is a model system for studying the stability of alloy phases and order-disorder transitions. In this section we utilize neutron scattering results from literature on the Cu-Au system (this work was done by Peter Bogdanoff, a former student in the Fultz research group) [7]. We apply the cluster expansion analysis described in the previous section for Fe-Cr on the results for Cu-Au, despite their poor counting statistics. The cluster expansion analysis is done to both correct for the neutron weighting and to analyze the effects of the phonon entropy on the critical temperature of the ordered phases, with an emphasis on Cu_3Au. The Cu-Au phase diagram is presented in Figure 5.19. At low temperatures the ordered FCC $L1_0$ and $L1_2$ phases are stable. At modest temperatures the random solid solution is the stable phase. Of the ordered phases present in this system, the $L1_2$-ordered Cu_3Au is best suited for a cluster expansion analysis. The $L1_0$ CuAu phase suffers from a tetragonal or orthorhombic lattice distortion depending on the temperature. The $L1_2$ $CuAu_3$ phase does not have a critical temperature at 25 at.% Cu and has sluggish ordering kinetics. The Cu_3Au phase has a critical concentration of 75 at.% Cu and a critical temperature of 390°C (663K).

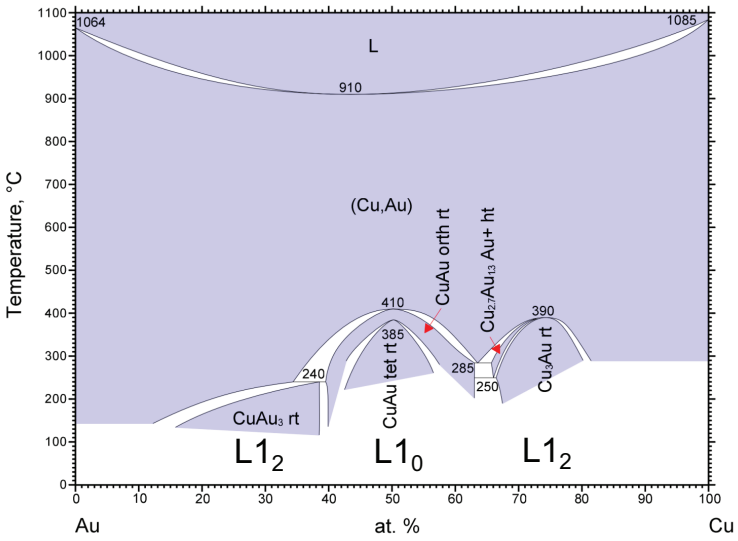

Figure 5.19: Cu-Au phase diagram adopted from ASM International Alloy Phase Diagrams Center [81, 82, 83, 84, 85].

5.3.2 Neutron Scattering

The Cu-Au system has been studied previously using the LRMECS instrument. Alloys of stoichiometric $Cu_{1-x_{Au}}Au_{x_{Au}}$ for $x_{Au} = \{1, 0.75, 0.50, 0.32, 0.25, 0.18, 0.04, 0\}$ in the disordered FCC phase were measured, along with the ordered Cu_3Au FCC alloy. The data analysis procedure used for this data set was similar to that used for the Fe-Cr system. The phonon scattering from natural Cu is 3.21 times stronger than from natural Au; $\sigma_{sc}^{Cu}/m_{Cu} = 3.21\sigma_{sc}^{Au}/m_{Au}$. The NWDOS of the random solid solutions are given in Figure 5.20 and for the ordered Cu_3Au the NWDOS is given in Figure 5.21.

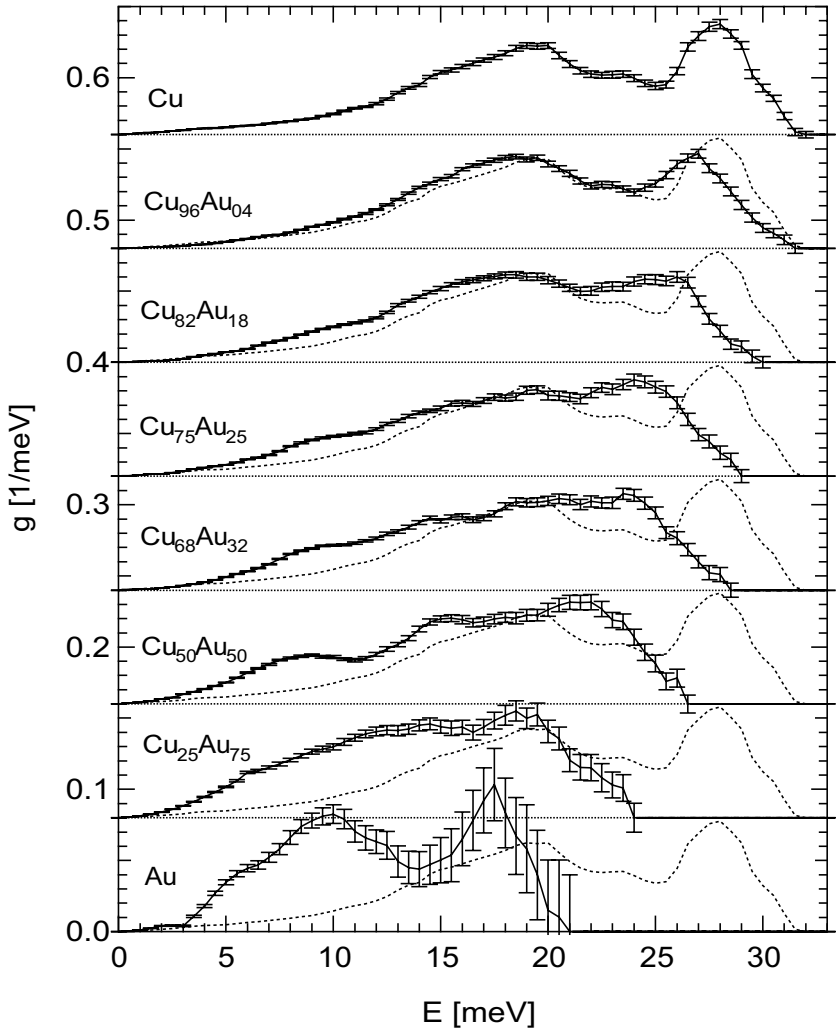

Figure 5.20: Measured phonon density of states curves. Curves are offset by integer multiples 0.08 meV^{-1} [7].

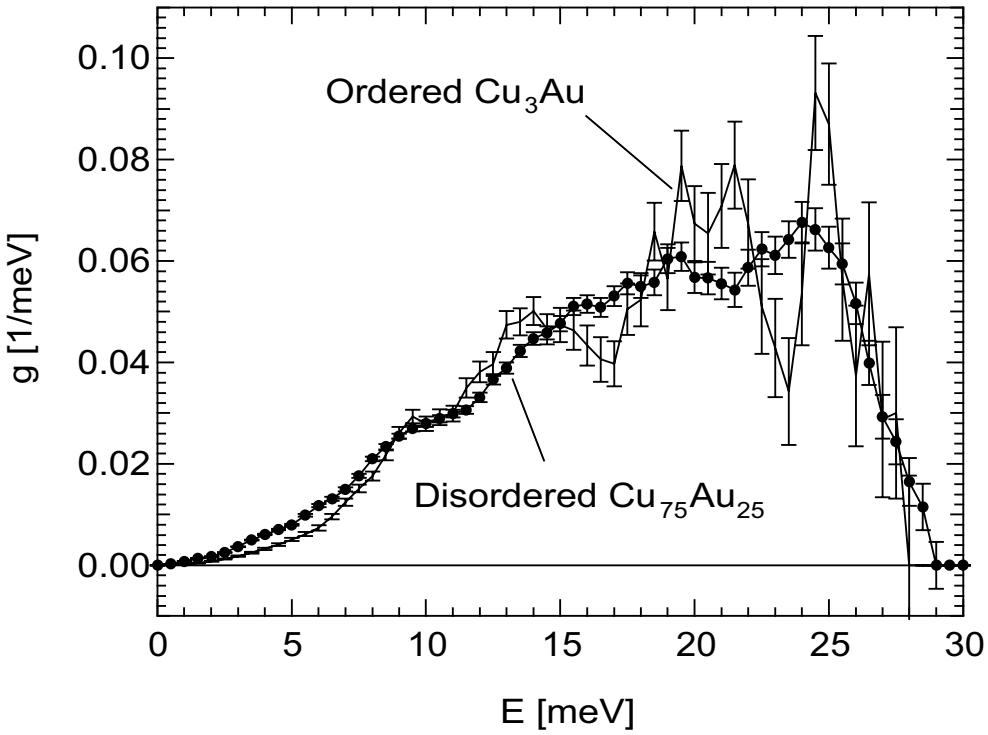

Figure 5.21: Measured phonon density of states curves for Cu_3Au ordered sample (line) and the disordered sample $Cu_{75}Au_{25}$ (points with error bars) [7]

The Cu-Au data set has several interesting features. First, unlike the Fe-Cr system, there is a large variation in the cutoff energy with composition. The dependence on the composition is approximately linear. Second, there is the presence of a resonance mode with a maximum at ~ 9 meV that is associated with higher concentrations of Au. This is especially evident in the $Cu_{50}Au_{50}$ alloy. Last, the ordered Cu_3Au shows much more structure than the disordered $Cu_{75}Au_{25}$. In particular, the optical phonon branch is very clear in the ordered structure (with a peak at ~ 25 meV). There are also clear van Hove singularities in the ordered structure that are not present in the disordered structure. This is consistent with what one might expect of the effects of chemical disorder on the lattice dynamics. Also, there are fewer low energy modes in the ordered structure as compared with the disordered structure.

5.3.3 Cluster Expansion Analysis

In the following analysis the Cu atoms are assigned $\sigma = +1$ and the Au atoms $\sigma = -1$. The first step in the cluster expansion analysis is to rescale the NWDOS by the phonon cutoff energy. The least-squares fitting method can be used to determine the interaction phonon cutoff energies. A four-term expansion is adequate for describing the cutoff in this system. The fit is given by the solid line in Figure 5.22 and the values of ϵ_n^c are given in Table 5.4. The interaction parameters indicate that the linear term dominates the concentration dependence. The rescaled NWDOS are given in Figure 5.23.

Table 5.4: Values of Interaction Cutoff Energy Parameters for Cu-Au

n	ϵ_n^c [meV]
0	26.5653
1	5.07003
2	-0.057372
3	0.428598

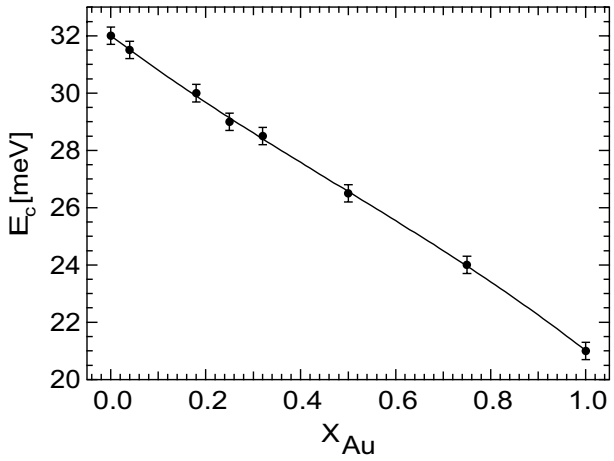

Figure 5.22: Cutoff energy as a function of composition for disordered samples measured (points with error bars) and fit with a four-term cluster expansion (line)

A least-squares fit can be performed to determine the NWIDOS functions from the rescaled NWDOS curves. In turn, the NWIDOS can be used in conjunction with the FCC correlation functions in Table 3.1 in a four-term GCE to determine the NWDOS for the ordered structures (see Figure 5.24). Here we are using a cluster expansion of the phonon properties of only random solid solutions to produce those for an ordered intermetallic compound. Figure 5.24 shows that for

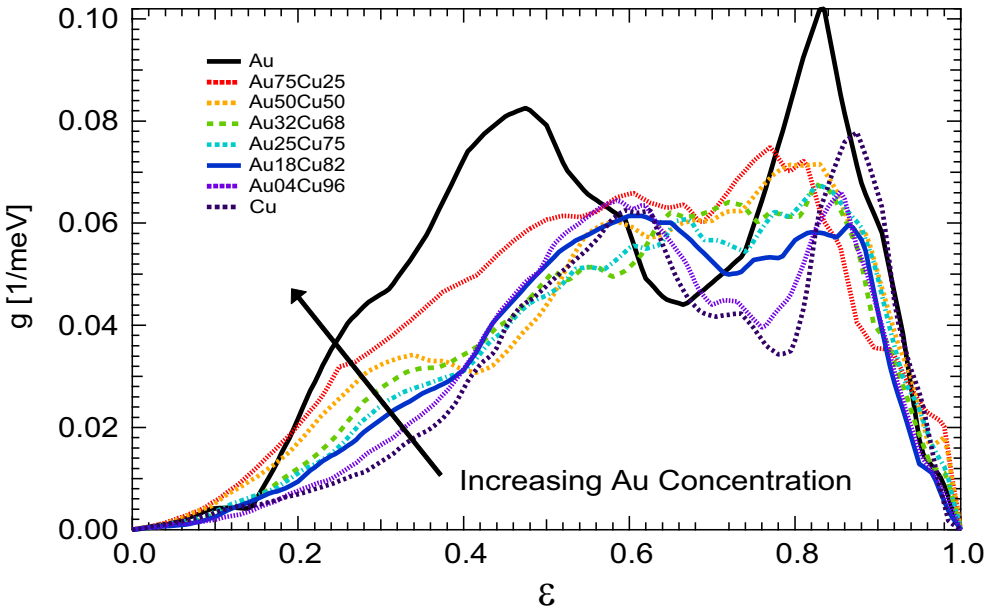

Figure 5.23: Neutron-weighted phonon density of states of Cu-Au random solid solutions measured at LRMECS using the energy relative to the cutoff

Cu_3Au the cluster expansion works remarkably well up to $\sim$ 20 meV; however, above $\sim$ 20 meV the fit is not as good.

The modes above 20 meV for the ordered Cu_3Au sample correspond to the optical phonon branch, whereas the disordered solid solution does not have optical modes. In an ordered intermetallic such as Cu_3Au with two different atoms, the lighter Cu atoms will move in phase with the heavier Au atoms in acoustic modes, and out-of-phase with the Au atoms in the higher-energy optic modes. The effect of disordering is extensive broadening of phonon groups due to the relatively shorter phonon lifetimes. A virtual crystal approximation for disordered alloys excludes the existence of optical modes, since only an average atom is considered. In a triple axis neutron experiment a single crystal of disordered Cu_3Au showed dispersions similar to pure Cu, with no optic modes present [86].

The poor match of the cluster expansion to the ordered sample indicates a fundamental problem with attaining the IDOS and IPDOS functions from disordered properties. When the cluster expansion is performed from measurements of random solid solutions the broadening cannot be "undone," therefore the ordered structures created from these IDOS will also suffer from a heavily broadened acoustic branch even if this is not what physically occurs in the ordered material. The opposite

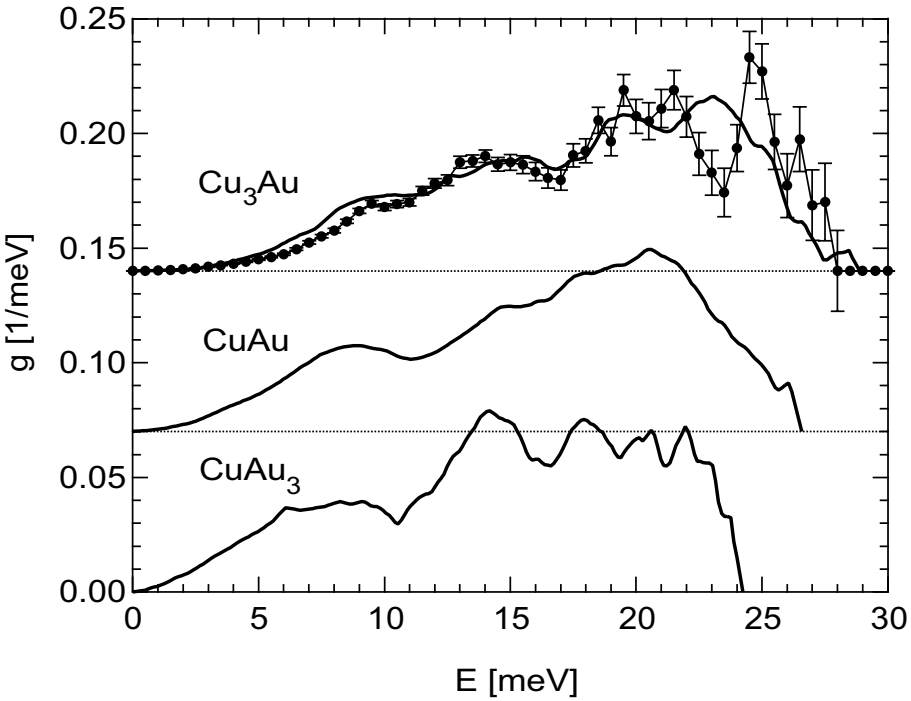

Figure 5.24: Solid lines show neutron-weighted phonon density of states curves for ordered Cu-Au samples from cluster expansion of measured phonon density of states curves of disordered samples using four-term GCE. Points with error bars show measured NWDOS for Cu_3Au-ordered sample. Curves are offset by 0.07 meV^{-1}.

problem occurs when the IDOS and IPDOS are determined from ordered structures only; the disordered structures may not reflect the absence of optical branches. This problem could possibly be solved by performing a cluster expansion on each of the three acoustic branches (one longitudinal and two transverse) and on each of the three optic branches along with appropriate broadening.

Fortunately, the phonon entropy is weighted to the low-energy modes where the cluster expansion works well for the ordered Cu_3Au intermetallic. Continuing with the cluster expansion analysis, the impurity PDOS of Au in Cu is approximated as a resonance mode with a maximum at 9 meV [7]. The impurity PDOS of Cu in Au is approximated using the Mannheim Method (Appendix C) with $K_{\mathrm{Au}}/K_{\mathrm{Cu-Au}} = 1.0$. The impurity PDOS are given in Figure 5.25. Following the method described in the section on Fe-Cr and in Appendix B, the IPDOS of Cu-Au are determined using the NWIDOS functions and impurity PDOS curves for Cu-Au. The IPDOS functions are given in Figure 5.26. From these functions it is apparent that the Cu atoms participate in phonons that are on average of higher energy than the Au atoms.

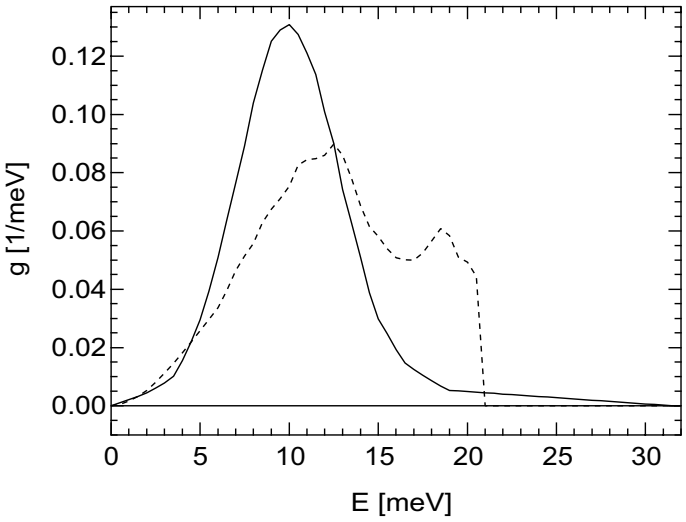

Figure 5.25: Impurity phonon partial density of states curves for Au in Cu (solid line) and Cu in Au (dashed line)

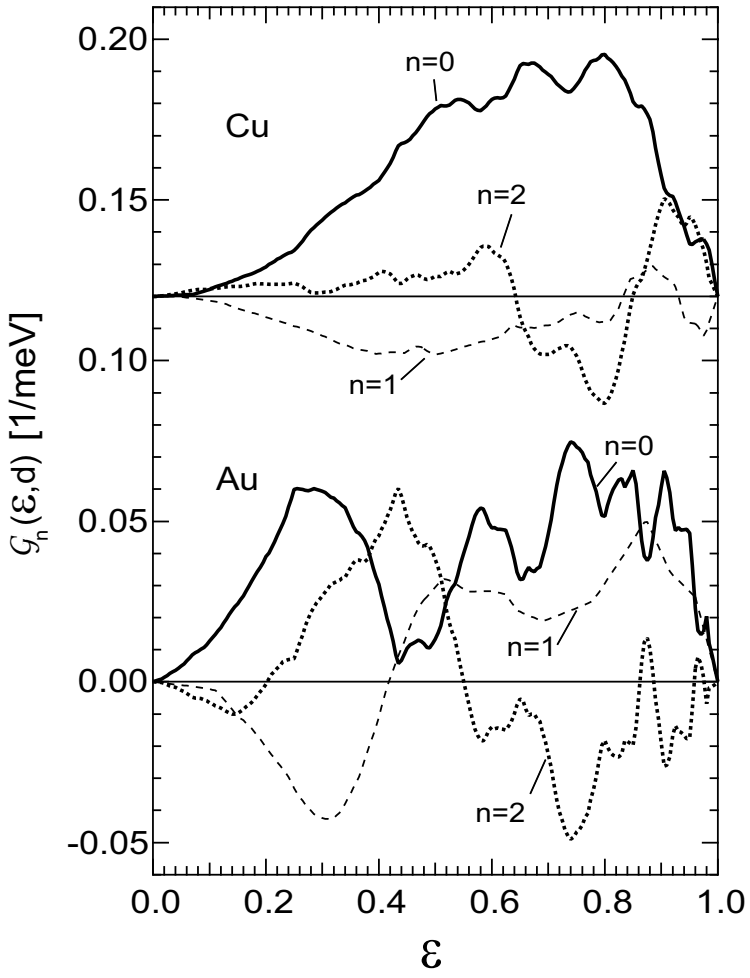

Figure 5.26: Interaction phonon partial density of states curves for Cu and Au in Cu-Au. The Cu IPDOS are offset by 0.12 meV^{-1}.

The IPDOS functions can be used to reconstruct PDOS in ordered and disordered Cu_3Au. This is shown in Figure 5.27. The effect of disordering is to "mix" the Cu and Au PDOS curves. The resonance mode is decreased in the Au PDOS upon disordering, along with increasing the number of high-energy Au modes. In the ordered sample, Au atoms are completely surrounded by Cu atoms in the 1NN shell. This is the reason why the Au PDOS in the ordered state is the same as the impurity Au in Cu PDOS (this would not be the case if we included clusters that extended to the 2NN).

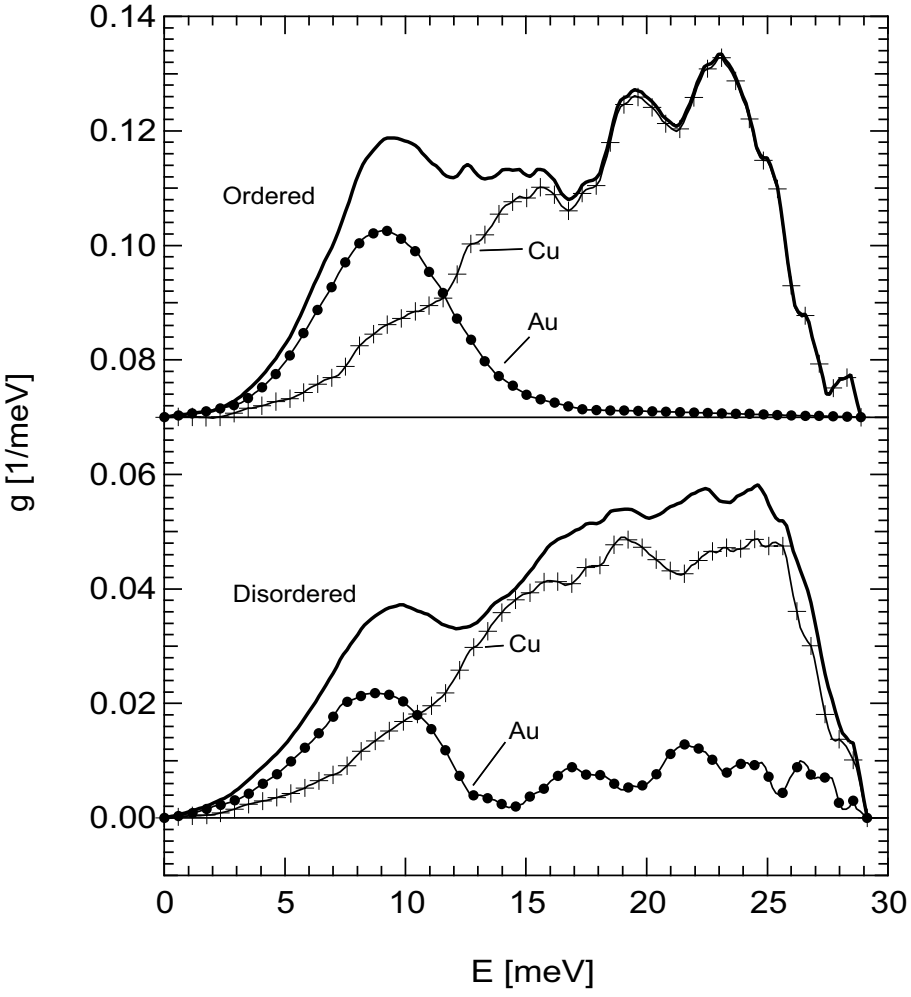

Figure 5.27: Composition-weighted phonon partial density of states curves of Cu (crosses) and Au (solid circles) for Cu_3Au in the ordered (offset by 0.07 meV^{-1}) and disordered states. The solid line indicates the sum of the two PDOS curves and is the neutron-weight-corrected phonon density of states.

5.3.4 Phonon Entropy

In the Fe-Cr system, a cluster expansion in both E and $\mathcal{E}$ gave very similar results owing to the weak configurational dependence of cutoff energy. This is not the case for the Cu-Au system. The dependence of the cutoff energy in this system is approximately linear, so only two terms of ϵ_n^c are necessary. Since a three-term LOCE was used for this system there are a total of 8 terms necessary to describe the IPDOS (ϵ_0^c,ϵ_1^c, $\mathcal{G}_0(\mathcal{E},\mathrm{Cu})$, $\mathcal{G}_1(\mathcal{E},\mathrm{Cu})$, $\mathcal{G}_2(\mathcal{E},\mathrm{Cu})$, $\mathcal{G}_0(\mathcal{E},\mathrm{Au})$, $\mathcal{G}_1(\mathcal{E},\mathrm{Au})$, and $\mathcal{G}_2(\mathcal{E},\mathrm{Au})$). Therefore to describe the phonon partial entropy a total of 8 terms are needed, meaning a four-term LOCE is necessary. This can be expressed mathematically as

$$\sum_{d}^{\mathrm{Cu,Au}} x_d \sum_{n=0}^{3} s_n^{\mathrm{ph}}(d)(1-2x_d)^n = \left[\sum_{n=0}^{1} \epsilon_n^c (1-2x_{\mathrm{Au}})^n\right]^{-1} \int_0^1 f^\star(\mathcal{E}) \left[\sum_{d}^{\mathrm{Cu,Au}} x_d \sum_{n=0}^{2} \mathcal{G}_n(\mathcal{E},d)(1-2x_d)^n\right] \mathrm{d}\mathcal{E}\ . \tag{5.20}$$

This equation shows how the phonon entropy (in terms of the interaction phonon partial entropy) on the LHS can be expressed by the phonon density of states curves (in terms of the interaction phonon partial density of states functions and the interaction cutoff energies) on the RHS. The interaction phonon partial entropies for the Cu-Au system determined in this analysis are given in Table 5.5. From the $s_n^{\mathrm{ph}}(d)$ it is evident that the Cu partial entropy is approximately linear (the $n = 1$ term is greater than the following terms). Also, the phonon entropy of mixing should be positive since $s_1^{\mathrm{ph}}(d)$ is negative for both atom types. The phonon entropy of mixing is also shifted towards pure Cu since $s_2^{\mathrm{ph}}(\mathrm{Au}) > s_2^{\mathrm{ph}}(\mathrm{Cu})$. The partial and total phonon entropies are plotted in Figure 5.28 and the entropy of mixing in Figure 5.29.

Table 5.5: Values of Interaction Phonon Entropies Evaluated at 293K

n	s_n^{ph}(Cu) [k_B/atom]	s_n^{ph}(Au) [k_B/atom]	s_n^{ph} [k_B/atom]
0	4.51	5.06	4.785
1	-0.84	-0.16	-0.615
2	0.13	0.55	-0.32
3	0.08	-0.13	-0.105
4	-	-	-0.05

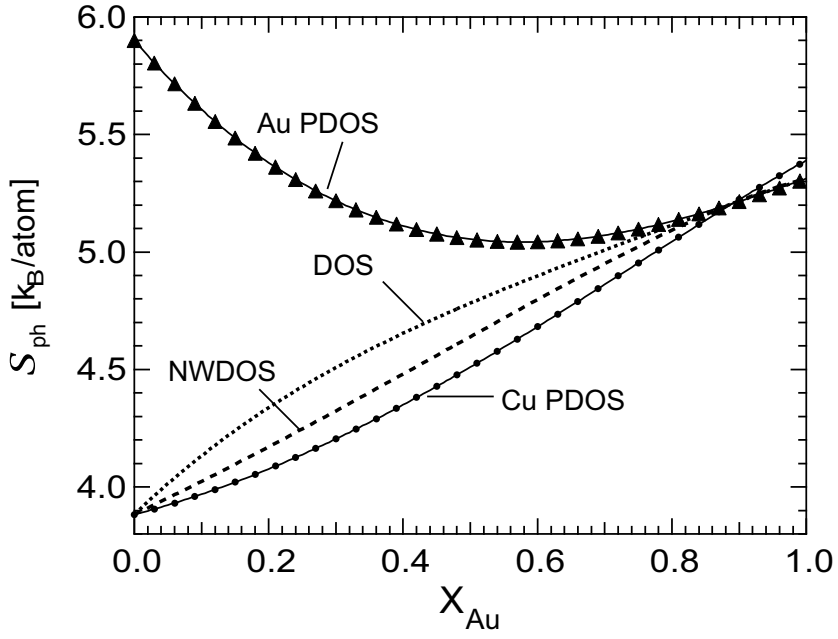

Figure 5.28: Total and partial phonon entropies in the Cu-Au system.

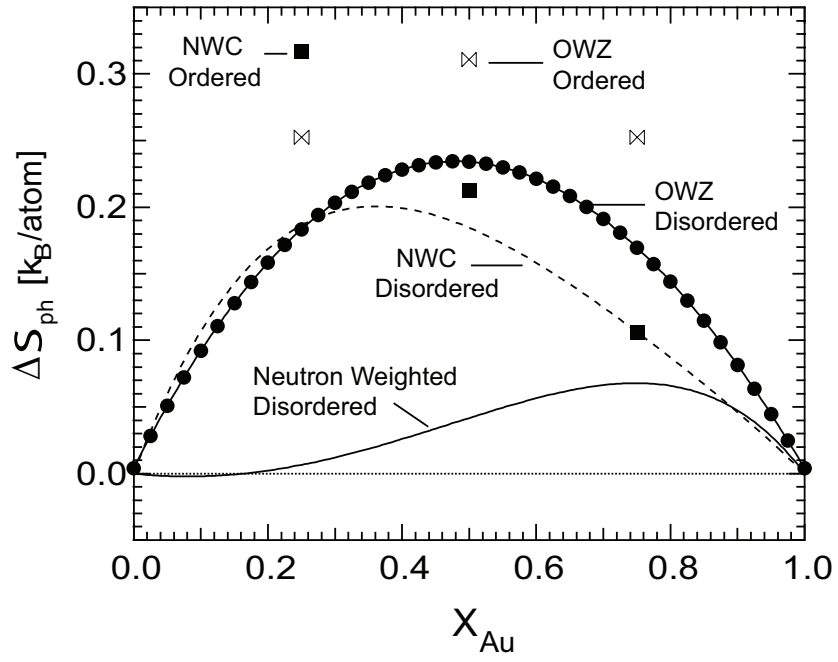

Figure 5.29: Phonon entropy of mixing from the cluster expansion analysis of neutron-weighted (solid line) and neutron-weight-corrected (dashed line) disordered phase in Cu-Au, and neutron-weight-corrected values for the ordered phases in Cu-Au (solid squares). The results of ab initio calculations are labeled OZW [87].

In the Fe-Cr system the neutron weight correction resulted in a small decrease in the phonon entropy of mixing. In stark contrast, the neutron weight correction changes both the shape and magnitude of the phonon entropy of mixing for Cu-Au. The results can be compared to ab initio calculations performed by Ozoliņš, Wolverton, and Zunger (OWZ). The results of the neutron weight correction are surprisingly similar to the results of the calculations. The results for the ordered structures do vary considerably, but they have the same sign and are on the same order of magnitude. In the next section the overall stability of the ordered phases is discussed.

5.3.5 Order-Disorder Phase Transition

In this section we go through the analysis performed on the 1-D linear chain in Chapter 2 for the Cu-Au system.

From the phase diagram of Cu-Au, we know that the FCC random solid solution does not undergo spinodal decomposition, so we concern ourselves only with the stability between the ordered phases and the random solid solution. To simplify the problem we assume that the Gibbs free energy curves for the ordered phases are sharp parabolas with minima at $x_{\mathrm{Au}} = \{0.25, 0.5, 0.75\}$ for Cu_3Au, CuAu, and $CuAu_3$, respectively. A cartoon of the Gibbs free energy curves for this system is given in Figure 5.30. Based on the phase diagram, this assumption is most valid for the Cu_3Au sample and is invalid for $CuAu_3$.

A full analysis of the ordered phases must take into account the configurational entropy as a function of composition, which can be done within the formalism of the cluster expansion. There is also the complication of changes in the short- and long-range order parameter with temperature. A less important correction is the dependence of the enthalpy and phonon entropy on these parameters. Here we examine only the critical temperature of the phase transition. With the assumptions made about the Gibbs free energy curves for the ordered phases, the transition temperature occurs when $G^{\mathrm{ord}} = G^{\mathrm{dis}}$. Therefore we can use the properties of the ordered phases $x_{\mathrm{Au}} = \{0.25, 0.5, 0.75\}$ in our analysis, and ignore the off-stoichiometry properties. Furthermore, we assume the ordered phases to be completely ordered, so that $\Delta S_{\mathrm{config}}^{\mathrm{mix,ord}} = 0$. Much experimental and theoretical work has been

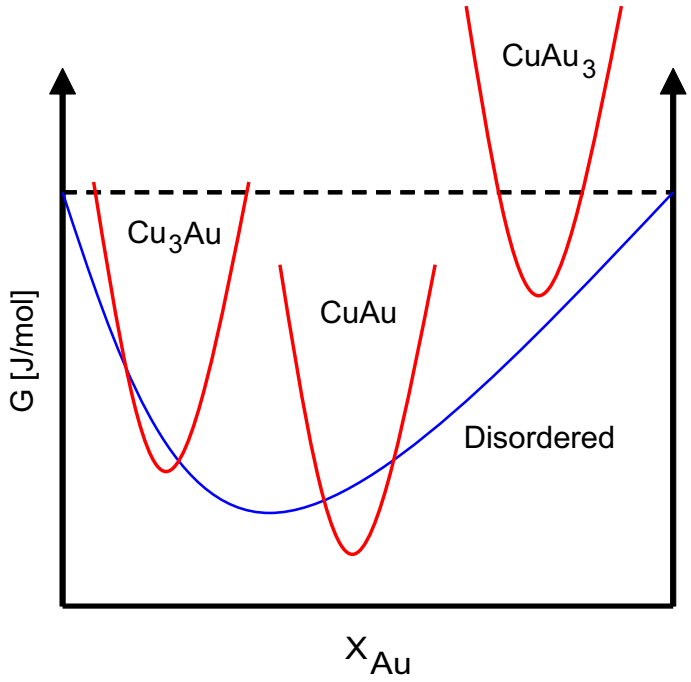

Figure 5.30: Cartoon of Gibbs free energy curves for the Cu-Au system at $T = 300°C$

done on the Cu-Au system, including measurements and calculations of the enthalpy of mixing in the ordered phases [88, 89, 90].

In our assessment we utilize the results of Orr et al. [88] as presented by Sundman et al. [89] for the enthalpy of mixing. The disordered random solid solution is fit using a four-term cluster expansion at both temperatures. From the interaction enthalpies of mixing $\mathcal{L}_n^{\text{mix}}$, the enthalpies of mixing for the ordered phases are constructed. For the 320K data, the ordered values from the cluster expansion match well with the data. For the temperature dependence $\mathcal{L}_n^{\text{mix}}$ a linear interpolation is performed between the 320K and 720K results. Table 5.6 summarizes the parameters used for the enthalpy of mixing.

Table 5.6: Values of Interaction Enthalpies of Mixing

	T[K]		$\mathcal{L}_n^{\text{mix}} = a + b\,T$	
$\mathcal{L}_n^{\text{mix}}$ [J/mol]	320	720	a [J/mol]	b [J/(mol K)]
$\mathcal{L}_0^{\text{mix}}$	-6451.3	-5015.97	-7599.56	3.588325
$\mathcal{L}_1^{\text{mix}}$	-1065.62	-1840.7	-445.556	-1.9377
$\mathcal{L}_2^{\text{mix}}$	6705.01	5081.27	8004.002	-4.05935
$\mathcal{L}_3^{\text{mix}}$	1094.31	1851.8	488.318	1.893725

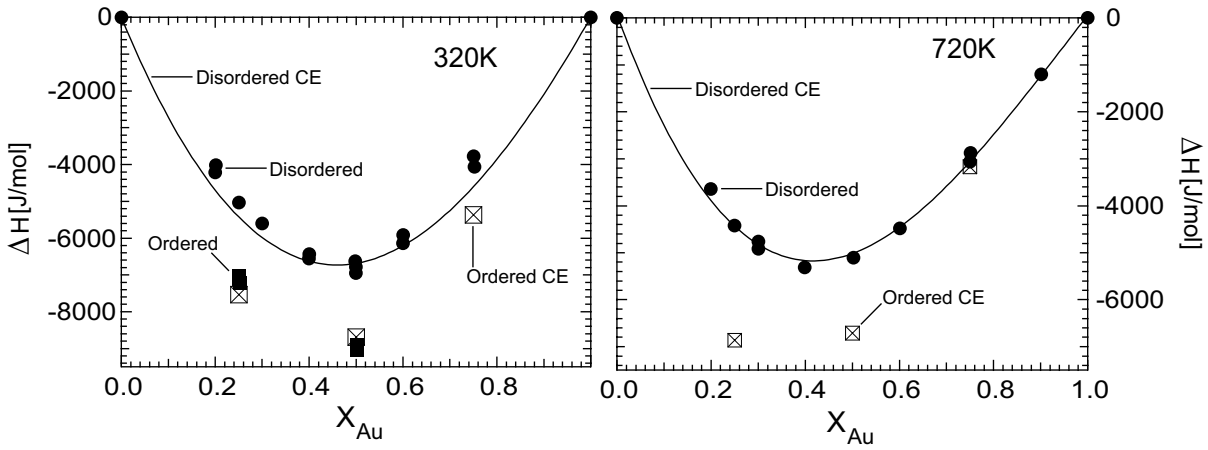

Figure 5.31: Enthalpy of mixing for Cu-Au at 320K (left) and 720K (right). The experimental disordered data are given by solid circles and the ordered data by solid squares. The fit to the disordered data using the cluster expansion is given by the solid line and the ordered properties from the interaction parameters are given by squares with an "X" inside.

The phonon entropies of mixing are shown in Figure 5.29, the configurational entropy of mixing for the disordered random solid solution is given by Equation 2.38, and the entropy of mixing is given by their sum. The configurational entropy of mixing in the ordered phases is assumed to be zero ($\Delta S^{\mathrm{mix,ord}}_{\mathrm{config}} = 0$), as discussed above. Figure 5.32 shows the entropies of mixing for the Cu-Au system used in this analysis.

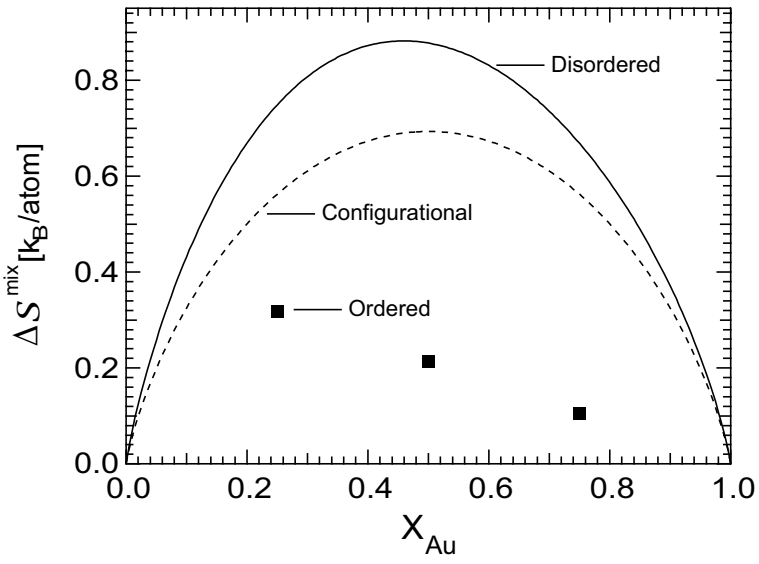

Figure 5.32: Entropy of mixing for the disordered phase (solid line) and ordered phases (solid squares). The configurational entropy of mixing for the disordered phase is given by the dashed line.

With the entropies and enthalpies of mixing, we can determine the Gibbs free energy of mixing for the disordered and ordered phases ($\Delta G^{\mathrm{mix}} = \Delta H^{\mathrm{mix}} - \Delta S^{\mathrm{mix}}\ T$). The temperature at which $\Delta G^{\mathrm{mix,ord}} = \Delta G^{\mathrm{mix,dis}}$ is the critical temperature T_c. Above this temperature the disordered random solid solution is more stable, and below it the ordered phase is more stable. The critical temperatures found using the phonon entropy of mixing determined from the cluster expansion analysis of the neutron scattering results are given in Table 5.7. These values are compared to the experimental ones from the phase diagram of CuAu (Figure 5.19). For Cu_3Au they are almost identical. The critical temperature deduced from the neutron scattering results follows the correct trend for the other ordered structures; however, the magnitudes are substantially different from experimental. At least part of the difference is caused by our failure to account for short- and long-range order parameters. Full ordering is not attained in the Cu-Au ordered phases (especially with the sluggish kinetics of the $CuAu_3$ sample) so that the configurational entropy is greater than zero. A correct account of $\Delta S^{\mathrm{mix,ord}}_{\mathrm{config}}$ would stabilize the ordered phase to higher temperatures, bringing the value of $\mathrm{T_c^{neutron}}$ into better agreement with the phase diagram.

Table 5.7: Critical Temperatures of Ordered Phases

	Cu_3Au	CuAu	$CuAu_3$
$\mathrm{T_c^{neutron}}$ [K]	676	387	247
$\mathrm{T_c^{exp}}$ [K]	663	658	473

5.3.6 Conclusion

The neutron scattering results presented by Bogdanoff et al. [7] were re-analyzed using the cluster expansion technique originally developed for the Fe-Cr system. The Cu and Au PDOS for this system were substantially different, so that the neutron weight correction significantly altered the phonon entropy of mixing that would have otherwise been deduced from the neutron scattering results. The phonon entropy of mixing is found to be positive due primarily to the negative pair interaction phonon partial entropy of the Cu atoms. The phonon entropy of mixing is shifted towards pure Cu due to the large and positive triangle interaction phonon partial entropy of the Au atoms.

The cluster expansion analysis is shown to work well, as the phonon entropy of mixing in the disordered phase matches well with ab initio values presented in the literature. The cluster expansion also does well in expressing the enthalpy of mixing of the ordered phases from the disordered enthalpies. The critical temperature derived from the results discussed in this chapter is quite accurate for the Cu_3Au ordered phase, and has the correct trend for the other two ordered phases. A proper account of the configurational entropy would help to correct the differences.

The cluster expansion fails to reproduce the optical phonon branches in the Cu_3Au ordered sample. This discrepancy is attributed to lifetime broadening of the optical phonon branch with disordering that is not captured with only a few terms in the cluster expansion. We expect this to be a problem for any system when using the cluster expansion to relate disordered DOS from ordered DOS, and vice versa. A solution may be achieved by performing a cluster expansion on the individual phonon branches and introducing a broadening function.

Chapter 6

Conclusions

6.1 Summary

In this thesis the cluster expansion technique was presented as a tool for the analysis of scattering experiments. The focus was on inelastic scattering, where the different types of scattering were discussed in Chapter 1. The cluster expansion was presented using a simple 1-D example in Chapter 2. In Chapter 3 the details of applying the cluster expansion to the phonon density of states (DOS) and phonon partial density of states (PDOS) curves were discussed. This chapter also outlined the application of this technique to other thermodynamic functions and values. In Chapter 4 the results of nuclear resonant inelastic X-ray scattering (NRIXS) performed on binary alloys of ^{57}Fe in V, Cr, and Co were presented. Analysis of the ^{57}Fe PDOS of these alloys revealed that only a few terms in the expansion were needed to characterize the chemical effects. Furthermore, the interaction phonon partial density of states (IPDOS) curves were capable of reproducing the PDOS of thin films of Fe-Cr. In Chapter 5 the cluster expansion was utilized to both correct for neutron weighting of the measured DOS and to show the effects of the phonon entropy on the phase diagram of Fe-Cr.

6.2 Key Points

There are a number of points made in this thesis that are emphasized in the following bullets:

• The cluster expansion can be extended to functions by allowing the interaction parameters to have an energy dependence in the case of the electronic and phonon density of states, and a volume dependence in the case of the bulk modulus. For the phonon density of states, the energy must be rescaled by the cutoff energy.

• The matrix condition number κ of the correlation function matrix $[\xi_{m,n}]$ provides an upper limit on the error bars for the interaction parameters and functions.

• For random solid solutions, the number of terms required for the cluster expansion can be determined experimentally using a least-squares analysis. A least-squares inversion can be performed to determine the interaction parameters and functions when there are more measurements than terms.

• When the number of terms required in the expansion is low, the interaction functions have an intuitive and physically significant interpretation.

• For Fe-Cr, the phonon properties of random solid solutions can be used to reconstruct with reasonable accuracy the properties of thin-film multilayers.

• The effect of alloying on the ^{57}Fe PDOS in the 3d series is a softening of the modes as the average atomic number Z decreases.

• For Fe-Cr, the phonon entropy of mixing is shifted towards pure Cr due to a large softening of the Cr PDOS associated with like and unlike pairs of atoms in the 1NN and 2NN shell of the Cr atoms. The large and positive phonon entropy of mixing plays an important role in the stability of the BCC phase.

• Analysis of the Cu-Au system indicates that the cluster expansion with only a few terms fails to properly account for optical phonons.

6.3 Avenues for Future Research

As with most research, this thesis has raised more questions than it has answered. The purpose of this section is to provide some of the possibilities for future work.

In Chapter 2 the cluster expansion was applied to various values and functions, which indicates that the same methods used to characterize the effects of chemical order on the DOS and PDOS can be used for other types of measurements. For example, the bulk modulus of Equation 3.55 may be measured with several different techniques. Ultrasonic transducers can be used to measure travel times of shear and longitudinal waves through a material of known thickness, giving the speed of sound through the material. Measurement of the density reveals the bulk modulus. Another method of measuring the bulk modulus is by applying isostatic pressure to a material and measuring the volume dependence. This can be accomplished using a diamond anvil cell (DAC) and synchrotron X-ray diffraction. These are elastic scattering experiments and are complementary to measurements of the DOS. Of course there are many other types of properties that depend on the chemical arrangement, so that the results of many other types of measurements may be amenable to analysis with the cluster expansion technique described in this thesis.

All of the measurements made in this thesis were performed at room temperature. When analyzing the effects of the phonon entropy on the phase diagram it was assumed that the anharmonic effects contributed little to the phonon entropy of mixing. This may or may not be the case. For Fe-Cr the DOS of Cr is known to soften substantially with temperature [91]. It would be much more scientifically rigorous to measure the DOS and ^{57}Fe PDOS for all the phases in the entire temperature range of the Fe-Cr phase diagram. Modern spallation neutron sources, such as the SNS at Oak Ridge National Lab, can perform measurements fast enough to make this possible.

Measurements as a function of temperature would also be useful for determining the nature of anharmonic effects in metals. Recent measurements on Ni [70] and Al [92] indicate that anharmonic effects in the DOS of pure metals can be described well by a damped harmonic oscillator function, at least in the case that they exhibit primarily phonon-phonon interactions (as opposed to electron-phonon). This raises the question of whether or not the same analysis can be applied to binary

systems. It is quite possible that separate dampening coefficients may be necessary for the PDOS of each atom. It will likely also be necessary to have a dampening coefficient for each type of mode. The same dampening function may also be able to resolve the issue for the Cu-Au system, where it was found that the cluster expansion failed to reproduce the optical modes of the ordered Cu_3Au sample from the disordered properties.

Some of the tools available to a materials scientist are density functional theory (DFT) computation packages such as VASP [93, 94, 95] and Wien2K [96]. These codes can be used in conjunction with lattice dynamics codes such as PHONON [97] to calculate the phonon density of states. These calculations offer valuable insight into the origins of chemical effects. These programs are especially useful because they can show all of the different contributions to the DOS, including the PDOS of each atom, the projection onto different polarizations, and so forth. The bulk modulus can be determined from the $E(V)$ curves output from VASP, and the electronic density of states may be used to assess the electron-phonon coupling [98, 99]. Calculations on ordered structures are usually straightforward. Unfortunately, calculations on disordered systems are computationally expensive. This is one of the primary uses of the cluster expansion, though there are other methods of attack, such as the use of quasi-random structures. Calculations of the PDOS of ^{57}Fe in Fe-V, Fe-Cr, and Fe-Co alloys would most certainly give a more accurate description of the origin of the observed softening with decreasing average atomic number. The calculations on Fe-Cr would also help to verify the PDOS of Cr atoms presented in Figure 5.15.

The measurements of the PDOS in this thesis were limited to BCC alloys of ^{57}Fe with 3d series elements. There are also large ranges of FCC stability when Fe is alloyed with Ni, Pd, Pt, and Au. These measurements were completed very recently (June 23, 2008) and are in the process of being analyzed. The results for Fe-Au alloys are presented in Figure 6.1 as an example of the quality of the data. One of the interesting aspects of this data set is that the PDOS curve of ^{57}Fe in $^{57}Fe_3Au_{97}$ appears to have a cutoff energy that is several meV higher than that of pure Au (see Figure 5.20). It will be interesting to determine whether or not the IPDOS functions will be able to reproduce the PDOS of ^{57}Fe/Au multilayers [100].

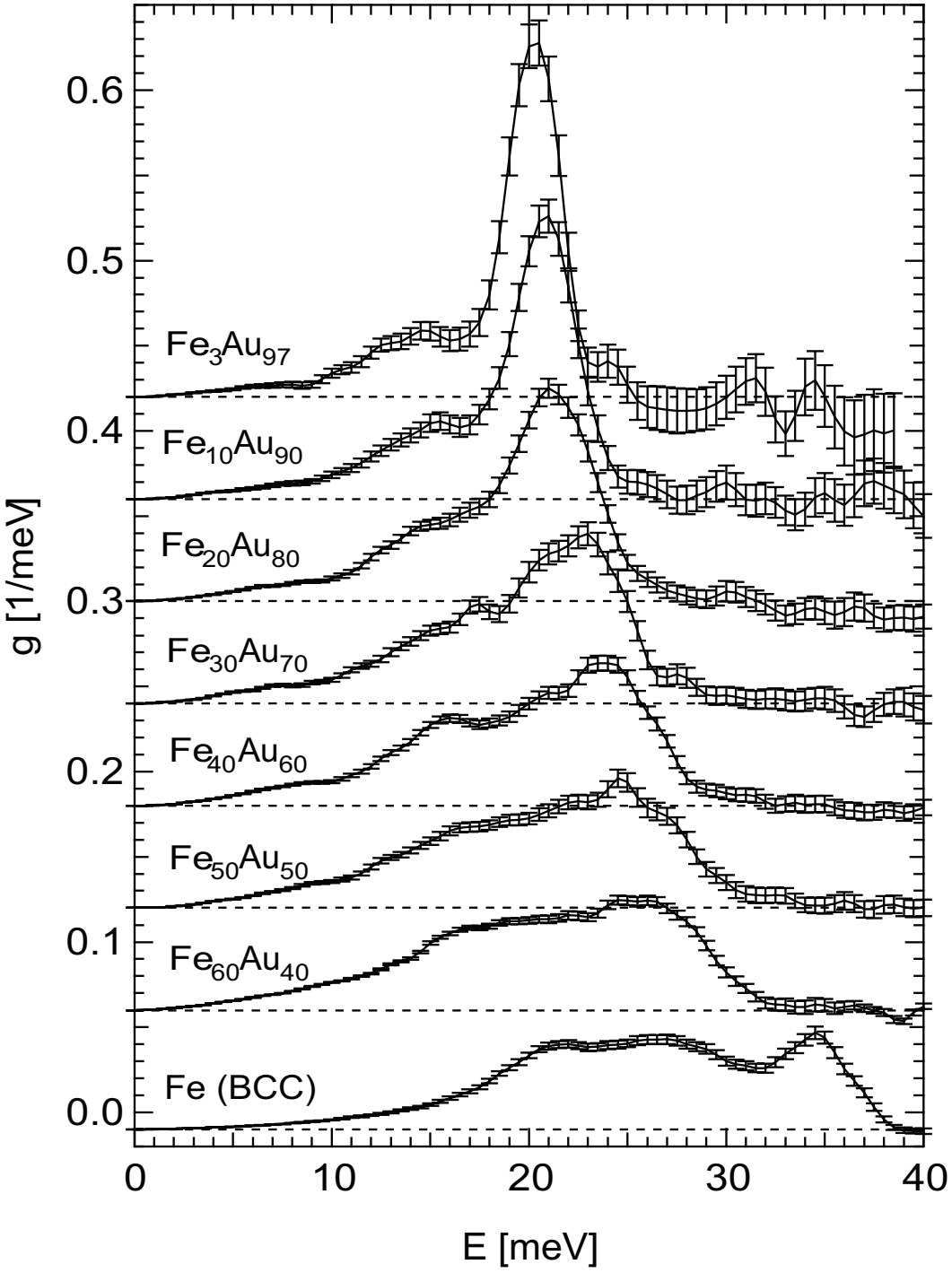

Figure 6.1: ^{57}Fe PDOS curves of FCC Fe-Au alloys recently measured at beamline 16ID-D of the Advanced Photon Source at Argonne National Lab. Curves are offset by integer multiples 0.06 meV^{-1}.

As was done for Fe-Cr, it would be quite advantageous to measure the total density of states curves for the alloys described in this thesis. Neutron scattering measurements on the alloys of Fe-V and Fe-Co would complete these data sets described in Chapter 4. This would allow for determination of the total phonon entropy of mixing, and give the contributions from each of the atom species. The scattering efficiencies of V and Co are similar to that of Cr, so that the analysis would be similar to that provided in Chapter 5 for Fe-Cr. Vanadium is almost entirely an incoherent scatterer, whereas Fe is almost completely coherent. Cobalt is also predominantly an incoherent scatterer. If the two types of scattering can be separated, either by clever masking of $S(Q, E)$ or with computations, this would offer another method of separating the PDOS functions without use of the cluster expansion.

One of the interesting implications of Figure 4.33 and Figure 4.36 is that it becomes possible to predict the ^{57}Fe PDOS based on the average atomic number, at least within the 3d elements between V and Co. If stable BCC phases exist, it is likely that the PDOS of Fe in ternaries and quartnaries may be estimated simply by the average atomic number and average mass.

Quoting from Callister [101], "The discipline of *materials science* involves investigating the relationships that exist between the structures and properties of materials. In contrast, *materials engineering* is, on the basis of these structure-property correlations, designing or engineering the structure of a material to produce a predetermined set of properties." In this thesis the phonon density of states curves of binary alloys were correlated with their chemical arrangement. Although binary alloys are not considered engineering materials, it is the hope of the author that the techniques described in this text will someday be capable of designing new materials with predetermined properties.

Appendix A

Relating the Cluster Expansion and Concentration of Pairs

As noted in Chapter 2, a three-term cluster expansion is equivalent to the concentration of pairs method, so that $S_{\rm ph}^{\rm CE}(\vec{\sigma}) = S_{\rm ph}^{\rm pairs}(\vec{\sigma})$. At first glance it may seem difficult to relate the two methods. Although they give the same answers, the characterizations of the chemical order and their parameterizations are quite different. To solve this problem we write the phonon entropies from each method explicitly in matrix form:

$$S_{\rm ph}^{\rm CE}(\vec{\sigma}) = \left\{ \begin{array}{ccc} \xi_0 & \xi_1 & \xi_2 \end{array} \right\} \left\{ \begin{array}{c} s_0^{\rm ph} \\ s_1^{\rm ph} \\ s_2^{\rm ph} \end{array} \right\} = \left\{ \begin{array}{ccc} \xi_0 & \xi_1 & \xi_2 \end{array} \right\} [\xi_{m,n}]^{-1} \left\{ \begin{array}{c} S_{\rm ph,1} \\ S_{\rm ph,2} \\ S_{\rm ph,3} \end{array} \right\} \tag{A.1}$$

$$\begin{aligned} S_{\rm ph}^{\rm pairs}(\vec{\sigma}) &= \left\{ \begin{array}{ccc} x_{\rm AA} & x_{\rm AB} & x_{\rm BB} \end{array} \right\} \left\{ \begin{array}{c} s_{\rm AA} \\ s_{\rm AB} \\ s_{\rm BB} \end{array} \right\} \\ &= \left\{ \begin{array}{ccc} x_{\rm AA} & x_{\rm AB} & x_{\rm BB} \end{array} \right\} [X_{m,j}]^{-1} \left\{ \begin{array}{c} S_{\rm ph,1} \\ S_{\rm ph,2} \\ S_{\rm ph,3} \end{array} \right\}, \end{aligned} \tag{A.2}$$

where $[X_{m,j}]$ is the matrix of pair concentrations, which in the 1-D example given is equal to the identity matrix. Equating the RHS of Equation A.1 to the RHS of Equation A.2 gives:

$$\left\{ \begin{array}{ccc} \xi_0 & \xi_1 & \xi_2 \end{array} \right\} [\xi_{m,n}]^{-1} \left\{ \begin{array}{c} S_{\mathrm{ph},1} \\ S_{\mathrm{ph},2} \\ S_{\mathrm{ph},3} \end{array} \right\} = \left\{ \begin{array}{ccc} x_{\mathrm{AA}} & x_{\mathrm{AB}} & x_{\mathrm{BB}} \end{array} \right\} [X_{m,j}]^{-1} \left\{ \begin{array}{c} S_{\mathrm{ph},1} \\ S_{\mathrm{ph},2} \\ S_{\mathrm{ph},3} \end{array} \right\} . \tag{A.3}$$

From the communitive property the phonon entropy can be eliminated from both sides, and placing the row vectors on the other side of their matrices as column vectors we have:

$$\left\{ \begin{array}{c} \xi_0 \\ \xi_1 \\ \xi_2 \end{array} \right\} = [\xi_{m,n}] [X_{m,j}]^{-1} \left\{ \begin{array}{c} x_{\mathrm{AA}} \\ x_{\mathrm{AB}} \\ x_{\mathrm{BB}} \end{array} \right\} . \tag{A.4}$$

This equation can be substituted into the first halves of Equations A.1 and A.2, and it is easy to show that a result similar to Equation A.4 arises for relating the interaction entropies and exchange entropies

$$\left\{ \begin{array}{c} s_0^{\mathrm{ph}} \\ s_1^{\mathrm{ph}} \\ s_2^{\mathrm{ph}} \end{array} \right\} = [X_{m,j}]^{\mathrm{T}} \left[[\xi_{m,n}]^{-1} \right]^{\mathrm{T}} \left\{ \begin{array}{c} s_{\mathrm{AA}} \\ s_{\mathrm{AB}} \\ s_{\mathrm{BB}} \end{array} \right\} . \tag{A.5}$$

Our 1-D example makes determination of $[X_{m,j}]^{\mathrm{T}} \left[[\xi_{m,n}]^{-1} \right]^{\mathrm{T}}$ and $[\xi_{m,n}] [X_{m,j}]^{-1}$ rather simple:

$$[X_{m,j}]^{\mathrm{T}} \left[[\xi_{m,n}]^{-1} \right]^{\mathrm{T}} = \frac{1}{4} \left[\begin{array}{ccc} 1 & 2 & 1 \\ 2 & 0 & -2 \\ 1 & -2 & 1 \end{array} \right] \tag{A.6}$$

$$[\xi_{m,n}] [X_{m,j}]^{-1} = \left[\begin{array}{ccc} 1 & 1 & 1 \\ 1 & 0 & -1 \\ 1 & -1 & 1 \end{array} \right] . \tag{A.7}$$

The interaction phonon entropies and the correlation functions of the cluster expansion can be written in terms of the exchange phonon entropies and pair concentrations of the concentration of pairs method:

$$\xi_0 = x_{\mathrm{AA}} + x_{\mathrm{AB}} + x_{\mathrm{BB}} = 1 \tag{A.8}$$

$$\xi_1 = x_{\mathrm{AA}} - x_{\mathrm{BB}} \tag{A.9}$$

$$\xi_2 = x_{\mathrm{AA}} - x_{\mathrm{AB}} + x_{\mathrm{BB}} \tag{A.10}$$

$$s_0^{\mathrm{ph}} = \frac{1}{4}\left[s_{\mathrm{AA}} + 2s_{\mathrm{AB}} + s_{\mathrm{BB}}\right] \tag{A.11}$$

$$s_1^{\mathrm{ph}} = \frac{1}{2}\left[s_{\mathrm{AA}} - s_{\mathrm{BB}}\right] \tag{A.12}$$

$$s_2^{\mathrm{ph}} = \frac{1}{4}\left[s_{\mathrm{AA}} - 2s_{\mathrm{AB}} + s_{\mathrm{BB}}\right] \quad . \tag{A.13}$$

It is important to note that this solution is true for any lattice in any number of dimensions. This universal dimensionality arises because both the concentration of pairs method and three-term cluster expansion reduce all problems to the 1-D case. As an example we consider the case of B2 order on a BCC lattice (Figure A.1). Tracing along the 1NN results in a chain of atoms that is exactly the same as Sample 2 of the example in Chapter 2.

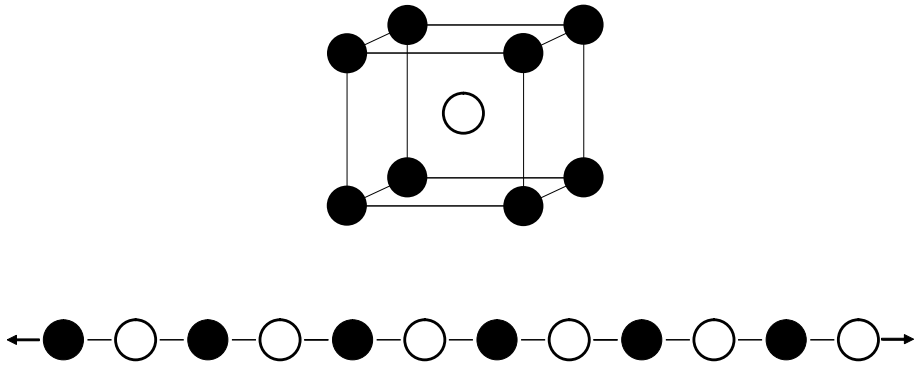

Figure A.1: Top: B2 lattice. Bottom: Chain created by tracing along only the 1NN pairs

Appendix B

Neutron-Weight-Correction Mathematics

First consider the basic problem for an A-B binary alloy using a four-term GCE, which requires 2×3 PDOS curves (2 atom species, three-term LOCE) to describe the 4 DOS curves. Figure B.1 shows that the 4 measured DOS (black squares) used for the GCE (solid line) can never provide enough information to acquire the two PDOS curves (dashed lines). In other words, there must be information on at least one PDOS curve for each atom species in order to solve for the remaining PDOS curves from the measured DOS curves. However, by measuring two DOS of slightly different concentrations than the two end members (open squares with crosses) the difference method described in the text can be used to extract the minority species PDOS (indicated by arrows). In this manner 6 measured DOS can be used to determine the 6 PDOS required to construct the IPDOS. In the remainder of this appendix we describe the mathematics used to extract the IPDOS from the NWDOS.

The NWDOS curves of Equation 5.12, $g_j^{\mathrm{nw}}(\mathcal{E}, \vec{\sigma})$, can be written using Equation 3.3 in the LOCE formalism,

$$g_j^{\mathrm{nw}}(\mathcal{E}, \vec{\sigma}) \left\langle \frac{\sigma_{\mathrm{sc}}}{m} \right\rangle_d^{-1} = \sum_d x_{j,d} \frac{\sigma_{\mathrm{sc},d}}{m_d} g_j(\mathcal{E}, \vec{\sigma}_l, d) \; , \tag{B.1}$$

$$= \sum_d C_j(d) \sum_{n=0}^{\nu_l - 1} \mathcal{G}_n(\mathcal{E}, d)[\xi_{j,n}(d)] \; , \tag{B.2}$$

$$= \sum_d C_j(d) \sum_{n=0}^{\nu_l - 1} [\xi_{j,n}(d)] \sum_{m=0}^{\nu_l - 1} g_m(\mathcal{E}, \vec{\sigma}_l, d) \; [\xi_{m,n}(d)]^{-1} \; , \tag{B.3}$$

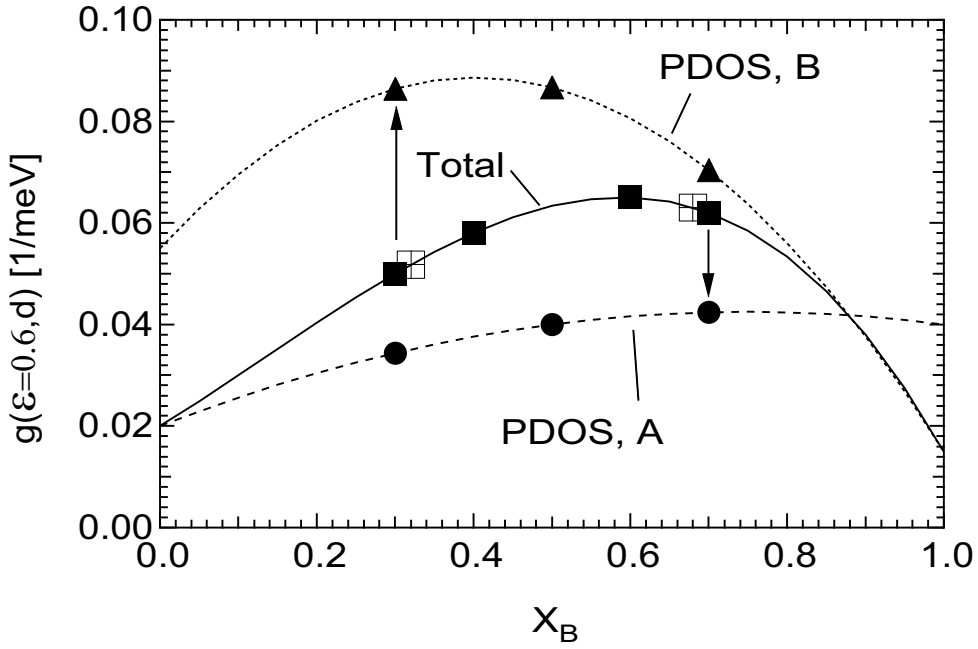

Figure B.1: Example of the cluster expansion method applied to the DOS and PDOS at a particular energy. See the text for a description of the symbols.

where

$$C_j(d) = x_{j,d}\frac{\sigma_{\mathrm{sc},d}}{M_d} \tag{B.4}$$

$$A_j^{-1}(\vec{\sigma}) = \sum_d x_{j,d}\frac{\sigma_{\mathrm{sc},d}}{M_d}\ . \tag{B.5}$$

Here $g_j^{\mathrm{nw}}(\mathcal{E},\vec{\sigma})$ are the NWDOS curves constructed from the cluster expansion for each chemical arrangement $\vec{\sigma}$ corresponding to j. Similarly, $g_m(\mathcal{E},\vec{\sigma}_l,d)$ are the IPDOS curves for each chemical arrangement $\vec{\sigma}$ corresponding to m, and are used to construct $\mathcal{G}_n(\mathcal{E},d)$. The concentrations of each atom species d corresponding to the chemical arrangement of j are $x_{j,d}$. The NWDOS curves may also be written using Equation 3.3 in the GCE formalism,

$$g_j^{\mathrm{nw}}(\mathcal{E},\vec{\sigma})\left\langle\frac{\sigma_{\mathrm{sc}}}{m}\right\rangle_d^{-1} \quad = \quad \sum_{n=0}^{\nu_g-1}\mathcal{G}_n^{\mathrm{nw}}(\mathcal{E})[\xi_{j,n}] \tag{B.6}$$

where $\mathcal{G}_n^{\mathrm{nw}}(\mathcal{E})$ is the neutron-weighted interaction DOS (NWIDOS) functions.

Equation B.6 and Equation B.2 can be used to relate $\mathcal{G}_n^{\rm nw}(\mathcal{E})$ to $\mathcal{G}_n(\mathcal{E},d)$:

$$\begin{aligned}
\mathcal{G}_0^{\rm nw}(\mathcal{E}) &= \frac{1}{2}[\frac{\sigma_{\rm sc,A}}{m_{\rm A}}\mathcal{G}_0(\mathcal{E},{\rm A})+\frac{\sigma_{\rm sc,B}}{m_{\rm B}}\mathcal{G}_0(\mathcal{E},{\rm B})] \\
\mathcal{G}_n^{\rm nw}(\mathcal{E}) &= \frac{1}{2}[\frac{\sigma_{\rm sc,A}}{m_{\rm A}}(\mathcal{G}_{n-1}(\mathcal{E},{\rm A})+\mathcal{G}_n(\mathcal{E},{\rm A})) \\
&+ (-1)^n\frac{\sigma_{\rm sc,B}}{m_{\rm B}}(\mathcal{G}_{n-1}(\mathcal{E},{\rm B})+\mathcal{G}_n(\mathcal{E},{\rm B}))], \\
\mathcal{G}_{\nu_g-1}^{\rm nw}(\mathcal{E}) &= \frac{1}{2}[\frac{\sigma_{\rm sc,A}}{m_{\rm A}}\mathcal{G}_{\nu_l-1}(\mathcal{E},{\rm A})+(-1)^n\frac{\sigma_{\rm sc,B}}{m_{\rm B}}\mathcal{G}_{\nu_l-1}(\mathcal{E},{\rm B})]\ .
\end{aligned} \tag{B.7}$$

This can be written in matrix form:

$$\vec{\mathcal{G}}^{\rm nw}(\mathcal{E}) = ([R]\bullet[C])\ \vec{\mathcal{G}}_{\rm d}(\mathcal{E})\ , \tag{B.8}$$

where the $\bullet$ represents a Hadamard (element-wise) product and $[R]\bullet[C]$ is the matrix that relates the NWIDOS vector $\vec{\mathcal{G}}^{\rm nw}(\mathcal{E})$ with the IPDOS vector $\vec{\mathcal{G}}_{\rm d}(\mathcal{E})$, which are defined as,

$$\vec{\mathcal{G}}^{\rm nw}(\mathcal{E}) = \left\{\begin{array}{c} \mathcal{G}_0^{\rm nw}(\mathcal{E}) \\ \mathcal{G}_1^{\rm nw}(\mathcal{E}) \\ \vdots \\ \mathcal{G}_{\nu_g-1}^{\rm nw}(\mathcal{E}) \end{array}\right\}\ ,\ \vec{\mathcal{G}}_{\rm d}(\mathcal{E}) = \left\{\begin{array}{c} \mathcal{G}_0(\mathcal{E},{\rm A}) \\ \vdots \\ \mathcal{G}_{\nu_l-1}(\mathcal{E},{\rm A}) \\ \mathcal{G}_0(\mathcal{E},{\rm B}) \\ \vdots \\ \mathcal{G}_{\nu_l-1}(\mathcal{E},{\rm B}) \end{array}\right\}\ . \tag{B.9}$$

The elements of the $\nu_g \times 2\nu_l$ matrix $[C]$ of scattering coefficients are given by:

$$C_{n\{j,d\}} = \frac{\sigma_{{\rm sc},d}}{m_d} \tag{B.10}$$

where $\{j,d\}$ is a compound index. For a three-term LOCE, the matrix $[R]$ is given by:

$$[R] = 1/2 \left[\begin{array}{ccc|ccc} 1 & 0 & 0 & 1 & 0 & 0 \\ 1 & 1 & 0 & -1 & -1 & 0 \\ 0 & 1 & 1 & 0 & 1 & 1 \\ 0 & 0 & 1 & 0 & 0 & -1 \end{array}\right] , \tag{B.11}$$

where the left half of the separation denotes the A atom type and the right half the B atom type. Note that the matrix $[R]$ relates the IDOS to the IPDOS functions,

$$\vec{\mathcal{G}}(\mathcal{E}) = [R]\, \vec{\mathcal{G}}_{\rm d}(\mathcal{E}) \ , \tag{B.12}$$

which should be compared to Equation B.8.

The NWIDOS, which are measured in the experiment, can now be written in terms of the PDOS:

$$\vec{\mathcal{G}}^{\rm nw}(\mathcal{E}) = ([R] \bullet [C]) \ \ [\,\overline{\xi}\,]^{-1}\, \vec{\rm g}_{\rm d}(\mathcal{E}) \tag{B.13}$$

where

$$\vec{\rm g}_{\rm d}(\mathcal{E}) = \left\{\begin{array}{c} g_0(\mathcal{E},{\rm A}) \\ \vdots \\ g_{\nu_l-1}(\mathcal{E},{\rm A}) \\ g_0(\mathcal{E},{\rm B}) \\ \vdots \\ g_{\nu_l-1}(\mathcal{E},{\rm B}) \end{array}\right\} \ , \ [\,\overline{\xi}\,] = \left[\begin{array}{cc} [\xi_{m,n}({\rm A})] & [0] \\ [0] & [\xi_{m,n}({\rm B})] \end{array}\right] . \tag{B.14}$$

Here $[\xi_{m,n}(d)]$ are the LOCE correlation function matrices corresponding to the PDOS curves $g_m(\mathcal{E},\vec{\sigma}_l,d)$, which are written as the vector $\vec{\rm g}_{\rm d}(\mathcal{E})$. The PDOS of $\vec{\rm g}_{\rm d}(\mathcal{E})$ must be selected to include the PDOS determined from the difference method (or Mannheim method), which are termed the "known" PDOS curves $\vec{\rm g}_{\rm k}(\mathcal{E},d)$. The remaining, or "unknown," PDOS curves $\vec{\rm g}_{\rm u}(\mathcal{E},d)$ can be

solved for by row reducing the augmented matrix $[([R] \bullet [C]) \;\; [\,\overline{\xi}\,]^{-1} \;\; \vec{\mathcal{G}}^{\mathrm{nw}}(\mathcal{E})]$ and rewriting the system of equations in parametric form [102]. The unknown PDOS curves can then be written as a function of the known PDOS curves and the NWIDOS functions,

$$\vec{g}_{\mathrm{u}}(\mathcal{E}, d) = [\mathcal{S}] \left\{ \begin{array}{c} \vec{\mathcal{G}}^{\mathrm{nw}}(\mathcal{E}) \\ \\ \vec{g}_{\mathrm{k}}(\mathcal{E}, d) \end{array} \right\} , \tag{B.15}$$

where $[\mathcal{S}]$ is the solution matrix and the term in brackets is an augmented column vector. Once $\vec{g}_{\mathrm{u}}(\mathcal{E}, d)$ has been determined, a direct inversion following:

$$\vec{\mathcal{G}}_{\mathrm{d}}(\mathcal{E}) = [\,\overline{\xi}\,]^{-1}\, \vec{g}_{\mathrm{d}}(\mathcal{E}) \tag{B.16}$$

produces the IPDOS functions $\mathcal{G}_n(\mathcal{E}, d)$.

Appendix C

Mannheim Method

The lattice dynamics of crystals with dilute impurities had been investigated by Mannheim using Green's function techniques [57] for interatomic force constants described by a single longitudinal stiffness. The assumption is made that the introduction of the impurity perturbs only the first-nearest-neighbor bonds around the impurity. The only information required for this theory is the DOS of the pure host $g(E, x_{\rm h} = 1)$, the mass ratio of the host to impurity atoms $M_{\rm h}/M_{\rm i}$, and the ratio of the host-host force constant to the impurity-host force constant $K_{\rm h}/K_{\rm i-h}$. $K_{\rm i-h}$ denotes the i $-$ h force constant of impurity i in host h. The PDOS of the impurity is obtained using the following equations, as presented in the article by Seto et al. [46]:

$$\begin{aligned} g(\omega, x_{\rm i}, {\rm i}) &= \left(\frac{M_{\rm h}}{M_{\rm i}}\right) g(\omega, x_{\rm h} = 1) \left\{[1 + \rho(\omega)S(\omega)]^2 + [\frac{\pi}{2}\omega g(\omega, x_{\rm h} = 1)\rho(\omega)]^2\right\}^{-1} \\ &+ \delta(\omega - \omega_L)\left(\frac{M_{\rm h}}{M_{\rm i}}\right)\left\{\rho^2(\omega)T(\omega) + \left(\frac{M_{\rm h}}{M_{\rm i}}\right) - [1 + \rho(\omega)]^2\right\}^{-1}, \end{aligned} \tag{C.1}$$

where

$$\rho(\omega) = \left(\frac{M_{\rm h}}{M_{\rm i}}\right) - 1 + \omega^2\left[1 - \frac{K_{\rm h}}{K_{\rm i-h}}\right]/\mu(+2), \tag{C.2}$$

$$S(\omega) = P\int_0^\infty \omega'^2(\omega'^2 - \omega^2)^{-1} g(\omega', x_{\rm h} = 1)d\omega', \tag{C.3}$$

$$T(\omega) = \omega^4\int_0^\infty (\omega'^2 - \omega^2)^{-2} g(\omega', x_{\rm h} = 1)d\omega', \tag{C.4}$$

$$\mu(n) = \int_0^\infty \omega^n g(\omega, x_{\rm h} = 1) d\omega \, . \tag{C.5}$$

Here ω_L denotes a localized mode frequency that exists only if $\omega_L > \omega_{max}$ and $1 + \rho(\omega_L) S(\omega_L) = 0$, $\delta(\omega - \omega_L)$ is the Dirac delta function, and P stands for the principal value of the integral.

Bibliography

[1] B. Fultz, T. Kelley, M. McKerns, J. Lin, J. Lee, M. Aivazis, and O. Delaire. *Inelastic Neutron Scattering with the ARCS Spectrometer*. http://www.cacr.caltech.edu/projects/ARCS/ARCS/ARCS_Software_Ref_alpha.pdf, 2005.

[2] B. Fultz and J. M. Howe. *Transmission Electron Microscopy and Diffractometry of Materials*. Springer, New York, 2002.

[3] M. L. Boas. *Mathematical Methods in the Physical Sciences*. John Wiley & Sons, New York, 1983.

[4] J. W. D. Connolly and A. R. Williams. *Phys. Rev. B*, 27:5169, 1983.

[5] David R. Gaskel. *Introduction to the Thermodynamics of Materials*. Taylor & Francis, Washington, DC, 1995.

[6] D. Morgan, J.D. Althoff, and D. de Fontaine. *Journal of Phase Equilibria*, 19:559, 1998.

[7] P. D. Bogdanoff, T. L. Swan-Wood, and B. Fultz. *Phys. Rev. B*, 68:14301, 2003.

[8] T. L. Swan-Wood, O. Delaire, and B. Fultz. *Phys. Rev. B*, 72:24305, 2005.

[9] H. Y. Geng, M. H. F. Sluiter, and N. X. Chen. *The Journal of Chemical Physics*, 122:214707, 2005.

[10] D. Chandler. *Introduction to Modern Statistical Mechanics*. Oxford University Press, New York, 1987.

[11] M. Winterrose. *Internal communication*, 2008.

[12] W. L. McMillan. *Phys. Rev.*, 167:331, 1968.

[13] S. Y. Savrasov and D. Y. Savrasov. *Phys. Rev. B*, 54:16487, 1996.

[14] B. N. Harmon and S. K. Sinha. *Phys. Rev. B*, 16:3919, 1977.

[15] F. Sacchetti. *J. Phys. F: Metal Phys.*, 10:801, 1980.

[16] J. Brenner. *The American Mathematical Monthly*, 79:626, 1972.

[17] R. Aldrovandi. *Special Matrices of Mathematical Physics: Stochastic, Circulant and Bell Matrices*. World Scientific, Singapore, 2001.

[18] G. B. Arfken and H. J. Weber. *Mathematical Methods for Physicists*. Elsevier, New York, 2005.

[19] L. May. *An Introduction to Mössbauer Spectroscopy*. Plenum Press, New York, 1971.

[20] R. Röhlsberger. *Nuclear Condensed Matter Physics Using Synchrotron Radiation*. Springer, New York, 2004.

[21] A. I. Chumokov and W. Sturhahn. *Hyperfine Interactions*, 123/124:781, 1999.

[22] T. S. Toellner. *Hyperfine Interactions*, 125:3, 2000.

[23] W. Sturhahn and V. G. Kohn. *Hyperfine Interactions*, 123/124:367, 1999.

[24] K. S. Singwi and A. Sjölander. *Physical Review*, 120:1093, 1960.

[25] M. Y. Hu, W. Sturhahn, T. S. Toellner, P. M. Hession, J. P. Sutter, and E. E. Alp. *Nucl. Instrum. Methods A*, 428:551, 1999.

[26] W. Sturhahn. *Hyper. Inter.*, 125:149, 2000.

[27] M. Seto, Y. Yoda, S. Kikuta, X. W. Zhang, and M. Ando. *Phys. Rev. Letters*, 74:3828, 1995.

[28] W. Sturhahn, T.S. Toellner, E.E. Alp, X. Zhang, M. Ando, Y. Yoda, S. Kikuta, M. Seto, C.W. Kimball, and B. Dabrowski. *Phys. Rev. Letters*, 74:3832, 1995.

[29] E. Burkel. *Rep. Prog. Phys.*, 63:171, 2000.

[30] W. Sturhahn. *J. Phys.: Condens. Matter*, 16:S497, 2004.

[31] J. B. Hastings, D. P. Siddons, U. van Bürck, R. Hollatz, and U. Bergmann. *Phys. Rev. Lett.*, 66:770, 1991.

[32] V. G. Kohn, A. I. Chumakov, and R. Rüffer. *Phys. Rev. B*, 58:8437, 1998.

[33] T. S. Toellner, M. Y. Hu, W. Sturhahn, K. Quast, and E. E. Alp. *Appl. Phys. Lett.*, 71:2112, 1997.

[34] M. Y. Hu, W. Sturhahn, T. S. Toellner, P. D. Mannheim, D. E. Brown, J. Zhao, and E. E. Alp. *Phys. Rev. B*, 67:094304, 2003.

[35] Y.-L. Chen and D.-P. Yang. *Mössbauer effect in Lattice Dynamics*. Wiley-VCH, Weinheim, 2007.

[36] K. Mikke and J. Jankowska. *Phys. Stat. Sol. (b)*, 55:K1, 1973.

[37] W. M. Shaw and L. D. Muhlestein. *Phys. Rev. B*, 4:969, 1971.

[38] B. Fultz, L. Anthony, J. L. Robertson, R. M. Nicklow, S. Spooner, and M. Mostoller. *Phys. Rev. B*, 52:3280, 1995.

[39] T. Ruckert, W. Keune, W. Sturhahn, M. Y. Hu, J. P. Sutter, T. S. Toellner, and E. E. Alp. *Hyperfine Interactions*, 126:363, 2000.

[40] B. V. Ryzhenko and S. V. Pridvizhkin. *Hyper. Inter.*, 72:313, 1992.

[41] H. Kuwano and K. Ôno. *J. Phys. Soc. Japan*, 42:72, 1977.

[42] M. Shiga and Y. Nakamura. *Phys. Stat. Sol. (a)*, 37:K89, 1976.

[43] I. R. Herbert, P. E. Clark, and G. V. H. Wilson. *J. Phys. Chem. Solids*, 33:979, 1972.

[44] M. Shiga and Y. Nakamura. *J. Phys. Soc. Japan*, 49:528, 1980.

[45] E. E. Alp, W. Sturhahn, T. S. Toellner, J. Zhao, M. Hu, and D. E. Brown. *Hyper. Inter.*, 144/145:3, 2002.

[46] M. Seto, Y. Kobayashi, S. Kitao, R. Haruki, T. Mitsui, Y. Yoda, S. Nasu, and S. Kikuta. *Phys. Rev. B*, 61:11420, 2000.

[47] K. C. H. Kumar and V. Raghavan. In *ASM Alloy Phase Diagrams Center*, edited by P. Villars. ASM, Materials Park, OH, http://www.asminternational.org/AsmEnterprise/APD, 1991.

[48] K. C. H. Kumar and V. Raghavan. *Calphad*, 15:307, 1991.

[49] H. Okamoto. *Phase Diagrams for Binary Alloys, Desk Handbook*, 1:1, 2000.

[50] F. Li, J. Yang, D. Xue, and R. Zhou. *J. Magn. Magn. Mater.*, 151:221, 1995.

[51] A. M. Van Der Kraan, D. B. De Mooij, and K. H. J. Buschow. *Phys. Status Solidi A*, 88:231, 1985.

[52] A. M. Van Der Kraan and K. H. J. Buschow. *Physica B+C*, 138:55, 1986.

[53] T. Nishizawa and K. Ishida. In *ASM Alloy Phase Diagrams Center*, edited by P. Villars. ASM, Materials Park, OH, http://www.asminternational.org/AsmEnterprise/APD, 1984.

[54] T. Nishizawa and K. Ishida. *Bull. Alloy Phase Diagrams*, 5:250, 1984.

[55] W. C. Ellis and E. S. Greiner. *Trans. Am. Soc. Met.*, 29:415, 1941.

[56] B. Fultz. *Phys. Rev. B*, 44:9805, 1991.

[57] P. D. Mannheim. *Phys. Rev.*, 165:1011, 1968.

[58] M. S. Lucas, M. Kresch, R. Stevens, and B. Fultz. *Phys. Rev. B*, 77:184303, 2008.

[59] O. Delaire and B. Fultz. *Phys. Rev. Lett.*, 97:245701, 2006.

[60] R. E. Watson and L. H. Bennett. *Phys. Rev. B*, 15:5136, 1977.

[61] R. E. Watson. *Phys. Rev. B*, 24:6211, 1981.

[62] H. Akai, S. Blügel, R. Zeller, and P. H. Dederichs. *Phys. Rev. Lett.*, 56:2407, 1986.

[63] J. Chojcan and M. Szuszkiewicz. *Physica Scripta*, 36:820, 1987.

[64] I. Dézsi, U. Gonser, and G. Langouche. *Phys. Rev. Lett.*, 62:1659, 1989.

[65] J. Chojcan and M. Szuszkiewicz. *Hyperfine Interactions*, 59:513, 1990.

[66] L. A. Terrazos and S. Frota-Pessôa. *Phys. Rev. B*, 56:13035, 1997.

[67] R. C. O'Handley. *Modern Magnetic Materials*. John Wiley and Sons, New York, NY, 2000.

[68] R. S. Eccleston. In *Neutron Data Booklet,* $2.6 : 1 - 8$, edited by Albert-José Dianoux and Gerry Lander. Old City Publishing, Philadelphia, PA, 2003.

[69] J. Tao, C. J. Benmore, T. G. Worlton, J. M. Carpenter, D. Mikkelson, R. Mikkelson, J. Siewenie, J. Hammonds, and A. Chatterjee. *Nucl. Ins. Meth. Phys. Res. A*, 562:422, 2006.

[70] M. Kresch, O. Delaire, R. Stevens, J. Y. Y. Lin, and B. Fultz. *Phys. Rev. B*, 75:104301, 2007.

[71] F. W. de Wette and A. Rahman. *Physical Review*, 176:784, 1968.

[72] V. F. Sears, E. C. Svensson, and B. M. Powell. *Can. J. Phys.*, 73:726, 1995.

[73] M. S. Lucas, A. Papandrew, B. Fultz, and M. Y. Hu. *Phys. Rev. B*, 75:54307, 2007.

[74] O. Delaire, T. Swan-Wood, and B. Fultz. *Phys. Rev. Lett.*, 93:185704, 2004.

[75] D. G. Howard and R. H. Nussbaum. *Phys. Rev. B*, 9:794, 1974.

[76] J.-O. Andersson and B. Sundman. *Calphad*, 11:83, 1987.

[77] T. Chart, F. Putland, and A. Dinsdale. *Calphad*, 4:27, 1980.

[78] A. Caro, M. Caro, E. M. Lapasso, and D. A. Crowson. *Applied Physics Letters*, 89:121902, 2006.

[79] P. Olsson, I. A. Abrikosov, L. Vitos, and J. Wallenius. *Journal of Nuclear Materials*, 321:84, 2003.

[80] E. G. Moroni and T. Jarlborg. *Phys. Rev. B*, 47:3255, 1993.

[81] H. Okamoto, D. J. Chakrabarti, D. E. Laughlin, and T. B. Massalski. In *ASM Alloy Phase Diagrams Center*, edited by P. Villars. ASM, Materials Park, OH, http://www.asminternational.org/AsmEnterprise/APD, 2006.

[82] H. Okamoto, D. J. Chakrabarti, D. E. Laughlin, and T. B. Massalski. In *Binary Alloy Phase Diagrams, II Ed.*, Vol. 1:358-362, edited by T. B. Massalski. ASM International, Materials Park, OH, 1990.

[83] K. Okamura, H. Iwasaki, and S. Ogawa. *J. Phys. Soc. Jpn.*, 24:569, 1968.

[84] M. Kogachi and S. Ishibata. *Nippon Kinzoku Gakkaishi*, 47:912, 1983.

[85] H. L. Yakel. *J. Appl. Phys.*, 33:2439, 1962.

[86] E. D. Hallman. *Can. J. Phys.*, 52:2235, 1974.

[87] V. Ozoliņš, C. Wolverton, and A. Zunger. *Phys. Rev. B*, 58:R5897, 1998.

[88] R. L. Orr, J. Luciat-Labry, and R. Hultgren. *Acta Metallurgica*, 8:431, 1960.

[89] B. Sundman, S. G. Fries, and W. A. Oates. *Calphad*, 22:335, 1998.

[90] W. Cao, Y. A. Chang, J. Zhu, S. Chen, and W. A. Oates. *Intermetallics*, 15:1438, 2007.

[91] J. Trampenau, W. Petry, and C. Herzig. *Phys. Rev. B*, 47:3132, 1993.

[92] M. Kresch, M. Lucas, O. Delaire, J. Y. Y. Lin, and B. Fultz. *Phys. Rev. B*, 77:024301, 2008.

[93] G. Kresse and J. Furthmüller. *VASP the Guide.* Institute für Materialphysik, Wien, Austria, 2005.

[94] G. Kresse and J. Furthmüller. *Comput. Mater. Sci.*, 6:15, 1996.

[95] G. Kresse and D. Joubert. *Phys. Rev. B*, 59:1758, 1999.

[96] P. Blaha, K. Schwarz, and P. Sorantin. *Comput. Phys. Commun.*, 59:399, 1990.

[97] K. Parlinsky. *Software PHONON.* Institute of Nuclear Physics, Polish Academy of Sciences, Cracow, Poland, 2005.

[98] O. Delaire, M. Kresch, J. A. Munõz, M. S. Lucas, J. Y. Y. Lin, and B. Fultz. *Phys. Rev. B*, 77:214112, 2008.

[99] O. Delaire, M. S. Lucas, J. A. Munõz, M. Kresch, and B. Fultz. *Phys. Rev. Lett. (submitted)*, 2008.

[100] E. E. Alp, W. Sturhahn, and T. S. Toellner. *J. Phys.: Condens. Matter*, 13:7645, 2001.

[101] Jr. W. D. Callister. *Materials Science and Engineering.* John Wiley and Sons, New York, NY, 2000.

[102] D. C. Lay. *Linear Algebra and its Applications*, Chapter 1. Addison Wesley, New York, NY, 2003.